Studies of field distortions in a Time Projection Chamber for the International Linear Collider

Dissertation

zur Erlangung des Doktorgrades
an der Fakultät für Mathematik, Informatik und
Naturwissenschaften

Fachbereich Physik
der Universität Hamburg

vorgelegt von

Klaus Zenker

aus Cottbus

Hamburg
2014

Tag der Disputation:	10.12.2014
Folgende Gutachter empfehlen die Annahme der Dissertation:	Prof. Dr. Erika Garutti Dr. Ties Behnke

Abstract

The International Linear Collider (ILC) will allow to do precision measurements of Standard Model parameter and to search for new physics. The ILD detector concept, which is developed for the ILC, uses a Time Projection Chamber (TPC) as central tracking device. The momentum resolution goal for the ILD TPC is $\delta(1/p_t) \simeq 10^{-4}\,(\mathrm{GeV/c})^{-1}$ at a magnetic field of $B = 3.5\,\mathrm{T}$.

Field distortions of the magnetic or electric field inside the sensitive volume of the TPC distort the momentum measurements. Therefore, one needs to keep them under control and correct them with high precision.

In this thesis the main sources of field distortions in the TPC are identified and their effects are determined. Furthermore, possibilities to reduce the identified field distortions are presented. One known source of distortions of the electric field are ions, produced by the gas amplification in the TPC anode, that drift into the sensitive volume of the TPC. In the first part of this work the creation of these ions in Gas Electron Multiplier (GEM), which are used for the gas amplification, is studied. It will be shown that the resulting field distortions are not acceptable at the ILD TPC. By tuning the parameters of the gas amplification at the anode the field distortion can be reduced, which is shown in measurements and simulations. In addition measurements using a modified GEM will show that it is possible to further reduce the field distortions with such a GEM.

In the second part of this work field distortions arising at boundaries between individual readout modules are investigated using simulation studies. It will be shown in simulations, which are verified by measurement results, that these field distortions significantly influence the readout module performance. Based on the simulation results the GEM based readout module developed at DESY is optimised and the field distortions are reduced. These performance improvements could also be verified in measurements.

Finally, a laser calibration system is used to study the overall field distortions in a large TPC prototype. In these measurements distortions of the electric field as well as of the magnetic field are found and quantified. With the presented measurements the capabilities of a laser calibration system are illustrated. They are not limited to measuring field distortions, but the laser calibration system also allows to monitor other TPC parameters. This is shown in the case of the drift velocity.

Kurzdarstellung

Für die Suche nach neuer Physik und die präzise Vermessung des Standard Modells ist ein neuer Linearbeschleuniger (ILC) geplant. Das ILD Detektorkonzept, welches für diesen Beschleuniger entwickelt wird, sieht die Verwendung einer Zeit-Projektionskammer (TPC) als zentrale Spurkammer vor. Die Impulsauflösung, die mit dieser TPC erreicht werden soll, beträgt $\delta(1/p_{\mathrm{t}}) \simeq 10^{-4}\,(\mathrm{GeV/c})^{-1}$ bei einer Magnetfeldstärke von $B = 3,5\,\mathrm{T}$.
Feldverzerrungen des elektrischen und des magnetischen Feldes in der TPC können zu einer Verfälschung der Messungen führen, was eine Reduktion der Impulsauflösung zur Folge hat. Daher ist das Ziel, die Auswirkungen der Feldverzerrungen zu beschränken, indem diese mit einer hohen Genauigkeit bestimmt und korrigiert werden.
Die vorliegende Arbeit beschäftigt sich damit, die Hauptquellen von Feldverzerrungen im sensitiven Volumen der TPC zu identifizieren, ihre Auswirkungen abzuschätzen und die gefundenen Quellen von Feldverzerrungen zu reduzieren. Eine bekannte Quelle von Verzerrungen des elektrischen Feldes im sensitiven Volumen der TPC sind Ionen, die bei der Elektronenverstärkung in der Anode erzeugt werden und durch das elektrische Feld in das sensitive Volumen der TPC gelangen. Im ersten Teil der Arbeit wird die Erzeugung der Ionen in der Gasverstärkung mit Gas Electron Multiplier (GEM) Folien studiert. Im Rahmen dieser Studie wurden sowohl Messungen mit einem Prototyp als auch detallierte Simulationen des Verstärkungsprozesses genutzt. Die Resultate zeigen, dass die erwarteten Verzerrungen durch Ionen in der TPC zu groß sind um die Ziele der ILD TPC zu erreichen. In diesem Zusammenhang wurden verschiedene Betriebsparameter getestet und gezeigt, wie der Einfluss dieser auf die Anzahl der das sensitive Volumen der TPC erreichenden Ionen ist. Anschließend wurde eine modifizierte GEM genutzt um zu zeigen wie man die Anzahl dieser Ionen mittels geeigneter GEMs verringern kann.
Im zweiten Teil der Arbeit wurden Simulationsstudien zu Feldverzerrungen an Prototyp-Auslesemodulen, die für den ILD entwickelt werden, durchgeführt. In Übereinstimmung mit Messdaten konnte gezeigt werden, dass an den Grenzen zwischen einzelnen Modulen signifikante Verzerrungen des elektrischen Feldes entstehen. Eine auf den Simulationsergebnissen basierende Optimierung des am DESY entwickelten Auslesemoduls führte zu einer Reduktion der Verzerrungen und einer Steigerung der Ausleseeffizienz am Modulrand. Dies konnte auch anhand von Messdaten verifiziert werden.
Abschließend wurde ein Laserkalibrationssystem für die Messung der Gesamtverzerrungen in einem TPC Prototypen genutzt. Dabei wurden sowohl Verzerrungen des elektrischen Feldes als auch des magnetischen Feldes gemessen. Im Rahmen dieser Studien werden auch weitere Anwendungsmöglichkeiten eines solchen Systems diskutiert.

Contents

1

Introduction

On 4 July 2012 the discovery of a new resonance with a measured mass of about 125 $\mathrm{GeV/c^2}$ [1, 2] was announced by the two general purpose experiments at the proton-proton collider LHC – ATLAS and CMS. This resonance is a strong candidate for the Higgs boson predicted by the Standard Model (introduced in Section 1.1) and its discovery would mark the latest success of the Standard Model. The formalism resulting in the prediction of the Higgs boson was first formulated in 1964 [3, 4]. Much later, in 1989, the first extensive search for the Higgs boson started at the predecessor machine of the LHC, which was an electron-positron collider called LEP. With this machine many quantities of the Standard Model, for example the mass of the W [5] and Z [6] boson, were measured very precisely for the first time. These measurements confirmed the Standard Model and put it on a solid basis of empirical data down to quantum-loop level. The discovery of the W and Z boson was worked out already at another collider at CERN[1], which collided protons and antiprotons (SPS). In between the shutdown of LEP and the first operation of the LHC, another hadron collider – the proton-antiproton collider Tevatron – was used to search for the Higgs boson. Although the experiments at the Tevatron could not claim the first Higgs discovery, in 1995 they could announce the discovery of the top quark [7], which was another missing piece in the experimental confirmation of the Standard Model. Moreover, its mass was found to be exactly the mass predicted from the Standard Model precision measurements at LEP and the Standford Linear Collider, which also collided electrons and positrons and was operated from 1992 to 1998.

[1]European Organization for Nuclear Research, CH-1211 Geneva 23, Switzerland

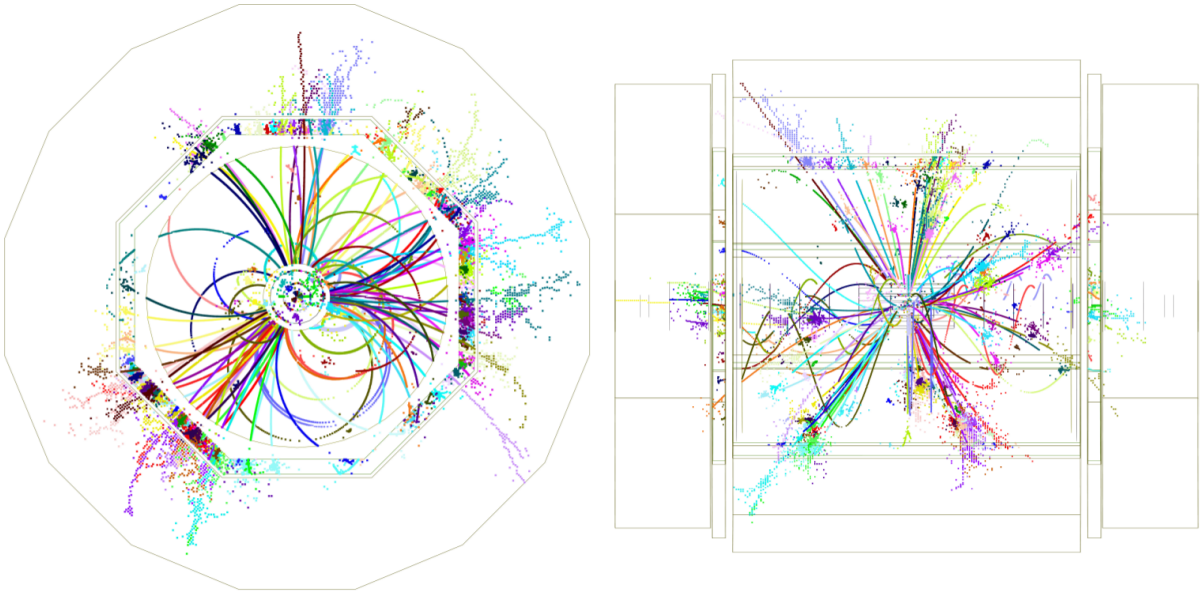

(a) Front view of the ILD detector. **(b)** Side view of the ILD detector.

Figure 1.1: Event display showing an event at a centre of mass energy of $\sqrt{s} = 1\,\text{TeV}$ and of the type: $e^+e^- \to t\bar{t}h$; $t\bar{t} \to 6q$; $h \to b\bar{b}$ [8].

This short historical survey of milestones in experimental particle physics of the last decades, illustrates the great success of the Standard Model. So far, all tested predictions of the Standard Model could be confirmed by experiments and no significant deviations were found. Nevertheless there are well established observed phenomena, like neutrino oscillation, dark matter or baryon asymmetry, that can not be explained by the Standard Model. This calls for extensions of the Standard Model by new physics, which should be observable via deviations from Standard Model predictions or the discovery of new resonances. Since usually the predicted deviations introduced by new physics are small, corresponding measurements require a high precision.

A very good candidate machine allowing such precision measurements is the International Linear Collider (ILC). This machine naturally continues the interplay between hadron colliders (SPS, Tevatron, LHC), which are particularly suitable for the discovery of new particles, and lepton colliders (LEP, Standford Linear Collider), which allow precision measurements.

Why a lepton collider allows measurements with high precision can be guessed from Figure 1.1. It shows the beauty of an event, where a pair of top quarks in association with a Higgs boson are produced. The decay channels in this figure are the most challenging ones, where all involved particles decay hadronically. Nevertheless, even by eye the individual

tracks can be resolved in the tracking detector and the corresponding contributions in the calorimeters can be attributed. The detector, that is used to create the shown event display is the International Large Detector (ILD). It is one of two proposed detector concepts of the ILC. A main feature of the ILD is its large tracking volume provided by a Time Projection Chamber (TPC). It provides an excellent momentum resolution ($\delta(1/p_\mathrm{t}) \simeq 10^{-4}\,(\mathrm{GeV/c})^{-1}$) and an superb pattern recognition capability, as illustrated in Figure 1.1.

However, there are aspects of the particle detection with a TPC that need to be investigated in order to ensure the desired performance in an environments such as it will be present at the ILC. The fundamental principle of a TPC is that charged particles, originating from a certain particle collision and traversing the TPC, ionise the gas inside the sensitive volume of the TPC. In this volume a homogeneous electric field is applied, which causes a drift of the created electrons and ions towards the ends of the TPC cylinder. At that side where the electrons arrive (anode), an amplification stage is placed, which is used to amplify the electron signal. Finally, the amplified signal is read out on a segmented anode, which allows to measure the projection of the incident particle track on the anode. In order to reconstruct the position along the cylinder axis, the arrival time at the anode in combination with the know time of the initial particle collision is used. This assumes a constant electron drift velocity, which is guaranteed by the constant electric field. Parallel to the electric field a magnetic field is applied, which in the end allows to measure the momentum of charged particles inside the TPC. If the electric and the magnetic fields are not homogeneous the momentum resolution will be deteriorated. Even small distortions of the field leading to displacements in the order of $\mathcal{O}(30\,\mu\mathrm{m})$ result in a 5 % deterioration of the momentum resolution, which shows that field distortions are a serious problem that needs to be studied.

In this thesis the three most relevant sources of field distortions are studied. The first source of distortions of the electric field inside the sensitive volume of the TPC are ions that are produced in the amplification stage and drift back into the sensitive volume. In order to study this phenomena the amplification process of the TPC is studied using a TPC prototype setup. In addition, a modified setup is introduced, which is suited for reducing the number ions reaching the sensitive volume.

A second source of distortions to the electric field, are the boundaries between individual modules, that are used for the signal amplification. It will be shown, that such distortions only appear in the vicinity of the modules at the anode. Therefore, they can be referred

to as local field distortions. Different methods to evaluate local field distortions will be presented and finally one possibility to reduce such distortions between module boundaries is introduced.

Finally, there are also field distortions introduced by inhomogeneities of the magnetic field or inhomogeneities introduced by the field cage of the TPC. Such distortions can effect the whole TPC volume and are therefore referred to as global field distortions. The overall field distortions, which include local and global distortions, are measured in a large TPC prototype using a laser calibration system. These measurements illustrate the effect of such distortions. In addition, a method to correct these distortions is introduced. Furthermore, the general capabilities of a laser calibration system are introduced and illustrated by the measurements of the drift velocity.

The contend of this thesis is structured as follows. In the beginning the ILC and the ILD are introduced in Chapter 2. Afterwards, the fundamental principles of a TPC are introduced and two advanced technologies used for the signal amplification are described in Chapter 4. A general introduction to the simulation tools used in this thesis is given in Chapter 5. Results of the signal amplification process characterisation and the study of the ion production in the amplification process are presented in Chapter 6. Finally, the studies on local field distortions (Section 7.2) and the measurements of the overall field distortions in a large TPC prototype (Section 7.3) are presented in Chapter 7. Finally, the conclusions of this work are given in Chapter 8. In the following a short summary of the Standard Model, which is the basis of our current knowledge of particle physics, is given.

1.1 Recapitulation of the Standard Model of particle physics

The Standard Model, developed during the second half of the 20th century, contains all the information of fundamental particles and particle interactions. It is a quantum field theory, where particles and interactions are represented by quantum fields. All particle fields have a spin of $1/2$ and therefore are fermions. The interactions are represented by bosonic fields with an integer spin. Except for the Higgs field, all boson fields have spin 1. The Higgs field is the only field in the Standard Model with spin 0. The Standard Model is characterised by the corresponding Lagrangian density, which is invariant under Lorentz transformation and special gauge transformations. Such gauge transformations are classified by gauge groups. They are used to describe the three fundamental forces included in the Standard Model,

which are the strong force, the weak force and the electromagnetic force . The strong force, mediated by eight massless gluon fields, is described by a $SU(3)_c$ group. Furthermore, the group $SU(2)_L \otimes U(1)_Y$ represents the electroweak interaction. Unless this symmetry is broken the corresponding mediators of the electroweak interaction are massless, which is in contradiction to observations. The introduction of an additional field (Higgs field) via the Higgs mechanism allows to break the $SU(2)_L \otimes U(1)_Y$ symmetry and give mass to some of the mediators. Finally, three massive fields ($W^{\pm}$- and Z-boson), the mediators of the weak force, and one massless field (photon), the mediator of the electromagnetic force result from the symmetry breaking. Effectively the resulting symmetry that is left is described by the $U(1)_Q$ group. In addition, a scalar field – the Higgs boson – is introduced by the Higgs mechanism. It turned out that also the fermion masses can be described as interactions with the Higgs field. The corresponding coupling strength, known as Yukawa coupling, can be directly connected to the fermion mass.

Apart from the great success of the Standard Model, in standing all tests of its predictions so far, there are phenomena that can not be described by the Standard Model. As mentioned before, such well-established phenomena are for example dark matter, the imbalance between baryonic and antibaryonic matter in the universe or the observation of neutrino oscillations. There are theories that try to include a description of such phenomena into the Standard Model by extending it. Such models for example introduce an additional symmetry, called super symmetry, or describe the Higgs boson as a composite particle. A common feature of such models is, that they result in small deviations from the Standard Model predictions or that they predict the existence of new particles. Possibly such new particles can not be produced at current or future colliders, since their mass is to high. But physics beyond the Standard Model enters in Standard Model predictions via higher order corrections, which results in the modification of observables that are measurable at energies reached today.

Consequently, if no new particles can be found, precision measurements are the only possibility to discover new physics. One candidate machine allowing to do high precision measurements is the ILC machine introduced in the following chapter.

2

The International Linear Collider

The ***I**nternational **L**inear **C**ollider* (ILC) is a planned machine colliding electrons and positions. The centre of mass energy in the collisions will not be fixed to only one value, but in order to exploit the full potential the machine will run at different energies. In the baseline design, the maximum centre of mass energy of the machine is $\sqrt{s} = 500\,\text{GeV}$. Both particles beams will be spin polarised, which allows to suppress background events and enrich signal samples. The foreseen maximum spin polarisation of the electron beam is $|P(e^-)| = 80\,\%$ and for the position beam it is $|P(e^+)| = 30\,\%$. Benefits of running an collider with polarised electrons and positrons at different centre of mass energies and the foreseen physics at the ILC are discussed in Section 2.1. The machine itself is introduced in Section 2.2.

Two detector concepts will be used at this machine sharing the same interaction point. This allows to cross check the results between the two independently designed experiments. In order to do so, the detector that is not taking data is pushed out of the interaction region into a parking position. After one of the detectors has collected a certain amount of data, the second detector will be pushed into the interaction region and collect the same amount of data. This idea is called push-pull operation mode and allows data taking with two experiments, whereby only one interaction region needs to be instrumented. One of the detector concepts is the ***I**nternational **L**arge **D**etector* (ILD) introduced in Section 2.3.

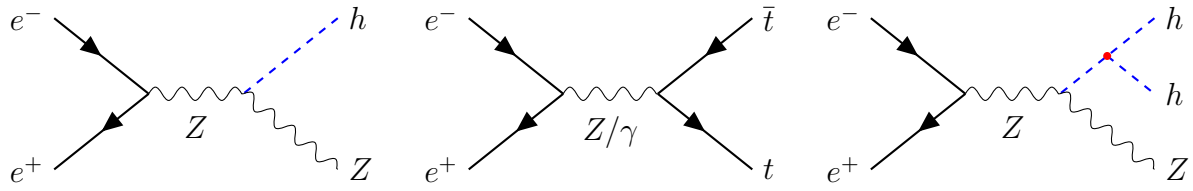

(a) Higgs production via Higgs-strahlung.

(b) Top pair production.

(c) Higgs self coupling diagram.

Figure 2.1: Selected diagrams for the production of Higgs bosons and top quark pairs at the ILC.

2.1 Physics at the ILC

The major advantage of colliding electrons and positrons compared to colliding hadrons, as done at the LHC, is that these particles are fundamental particles. This means that the initial state quantum numbers and energies of these point-like particles are known. Furthermore, the final state of a collision between fundamental particles contains much less particles and therefore it is easier to reconstruct and analyse the particle collision. In consequence, measurements can be done with a much higher precision. Also from the perspective of theory, the collision of electrons and positrons is beneficial, since corresponding theoretical calculations result in much smaller uncertainties. This is because here no QCD cross section calculations are involved, which introduce large theoretical uncertainties (typically 30 %–50 % for NLO QCD cross section calculations [9]). At the ILC the precision measurements only rely on electroweak interactions with radiative corrections at the few percent level [9]. Finally, the use of polarised particles beams allows to enhance or reduce the cross section of certain processes. This allows to enrich signal samples and reduce the contribution from background processes. A detailed discussion about the advantages of polarised beams can be found in Ref. [10].

The physics programme foreseen at the ILC covers many different measurements. An overview can be found in Ref. [9]. As mentioned before, the ILC will be operated at different centre of mass energy allowing different measurements. In the following some key physics explorations at different energies will be introduced.

At a centre of mass energy of $\sqrt{s} = 250\,\text{GeV}$ the Higgs-strahlung process, illustrated in Figure 2.1a, has a maximum cross section, which can be seen in Figure 2.2a. For an integrated luminosity of $250\,\text{fb}^{-1}$ the expected number of Higgs bosons produced at the ILC is $8 \cdot 10^4$. With this amount Higgs-strahlung events it is possible to calculate the cross

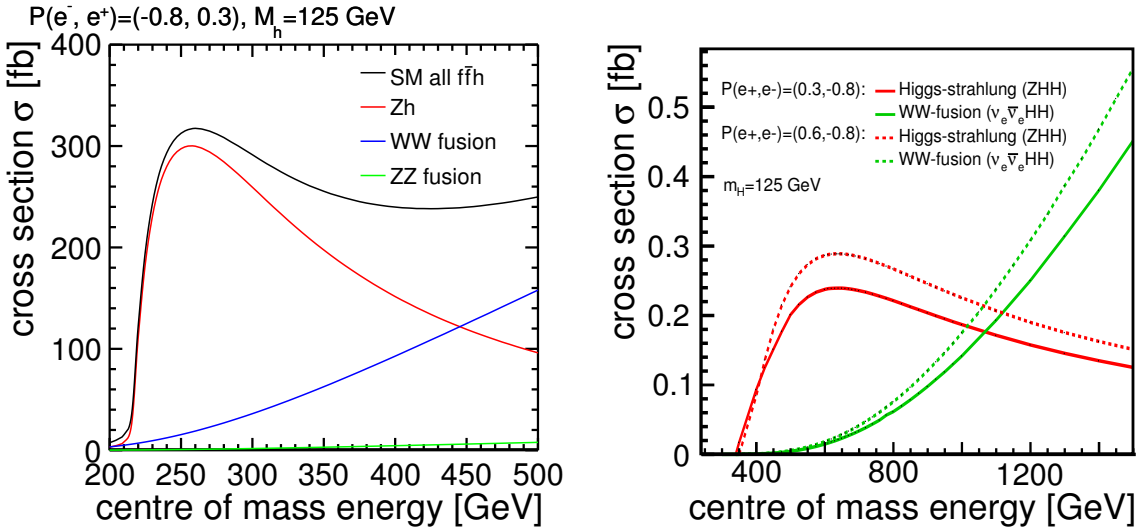

(a) Production cross section for the Higgs-strahlung process and the WW and ZZ fusion process as function of the centre of mass energy [9].

(b) Production cross section for two Higgs self-coupling processes as function of the centre of mass energy for different polarisations of the colliding electrons and positrons [12].

Figure 2.2: Different Higgs production cross sections.

section of this process with a relative accuracy of 2.5 % [9]. This measurement of the cross section is a particular feature of ILC experiments compared to LHC experiments, where only measurements of the product of the cross section and the branching ratio for a certain Higgs decay mode can be done. The analysis of the Higgs-strahlung process also allows to measure the Higgs mass independently of the Higgs decay modes. This can be done by reconstructing the final Z boson of the Higgs-strahlung process and calculating the corresponding recoil mass M_{recoil}:

$$M_{\text{recoil}} = s + M_Z^2 - 2E_Z\sqrt{s}. \tag{2.1}$$

Among all possible Z decay modes, the decays $Z \to \mu^+\mu^-$ and $Z \to e^+e^-$ in particular are advantageous, since the corresponding events result in a clean signal. The recoil mass can finally be identified with the Higgs mass and the measurement combining both mentioned decay modes of the Z boson leads to a mass uncertainty in the order of 30 MeV [11]. One should note, that the precise measurement of the recoil mass in the $Z \to \mu^+\mu^-$ channel at higher center of mass energies defines the required momentum resolution ($\Delta p/p^2 = 5 \times 10^{-5}\,(\text{GeV/c})^{-1}$) of the ILC detectors.

At a centre of mass energy around $\sqrt{s} = 350\,\text{GeV}$ a prominent rise in the e^+e^- annihilation cross section is expected, which is connected to the top-antitop quark pair production with

a threshold of about two times the top mass. The corresponding diagram is shown in Figure 2.1b. Since the top quark has a very short life time, it has no stable bound states. This results in the threshold structure of the top pair production cross section, which is precisely described by perturbative QCD. By measuring the threshold shape, the top quark mass can be measured with an accuracy of 100 MeV [9]. Furthermore it is also possible to measure the total decay width Γ_t and the QCD coupling strength α_s (see Ref. [13, 14]). For the ILC detectors, the identification of $t\bar{t}$ quark pairs requires the reconstruction of the top quark decay products, which are a W boson and a jet resulting from the hadronisation process of a quark. Since in most of the cases the quark produced in the top decay is a bottom quark ($\Gamma(Wb)/\Gamma(Wq(q = b, s, d)) = 0.91$ [15]), the identification of secondary and tertiary vertexes, which result from the decay of B- and D-mesons in the jet, is crucial for the top quark identification. As a consequence a very good resolution on the impact parameter ($\sigma_b < 5 \oplus 10/p \sin^{3/2}\theta\,\mu\text{m}$) of charged particles is required in order to achieve a high vertex detection performance.

Finally, at a centre of mass energy of $\sqrt{s} = 500\,\text{GeV}$ the Higgs self-coupling can be studied. One diagram relevant for the Higgs self-coupling at the ILC is shown in Figure 2.1c. The corresponding cross section is shown in Figure 2.2 (red line) in dependence on the centre of mass energy. The measurement of the Higgs self-coupling is indispensable for understanding the electroweak symmetry breaking, since it is the key ingredient of the Higgs potential. Furthermore, at this centre of mass energy the top Yukawa coupling can be studied in processes, where a Higgs boson is radiated by the top quark shown in Figure 2.1b. This allows to understand the fermion mass generation as result of the fermion interaction with the Higgs potential. Both studies require excellent tracking capabilities in order to reconstruct the complex event structure. An example event contributing to the top Yukawa measurement is shown in Figure 1.1. The shown event corresponds to a process shown in Figure 2.1b, where an additional Higgs boson is radiated from the top quark.

In addition, asymmetries in the pair production of fermions allow to test Standard Model predictions. In particular the forward-backward asymmetry in the production of top-antitop ($t\bar{t}$) pairs is of interest, since the large top quark mass implies that this is the Standard Model particle that is most strongly coupled to the mechanism of electroweak symmetry breaking. The forward-backward asymmetry is defined as

$$A_{\text{FB}} = \frac{N(\cos(\theta > 0)) - N(\cos(\theta < 0))}{N(\cos(\theta > 0)) + N(\cos(\theta < 0))}, \tag{2.2}$$

where N is the number of top quarks reconstructed in a certain detector hemisphere and θ is the angle between the top quark and the incoming electron. The expected precision on the measurement of A_{FB} is about 2 % [16]. Such a measurement not only requires the identification of jets associated to a $t\bar{t}$ pair, but also the assignment of the individual jets to a top quark or an antitop quark. This can be done by measuring the charge sum of the reconstructed vertexes.

As indicated in the previous chapter, there are well-established and observed phenomena that can not be explained with the Standard Model. In the following two different extensions of the Standard Model and corresponding observables at the ILC are introduced, which are exemplary for physics beyond the Standard Model (BSM) and expected deviations from the Standard Model at the ILC.

In a Minimal Supersymmetric Standard Model (MSSM) [15] there exist five Higgs bosons, where one light Higgs h_{BSM} has a mass similar to the Standard Model Higgs h. The masses of the other additional Higgs bosons m_A can be as heavy as $1\,\mathrm{TeV/c^2}$. The expected deviations from the Standard Model Higgs coupling to bottom quarks (b) and tau leptons (τ) is given by [9]:

$$\frac{g_{h_{\mathrm{BSM}}bb}}{g_{hbb}} = \frac{g_{h_{\mathrm{BSM}}\tau\tau}}{g_{h\tau\tau}} \simeq 1 + 1.7\,\% \left(\frac{1\,\mathrm{TeV/c^2}}{m_A}\right)^2 . \tag{2.3}$$

As stated above, the expected deviation is at the few percent level. Similarly, in models assuming that the Higgs boson is a composite bound state of fundamental fermions with a compositeness scale Λ around the TeV scale [17], deviations from the Standard Model are given by [9]:

$$\frac{g_{h_{\mathrm{BSM}}VV}}{g_{hVV}} \simeq 1 - 3\,\% \left(\frac{1\,\mathrm{TeV/c^2}}{\Lambda}\right). \tag{2.4}$$

Here g_{hVV} is the coupling of the Higgs boson to other vector bosons, like the Z boson. It can be measured for example in a process illustrated in Figure 2.2a. Again a deviation of a few percent is expected.

To sum up, it was shown that in order to allow precision tests of the Standard Model as well as for the observation of deviation from the Standard Model, measurements need to be done with a precision in the order of a few percent. This defines the desired beam parameters on the one hand and the detector requirements on the other hand. In the following the current ILC design (Section 2.2) and one of the experiments (Section 2.3) are introduced. Both were optimised with respect to the physics requirements.

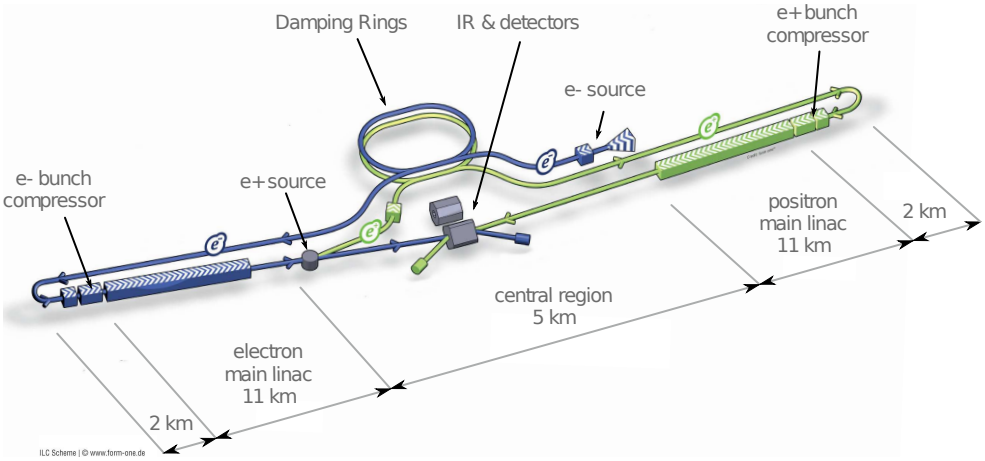

Figure 2.3: Schematic view of the ILC showing the main components and indicating the total size (adapted from Ref. [18] and not to scale).

2.2 Machine design

A schematic view of the ILC is shown in Figure 2.3. It shows the main components of the machine, which are the particle sources, the damping rings, the main linear accelerator (linac), the interaction region hosting two detectors and beam dumps. The machine is planned as a staged machine, with two possible major upgrades. In the baseline design the maximum centre of mass energy is $\sqrt{s} = 500\,\text{GeV}$ and total length of the ILC is about 31 km. The first upgrade will increase the luminosity by a factor two by doubling the number of bunches per beam pulse. Major parts of the machine can deal with these conditions already in the base line design. A second upgrade will increase the maximum centre of mass energy to $\sqrt{s} = 1\,\text{TeV}$. This requires to install more accelerator modules and in consequence the total length of the machine will be increased to about 50 km. In the following the main components of the ILC, as foreseen in the baseline design, are introduced. The details about the ILC design can be found in Ref. [18].

2.2.1 Particle sources

Polarised electrons are produced by illuminating a semiconductor (GaAs) photocathode with a polarised high-power laser inside a DC gun. Thus, a beam spin polarisation of 90 % [18] can be achieved. The electrons are subsequently pre-accelerated to 76 MeV by a normal-conducting structure. Afterwards the beam is accelerated in a superconducting linac to reach an energy of 5 GeV, which is required in the damping ring.

The positron source is located behind the electron main linac. First, the electrons, extracted from the main linac, generate photons with energies from $\sim 10\,\mathrm{MeV}$ to $\sim 30\,\mathrm{MeV}$ in a 147 m long superconducting helical undulator. These photons are directed onto a Ti-alloy target producing pairs of polarised electrons and positrons. The positrons are extracted, pre-accelerated and finally injected into the positron damping ring. In the baseline design of the ILC a positron beam spin polarisation of 30 % can be reached by using the discussed scheme.

2.2.2 Damping rings

There are two damping rings each with a circumference of 3.2 km – one used for the electrons and the other is used for the positrons. The main task of the damping ring is to reduce the transverse and longitudinal emittance of the beams. The damping is accomplished by wigglers operated at 4.3 K with a peak-field of 2.16 T. The beam energy inside the damping ring is 5 GeV. As shown in Figure 2.5, where the ILC bunch structure is shown, each beam pulse has a length of 218 km. In consequence, the beam pulse needs to be compressed by a factor of 90 to fit into the damping ring. Furthermore, the kickers used to inject and extract the beam need to have a rise and fall time of approximately 8 ns in the baseline design. The total time that is available for the damping is fixed by the machine frequency to 200 ms.

2.2.3 Main linac

There are two main linacs, each with a length of 11 km. One is used for accelerating the electrons and one is used for the positrons. The total length of the linacs is fixed by the field gradient, which is available for the acceleration, and the desired energy in the collisions. In the baseline design of the ILC, superconducting radio-frequency cavities (RF cavity) with a maximum field gradient of 31.5 GV/m are used to achieve the maximum centre of mass energy of $\sqrt{s} = 500\,\mathrm{GeV}$. The cavities are operated at a frequency of 1.3 GHz and at a temperature of 2 K. The cavities are made of niobium and they are approximately 1 m long. Each cavity consists of nine cells. A computer animation of the field inside the cavity, where also the cells can be seen, is shown in Figure 2.4.

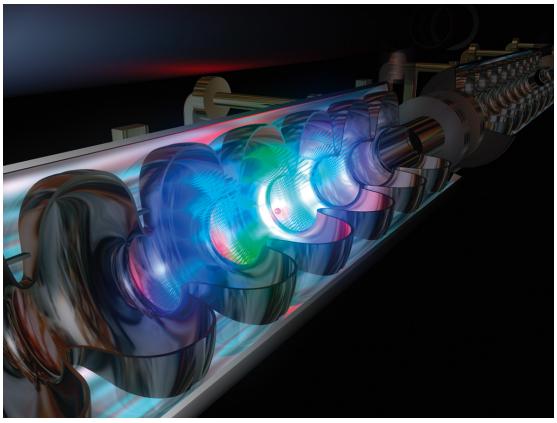

Figure 2.4: Computer animation of the field inside a RF-cavity of the ILC (Copyright: ©DESY 1999).

Table 2.1: Selected machine parameters of the baseline ILC design[18].

centre of mass energy	500 GeV
collision rate	5 Hz
bunch population	$2 \cdot 10^{10}$
horizontal emittance	10 µm
vertical emittance	35 nm
electron polarisation	80 %
position polarisation	30 %

In total approximately 7400 cavities will be assembled in $\sim$ 850 cryogenic modules. The technology was first proved to work at the ***F**ree Electron **La**ser **H**amburg* (FLASH) at DESY, which is a 260 m long test facility using ILC cavities for electron acceleration. The same cavities are also used in a second project at DESY, which is the *European X-Ray Free-Electron Laser* (XFEL). Here a 3.5 km long linac is currently installed. The cavities will be operated at a field gradient of 23.6 GV/m [19] leading to a maximum electron energy of 20 GeV [19].

2.2.4 Beam delivery system and the interaction region

The beam delivery system transports the particle beams from the end of the linac to the interaction region and afterwards to the beam dump. On this path several subsystems of the beam delivery system are installed to achieve different goals:

- Beam diagnostics and corrections
- Beam collimation to remove beam-halo particles
- Focusing of the beam at the interaction point

The crossing angle of the beams is 14 mrad, which in principle would significantly reduce the cross-section of the collisions as the geometric overlap of the bunches is reduced by crossing angle. In order to recover the full luminosity, so-called crab cavities are used. They rotate the bunches in the horizontal plane for effective head-to-head collisions.

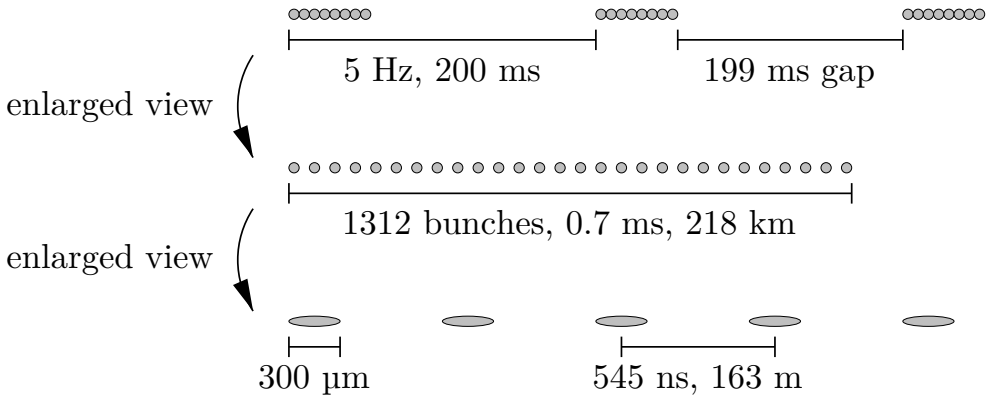

Figure 2.5: Sketch of the ILC bunch structure for the baseline design [18] (adapted from Ref. [20]).

The whole beam delivery system is a very complex system and the individual components are quite expensive. This is the reason why only one interaction region is foreseen for the ILC and the experiments need to share the beam time.

2.2.5 Beam parameters and the ILC bunch structure

Most important beam parameters corresponding to the ILC baseline design at a centre of mass energy of $\sqrt{s} = 500\,\text{GeV}$ are summarised in Table 2.1 and illustrated in Figure 2.5. These parameters are common for all energies considered for the ILC baseline design physics programme. They define the conditions in the ILD TPC and the time scales at which signals are produced in the TPC. In particular, one can see that the time between individual collisions is only 545 ns, whereas the time between the trains of the 1312 bunches is rather large (199 ms). A detailed discussion on the consequences from the ILC bunch structure is given in the following Section 2.4. The expected beam size at the interaction point depends on the chosen centre of mass energy and is smallest at $\sqrt{s} = 500\,\text{GeV}$: RMS horizontal beam size of 474 nm, RMS vertical beam size 5.9 nm. Different beam sizes directly effect the luminosity, which ranges from $0.75 \times 10^{34}\,\text{cm}^{-2}\text{s}^{-1}$ at $\sqrt{s} = 250\,\text{GeV}$ to $1.8 \times 10^{34}\,\text{cm}^{-2}\text{s}^{-1}$ at $\sqrt{s} = 500\,\text{GeV}$.

2.3 The International Large Detector

The ***I**nternational **L**arge **D**etector* (ILD) is one of two detector concepts proposed for the ILC. It is a multi-purpose detector, which consists of a tracking system and a calorimeter

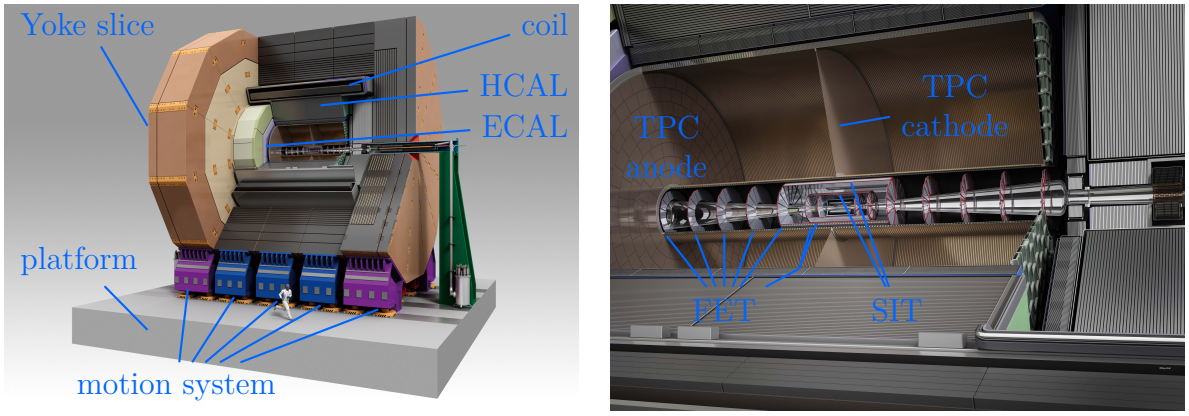

(a) Overview of the detector concept. **(b)** Enlarged view of the ILD tracking system.

Figure 2.6: Artistic view of the ILD detector concept (Copyright: ©Rey.Hori/KEK).

system. These systems are located inside a solenoid, which provides a magnetic field of 3.5 T. Furthermore, the magnet return yoke is instrumented as a muon system and a tail-catcher of the calorimeter. In addition, there are two detector systems in the forward region (LumiCal and BeamCal) measuring the luminosity via Bhabha scattering and beam parameters. Detailed information about the instrumented yoke, the BeamCal and the LumiCal can be found in Ref. [8].

In total the ILD has a height of 15.7 m and a length of 13.2 m. An overview of the ILD design is shown in Figure 2.6a. This figure also shows the platform, where the detector is placed on in order to preserve the detector alignment when it is pushed into the parking position and the second detector is taking data. Furthermore the magnet yoke is made out of slices. Each slice has its own motion system, that is based on air pads and grease pads. It can be seen at the bottom of the ILD in Figure 2.6a and allows to open the detector for maintenance, when it is not taking data.

The whole detector design is optimised for precision measurements. This includes not only state of the art detector technologies, but also the way events are reconstructed. The event reconstruction is based on the particle flow concept, which is introduced in following. This concept in combination with the aimed physics measurements defines the design of the individual detector system, which are introduced afterwards.

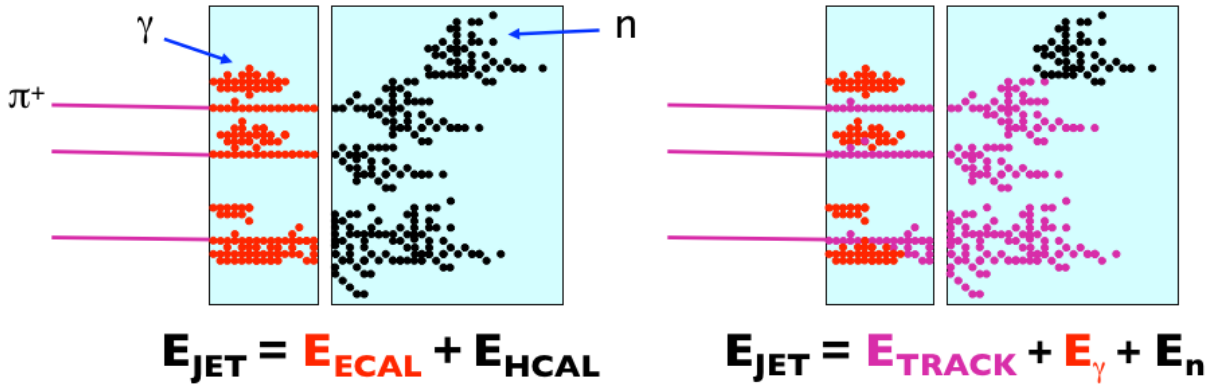

(a) Classical approach. **(b)** Particle Flow approach.

Figure 2.7: Sketch of different approaches to measure the jet energy [21].

2.3.1 Particle flow concept

The Particle Flow Concept is a novel approach of measuring the energy of particle jets resulting from the hadronisation process of a quark. In the classical approach of event reconstruction the jet energy is calculated as the sum of the energy measured in the electromagnetic calorimeter (ECAL) and the hadronic calorimeter (HCAL). This is a simple and robust approach, which is sketched in Figure 2.7a. The drawback of this approach is, that the energy resolution in the calorimeters is limited, which restricts the overall precision of measurements that include the jet energy.

The particle flow concept allows to overcome these limitations. The idea is to measure the energy of all individual components of a particle jet as best as possible. For charged particles this means to calculate their energy from the momentum measured with the tracking system using the relation $E^2 = m^2 + p^2$. Here either the mass is neglected for high momentum particles or it is know from the particle identification based on a multivariate analysis of tracker and calorimeter observables. The energy deposited by charged particles in the calorimeters is identified and removed, which leaves only energy deposited by neutral charged particles. Photons are identified as clusters in the electromagnetic calorimeter (ECAL) with no corresponding track in the tracking system. Finally, only the energy of neutral charged hadrons is measured in the hadronic calorimeter (HCAL). In the end the jet energy is given by the individual components as shown in Figure 2.7b. The jet energy resolution is given by the following equation:

$$\frac{\sigma_{\text{jet}}}{E} = f_{\text{ch}} \frac{\sigma_{\text{tracker}}}{E} \otimes f_{\gamma} \frac{\sigma_{\text{ECAL}}}{E} \otimes f_{h^0} \frac{\sigma_{\text{HCAL}}}{E} \otimes \sigma_{\text{confusion}}. \tag{2.5}$$

In average the different contribution to a jet are as follows:

- $f_{\mathrm{ch}} = 60\,\%$: contribution of charged particles
- $f_{\gamma} = 30\,\%$: contribution of photons
- $f_{\mathrm{h^0}} = 10\,\%$: contribution of neutral charged particles

This illustrates, that only a small fraction of the jet energy needs to be measured in the HCAL, which has the worst resolution. Therefore, the overall jet energy measurement using the Particle Flow Concept is improved. The so-called confusion term $\sigma_{\mathrm{confusion}}$ in Equation 2.5 summarises all uncertainties introduced by the particle flow algorithm itself. They can be attributed to a wrong assignment of calorimeter clusters to a certain particle type (charged particle, photon or neutral charged particle). In order to fully exploit the particle flow algorithm the confusion term needs to be kept low. On the one hand this challenges the software pattern recognition algorithms. On the other hand this challenges all sub-detectors of the ILD, by requiring an excellent pattern recognition in the tracking system and a high longitudinal and transverse segmentation of the calorimeters.

2.3.2 Calorimeter system

As indicated in the previous section, the calorimeters are not only required to give a good energy resolution, but also to have imaging capabilities. This requires a fine segmentation in longitudinal and transverse direction, which increases the number of layers and reduces the cell size. Specifications of the ECAL and the HCAL are given in the following.

Electromagnetic calorimeter

The ECAL is a tungsten-silicon sampling calorimeter. In total 30 readout layers are used. The current design includes silicon pin diodes with a size of $5\,\mathrm{mm} \times 5\,\mathrm{mm}$, but the optimisation of the layout is still ongoing. As an alternative to the silicon pin diodes, scintillator strips with a size of $5\,\mathrm{mm} \times 45\,\mathrm{mm}$ are a second option. The thickness of the ECAL in terms of radiation lengths is $24X_0$. Since tungsten is used, which has a radiation length of $X_0 = 3.5\,\mathrm{mm}$, the ECAL can be build compact with a thickness of $20\,\mathrm{cm}$.

Hadronic calorimeter

The HCAL is also a sampling calorimeter using iron absorbers. Since the ratio between the hadronic interaction length of iron ($\lambda_I = 17\,\text{cm}$) and its radiation length ($X_0 = 1.8\,\text{cm}$) is moderate a fine segmentation in terms of X_0 can be realised. This is beneficial for a measurement of the electromagnetic energy part in the hadronic shower and for a topological resolution of the shower substructure.

Two options for the active layer of the HCAL are proposed:

1. Analogue readout using scintillating tiles ($3\,\text{cm} \times 3\,\text{cm}$).
2. Semi-digital readout using gaseous devices ($1\,\text{cm} \times 1\,\text{cm}$).

In any case 48 layers will be used leading to a thickness of 6 λ_I.

2.3.3 Tracking system

The ILD tracking system consists of a vertex tracker (VTX) and a TPC, which is introduced in the next section. One the of the main tasks of the VTX is to identify heavy quarks (charm and bottom) and tau leptons by reconstructing corresponding decay vertexes. This requires a good resolution on the impact parameter, which will be $\sigma_b < 5 \otimes 10/p \sin^{3/2}\theta\,\mu\text{m}$ for the ILD VTX. It consists of three layers of double-sided ladders located in the barrel region of the ILD. On each side of the ladder there is a pixels sensor and the distance between the sensors is 2 mm. This allows to construct vectors out of the hits per track. This information on the track direction can be used to improve the tracking performance. The spacial resolution of the first layer is $\sigma_{\text{VTX,1.}} = 2.8\,\mu\text{m}$, whereas it is $\sigma_{\text{VTX,2.}} = 6\,\mu\text{m}$ for the second layer. The remaining four layers have a spacial resolution of $\sigma_{\text{VTX,3.-6.}} = 4\,\mu\text{m}$. The first layer is is located at a radius of 16 mm and the last layer is at a radius of 60 mm. The ILD goal is to limit the material budget to $\sim 15\,\%X_0$ per VTX layer. The benefits of a low material budget are discussed in case of the TPC in the following section. Similar arguments also apply to the VTX.

In the barrel part of the ILD there are two additional layers of silicon strip detectors (SIT, $\sigma_{\text{SIT}} = 7\,\mu\text{m}$) in between the VTX and the TPC. Furthermore, there are two silicon strip layers (SET, $\sigma_{\text{SET}} = 7\,\mu\text{m}$) outside of TPC in front of the ECAL. The SIT and the SET will provide precise space points before and after the TPC, which improves the momentum resolution and helps to link tracks measured in the VTX and in the TPC. In the forward

region, the tracking system consists of two silicon-pixel ($\sigma_{\mathrm{FTD,pixel}} = 2\,\mu\mathrm{m} - 6\,\mu\mathrm{m}$) discs and five silicon-strip discs ($\sigma_{\mathrm{FTD,strip}} = 7\,\mu\mathrm{m}$) providing low angle tracking coverage (FTD). The whole tracking system is shown in Figure 2.6b. The combined momentum resolution of the tracking system for high momenta will be $\sigma_{1/p_\mathrm{t}} = 2 \times 10^{-5}\,\mathrm{GeV}^{-1}$.

2.4 The ILD Time Projection Chamber

The ILD TPC provides two tracking volumes, which are separated by a central cathode (see Figure 2.6b). On each side of the TPC is an anode, which houses readout modules. These readout modules are responsible for the signal amplification and the signal readout. Details about the module technologies and different design options will be given in Chapter 4. In the following, first of all a common coordinate system is introduced. It describes the ILD TPC and the individual modules, but it is also used to describe the prototypes used in this thesis. Afterwards, a motivation for the TPC as central tracking detector is given. Afterwards, one of the main measurements – the momentum of charged particles – is introduced. Finally, the resulting requirements on the ILD TPC are presented.

2.4.1 Definition of the TPC coordinate system

The coordinate system that is used to describe a TPC is naturally a cylindrical coordinate system. The z direction is given by the TPC cylinder axis, which is identical to the beam direction of the ILC in case of the ILD TPC. The other two coordinates are the radial distance R and azimuth angle ϕ. The centre of the coordinate system in case of the ILD TPC is at the centre of the ILD TPC, which means the cathode is located at $z = 0$.

In order to distinguish different readout modules or to describe effects inside a readout module, in this thesis the following relations defining top, bottom, left and right are used:

$$R_{\mathrm{bottom}} < R_{\mathrm{top}}$$
$$\phi_{\mathrm{left}} < \phi_{\mathrm{right}}$$

2.4.2 Motivation for a TPC as central tracking device

The TPC provides a continuous tracking using a large number of three-dimensional space points. This large number of measurement points, which in case of the ILD TPC is in the order of up to $\mathcal{O}(200)$ per track, results in a good momentum resolution, although the point resolution is worse compared to silicon tracking devices. This will become clear in the next section, where the momentum resolution is introduced. In the end the TPC significantly contributes to the overall ILD momentum resolution.

The continuous tracking allows the reconstruction of non-pointing tracks, like long lived neutral particles that decay inside the TPC volume into charged particles. Such particles are known from the Standard Model (for example Kaons) or particles predicted by some models beyond the Standard Model. Closely connected to non-pointing tracks is the reconstruction of kinks in particle tracks, which help to identify the decay of charged particles in the TPC Volume. In addition, it is possible to observe and identify particles, that are scattered back at the calorimeter into the TPC volume or particles that reenter the TPC volume due to their low momentum and the magnetic field of the ILD detector. In particular, the capabilities mentioned above are important to achieve a good performance of the Particle Flow algorithm. This can be illustrated with a small example. Imagine a charged particle that points in the direction of the calorimeter. At the calorimeter it is scattered back into the TPC leaving no energy depositions in the calorimeter. If this scattering could not be observed, the Particle Flow algorithm would try to assign energy depositions in the calorimeter to the particle pointing towards the calorimeter. But this would be wrong, since the particle never reached the calorimeter. In the end, if something similar happens to particles of a jet, the final measured jet energy would be wrong.

Finally, the TPC will be read out continuously (in time), which allows to reduce background hits. One source of background is the conversion of photons into low energetic electrons and positrons, which is known as pair background. Such photons are produced by beamstrahlung. The amount of TPC hits arising from the pair background compared to TPC hits arising from a signal event is illustrated in Figure 2.8. Here all TPC hits corresponding to a single $t\bar{t}$ event at $\sqrt{s} = 500\,\mathrm{GeV}$ are shown in blue. In addition, background hits produced by the pair background corresponding to 150 bunch crossings are overplayed and shown in red. The low energy pair background particles form small radius helices parallel to the beam axis, which can be seen in Figure 2.8a. Such micro-curlers deposit charge on a small number of TPC readout channels over a large number of bunch crossings. Nevertheless

(a) TPC hits shown in side and front view of the ILD TPC.

(b) Reconstructed tracks in the TPC after applying a micro-curler removal algorithm.

Figure 2.8: TPC hits from a $t\bar{t}$ event at $\sqrt{s} = 500\,\text{GeV}$ (blue) overplayed with beam background resulting from 150 bunch crossings (red) [22].

Figure 2.8 illustrates, that this kind of background can be removed effectively in the track reconstruction thanks to the continuous readout.

Another advantage of the TPC is its particle identification capability, which is based on the measurement of the energy loss per path length $\mathrm{d}E/\mathrm{d}x$ by ionisation. This will be introduced and discussed in Section 3.1. The knowledge of the particle identity, allows to improve the track fit by taking into account the correct particle mass. In the end this also improves the Particle Flow performance and the jet energy measurement. Closely related to this, is the capability of determining the vertex and jet charge, which allows to distinguish between quarks and anti quarks produced in the initial collision. This is an important feature, needed to do precision measurements of asymmetries such as the forward-backward asymmetry introduced before.

Last but not least, the TPC presents a minimum amount of material. This is beneficial for the calorimeter performance, since a low material budget in front of the calorimeter results in a minimum energy loss prior to the energy measurement. Furthermore, the low material budget results in a minimum of multiple scattering of low momentum particles. In addition, a low material budget limits the conversion probability of the beamstrahlung photons, which reduces the pair background.

2.4.3 Momentum resolution in uniform magnetic fields

The trajectory of a particle with charge q in a uniform magnetic field $\vec{B}$ is a helix. It can be described with the curvature radius R and the pitch angle λ. The relation between the transverse momentum p_t (perpendicular to the magnetic field) and the radius R is given by [15]:

$$p_\mathrm{t} = p\cos\lambda = 0.3 \cdot qBR, \tag{2.6}$$

where the transverse momentum is measured in GeV/c, B is measured in T and R is measured in meters. One finds, that the distribution of measured curvatures $k = 1/R$ is a Gaussian distribution. The uncertainty of k consists of a component related to the finite measurement resolution δk_res and a component related to the uncertainty due to multiple scattering δk_MS leading to:

$$(\delta k)^2 = (\delta k_\mathrm{res})^2 + (\delta k_\mathrm{MS})^2 . \tag{2.7}$$

For N uniformly spaced position measurement along the particle trajectory in a uniform medium and $N \geq 10$, $\delta(k_\mathrm{res})$ is given by [23]:

$$\delta(k_\mathrm{res}) = \frac{\sigma_{R\phi}}{L'^2}\sqrt{\frac{720}{N+4}}, \tag{2.8}$$

where L' is the projected length of the track onto the bending plane and $\sigma_{R\phi}$ is the measurement uncertainty for each point, perpendicular to the trajectory. If in addition a vertex constraint can be applied at the origin of the track, the coefficient under the radical is reduced from 720 to 320. An approximation of δk_MS is given by [15]:

$$\delta k_\mathrm{MS} \approx \frac{q \cdot 0.016\,\mathrm{GeV/c}}{p\beta\cos^2\lambda}\sqrt{\frac{1}{LX_0}}, \tag{2.9}$$

where L is the total track length and X_0 is the radiation length.

Finally, the uncertainty on the measurement of the transverse moment is characterised by:

$$\delta\left(\frac{1}{p_\mathrm{t}}\right) \sim \text{const.}\frac{\sigma_{R\phi}}{BL'^2\sqrt{N}} + \text{const.}\frac{1}{Bp_\mathrm{t}\cos\lambda\sqrt{LX_0}}. \tag{2.10}$$

The second term is most relevant for low transverse momentum, whereas at high transverse momenta the resolution is limited by the single point resolution.

2.4.4 Requirements for the ILD TPC

In the following requirements for the ILD TPC will be motivated and presented. A good starting point to define requirements for the ILD TPC is the momentum resolution defined in the previous section. Using Equation 2.10 the following requirements can be formulated, that result in a good momentum resolution:

- The TPC should be operated in a high magnetic field.
- The number of measurement point along a track should be high.
- A large size of the TPC is preferred to increase L, L'.
- A low material budget should be involved in the TPC to reduce multiple scattering by increasing X_0.

In order to achieve a low material budget, the field cage will be made out of advanced composite materials. Details on a prototype made of such materials are given in Section 4.2. To achieve a good momentum resolution as well as to grantee the tracking capabilities introduced in Section 2.4.2 the point resolution on the anode plane ($R\phi$) and the point resolution in drift direction (Rz) should be as small as possible. Both resolutions are defined by the readout modules design and chosen TPC gas. The TPC gas will be discussed in detail in Section 4.1.

A summary of the desired ILD TPC parameters is given in Table 2.2. Compared to the best ever reached momentum resolution in a TPC ($\delta(1/p_\mathrm{t}) \simeq 1.2 \cdot 10^{-3}\,(\mathrm{GeV/c})^{-1}$ with the ALEPH TPC [24]) the ILD momentum resolution has to be ten times better. This finally illustrates the ambitious design goal of the ILD TPC. One additional requirement of the ILD TPC is the homogeneity of the electric and magnetic field inside the sensitive volume of the TPC. In case of inhomogeneities of the magnetic field their impact on the momentum resolution is discussed in Ref. [25, 26]. As stated in these references, systematic effects

Table 2.2: Performance and design parameters of the ILD TPC [8].

Parameter			
Geometrical parameters	R_{in}	R_{out}	z
	329 mm	1808 mm	$\pm$2350 mm
Solid angle coverage	up to $\cos\theta \simeq 0.98$ (10 pad rows)		
TPC material budget	$\simeq 0.05 X_0$ including outer field cage in R		
	$< 0.25 X_0$ for readout endcaps in z		
Number of pads/timebuckets	$\simeq 1 - 2 \times 10^6/1000$ per endcap		
Pad pitch/no. pad rows	$\simeq 1 \times 6\,\text{mm}^2$ for 220 pad rows		
σ_{point} in $R\phi$	$\simeq 60\,\mu\text{m}$ for zero drift, $< 100\,\mu\text{m}$ overall		
σ_{point} in Rz	$\simeq 0.4\,\text{mm}, 1.4\,\text{mm}$ (for zero drift and full drift)		
2-hit resolution in $R\phi$	$\simeq 2\,\text{mm}$		
2-hit resolution in Rz	$\simeq 6\,\text{mm}$		
$\text{d}E/\text{d}x$ resolution	$\simeq 5\,\%$		
Momentum resolution at 3.5 T	$\delta(1/p_{\text{t}}) \simeq 10^{-4}\,(\text{GeV/c})^{-1}$ (TPC only)		

arising from field inhomogeneities in the TPC track reconstruction should be corrected to an accuracy of about 30 µm:

$$\sigma_{R\phi}^2 = (100\,\mu\text{m})^2 + (30\,\mu\text{m})^2 = (105\,\mu\text{m})^2 \tag{2.11}$$

This is motivated by allowing at most for a 5 % degradation in the momentum resolution, which is achieved fulfilling the requirement above since $\delta(1/p_{\text{t}}) \sim \sigma_{R\phi}$ (see Equation 2.10).

In the following two sources of inhomogeneities of the electric field will be introduced. Both can be attributed to ions that traverse the sensitive volume of the TPC. The limitation of the field distortions arising from these ions, which in the end deteriorate the TPC performance and in particular the momentum resolution, will result in an additional requirement for the ILD TPC.

Ions in the ILD TPC

There are two sources of ions in a TPC. First of all, fast charged particles produced in the electron-positron collision ionise the gas in the sensitive volume of the TPC. The corresponding process is called primary ionisation. It is introduced in the following chapter. The pairs of ions and electrons resulting from the primary ionisation are separated by the electric field inside the TPC. The resulting distribution of the produced ions inside the TPC

depends on the ILC beam parameters and the physics processes. Since the drift velocity of ions ($\mathcal{O}(1\,\mathrm{m/s})$) is much smaller compared to electrons ($\mathcal{O}(10\,\mathrm{m/ms})$), they need much more time to leave the TPC volume. Until they reach the cathode they stay in the sensitive volume and distort the electric field inside the TPC. Electrons produced subsequent to the first ionisation, drift in the distorted electric field. In consequence, the electron path is distorted compared to the ideal case, where the electric field is parallel to the field cage and the magnetic field. Since the production of such ions is connected to the working principle of the TPC they can not be avoided. The number of ionising collisions per path length depends on the gas used in the sensitive volume. Therefore, the choice of the TPC gas allows to influence the number of ions produced in the primary ionisation. Here one should keep in mind, that a reduction in the number of ions produced in the primary ionisation also means that there are less signal electrons. This in consequence results in a degradation of the momentum resolution, since the point resolution depends on the number of primary electrons. This will be shown in the following chapter in Section 3.3.2. Calculations presented in Ref. [8] indicate, that the distortions expected from the primary ionisation in the considered ILD TPC gas (introduced in Section 4.1) are acceptable with regard to the desired momentum resolution.

The second source of ions in the sensitive volume of the TPC is the amplification stage in the anode. Electrons produced in the primary ionisation after an ILC bunch crossing enter the amplification stage and a certain amount of ions produced in the amplification process will drift back into the sensitive volume of the TPC. The ratio between the number of electrons that enter the amplification stage and the number of ions that reach the sensitive volume is called ion feedback ratio (IFR). This ratio depends on the technology used in the amplification stage. With each bunch crossing ions are produced in the amplification stage and start drifting through the whole TPC volume. Within one bunch train, with a length of 1 ms, 1312 bunch crossings happen (see Figure 2.5). Until the next bunch train arrives after 199 ns no ions are produced. Therefore, the ions produced during one bunch train that travel through the TPC effectively form an ion disc with a width of approximately 1 cm. Finally, in case of the considered ILD TPC gas three ion discs will be present in the sensitive volume at any time. This is a consequence of the ion drift velocity in the ILD TPC gas and the ILD TPC drift length.

The sketch shown in Figure 2.9a illustrates the primary ionisation by a traversing particle (green) as well as the ion discs resulting from the signal amplification in the anode. The paths of the electrons produced in the primary ionisation are depicted by the blue lines. In the top half of this figure the distortions resulting from the ion discs are illustrated, whereas

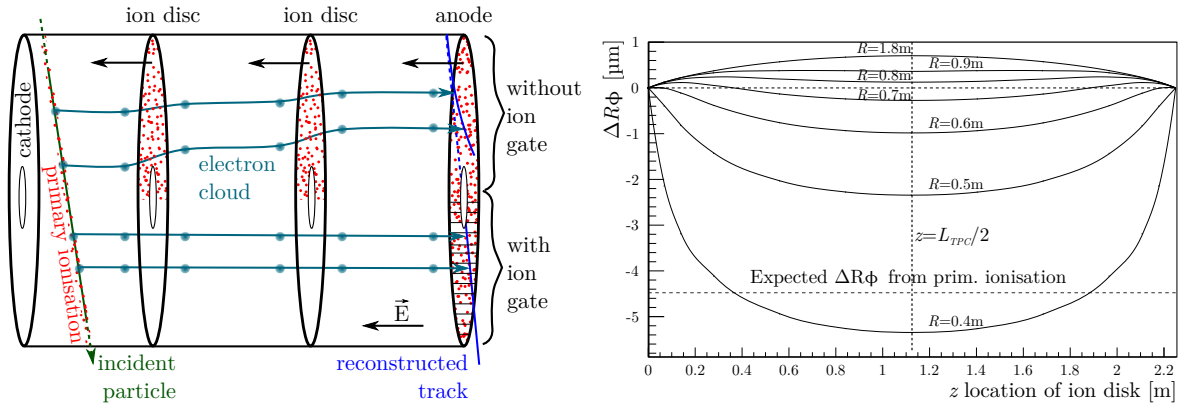

(a) Sketch of the electron paths with (upper half) and without (lower half) distortions caused by ions in the sensitive volume of the TPC. Red points depict ions and two ion disc are shown.

(b) Expected distortions in $R\phi$ simulated for one ion disc at different positions along the TPC axis and for different radii. In the simulation the ion feedback ratio was set to one.

Figure 2.9: Illustration of the effect of ions in the TPC volume and corresponding results of a simulation (adapted from Ref. [8]).

in the bottom half of the figure no ion discs are present. Here a gating device added to the anode prevents ions from penetrating the sensitive volume of the TPC. The reconstructed track on the anode plane is shown in dark blue. In the top half the reconstructed track deviates from the projection of the incident particle track, whereas in the lower half the particle track projection is ideally reconstructed.

In Figure 2.9b the expected distortions resulting from one ion disc in the TPC in dependence on the position of the ion disc are shown. The centre of the TPC is indicated by the vertical dashed line and the assumed ion feedback ratio is one. Furthermore, the distortions are given for the maximum drift length. Therefore, this figure shows the maximum expected distortions. It can be seen, that the expected distortions are at maximum close the inner field cage wall of the TPC ($r = 0.4\,\mathrm{m}$). This results from the radial ion density in the TPC, which is higher at lower radii. The horizontal dashed line indicates the expected distortions from primary ionisation, which is only 20 % lower than that expected from the ion disc. This is only true for one disc and an ion feedback ratio of one, but as mentioned above there are three discs in the ILD TPC and a realistic ion feedback ratio is three. Thus, the values shown in Figure 2.9b need to be multiplied by a factor of 9 in order to estimate the distortions at the ILD.

Finally, the maximum expected distortions in $R\phi$ are in the order of $\sim 60\,\mu\mathrm{m}$. This is in the same order as the required point resolution in $R\phi$ (see Table 2.2). Hence this feedback ratio is not acceptable and the ion feedback needs to be reduced. In order to limit the

distortions already at the hardware level to $\sim 30\,\mu m$ the ion feedback ratio needs to about one. This is the requirements mentioned above, that results from the ILC bunch structure the ILC pair background in the ILD and the required field homogeneity, which limits the effect on the momentum resolution to about 5 %.

As indicated in Figure 2.9a this can be done with a gating device integrated in the anode, that stops ions from penetrating into the sensitive volume of the TPC. How such a device can be realised is currently under investigation. One possibility is a wire gate, which by applying sufficient potentials to the wires efficiently blocks ions. Such wires gates were already used in former experiments as for example at the ALEPH detector, where all ions were blocked in between bunch crossings [27]. At the ILC the gating between individual bunches would not be possible, since the time between bunch crossings is only 545 ns. Therefore, one would need to block all ions produced during one bunch train. In general a wire gate introduces additional material needed to stretch the wires, which is unfavoured. A second possibility is to use Micro Pattern Gaseous Detectors, which are introduced in Section 3.4, to reduce the ion feedback ratio. Basically these devices are used in the signal amplification, but they can also be tuned to act as ion gate. This application of Micro Pattern Gaseous Detectors is studied in Chapter 6.

3

Fundamental principles of a Time Projection Chamber

A Time Projection Chamber (TPC) will be the central tracking detector of the ILD detector. The main parts of a TPC are a cathode, a field cage and segmented anode as sketched in Figure 3.1. By applying a high electric potential to the cathode and grounding the anode, a constant electric field inside the field cage is created. The volume inside

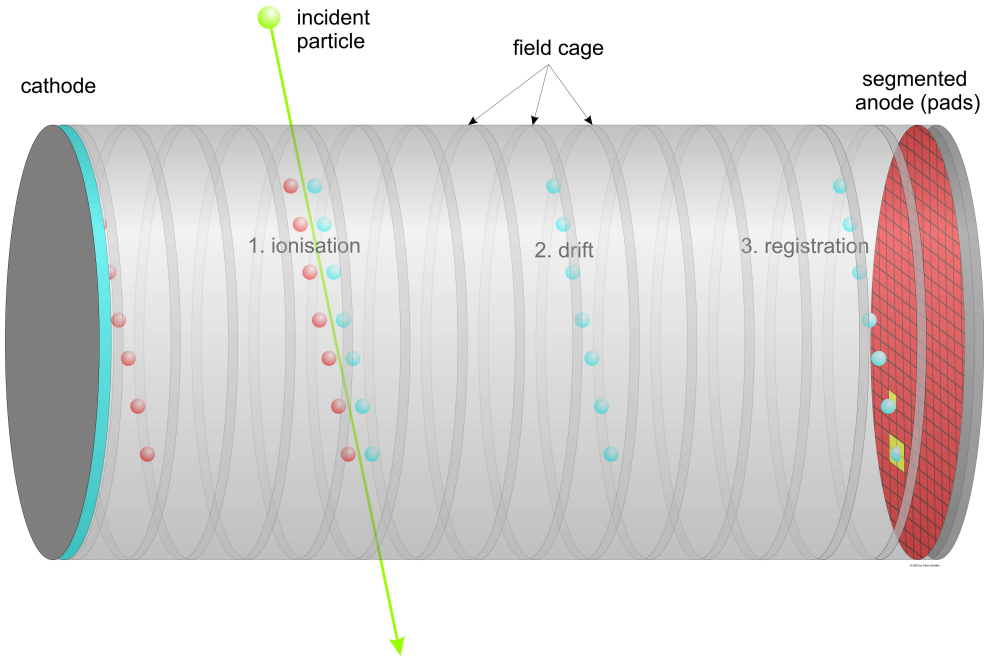

Figure 3.1: Sketch of a TPC illustrating the fundamental working principle [28].

the field cage is the sensitive volume of detector. It is filled with gas so that incident ionising particles produce pairs of electrons and ions along their path trough the sensitive volume.

In addition, parallel to the electric field inside the sensitive volume a magnetic field is applied. This causes a curvature of the incident particle due to the Lorentz force, which allows to measure its momentum. The momentum measurement and the gas ionisation are introduced in Section 3.1.

Caused by the electric field, subsequently the ions drift towards the cathode and the electrons drift towards the anode. The particle drift in gases under the influence of electric and magnetic fields is discussed in Section 3.3. At the anode the electron signal is amplified and finally recorded on the segmented anode. The amplification is realised with micro-pattern gaseous detectors introduced in Section 3.4.

3.1 Primary ionisation in the sensitive volume of a TPC

The energy loss per unit of path length of relativistic charged heavy particles traversing the sensitive volume of the TPC is given by [15]:

$$\frac{\mathrm{d}E}{\mathrm{d}x} = \frac{e^4 N_A}{4\pi\epsilon_0 m_e c^2} q^2 \frac{Z}{A}\frac{1}{\beta^2}\left[\ln\left(\frac{2m_e c^2\beta^2\gamma^2}{I_0}\right) - \beta^2 - \frac{\delta(\beta\gamma)}{2}\right], \tag{3.1}$$

where the concerned quantities are the following:

m_e	electron mass
N_A	Avogadro's number
Z	atomic number of the traversed matter
A	atomic mass of the traversed matter
ϵ_0	dielectric constant
e	elementary charge
q	charge of the travelling particle
c	speed of light
β	speed of the incoming particle in units of c
$\gamma = \sqrt{1/(1-\beta)}$	Lorentz factor
I_0	mean excitation energy of the atom

$\delta(\beta\gamma)$ density effect correction to ionisation energy loss

According to this equation, which in literature is often referred to as Bethe-Bloch equation, for low β the energy loss decreases like $1/\beta^2$. A minimum in the energy loss is reached at $\sim 3.2\beta$ and particles with such a momentum are called minimum ionising particles (MIP). At high β the energy loss is restricted by last term in Equation 3.1. This restriction can be understood as a shielding of the field from the incident particles by the medium, which becomes polarised.

One important consequence of Equation 3.1 with regard to the TPC as central tracking detector is, that the deposited energy is different for different charged particles with same momentum. In consequence, the TPC can be used for particle identification. Figure 3.2 shows the measured energy deposited per unit path length. Clearly different regions of energy deposits can be identified for a particle momentum below 1 GeV/c. They can be assigned to different particles and therefore allow a particle identification by the energy loss measurement in the TPC. For particle momenta above 10 GeV/c the energy deposit per unit path is similar for different charged particles and thus a particle identification using this quantity can no longer be used.

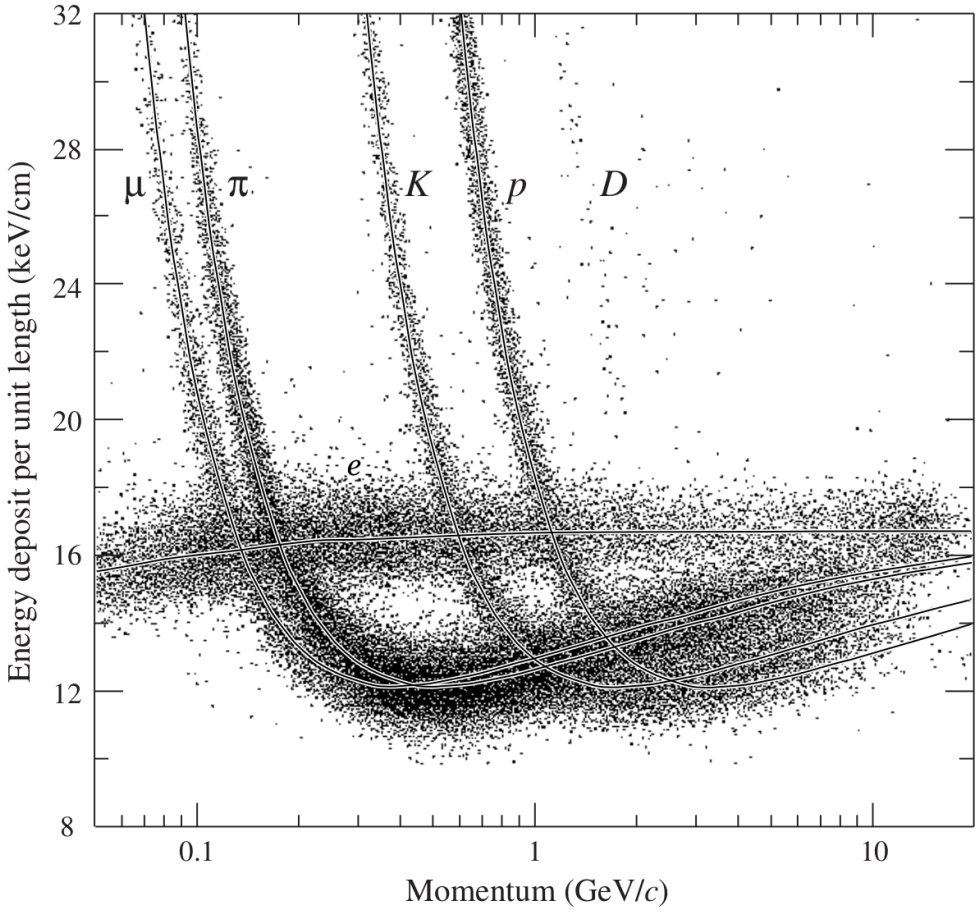

Figure 3.2: Measured energy deposition in a TPC using a Ar:CH_4 (80 %:20 %) gas mixture[15].

3.2 Interaction of photons with matter

Depending on the photon energy different processes are relevant. At low photon energies the photoelectric effect is dominant. It describes the interaction of the photon with an electron of an atomic shell, which results in the liberation of an electron and an excited atom/molecule. The latter one returns to ground state through fluorescence or a radiationless process (called Auger effect). For medium photon energies incoherent scattering is dominant, which is described by the Compton effect. At high photon energies photons convert into an electron-position pair.

Since these processes are statistical, the intensity I of a photon beam with input intensity I_0 passing through a material with thickness x is given by:

$$I = I_0 \mathrm{e}^{-\mu x}, \tag{3.2}$$

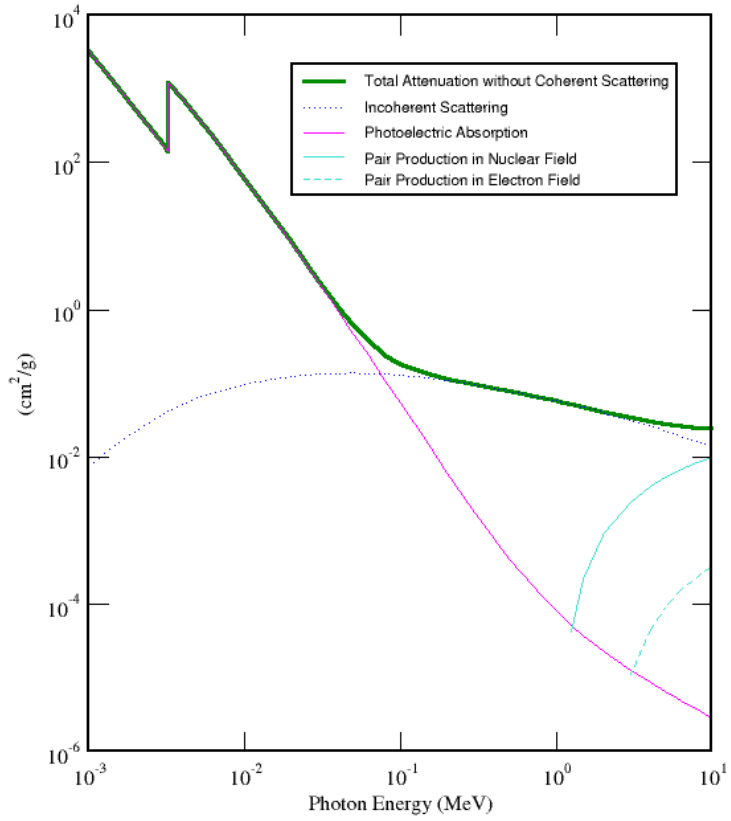

Figure 3.3: Total mass attenuation coefficient for T2K [29]. In addition, the contributions of the individual processes are shown.

where μ is the attenuation coefficient that depends on the photon-absorption cross section σ according to:

$$\mu = \sigma\rho\frac{N_A}{A}. \tag{3.3}$$

Here ρ is the density of the material.

As an example the total mass attenuation coefficient for T2K is shown in Figure 3.3. In addition, the different contributions discussed before are shown and illustrate the different regions.

3.3 Charge transport and amplification in a TPC

3.3.1 Particle drift in gases

In general the drift of particles, with charge q, in gases under the influence of magnetic and electric fields can be described by the corresponding equation of motion:

$$m\frac{\mathrm{d}\vec{v}}{\mathrm{d}t} = \vec{E}q + q\left(\vec{v}\times\vec{B}\right) + \vec{Q}(t), \tag{3.4}$$

where m is the mass of the particle and $\vec{v}$ is the velocity of the particle. Furthermore $\vec{Q}(t)$ denotes a noise term connected to stochastic scattering with gas molecules. A stationary solution, given for $\tau \ll t$, with $v_{\mathrm{drift}} = \langle\vec{v}\rangle$ can be written as:

$$0 = \left\langle m\frac{\mathrm{d}\vec{v}}{\mathrm{d}t}\right\rangle = \vec{E}q + q\left(\vec{v}_{\mathrm{drift}}\times\vec{B}\right) - \frac{m}{\tau}\vec{v}_{\mathrm{drift}}, \tag{3.5}$$

where the latter term describes a frictional force with a characteristic time of τ. This time can be identified as the mean collision time in the microscopic picture.

Using the cyclotron frequency $\omega = Bq/m$ and the mobility $\mu = \tau q/m$, Equation 3.5 can be rewritten and finally the drift velocity can is given as (see Ref. [30]):

$$\vec{v}_{\mathrm{drift}} = \frac{\mu E}{1+(\omega\tau)^2}\left[\hat{e}_E + \omega\tau\left(\hat{e}_E\times\hat{e}_B\right) + (\omega\tau)^2\left(\hat{e}_E\cdot\hat{e}_B\right)\hat{e}_B\right], \tag{3.6}$$

where $\hat{e}_E$ and $\hat{e}_B$ are unit vectors co-directional with the electric and the magnetic field. As a consequence of Equation 3.6, electrons follow rather the magnetic field lines, since for large magnetic fields the last term becomes dominant. This is because for $\omega\tau$ electrons typically one finds $\omega\tau \sim \mathcal{O}(1)$. Contrary to this, for ions one finds $\omega\tau \sim \mathcal{O}(10^{-4})$ which means they tend to follow the electric field lines.

In most cases the electric field will be parallel to the magnetic field. Hence, the cross product term in Equation 3.6 vanishes. Consequently, the drift velocity is given by:

$$\vec{v}_{\mathrm{drift}}\Big|_{\vec{B}||\vec{E}} = \mu\vec{E}. \tag{3.7}$$

In other words the drift velocity does not depend on the magnetic field and is given by the mobility of the particle and the field strength. Figure 3.4 shows the dependency of the electron drift velocity on the electric field for the gas mixture called P5 (95 % Ar, 5 %CH_4).

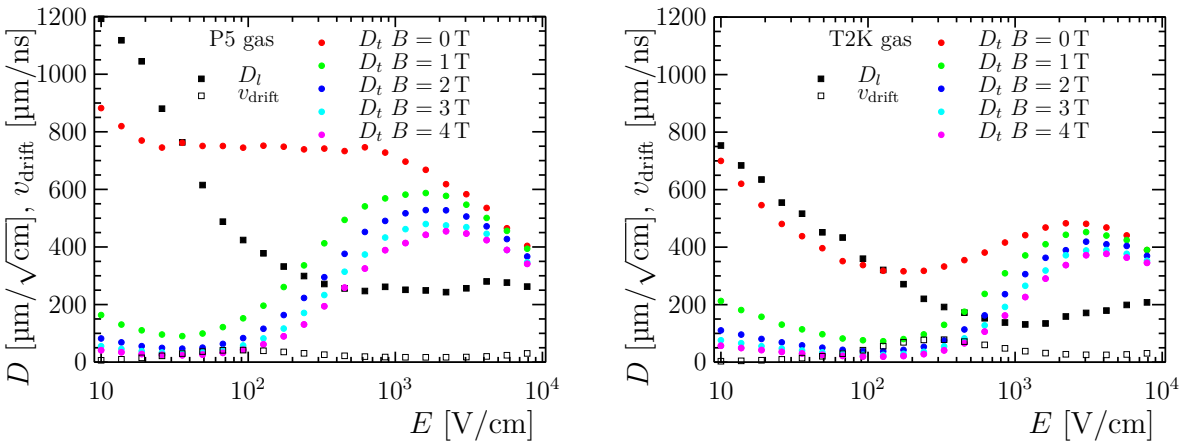

(a) P5 gas mixture: 95 % Ar, 5 % CH_4.

(b) T2K gas mixture: 95 % Ar, 3 % CF_4, 2 % iC_4H_{10}.

Figure 3.4: Parameters of common TPC gas mixtures. Shown are the drift velocity, the transverse diffusion for different magnetic fields and the longitudinal diffusion.

It can be seen, that the electron mobility is not constant, since the drift velocity does not grow linearly with the field strength. Furthermore, a maximum of the drift velocity around 90 V/cm can be observed. An explanation of this maximum is given below by considering the microscopic description of the electron drift. The drift velocity of the second gas mixture that is shown in Figure 3.4b is increased compared to P5 gas, which is in general a desired effect, since it allows a faster readout out of the signal electrons.

However, if the electric field is not perfectly aligned with the magnetic field the cross product term of $\hat{e}_E \times \hat{e}_B$ does not vanish completely. This leads to distortions of drift paths, which is more relevant for electrons than for ions due to their difference in $\omega\tau$. Such effects resulting from field inhomogeneities are in the following referred to as $E \times B$ effects.

Microscopic picture

It is also possible to derive a description of the particle drift based on individual collisions of a particle with gas atoms/molecules. The basic idea is that after a collision the drifting particle has a instantaneous velocity $v_{\text{collision}}$, which is randomly oriented. Before the next collision the drifting particle gains additional kinetic energy in the electric field, leading to an additional velocity v_{field} in the direction of the field. This velocity can

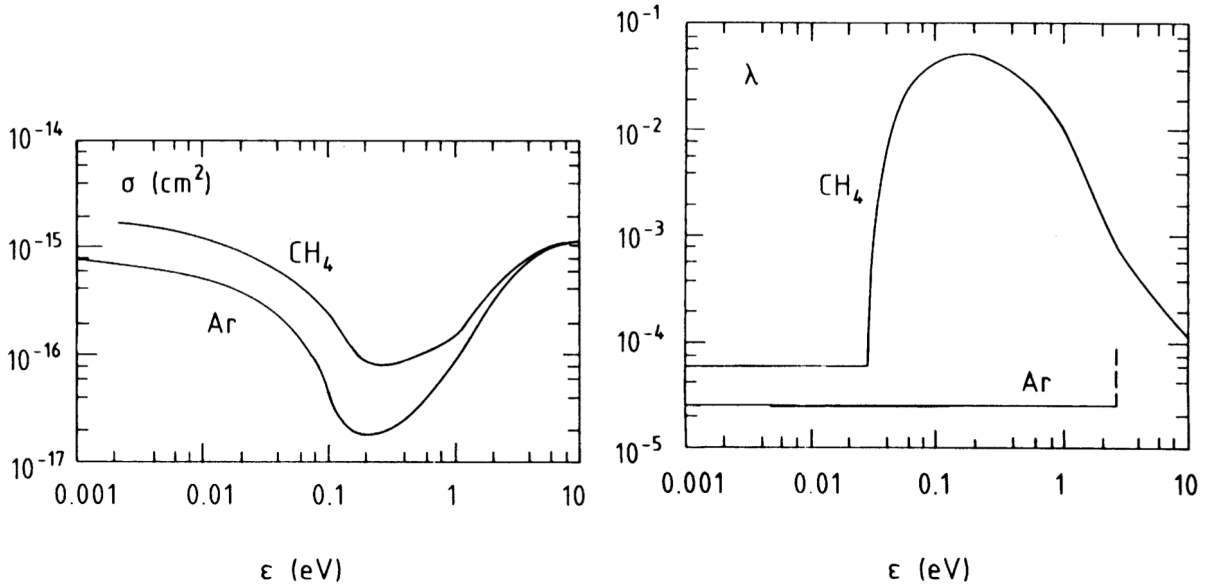

(a) Effective cross-section $\sigma(\epsilon)$ [30]. **(b)** Fraction $\lambda(\epsilon)$ of energy loss per collision [30].

Figure 3.5: Microscopic gas parameters for argon and methane.

macroscopically be identified with the drift velocity. In Ref. [30] both velocities are given as:

$$v_{\text{collision}} = \frac{qE}{mN\sigma}\sqrt{\frac{2}{\lambda}} \tag{3.8}$$

$$v_{\text{field}} = \frac{qE}{mN\sigma}\sqrt{\frac{\lambda}{2}}, \tag{3.9}$$

where σ is the effective collision cross-section, N is the number density of the gas atoms/molecules, m is the mass of the drifting particle and λ is the fraction of energy loss. The dependency of σ on the energy of the drifting particle is shown in Figure 3.5a. Clearly a minimum for argon and methane around $\epsilon \approx 0.2\,\text{eV}$ can be observed. This minimum is due to quantum mechanical processes in the scattering of electrons with the gas atoms/molecules. It was first observed by Ramsauer [31] and is known as Ramsauer minimum. Since the drift velocity is indirect proportional to the cross-section (Equation 3.9), the Ramsauer minimum explains the maximum in the drift velocity seen in Figure 3.4. Figure 3.5b shows the fractional energy loss per collision for argon and methane. The excitation threshold for methane is at 0.03 eV, which is much below that of argon (11.5 eV). This can be explained with additional rotational states of methane compared to argon. Furthermore, this significant difference in the fractional energy loss per collision shows, that the drift velocity (see Equation 3.9) is very sensitive to even small additives of molecular gases. For

example in pure argon at a drift field of 90 V/cm the drift velocity is 2.3 µm/ns, whereas it is a factor 20 larger for P5 and T2K gas (42 µm/ns, see Figure 3.4).

3.3.2 Diffusion

The diffusion of a drifting particle caused by collisions with gas atoms/molecules can be described by a Gaussian density function and a diffusion coefficient $\tilde{D}$:

$$n = \left(\frac{1}{\sqrt{4\pi\tilde{D}t}}\right)^3 \exp\left(\frac{-(x^2+y^2+(z-v_{\text{drift}}t)^2}{4\tilde{D}t}\right). \tag{3.10}$$

Here it is assumed that the drift field is parallel to the z direction and the deviations caused by random scatterings are equal in all directions. Therefore, the width of an initially point-like charge cloud after a drift distance L can be defined in terms of the variance of the Gaussian density function as:

$$\sigma^2_{\text{diff.}} = 2\tilde{D}t = D^2 L \tag{3.11}$$

$$D = \sqrt{\frac{2\tilde{D}}{v_{\text{drift}}}} \tag{3.12}$$

In measurements presented in Ref. [32] it was found, that the diffusion perpendicular to the electric field is different from the diffusion in field direction. Consequently, one has to distinguish between the longitudinal diffusion D_l parallel to the drift field and the transverse diffusion D_t perpendicular to the drift field. Both quantities are shown for the P5 and T2K gas mixture in Figure 3.4. The longitudinal diffusion decreases with increasing drift field until it is almost constant starting from approximately 500 V/cm. Contrary to this, with rising magnetic field strength a minimum in the transverse diffusion can be observed at low drift fields. In absence of a magnetic field the transverse diffusion is almost constant in the region between 50 V/cm and 1000 V/cm for P5 gas, whereas it shows a minimum around 150 V/cm for T2K gas. In general, a reduction of the diffusion for T2K gas is observed compared to P5 gas, which is advantageous for the TPC operation.

This dependency of the transverse diffusion on the magnetic can be understood by considering the electron path between individual collision. In absence of a magnetic field the path is a straight line. If a magnetic field parallel to the drift direction is present, the Lorentz force leads to circular paths for particle movements transverse to the drift direction. The radii of the circles in the plane transverse to the drift direction are indirect

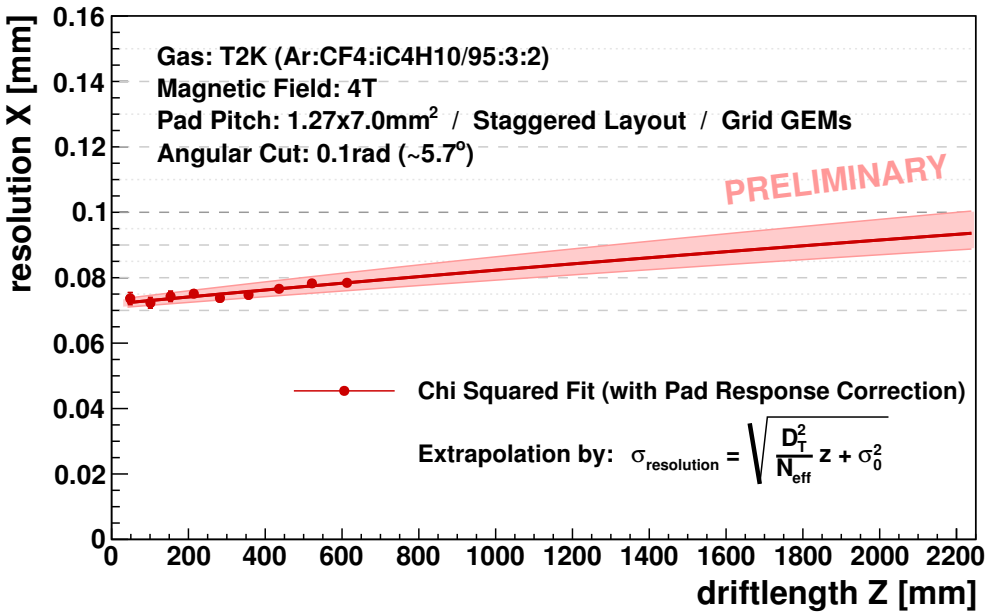

Figure 3.6: Measured point resolution using data taken with a stack of three GEMs at a magnetic field of 4 T with T2K gas [8].

proportional to the cyclotron frequency ω and thus the magnetic field strength. Particle movements in drift direction are not influenced by the magnetic field, since the Lorentz force for $\vec{v}||\vec{B}$ vanishes. In consequence the longitudinal diffusion is independent of the magnetic field, whereas the dependency of the transverse diffusion on the magnetic field is given by [30]:

$$D_t(\omega) = \frac{D_t(\omega = 0)}{1 + \omega^2\tau^2}. \tag{3.13}$$

Finally, the diffusion is directly connected the point resolution of a TPC. It is given as:

$$\sigma_{\text{point}} = \sqrt{\frac{\sigma^2_{\text{diff.}}}{N_{\text{eff.}}} + \sigma_0^2}, \tag{3.14}$$

where $N_{\text{eff.}}$ is the effective number of electrons produced in the primary ionisation process and σ_0 is the additional diffusion in the amplification stage of the TPC. In practice $N_{\text{eff.}}$ and σ_0 can be determined from measurements of the resolution in dependence on the drift length. One example of such a measurement is shown in Section 3.3.2. This measurement was done using the gas and the GEM modules introduced in the next chapter.

3.3.3 Gas amplification

If the electric field in a gas exceeds a certain threshold electrons drifting through the gas gain enough energy between collisions to ionise the gas. This starts an avalanche process, which evolves until the hole gas is ionised or the field decreases. The amplification in the avalanche process is characterised by the first Townsend coefficient α. The increase in the number of electrons per path length $\mathrm{d}s$ is given as:

$$\mathrm{d}N = N\alpha \, \mathrm{d}s. \tag{3.15}$$

Therefore, the number electrons produced by N_0 initial electrons on their way from x_{start} to x_{end} is given by:

$$N\left(x_{\mathrm{end}}\right) = N\left(x_{\mathrm{start}}\right) \exp\left(\int_{x_{\mathrm{start}}}^{x_{\mathrm{end}}} \alpha(s) \, \mathrm{d}s\right). \tag{3.16}$$

Here α depends on the chosen path, since it depends on the local conditions. In detail, α depends on the strength of the electric and the gas density, which in turn depends on the gas pressure and the gas temperature. The ratio between the number of electrons before and after the amplification defines the gain G:

$$G = \frac{N\left(x_{\mathrm{end}}\right)}{N\left(x_{\mathrm{start}}\right)} = \exp\left(\int_{x_{\mathrm{start}}}^{x_{\mathrm{end}}} \alpha(s) \, \mathrm{d}s\right) \tag{3.17}$$

In practise a TPC is most often operated at atmospheric pressure. Thus, the gas density of the drift gas will follow the atmospheric pressure proportionally. The relation between density changes $\Delta\rho$ and changes of the gain ΔG is given as [30]:

$$\frac{\Delta G}{G} \sim -\frac{\Delta\rho}{\rho} \tag{3.18}$$

3.3.4 Attachment

The process of attachment does only apply to electrons and means the attachment of electrons to atoms/molecules of the drift gas. It is characterised by the electron affinity, where a high electron affinity results in a high probability of attachment. For noble gases the collision energy typically reached when drifting in a TPC is not sufficient to achieve attachment. The required collision energy for other drift gas components are lower. A high electron affinity can be found for oxygen, which means the attachment rate in oxygen is high. Consequently, one tries to keep the oxygen content in the TPC gas as low as possible.

In practice oxygen is introduced into the TPC, when it is opened for maintenance or if there is a leakage in the TPC and air enters the TPC volume.

With respect to the TPC performance, one can say that the attachment effectively causes a reduction of the number of electrons produced by the primary ionisation in the sensitive volume. In other words $N_{\text{eff.}}$ is reduced, which results in a degradation of the point resolution (see Equation 3.14).

The attachment is characterised by the attachment coefficient μ. The number of electrons N, which are left after a drift distance of x is given by:

$$N = N_0 \exp(-\mu x), \tag{3.19}$$

where N_0 is the number of initial electrons. Thus, the attachment probability for a drift distance x is given by:

$$A = \frac{N}{N_0} = \exp(-\mu x) \tag{3.20}$$

3.3.5 Penning effect

The Penning effect describes the possibility for an excited atom or molecule (A^*) to deexcite via hitting another atom or molecule (B) with a lower ionisation potential:

$$A^* + B \longrightarrow A + B^+ + e^-$$

Consequently, the deexitation produces an additional electron instead of a deexitation via photon emission or collisions with a wall. Therefore, the Penning effect enhances the gas amplification as well as the primary ionisation yield. Measurements of the Penning effect for selected argon based gas mixtures can be found in Ref. [33].

3.4 Gas amplification with Micro-pattern gaseous detectors

Traditionally, multi-wire proportional chamber, introduced by Georges Charpak [34], have been used in a TPC for the gas amplification. Such chambers are made of tense parallel wires forming a plane. The wire plane consists of field wires and sense wires with alternating potentials. In the end, electrons are accelerated in the resulting high electric field towards the sense wires. The drawbacks of this classical approach is, that the distance between

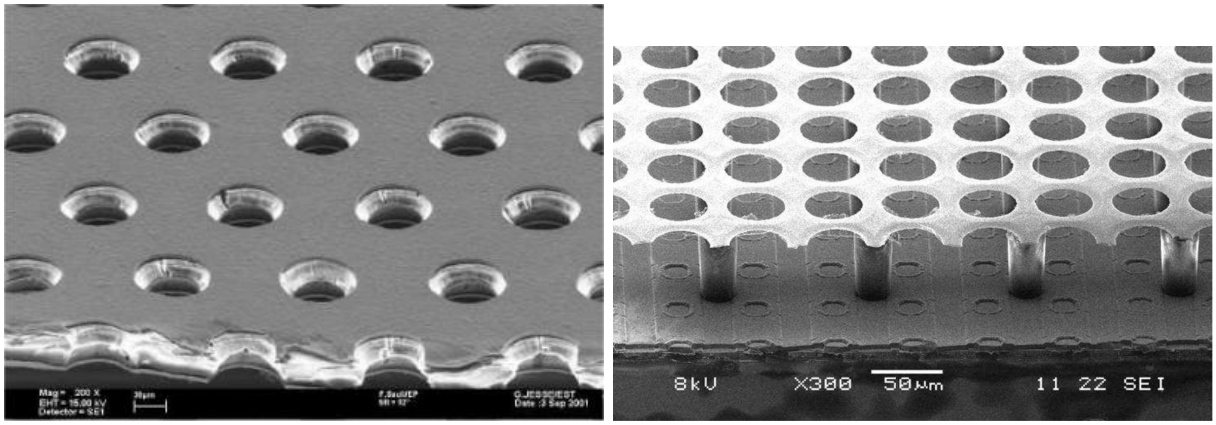

(a) Microscopic picture of a GEM produced at the CERN workshop [36].

(b) Microscopic picture of a MicroMegas [37].

Figure 3.7: Different micro-pattern gas detector technologies.

wires is mechanically limited to about 1 mm. This makes it difficult to separate two nearby tracks and sets limits to the possible resolution in $R\phi$. In addition, a high material budget is needed to avoid sagging of the wires. Measurements with multi-wire proportional chamber showed that the achieved point resolution at $B = 4\,\mathrm{T}$ is a factor three larger than the ILD requirements [35]. Therefore, other technologies need to be considered for the ILD TPC readout.

Since the end of the 1990s commercial technologies for producing integrated circuits are also considered for gaseous particle physics detectors. This allows the creation of structures with sizes in the order of $\mathcal{O}(50\,\mu\mathrm{m})$ leading to Micro-pattern gaseous detectors (MPGDs). Such detectors allow to overcome the limitations of the classical gas amplification using wires, leading to an improved performance of MPGDs including an excellent spacial resolution ($\sim 30\,\mu\mathrm{m}$ [15]) and a high rate capability ($> 10^6\,\mathrm{Hz/mm^2}$ [15]).

In the following two different MPGD technologies will be discussed. A microscopic picture of the first technology called ***G**as-**E**lectron **M**ultiplier* (GEM) is introduced in Section 3.4.1 and shown in Figure 3.7a. The second technology called ***Micro Me**sh **Ga**seous Detector* (MicroMegas) is introduced in Section 3.4.2 and shown in Figure 3.7b.

Apart from the applications of MPGDs shown in this thesis there are many more. Both MPGD technologies introduced in following are used in the COMPASS experiment [38] in various configuration and with different purposes. As mentioned in Section 2.3.2, one option considered for the active layer in the ILD HCAL are gaseous devices. The CALICE[1] collaboration is investigating the possibility to use MPGDs. In this case the charged particle

[1] CAlorimeter for LInear Collider Experiment

is not detected indirectly via signal electrons produced in a gas, like in a TPC, but it directly crosses the MPGD and creates the detectable signal.

Finally, the MPGD technology has also application in fields other than particle physics. One application is presented in Ref. [39], where a system for early forest fire detection based on GEMs is introduced. Furthermore, GEMs are used in a novel nuclear-imaging technique for medical purposes as reported in Ref. [40].

3.4.1 Gas-Electron Multiplier

The Gas-Electron Multiplier (GEM) technology was introduced in 1997 by Sauli [41]. In principle can be described as a perforated capacitor with an insulator enclosed by conductive material, which can be seen in Fig. 3.7a.

In any case the starting point for producing a GEM is a foil made of insulating material, which is most often Kapton®- a polyamide film developed by DuPont[2], covered by copper on both sides. Basically three ways of producing the holes inside this foil are considered:

1. Drilling the holes with a laser.
2. Etching the holes with chemicals.
3. Drilling the holes with a drill.

The latter method can only be used for GEMs with a thickness in the order of $\mathcal{O}(0.5\,\mathrm{mm})$ and a hole pitch in the order of $\mathcal{O}(1\,\mathrm{mm})$. This is not sufficient to meet the goals for the point resolution of the ILD TPC. Therefore, the other two methods are considered for producing GEMs leading to typical hole sizes between 25 µm and 150 µm with hole pitches of 50 µm and 200 µm. The field strength in the holes is about $50 - 70\,\mathrm{kV/cm}$ leading to a gas gain for a single GEM in the order of $\mathcal{O}(100)$. It is fixed by the applied voltage difference between the two copper layers, which in the following is referred to as GEM voltage U_{GEM}. Nowadays there are different companies worldwide producing GEMs. For the module introduced in Sec. 4.3.1, GEMs fabricated at CERN are used. They are produced by etching the holes from two sides resulting in a double conical structure with an inner hole radius of $r = 25\,\mu\mathrm{m}$ and an outer hole radius of $R = 35\,\mu\mathrm{m}$. The masks used to create the holes need to be aligned with high precision in order to get a GEM with homogeneous holes.

[2] http://www.dupont.com/

Technically the total GEM size is limited by the process of aligning the two masks. This fact leads to the development of GEMs, where the holes are etched only from one side with a single mask. Such GEMs can also be produced with larger areas in the order of $\mathcal{O}(1\,\mathrm{m}^2)$. Both techniques - double mask and single mask - are described in Ref. [42]. As indicated in this paper, the exact hole shape influences the characteristics like electron collection efficiency, electron extraction efficiency and gain of the GEM.

The production of holes with lasers results in cylindrical holes. Those are produced for example by the company SCI Energy[3]. Such SCI Energy GEMs are used for the module introduced in Sec. 4.3.2. Their insulator thickness is 100 µm and the hole diameter is 70 µm. Instead of Kapton® a liquid crystal polymer is used as insulator. A comparison between different GEMs in terms of their performance can be found in Ref. [43].

One big advantage of GEMs is, that they can be used in a stack limiting the gain and stored energy per GEM, while giving a high total gain as sum of the single GEM gains. In such a setup the region between GEMs is called transfer region and the corresponding distance is d_{transfer}. The region between the anode and a GEM is called induction region and the corresponding distance is $d_{\mathrm{induction}}$.

Furthermore a GEM intrinsically collects a significant amount of ions produced in the avalanche process. Especially if used in a TPC this effect is advantageous, since ions reaching the sensitive volume of a TPC cause unwanted field distortions as discussed in Section 2.4.4.

3.4.2 Micro Mesh Gaseous Detector

A Micro Mesh Gaseous Detector (MicroMegas) is a parallel plate detector invented by Giomantaris *et al.* in 1995 [44]. It uses a thin metal foil with holes on top of the readout plane, which can be seen in Fig. 3.7b. The amplification takes place in the region between this foil and the readout plane by applying a proper voltage on the foil. For a typical size of the amplification region of 100 µm and a typical voltage difference between the readout plane and the foil of 400 V the field in the amplification region is $E_{\mathrm{induction}} = 40\,\mathrm{kV/cm}$. In order to guarantee a constant gain for the whole sensitive area of the MicroMegas, the metal foil needs to be equidistant to the readout plane all over the sensitive area. This is achieved by small pillars between the readout plane and the metal foil. The whole MicroMegas

[3]SCI Energy 4100 Alpha Road, Suite 900, Dallas, TX, 75244, USA

structure is produced in several steps of depositing and patterning material. A detailed description of the fabrication process is given in Ref. [37].

Heavily ionising particles can trigger a spark in the MicroMegas detector. Amplified by the avalanche process a critical charge density can be reached and evolve into a discharge. This discharge finally reaches the readout plane and possibly harms the connected readout electronics. Furthermore, in such case a large fraction of charge on the foil defining the amplification field is lost. The time needed to recover the field, limits the high rate operation of the detector. One solution to this problem is to prevent the charge from reaching the readout plane. This is done by covering the readout plane with a high resistivity foil. The charge produced by the developing streamer is deposited in the foil. Subsequently the potential produced by this charge reduces the amplification field, resulting in a quenching of the streamer. Thus, by using such foil the charge transfer is limited, the electronics is protected and a total discharge of the mesh is avoided, which reduces the dead time of the detector [45].

4

Design of the ILD TPC

In this chapter several aspects connected to the design of the ILD TPC are discussed. In detail these are the choice of the TPC gas, the construction of the TPC field cage using novel compound materials, the signal amplification using MPGD technologies and the electronics considered for the TPC readout.

The research and development for the ILD TPC is done by the ***L**inear **C**ollider **TPC*** collaboration with members from all over the world. Its major goal is to show, that a TPC fulfilling the requirements introduced in Section 2.4.4 and summarised in Table 2.2 can be realised. Therefore, different work packages were formed. They cover all challenges connected to the ILD TPC, ranging from mechanics, electronics, calibration to software issues.

From the physics point of view the LCTPC collaboration need to show that it is possible to reach the momentum resolution of $\delta(1/p_t) \simeq 1.2 \cdot 10^{-3}\,(\mathrm{GeV/c})^{-1}$. This includes to proof that the required single point resolution (see Table 2.2) can be reached and that field distortion in the sensitive volume are sufficiently small and under control. Finally, it needs to be shown that the TPC can be operated in stable condition for a long time, as the ILC physics programme covers several years of data taking. In order to achieve these goals, within the LCTPC collaboration a large TPC prototype was constructed and build. It is introduced in Section 4.2. This prototype allows to test different technologies and designs of TPC readout modules under comparable conditions.

The modular readout scheme chosen for the ILD TPC has several advantages over the construction of a readout with one big MPGD surface. First of all in a modular design

the MPGD area is limited, which results in a lower probability of a destructive discharge. Furthermore, if a module is lost due to a destructive discharge only a small part of the anode readout is off. Last but not least, the total area of a MPGD is limited by the production process.

The size of the ILD TPC readout modules has not yet been fixed. In the introduction (Figure 2.6b) a design with 8 different module sizes was shown. In practice this means that 8 different module geometries need to be produced. This is necessary in order to adapt each module geometry to the corresponding position (radius) in the anode end plate keeping the dead space between modules at a minimum. Using even larger modules would further reduce the number of different module geometries. In consequence, the maintenance and exchange of modules would be easier. An additional aspect of the module design is the influence of the module size on the mechanical and thermal stability of the end plate. Studies on the mechanical stability with an end plate prototype can be found in Ref. [46].

The readout module design options and technologies are introduced in Section 4.3. Finally, the electronics used for the different module designs are introduced in Section 4.4. The prototype and the readout modules introduced in this chapter are used in the measurements, that will be presented in Chapter 7. The drift gas that is used in all measurements and simulations presented in this thesis is introduced in the following.

4.1 Drift gas

In general the TPC gas has to be chosen with respect to the environment in which the TPC will be operated. Several aspects need to be taken into account when selecting a certain drift gas for the TPC:

- For safety reasons the gas should not be flammable.
- The drift velocity should be fast in order to realise a fast readout.
- The diffusion should be low in order to gain a good spacial resolution.
- The attachment coefficient should be low in order to keep the loss of electrons in the sensitive volume low.
- A high ion mobility is preferred in order to remove ions as fast as possible and limit field distortions caused by ions.

- The hydrogen content should be low in order to reduce neutron scattering in the drift gas.
- The gas density should be low and the radiation length should be high, which limits the multiple scattering of traversing particles.
- The ionisation rate is a compromise between the number electrons produced by primary ionisation (more electrons improve the spacial resolution and $\mathrm{d}E/\mathrm{d}x$ measurements) and the number ions.
- Photons with an energy in the UV range produced in the TPC, mainly in the amplification stage, should be absorbed by the gas in order to avoid electron production by these photons via the photoelectric effect.

Since so far no gas mixtures has been identified fulfilling all the requirements at the same time one has to live with compromises. A detailed discussion about the gas choice in case of the ALICE TPC can be found in Ref. [47]. Currently the non flammable gas mixture called T2K (95 % Ar, 3 % CF_4, 2 % iC_4H_{10}) is investigated as possible drift gas. Compared to other commonly used drift gases it has a high drift velocity and a low diffusion. Furthermore the gas amplification is higher than in other gases. Hence, the advantages of this gas mainly affect the performance of the TPC with respect to a good spacial resolution and a fast signal readout. Contrary, the disadvantages of this gas are more connected to the increased neutron scattering in the drift gas due to the Isobutane compared to other possible drift gases. In addition, the decomposition of CF_4 produces toxic gases like carbonyl fluoride and carbon monoxide. Further, in combination with oxygen the substance hydrogen fluoride can be produced, which forms corrosive and penetrating hydrofluoric acid. This acid in turn can harm the field cage of the TPC and readout modules. If the discussed effects are really a problem for the ILD TPC still need to be investigated in long term tests.

4.2 The Large Prototype TPC

The TPC prototype called Large Prototype TPC (LPTPC) was constructed and build within the LCTPC collaboration. The main idea was, to have a unified prototype for testing different MPGD technologies under comparable conditions. Furthermore the construction of a light weight field cage using novel compound materials could be developed and tested.

The overall size of the LPTPC is chosen such, that it fits into a large superconducting magnet available at the DESY Test Beam area T24. This magnet allows to operate the LPTPC in a 1 T magnetic field and is introduced later in Section 7.3.3. The anode design of the LPTPC was motivated by the idea to operate at least one module, that is surrounded by other modules. Thus, the module performance under ILD TPC like conditions can be tested. Therefore, at least three module rows need to installed to have a module on top and on bottom of the central module. Furthermore, at least three modules need to be installed in the central module row. In the end the anode can house up to seven readout modules, whose size (17 cm × 21 cm) is defined by the number of modules in the anode in combination with LPTPC size fixed by the magnet.

In the following components of the LPTPC – field cage, anode and cathode – are introduced in detail.

4.2.1 Field cage

The field cage was manufactured by DESY [48] in cooperation with a company [1].Its composite wall consists of honeycomb spacer material sandwiched in glass fibre reinforced plastic (GRP). On top and bottom there are Kapton® sheets used as insulator layer. Finally, there is a grounded copper layer on the outer field cage wall, which shields the field cage from outside disturbances. In total the material budget of the LPTPC field cage wall is 1.21 $\%X_0$ [48], which is close to the targeted value for the inner barrel of the ILD TPC of 1 $\%X_0$ [8].

In Figure 4.1a the prototype design is shown. The total length is $l = (61 \pm 0.1)$ cm and the diameter is $d = (72 \pm 0.07)$ cm, which is close to the diameter of $d_{\text{in}} = 658$ mm foreseen for the inner field cage of the ILD TPC . Figure 4.1b shows the result of a survey of the field cage after it was manufactured. It can be seen that a misalignment of the LPTPC axis was observed in this survey. This fact will become relevant for the measurements presented in Section 7.3, where field inhomogeneities in the LPTPC are studied. At this point it can only be estimated that the observed misalignment of the LPTPC axis influences the LPTPC performance and measurements done with it, since the electric field can not be expected to be perfectly aligned with LPTPC axis.

The electric field inside the TPC is produced by applying a high voltage to the cathode and ground to the readout anode. The maximum applicable voltage is about 25 kV, which

[1] Haindl Kunststoffverarbeitung GmbH, Am Knick 4, 28777 Bremen, Germany

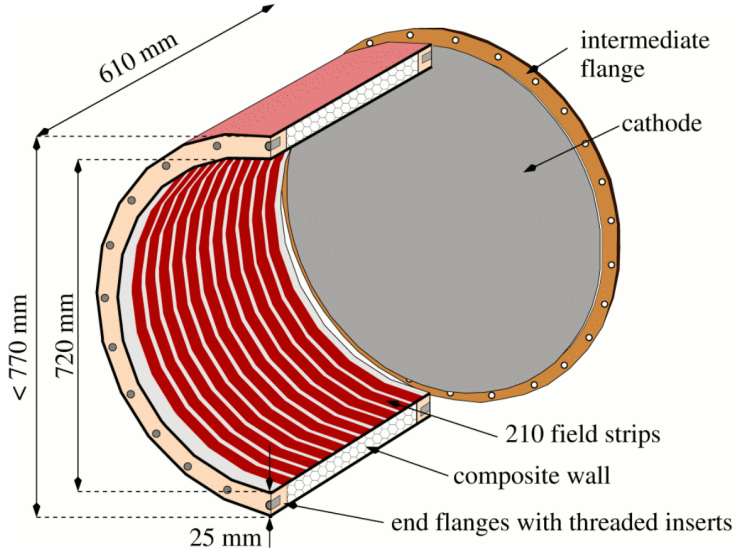

(a) Sketch of the LPTPC.

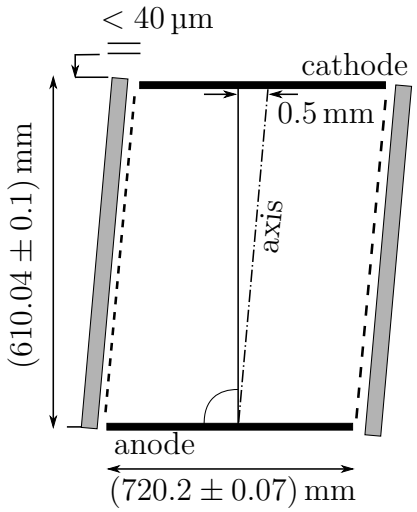

(b) Measured shape of the LPTPC.

Figure 4.1: Designed and measured dimensions of the LPTPC [48]. The right Figure shows, that except of the field cage axis, which is misaligned by 500 µm, the desired lengths, the alignment of the end flanges and the roundness of the barrel was achieved.

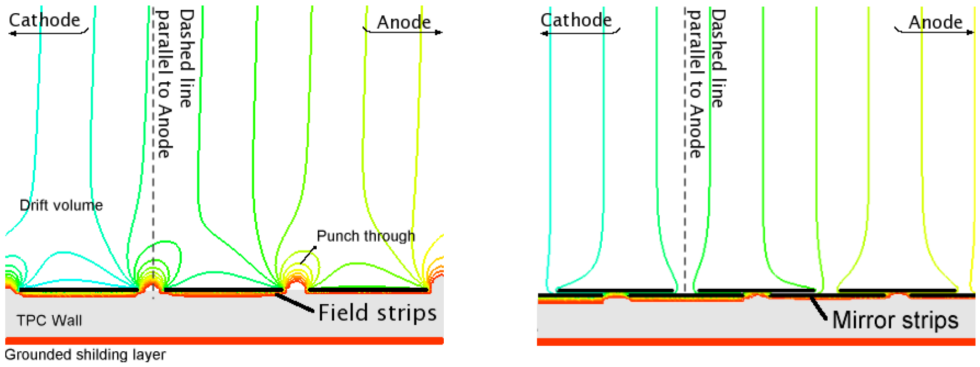

Figure 4.2: Equipotential lines of the electric field with and without shielding mirror strips [49]. Left side: punch through of the ground potential in the unshielded design. Right side: field lines with shielding by mirror strips.

corresponds to a drift field of $E_{\text{drift,max}} = 350\,\text{V/cm}$. In order to guarantee a homogeneous electric field inside the sensitive volume the inside of the field cage is covered with conductive copper rings, which are connected via resistors. A second layer of strips, so-called mirror strips, is installed below the field strips, separated by an insulation layer. The improvement in field homogeneity achieved by introducing the mirror strips is shown in Figure 4.2. Together the two layers shield the internal field from the ground potential applied to the shielding layer on the outer field cage wall. Furthermore, they result in a stepwise decrease of the potential from the cathode to the anode, which guarantees a homogeneous field along

the sensitive volume. The aimed field homogeneity of the LPTPC is $\Delta E/E \leq 10^{-4}$. Further information about the field cage itself can be found in Ref. [48].

4.2.2 Anode end plate

The anode end plate is made of aluminium alloy and was designed and produced at Cornell University. As mentioned above in total seven readout modules can be mounted in the anode, representing a small cut-out of the ILD TPC.

On the inside there are so-called shield elements mounted to the anode plate, which surround the installed modules. These shields are made of G10, which is covered with copper. G10, a commonly used insulator, is a glass epoxy laminate. These elements together with the modules form a homogeneous surface with a constant electric potential – the anode of the LPTPC. It is also possible to insert so-called dummy modules. Such modules are also made of G10 covered with copper similar to the shield elements. They can replace readout modules in case one wants to operate the LPTPC with less than seven readout modules. A technical drawing of the LPTPC anode end plate can be found in Figure A.4.

In order to further reduce the material budget of the anode end plate, a second version was designed and produced at Cornell University. Details about this end plate, which was not used for the measurements presented here, are given in Ref. [46].

4.2.3 Cathode end plate

The cathode of the LPTPC is made of aluminium with a copper layer on top facing the sensitive volume of the LPTPC. At defined positions the copper was removed leading to a pattern of aluminium dots, each with a diameter of (3 ± 0.1) mm. If UV light is shined on the cathode, electrons are created from the aluminium dots via the photoelectric effect. The reconstruction of the produced electrons on the anode side allows an investigation, among other studies, of the electric and magnetic fields inside the sensitive volume of the LPTPC, which is presented in Section 7.3. Since the anode can house up to seven readout modules the pattern was designed to face 56 aluminium dots towards each module. In addition, one line of copper per module is removed from the cathode, which mimics a signal of a charged particle track. Hence, in total there are 7 aluminium lines and 392 aluminium dots on the cathode, which is illustrated in Figure 4.3a. Unfortunately not the designed pattern was

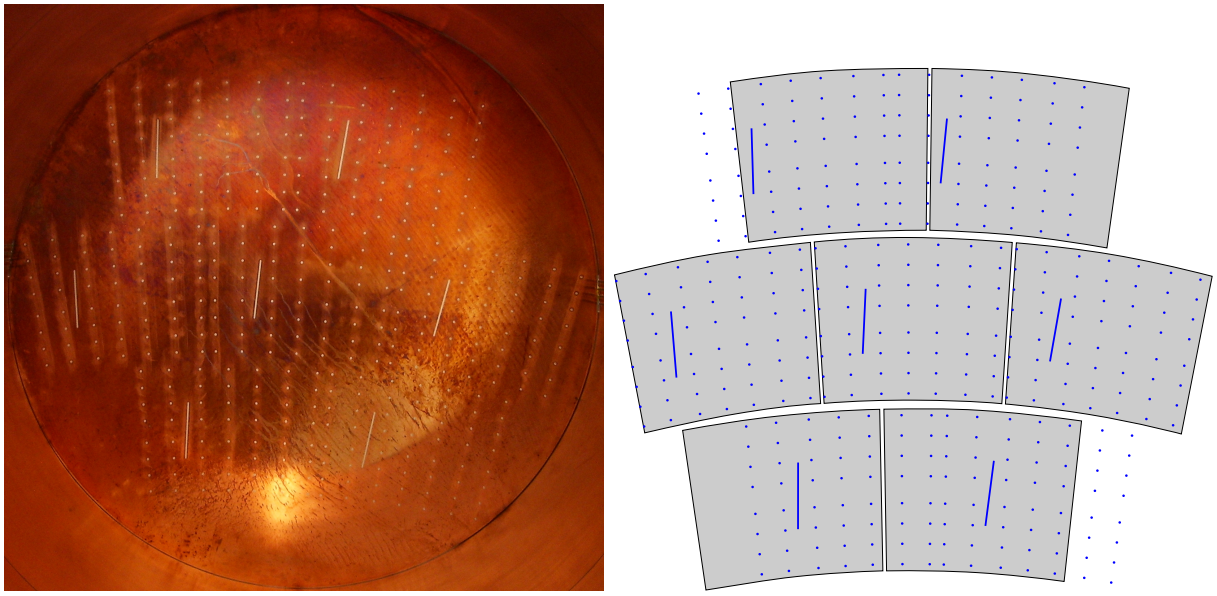

(a) Aluminium pattern on the cathode.

(b) Aluminium pattern projected onto the anode. Also the module outlines are shown in grey.

Figure 4.3: Illustration of the pattern of aluminium dots and lines on the LPTPC cathode.

created on the cathode, but the mirrored pattern. Therefor the pattern is not aligned with the readout modules, which can be seen in Figure 4.3b.

4.3 Readout module design options

In the following three different readout module design options are presented. As introduced in the previous section a common module size, defined by the LPTPC anode, of 17 cm × 21 cm is used for all options. This allows to compare the different options in a comparable setup. The design options involve different technologies for the signal amplification as well as the readout. Based on the results gained with the prototype modules a decision about the option considered for the ILD TPC will be taken in a later phase.

The requirements for the readout modules result directly from the ILD TPC requirements (see Table 2.2). The material budget should be low in order to keep the material budget of the TPC endcap below $0.25\,X_0$. Furthermore, a constant gain over the whole module area is required to achieve the target dE/dx resolution of $\sim 5\,\%$. Finally, the dead space should be as low as possible to guarantee a high detection efficiency of the electrons produced in the primary ionisation.

The technologies that are considered for the signal amplification are GEMs and MicroMegas. Both technologies can be combined with each of the available read out technologies:

1. Pad based signal collection with pad areas of about $6\,\mathrm{mm}^2$.
2. Signal collection using silicon pixel detectors with pixel sizes of $55\,\mu\mathrm{m} \times 55\,\mu\mathrm{m}$.

Particularly, the combination of a silicon pixel detector with a MicroMegas is interesting, since each primary electron reaching the MicroMegas mesh will fire exactly one pixel. Thus, each primary electron can be resolved. This is not possible using GEMs, because here the signal is broadened between the GEMs. In the end clusters of pixel instead of single pixel fire per detected primary electron. First promising results on these technologies can be found in Ref. [50, 51]. If a pixel based read out is needed for the ILD TPC is still in question, since it introduces a large number of readout channels and a significant amount of material. One possibility is to use a pixel based read out only in the innermost region of the TPC, where the occupancy is highest, thus the occupancy there could be significantly reduced using this technology.

Compared to the pixel based read out, the pad based readout and the corresponding module developments are more advanced and closer towards ILD TPC modules. In the following subsections they are introduced in more detail. In principle, all pad layouts currently used by LCTPC use keystone shaped pads. This shape gives the best resolution in $R\phi$ for ILD TPC like pad layouts as shown in Ref. [52]. Also the pad size was motivated by resolution studies like those presented in Ref. [52].

Two different concepts are used concerning the pad size, which are:

1. Constant pad width and variable number of pads per row.
2. Constant number of pads per row and variable pad size.

Option one is used for the GEM based module developed at DESY. The second option is considered by the GEM based module developed in Asia and by the MicroMegas module. Main parameters needed to characterise the pad plane – pad width w_{pad}, pad pitch p_{pad}, pad height h_{pad} and row height h_{row} – are shown in Figure 4.4. An overview of all module pad planes is given in Table 4.1 and drawings of the module are shown in Figures 4.5 and 4.7.

Table 4.1: Characterisation of the different pad planes used by the LCTPC collaboration.

module type	channels	rows	number of pads per row	w_{pad} [mm]	h_{pad} [mm]
DESY GridGEM module	4839	28	164 - 182	1.05	5.65
Asian module	5208	14	176	1.09 - 1.15	5.25
		14	196	1.05 - 1.20	5.25
MicroMegas module	1728	24	72	2.75 - 3.06	6.74

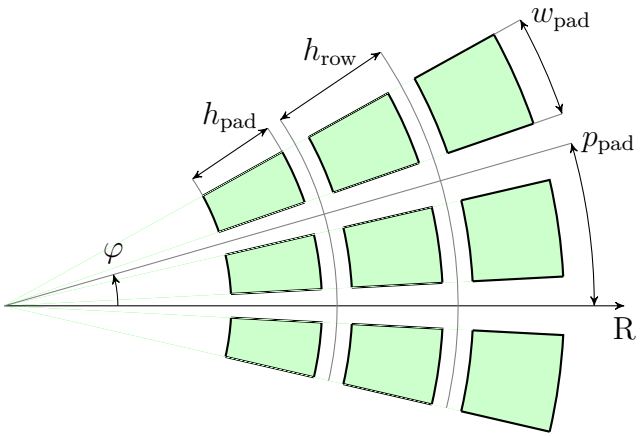

Figure 4.4: Sketch illustrating the parameters used to characterise a pad plane.

4.3.1 DESY GridGEM module

The idea behind this module design is to create a compact, low mass module with a minimal amount of dead space. Usually additional material and dead space is introduced to a module in order to stretching the GEMs of the module and to support the arising forces. This ensures flatness of the GEM foils and constant distances between GEMs, which is required for a homogeneous gain over the module surface and stability of the overall system. In case of the DESY GridGEM module the GEMs are not stretched, which reduces the additional material and dead space.

The DESY GridGEM module, shown in Figures 4.5a and 4.6, consists of three GEMs with the following distances between the GEMs: $d_{\text{induction}} = 3\,\text{mm}$, $d_{\text{transfer}} = 2\,\text{mm}$. These distances and the support of the GEMs is realised by frames made of alumina with a purity of 96 % (CeramTech Rubalit® 708S [53]), a width of 1.4 mm and a height of 1 mm. This material is chosen for its low radiation length and mechanical stability. In order to avoid sagging of GEMs and thus a non uniform gain of the module the alumina frame includes additional vertical and horizontal bars providing additional stability of the GEMs. By

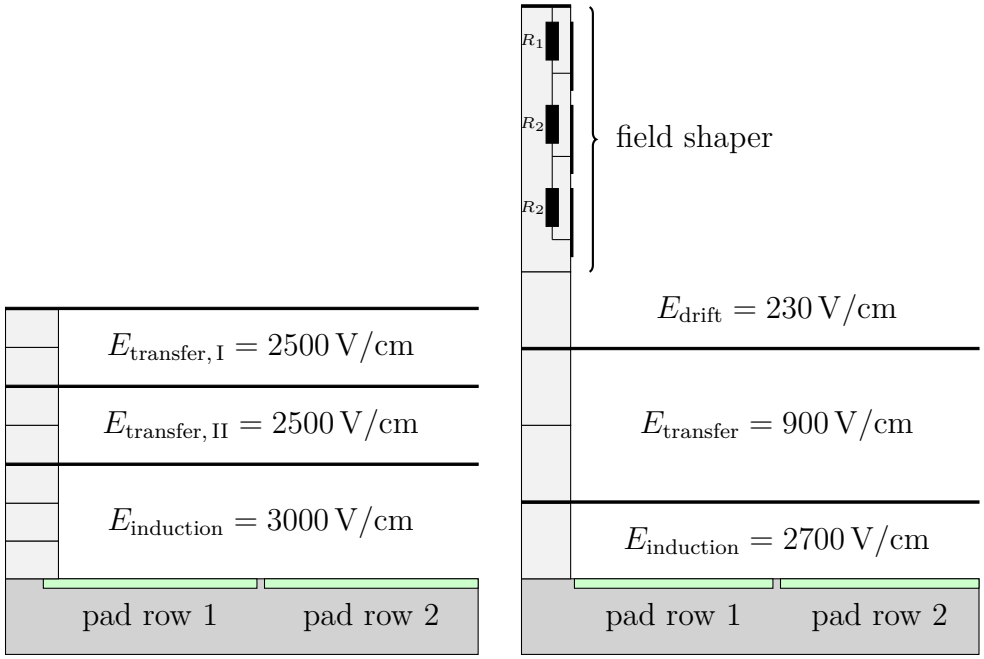

(a) DESY GridGEM module. The GEM support shown on the left side (light grey) covers all module edges.

(b) Asian module. The GEM support shown on the left side (light grey) covers only the top and bottom edge of the module, whereas the field shaper covers all module edges.

Figure 4.5: Scale drawing of GEM based readout modules developed within the LCTPC collaboration. Supporting material is shown in grey and readout pads are is shown in green.

properly adjusting the grid of bars to the typical length scale by which GEM foils undulate, the GEM foils can be flattened without applying undue mechanical stress. The current version of the DESY GridGEM module includes one vertical and one horizontal bar, which can be seen in Figure 4.6a. Obviously these bars introduce a small amount of dead space to the module and divide it into four sectors. A detailed study on the influence of the bars on the modules performance is presented in Ref. [54, 43]. It was shown in these references that variations of the energy resolution due to fluctuations of the distances between GEMs can be limited to 5 % using the bars for supporting GEMs. This meets the requirements of the ILD TPC formulated above.

Furthermore, the sectioning introduced by the bars is also realised directly on the GEMs by dividing the copper surface into four sectors. The advantage of this sectioning is, that the stored energy per sector is limited by the size of each sector, which reduces the probability of destructive discharges of a GEM. Hence the dead space introduced by the bars is utilised to increase the system stability. The GEM surface facing the sensitive volume of the TPC

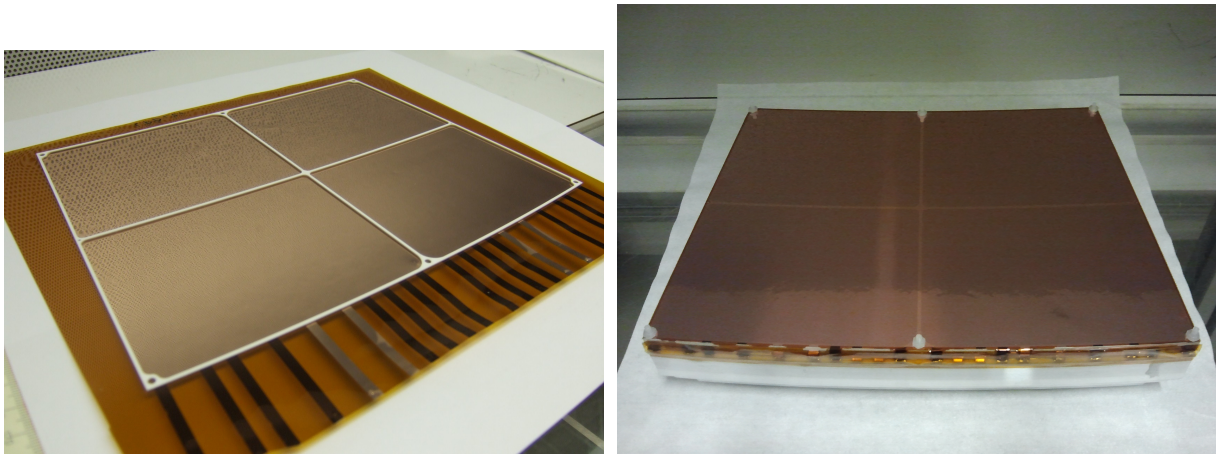

(a) Photo of a GEM with an alumina frame glued on top.

(b) Photo of an assembled DESY GridGEM module.

Figure 4.6: The readout module developed at DESY.

is not segmented in order to not introduce field distortions. An example of such field distortions is shown in Section 7.2.

The pad plane of this module consists of 4839 pad with constant pad size: $w_{\text{pad}} = 1.05\,\text{mm}$, $p_{\text{pad}} = 1.26\,\text{mm}$, $h_{\text{pad}} = 5.65\,\text{mm}$, $h_{\text{row}} = 5.85\,\text{mm}$. Due to the chosen pad layout with constant pad sizes the number of pads increases with the radius from 164 pads per row to 182 pads per row. Furthermore the pads are staggered, which gives a better resolution in $R\phi$ compared to unstaggered pads (see Ref. [52]). This means pads are shifted by a half pad width along the pad row with respect to neighbouring rows. Furthermore the first and the last pad row are partially covered by the alumina frames, which can be seen in Figure 4.5a. The overlap is 0.4 mm.

4.3.2 Asian GEM module

In contrast to the DESY GridGEM module, stretching of GEMs is considered for the Asian GEM module [55]. The idea is, that in R direction a lot of measurement points along a track are taken. Since the momentum resolution is proportional to $(N)^{-1/2}$ (see Equation 2.8), reducing the sensitive area along R will not much reduce the momentum resolution. Therefore, the material supporting the GEM stretching is on top and on bottom of the module. A scale drawing of the module is shown in Figure 4.5b, where the supporting material is shown in light grey below the field shaper and between the GEMs. Furthermore, the aim is to keep the dead space between modules in ϕ direction

as low as possible by leaving out a supporting structure on the left and right side of the module.

The amplification is realised with 2 GEMs, which are separated by the following distances: $d_{\text{transfer}} = 4\,\text{mm}$, $d_{\text{induction}} = 2\,\text{mm}$. In addition, the module design foresees to mount an ion gating structure on top of the module. This requires a certain drift distance between the GEM and the gating structure. This distance is set to 9 mm for this module and also shown in Figure 4.5b on top of the upper GEM. It can be seen from this drawing, that this distance is inside the module. Thus, the gating structure is foreseen to face the sensitive volume of the TPC in case of the Asian module. The field between the gating structure and the upper GEM is shaped by setting proper voltages on three copper strips attached to the module wall. The voltage of this strips is provided by a resistor chain also shown in Figure 4.5b, where $R_1 = 0.5\,\text{M}\Omega$ and $R_2 = 1\,\text{M}\Omega$. The module wall, with a width of 1.3 mm, embraces the whole module boundary in the region between the GEM and the gating structure. This part is called the field shaper. In contrast to the field shaper, the GEM frames are only on the top and the bottom module boundary as mentioned before. In addition to the copper strips on the field shaper walls, also copper is on top of the field shaper. Applying a proper voltage here reduces field distortions between modules.

In principle the number of pads on the pad plane for this module is kept constant. In the first 14 rows the number of pads is 176 and the pad size increases from $w_{\text{pad}} = 1.09\,\text{mm}$ to $w_{\text{pad}} = 1.15\,\text{mm}$. Also the pad pitch increases from $p_{\text{pad}} = 1.19\,\text{mm}$ to $p_{\text{pad}} = 1.25\,\text{mm}$. Starting with row 15 the number of pads is increased to 196 in order to ensure a reasonable pad size and active area. Therefor, the pad size is adopted to $w_{\text{pad}} = 1.05\,\text{mm}$ and increases until row 28 to $w_{\text{pad}} = 1.20\,\text{mm}$. The pad height and the row height are constant for all rows: $h_{\text{row}} = 5.35\,\text{mm}$, $h_{\text{pad}} = 5.25\,\text{mm}$. Furthermore the first and last pad row are 1.4 mm away from the module boundary and thus 0.1 mm away from the field shaper. In contrast to the DESY GridGEM module, pads of the Asian module are not staggered, but aligned to the pads in neighbouring rows.

4.3.3 MicroMegas module

The problems of stretching surfaces and supporting arising forces does not apply to the MicroMegas modules, since the mesh metal foil is supported by the pillars (see Section 3.4.2). Furthermore, only one potential needs to be provided and set to on the metal foil. A scale drawing of one module edge is shown in Figure 4.7, were on the left side a surrounding copper layer is shown. The potential on this copper layer is fixed to 0 V since it is connected

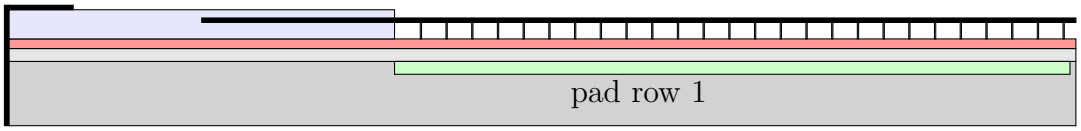

Figure 4.7: Scale drawing of the MicroMegas readout module developed within the LCTPC collaboration. Materials are colour coded: photoresist in blue, prepreg in light grey, PCB in grey, pad in green. In addition, the mesh and corresponding pillars are shown. Furthermore the surrounding shield made of copper is shown in black on the left side.

to the anode plane. Furthermore, Figure 4.7 shows that the mesh is 1 mm below the bounding frame of the module. The bounding frame is made of a photoresist. In between the resistive layer and the pad plane is a 100 µm thick layer of LF 0121 Pyralux®Bondply material.

As discussed in Section 3.4.2, the readout plane is covered with a resistive layer. One consequence of this layer is a broadening of the narrow avalanche signal produced in the amplification region of the MicroMegas detector. Therefore, the signal can be spread over several anode pads, which allows to overcome resolution limitations, defined by the pad size ($\sigma_{\text{row}} = w_{\text{pad}}/\sqrt{12}$), in case of only one pad collects charge. The amount of signal broadening can be controlled via the sheet resistivity of the resistive layer. It needs to be adapted to the anode pad size, which is 2 mm × 6 mm for the current design. The current resistive layer is made of Dupont 100 XC10E5 resistive Kapton® with a sheet resistance of 3 MΩ/□ and a thickness of 75 µm. It was shown in Ref. [56], that the chosen combination of pad size and sheet resistivity results in a sufficient point resolution.

Similar to the Asian module the pads are not staggered, but aligned to the pads in neighbouring row. From row 1 to row 24 the pad width increases: $w_{\text{pad}} = 2.88\,\text{mm}$ - 3.06 mm. The number pads per row is 72 and the pad height is $h_{\text{pad}} = 6.74\,\text{mm}$ for all pads. Also the row height is fixed to $h_{\text{row}} = 6.84\,\text{mm}$.

4.4 Electronics

4.4.1 Electronics for GEM based modules

The electronics used to read out the charge signals on the anode basically consists of two chips. First there is a programmable application specific integrated circuit (ASIC), called PCA16. It is an analog chip used for signal shaping and signal amplification. Second there

is a digitisation chip, which is a modified version of the so-called ALTRO chip used in the ALICE[2] electronics. Both parts are combined on a front end card (FEC). It hosts 8 PCA16 chips and 8 ALTRO chips providing in total 128 readout channels. The FECs are connected to the pads of the DESY GridGEM module via flexible Kapton® cables, each with 32 channels. Thus, 4 Kapton® cable are connected to each FEC. The data of the FECs is collected and packaged via a so-called Readout Control Unit (RCU), which than sends it to the Data Acquisition (DAQ) computer. In addition, it also initialises and monitors the FECs. This means the settings of the PCA16 chip and the ALTRO chip on each FEC can be tuned to the needs of the experiment. Such settings are for example the polarity, preamplification, peaking time, gain and decay time in case of the PCA16 chip and zero suppression and the number pre and post samples in case of the ALTRO chip. The maximum possible sampling frequency is 40 Mhz and it was set to 20 MHz in the measurements presented here. This results in a signal sampling in steps of 50 ns. For further information see Ref. [57, 58].

4.4.2 Electronics for MicroMegas modules

The electronics used for the MicroMegas modules is based on the electronics of the T2K experiment. This experiment based in Japan is investigating neutrino oscillations with an neutrino beam travelling 295 km. One of the detectors used in this experiment is a TPC using MicroMegas for the signal amplification (see Ref. [59]). The number of channels per MicroMegas module (24 rows with 72 pads) was matched to the number of channels per T2K module (48 rows with 36 pads). This allows to use similar electronics for the measurements using MicroMegas, which are presented in Sec. 7.3. One should note that the requirements to the electronics for an ILD TPC might not be fully met by these electronics, since the requirements for the T2K experiment and the ILC are different.

The smallest block of the electronics is an ASIC, called AFTER, which processes signals on the pads and buffers them in a 511-time bin switched capacitor array. It can handle the signals of 72 pads. Four of such AFTER chips and the required external ADCare mounted on a FEC, reading 288 channels. Finally, 6 FECs are connected to a front-end mezzanine card (FEM), which aggregates the data, performs zero-suppression and sends the data over a 2 Gbps optical link to a back-end data concentrator card. This card, placed in the measurement hut away from the TPC and the magnetic field used in the measurements, communicates with the DAQ computer and provides trigger and configuration information

[2] One of the four experiments at the LHC at CERN.

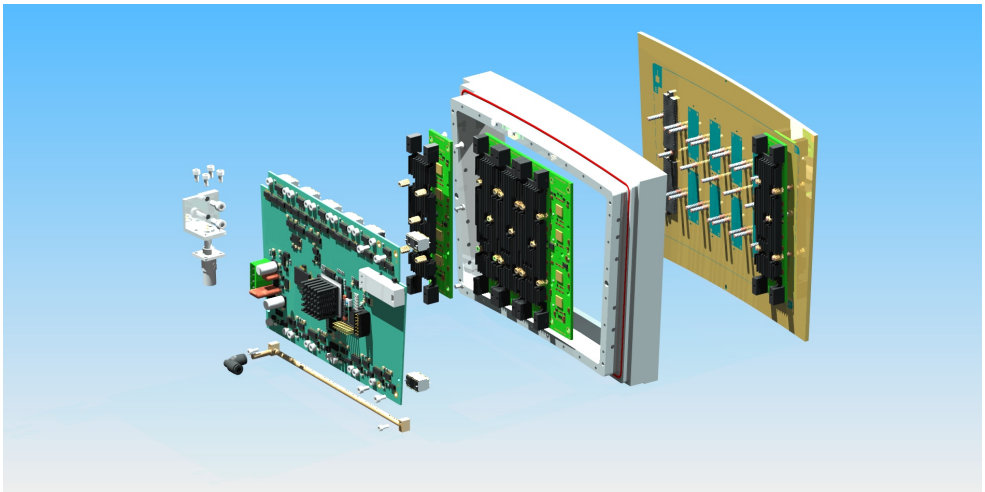

Figure 4.8: Sketch of a MicroMegas module showing the integrated electronics [60].

to the FEM. The master clock of the electronics runs at a frequency of 100 MHz. The sampling frequency is derived from this clock by dividing it by integer numbers $i \in [1, 64]$, leading to sampling frequencies of 100 MHz . . . 1.5625 MHz. In the measurements presented in Section 7.3 the sampling frequency was set to 25 MHz, resulting in a sampling of the input signal in steps of 40 ns.

The original FEC size of a T2K FEC is about 14 cm × 25 cm, which is to big too be integrated in one MicroMegas module as it is proposed for the ILD TPC. Therefor a redesign of the FEC was done within the LCTPC collaboration leading to a modified FEC with a size of 2.8 cm × 12.5 cm. In order to achieve this, the AFTER chips (3.5 cm × 3.5 cm) needed to be unpacked and wire bonded directly to the FEC resulting in a reduced space needed per AFTER chip (0.74 cm × 0.78 cm). A module with the electronics is shown in Fig. 4.8. This figure shows a version where the cooling was done using compressed air blown through the pipe shown in the bottom left part of the sketch. This pipe distributes the air to the six radiators (one per FEC), which are also visible in this sketch. The electronics used for the measurements presented in Section 7.3 was modified and the radiators were replaced by cooling pipes. Instead of compressed air CO_2 provided by a system called TRACI [61] was used for cooling. The usage of CO_2 allows for small tubing resulting in a reduced material budget of the readout module [62].

5

Simulation of MPGDs

A simulation of MPGDs requires first of all a detailed description of the electric field produced by MPGD. If the electric field is known, a Monte Carlo simulation of electrons drifting in the electric field can be used to study MPGDs under different conditions. The particle drift should include all effect introduced in previous chapter, ranging from the primary ionisation, the charge transport in electric and magnetic field and finally the amplification process in the MPGD itself.

In the following, a frame work allowing such a simulation of MPGDs above is introduced. It is split into two parts – the simulation of electric fields and the particle drift including the amplification process in the MPGD. The field simulation is done here using a finite element based software introduced in Section 5.1. In Section 5.3, the drift and amplification of charged particles in gases under the influence of electric and magnetic fields is introduced.

Within the following chapters the simulation frame introduced here will be used to do detailed simulations of the gas amplification in GEMs (Chapter 6) and to study field distortions (Chapter 7) and their impact on the ILD TPC performance.

5.1 Field simulations using finite elements

The simulation of electric fields is done here with the software CST™[1]. It makes use of finite elements and solves Maxwell's equations in their integral form using the *Finite Integration*

[1]CST AG, Bad Nauheimer Str. 19,64289 Darmstadt,Germany

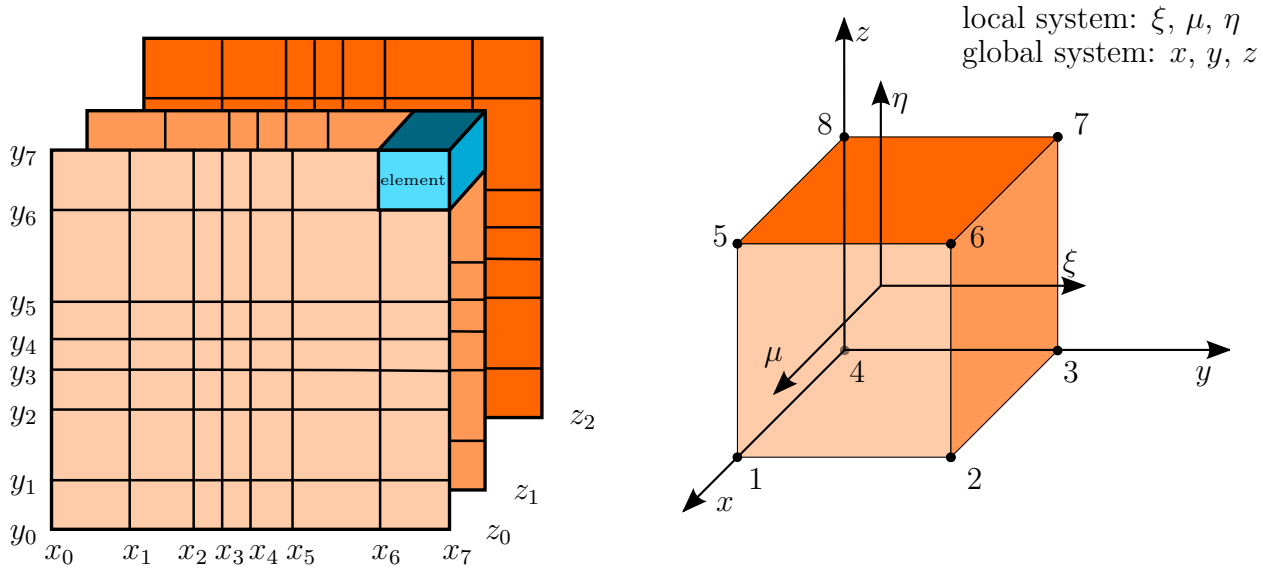

(a) Illustration of the mesh with brick like elements. **(b)** Coordinate systems used for brick like elements.

Figure 5.1: Sketches illustrating the mesh and the elements used in CST™.

Technique introduced in Ref. [63, 64].

In detail, here a regular mesh of bricks, representing the finite elements, is used. In this context regular means, that the mesh in the $x-y$ plane is the same for all z positions. Nevertheless the brick size in the mesh can be very different and is set in the meshing step of the calculation. It is set by an adaptive meshing algorithm, which chooses the mesh size in dependence on the field gradient. Hence, in areas, where the field gradient is high and thus the electric field changes most quickly, the mesh size will be small compared to areas, where the gradient is small and the field is rather constant. Figure 5.1a illustrates a mesh with different element sizes, where in addition one of the finite elements of the mesh is shown in blue. Following this illustration the mesh is characterised by the node positions x_i, y_i and z_i leading to N_x, N_y and N_z nodes along the coordinate axes. Hence, the total number of elements is given by:

$$N_{\text{elements}} = (N_x - 1)(N_y - 1)(N_z - 1) \tag{5.1}$$

During the field calculation the material of each element needs to be know in order to assign relevant material properties. If an element is not completely filled with only one material, CST™ uses an algorithm called *Perfect Boundary Approximation* (PBA) [65]. It mixes the two materials inside the element using sub-cellular information on the material properties

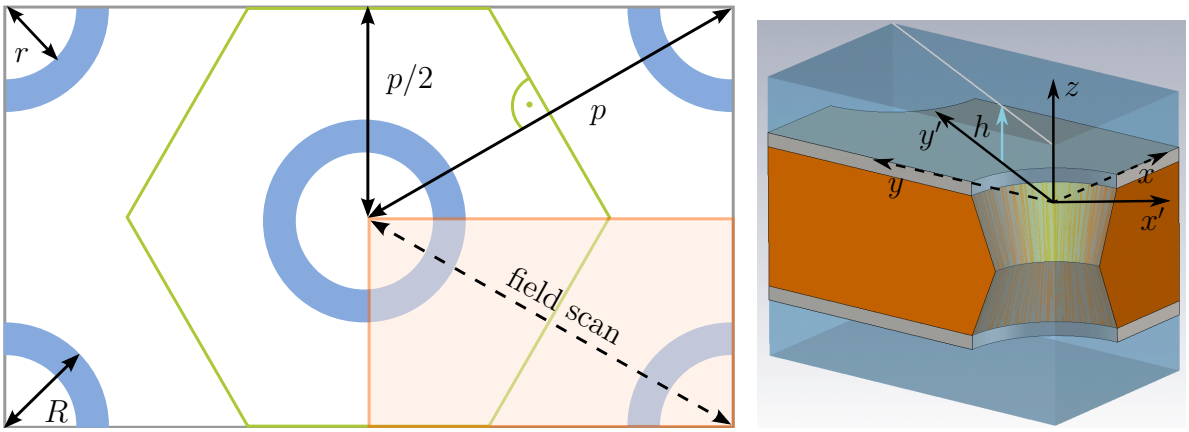

(a) GEM geometry with characterising parameters. The green hexagon and the orange box depict two possible definitions of an elementary cell, that can be used to reproduce the GEM geometry.

(b) GEM model build in CST™, where Kapton® is shown in orange and the grey surfaces are made of copper. The length h is the height of the volume on top of the GEM.

Figure 5.2: Illustrations of the GEM geometry. The orange area in (a) shows the elementary cell modelled in CST™ and shown in (b). The dashed line in (a) corresponds to the grey line in (b), which shows the direct connection between two holes. This line defines the y' direction shown in (b).

and assigns a compound material property. This allows to model arbitrary shaped object using a regular mesh as introduced above. In the simulations presented in this thesis the number of elements treated by the PBA algorithm is kept small by using a fine mesh size to avoid material mixing in elements.

The result of a CST™ simulation are the electric potential for each node. This information is afterwards used in the next step – the particle drift. Details about the data export from CST™ and the import to the subsequent program are given in Section 5.2. More details about the modelling of a MPGD are given in the following for the case of a GEM simulation.

5.1.1 CST™ GEM model and boundary conditions

The basic GEM geometry, as shown in Figure 3.7a, is sketched in Figure 5.2a. It is characterised by the hole pitch p and the inner and outer radius of the GEM holes r and R. Parameters of GEMs produced at the workshop at CERN, which in the following are referred to as standard CERN GEMs, are as follows: $p = 140\,\mu\text{m}$, $R = 35\,\mu\text{m}$, $r = 25\,\mu\text{m}$. By exploiting the periodic structure of a GEM the smallest segment needed to form the

GEM geometry by applying symmetries can be found. This elementary cell of a GEM is illustrated in Figure 5.2a as orange box. Its model in CST™ is shown in Figure 5.2. Here the orange part of the model is build out of Kapton® and the grey part is build out of copper. The Kapton® height is 50 µm and each copper layer has a height of 5 µm. The material property that is relevant for the electrostatic simulation is the relative permittivity, which in case of Kapton® is set to $\epsilon_{r,\text{Kapton}} = 3.5$. Each copper layer is treated as a perfect electric conductor in the simulation. The potential of the copper layers are fixed according to the desired GEM voltage.

The boundary conditions in the simulation are chosen such, that the field at each point of the boundary surface is parallel to it, except for the top and bottom boundary. Here a fixed potential is applied, which in combination with the potential on the copper surfaces of the GEM results in the desired fields at the top and bottom boundary. It should be noted that setting these boundary potentials is not straight forward. In principle the field between two surfaces is fixed by the applied voltage difference and the distance between the surfaces. But since the copper surface of the GEM has holes, the high field from inside the GEM holes penetrates into the surrounding drift volume and influences the field there. In consequence, the field resulting from a certain potential configuration is different from what one expects by calculating the ratio of the voltage difference and the surface distance. In practice the voltage at the boundaries is varied in an iterative process. After each iteration step a scan of the electric field component perpendicular to the drift direction (E_z) is performed. The field scan is done along y', which is the direction connecting two GEM holes as indicated by the dashed line in Figure 5.2a. Furthermore the length of the scanned path corresponds to the GEM hole pitch. The iterative process is stopped if the field in the field scan matches the desired field E_{set} at the boundary within $\pm 0.001\,\text{V/cm}$. This allows to combine individual single GEM simulations later on, since a uniform field at the boundaries guarantees a continuous electric field at the interface between the simulations.

Figure 5.3a shows the field component investigated in the iterative process in the case of $U_{\text{GEM}} = 250\,\text{V}$, $E_{\text{top}} = 250\,\text{V/cm}$ and $E_{\text{bottom}} = 1500\,\text{V/cm}$. It can be seen, that the high field present inside the GEM hole leaks into the space above and below the GEM. At the boundaries of this simulation, 400 µm above and 300 µm below the GEM, the field is homogeneous.

Furthermore, Figure 5.3b shows difference between the set field component in drift direction E_{set} and the field component E_z resulting from the simulation. Exactly this difference $|E_z - E_{\text{set}}|$ is used in the iterative process of the simulation. Figure 5.3b shows the result of

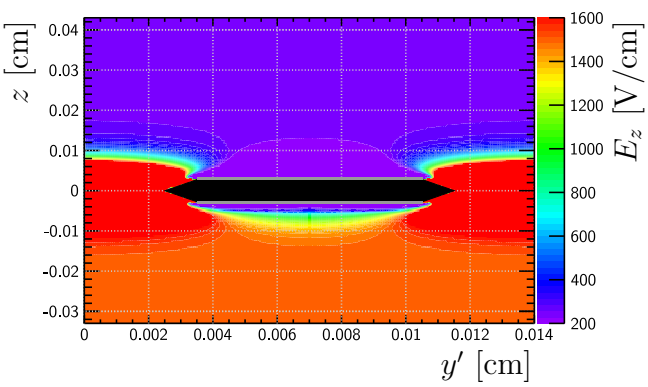

(a) Electric field component perpendicular to the GEM surface. The GEM is depicted in black (Kapton®) and grey (copper).

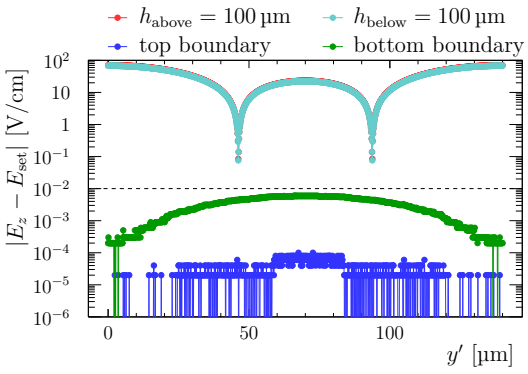

(b) Field scan along lines parallel to the GEM surface at different distances to the GEM. The dashed line depicts the maximum allowed deviation from the desired field E_{set}.

Figure 5.3: Results of a CST™ simulation of a GEM. The applied GEM voltage is $U_{\text{GEM}} = 250\,\text{V}$, the field above the GEM is $E = 250\,\text{V/cm}$ and the field below the GEM is $E = 1500\,\text{V/cm}$.

field scans at the boundary of the simulation as well as at a distance of $h = 100\,\mu\text{m}$ to the GEM in the region above and below the GEM. On the one hand it can be seen that at the boundaries the deviations from the desired field E_{set} are within $0.001\,\text{V/cm}$ as required in the iterative process. On the other hand, larger deviations from field uniformity are observed at a distance of $100\,\mu\text{m}$ above and below the GEM. In detail, at a distance of $100\,\mu\text{m}$ to the GEM surface the field above the hole sectors is higher compared to the field at the centre of the elementary cell. This could already seen in qualitatively in Figure 5.3a and shows again the penetration of the high GEM hole field into the surrounding volume of the GEM. This illustrates, that it is necessary to add additional space, modelled as vacuum, above and below the GEM in order to reach field homogeneity at the boundaries.

It was checked that the amount of additional space does not influence the simulation results. This was done by changing the size of the additional space on top and comparing the result of the field scan at a distance of $h = 100\,\mu\text{m}$ to the GEM surface. As long as the field uniformity required in the iterative process could be satisfied no difference in the resulting field in the scans is observed. If the size of the added space becomes too small the field condition in the iterative process can not be satisfied anymore. Hence, the minimum size of the additional space is determined. Furthermore, this test shows that the simulation results do not depend on the size of the added space above and below the GEM, which is what one would expect.

Finally, it was found that an additional space of $300\,\mu\text{m}$ above and below the GEM is

sufficient if $E_{\text{set}} > 1000\,\text{V/cm}$. If a GEM facing the TPC drift volume is simulated the field above the GEM is less than 1000 V/cm and the additional space needs to be increased to 400 µm in order to fulfil $|E_z - E_{\text{set}}| < 0.001\,\text{V/cm}$ at the top boundary.

5.2 A CST™ interface for Garfield++

In this section an interface between CST™, used for the electrostatic field simulation, and Garfield++, which is used for the particle drift in gases and which will be introduced in Section 5.3. As introduced above the result of a CST™ simulation are the potentials at all nodes of the mesh. In principle also the electric field is calculated, but the information of the node potential is sufficient for the data export, since the electric field can be reconstructed from the potential. In addition, the export of the potential (Φ_i) reduces the data to be exported by a factor of three compared to the export of the electric field ($E_{x,i}$, $E_{y,i}$, $E_{z,i}$).

What needs to be provided by the interface is a method to calculate the electric field at an arbitrary point $P(x, y, z)$ given the potentials at the mesh nodes calculated by CST™. Furthermore, the method should give the information about the material at this point, which is needed to decide if a drifting particle reached a boundary of the drift volume (for example the GEM surface). This method can be subdivided into three different tasks:

1. **Element search:** Find the element which contains the given point P.
2. **Material determination:** Determine the element material and decide if it should be considered for drift or not.
3. **Field shaping:** Calculate the field inside the element using the potentials at the element nodes.

These tasks are discussed in the following. More information about the concrete implementation can be found in Ref. [66].

5.2.1 Element search and material assignment

Since the mesh in CST™ is regular, the element search is straight forward and can be done for each component of the given point $P = (x, y, z)$ individually. For example, in case of

Table 5.1: Node coordinates in the local coordinate system.

node q	1	2	3	4	5	6	7	8
μ_q	1	1	-1	-1	1	1	-1	-1
ξ_q	-1	1	1	-1	-1	1	1	-1
η_q	-1	-1	-1	-1	1	1	1	1

the x component the searched element must fulfil: $x_i \leq x < x_{i+1}$, where x_i and x_{i+1} are element boundaries as shown in Figure 5.1a.

After the element, that contains P, has been found a material has to be assigned. In principle this can be done by investigating the relative permittivity of the element. If the PBA algorithm mixed materials inside the found element, the permittivity does not match exactly the values corresponding to the materials considered in the model. Therefore, a permittivity window is used to assign the material of elements. In detail, the element material is set to Kapton® if $3.4 < \epsilon_r < 3.6$, where ϵ_r is taken from one of the nodes. For copper ϵ_r is set to infinity, since it is treated as perfect electric conductor.

One consequence of the element based material assignment is that the shapes considered in the model are quantised by the elements of the mesh, meaning curved shapes are no longer curved. But this only affects the decision if an element is treated driftable or not in the drift simulation. The field calculation presented in the following is still based on the potentials of each element node, which are calculated by CST™ using the full information of the PBA algorithm handling curved shapes correctly.

5.2.2 Field shaping

The field shaping is done using local coordinates μ, ξ and η of the element, which are illustrated in Figure 5.1b. The local coordinate axes are chosen such that they are aligned with global coordinate axes. Furthermore the origin of the local coordinate system is in the centre of the element and points inside the element are characterised by $\mu, \xi, \eta \in [-1, 1]$. Table 5.1 shows the node coordinates of the element with respect to the local coordinate system. For example node number one has the coordinates (1,-1,-1), which can also be seen in Figure 5.1b.

The first step is to transform the coordinates of the point $P(x, y, z)$ into local coordinates $P(\mu, \xi, \eta)$. Following the isoparametric notation introduced in Ref. [67] the element geometry

is described by

$$\begin{pmatrix} 1 \\ x \\ y \\ z \end{pmatrix} = \begin{pmatrix} 1 & 1 & \cdots & 1 \\ N_{x,1} & N_{x,2} & \cdots & N_{x,8} \\ N_{y,1} & N_{y,2} & \cdots & N_{y,8} \\ N_{z,1} & N_{z,2} & \cdots & N_{z,8} \end{pmatrix} \begin{pmatrix} S_1 \\ S_2 \\ \vdots \\ S_8 \end{pmatrix}, \tag{5.2}$$

where $N_{x,q}$, $N_{y,q}$ and $N_{z,q}$ are the coordinates of node i in the global coordinate system and μ_q, ξ_q and η_q are the node coordinates in the local coordinate system as given in Table 5.1. Furthermore, S_q are so called *Shaping Functions* used to describe each point in the element using the node coordinates. These function are given in the following [68]:

$$S_q = \frac{1}{8}(1 + \mu_q\mu)(1 + \xi_q\xi)(1 + \eta_q\eta) \tag{5.3}$$

In principle now the system of equations given in Equation 5.2 can be used to calculate the coordinates μ, ξ, η for the given point $P(x, y, z)$. This is necessary for arbitrary shaped hexahedral elements and will be done in the case of two dimensions in Chapter 7.

At this point the regular mesh consisting of simple bricks can be exploited and the coordinates of P in the local coordinate system can be calculated as follows:

$$\mu = x_i + \frac{x - x_i}{|x_i - x_{i+1}|} \tag{5.4}$$

$$\xi = y_i + \frac{y - y_i}{|y_i - y_{i+1}|} \tag{5.5}$$

$$\eta = z_i + \frac{z - z_i}{|z_i - z_{i+1}|}, \tag{5.6}$$

which makes makes the coordinate calculation much more easy.

The shaping functions also be used to interpolate the electric potential inside the element as follows:

$$\Phi(\mu, \xi, \eta) = \sum_{q=1}^{8} \Phi_q S_q \tag{5.7}$$

This results in a linear interpolation of the electric potential inside the element, using the information about the known potentials Φ_q at the node positions. Finally, the potential at the point P can be used to calculate the electric field:

$$\vec{E}(x, y, z) = -\vec{\nabla}_{x,y,z}\Phi(x, y, z) \tag{5.8}$$

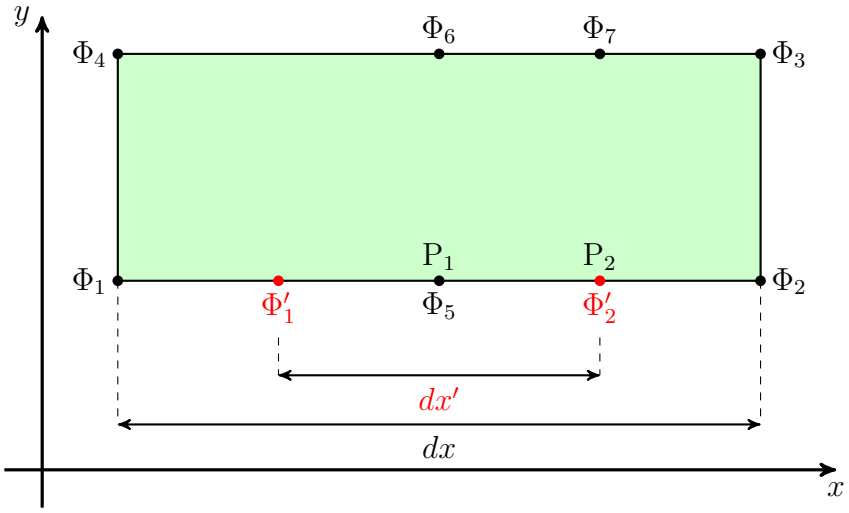

Figure 5.4: Sketch showing a two dimensional element with edges aligned to the coordinate axes.

But since Φ is given in local coordinates and the electric field is ask for in global coordinates, a coordinate transformation has to be performed. This can be done using the *Jacobian* $\boldsymbol{J}$ of the transformation:

$$\boldsymbol{J} = \begin{pmatrix} \frac{\partial x}{\partial \xi} & \frac{\partial y}{\partial \xi} & \frac{\partial z}{\partial \xi} \\ \frac{\partial x}{\partial \mu} & \frac{\partial y}{\partial \mu} & \frac{\partial z}{\partial \mu} \\ \frac{\partial x}{\partial \eta} & \frac{\partial y}{\partial \eta} & \frac{\partial z}{\partial \eta} \end{pmatrix}, \tag{5.9}$$

where x, y and z are substituted following Equation 5.2. The inverse of this matrix $\boldsymbol{J}^{-1}$ can now be used to calculate the electric field as follows:

$$\overrightarrow{E}(x,y,z) = -\boldsymbol{J}^{-1}\overrightarrow{\nabla}_{\xi,\mu,\eta}\Phi(\xi,\mu,\eta) \tag{5.10}$$

$$= -\sum_{q=1}^{8} \Phi_q^{\text{node}} \boldsymbol{J}^{-1} \begin{pmatrix} \frac{\partial N_q}{\partial \xi} \\ \frac{\partial N_q}{\partial \mu} \\ \frac{\partial N_q}{\partial \eta} \end{pmatrix}. \tag{5.11}$$

Remark about the consequences of the field shaping

By construction the electric field component E_x along the x direction inside an element will be constant, while E_y and E_z are not necessarily constant along this direction. This can be illustrated using Fig. 5.4, where one face of an element with node potentials Φ_1, Φ_2, Φ_3 and Φ_4 is shown in green. As a consequence of the linear interpolation using the shaping

function, the potential can be calculated everywhere inside the element using Equation 5.7. By construction the electric field is always calculated as the potential difference between the surface potentials. For example in the field calculation at the position P_1 as well as at P_2 the potentials Φ_1 and Φ_2 are considered when calculating the field component E_x:

$$E_x(P_1) = E_x(P_2) = \frac{\Phi_2 - \Phi_1}{dx}.$$

In order to calculate the y component of the electric field different potentials are considered, which result from the linear interpolation of the potentials realised by the shaping functions. The y components for P_1 and P_2 are given by:

$$\begin{aligned} E_y(P_1) &= \frac{\Phi_6 - \Phi_5}{dy} \\ E_y(P_2) &= \frac{\Phi_7 - \Phi_2'}{dy} \neq E_y(P_1) \end{aligned}$$

This shows that in case of the y component of the electric field is different for P_1 and P_2. Now one could ask why not use the potential information resulting from the shaping to calculate $E_x(P_1)$ with a reduced element size of dx' instead of dx. The answer is, that one does not gain any information and the result will be still the same, as long as a linear interpolation of the potential is used:

$$E_x'(P_1) = \frac{\Phi_2' - \Phi_1'}{dx'} = \frac{\frac{3}{4}(\Phi_2 - \Phi_1) - \frac{1}{4}(\Phi_2 - \Phi_1)}{dx/2} = E_x(P_1)$$

In other words, the shaping guarantees the most accurate field calculation possible. It can only be improved by putting in assumptions about the field shape inside the elements or by reducing the element size in the field simulation.

5.3 Simulation of particles in gases using Garfield++ and Magboltz

A detailed description of processes of the fundamental processes in a TPC, including the description of the primary ionisation process, the particle drift, the gas amplification process and the electronics simulation, is provided by the software package Garfield++ [69, 70]. It is developed at CERN and makes used of other sub-packages dealing with sub-processes. In this thesis only the particle drift in gases under the influence of electric and magnetic fields and the gas amplification process are relevant. The implementation of these processes in Garfield++ is introduced in the following.

5.3.1 Microscopic and macroscopic gas parameters

First of all the Penning effect introduced in Chapter 4 is included in Garfield++ via a macroscopic gas parameter, called Penning rate r_p. It describes the general probability to produce additional electrons in an avalanche. Measurements for selected gas mixtures exist and are presented in Ref. [33]. Unfortunately the penning effect for T2K gas was not yet measured. Therefore, in this thesis it is estimated from measurements presented in Section 6.3.4.

All other gas parameters that are involved in a Garfield++ simulation are handled by Magboltz [71]. This sub-package is responsible of calculating macroscopic gas parameters such as the drift velocity, diffusion coefficients, Townsend coefficient and attachment of electrons and ions in gases with applied electric and magnetic fields at arbitrary angles. Main input parameters to a Magboltz calculation of these macroscopic gas parameters are the gas composition, the electric and magnetic field strength and the angle between the fields. Furthermore the precision of the calculation is steered by the number of considered collisions, since internally a Monte Carlo simulation is used to determine macroscopic gas parameters. In all Magboltz calculations presented here the number of collisions is set to $20 \cdot 10^7$ leading to relative uncertainties below 5 % for all calculated quantities.

The internal Magboltz simulation is based on microscopic gas parameters. Therefore, Magboltz includes a data base of microscopic gas parameters, such as the energy dependent collision cross sections as introduced in Section 3.3. For T2K gas the following data base revisions are used in Magboltz: ARGON ANIS 2011, CF4 ANISO 2008, ISOBUTANE 2009A. Microscopic gas parameters like the collision cross sections can also be directly accessed, which allows to implement a microscopic description of particles in gases based on the Magboltz database. Therefore, Magboltz allows for two different approaches to describe particles in gases, which are based either on macroscopic or on microscopic gas parameters. Both possibilities are considered in this thesis. They are introduced in the following.

5.3.2 The microscopic and macroscopic concept in Garfield++

As introduced in Section 3.3.1 and mentioned above, the drift of particles can be described with macroscopic parameters or with the microscopic approach. These two different approaches of treating the particle drift and amplification are also implemented in Garfield++:

1. Monte Carlo Integration approach based on macroscopic gas parameters.
2. Microscopic approach based on scatterings.

The first approach is based on solving Equation 3.6 in steps of distances Δs or in time steps $\Delta t = \Delta s / v_{\text{drift}}$. In addition, a diffusion step is added by sampling a Gaussian distribution with a variance of $\sigma_l = D_l \sqrt{\Delta s}$ in drift direction and two uncorrelated Gaussian distributions with a variance of $\sigma_t = D_t \sqrt{\Delta s}$ in the direction transverse to the drift direction. Finally, both steps are added and the particle location is updated. The macroscopic gas parameters needed for the macroscopic particle drift can be calculated beforehand using Magboltz in the case of electrons. For ions the cannot be calculated with Magboltz but need to be taken from literature. In this thesis it is assumed that argon ions drift in argon, which is reasonable since 95 % of the drift gas T2K is argon. The corresponding gas parameters can be found in Ref. [72].

An advantage of this approach is, that certain effects can be easily enabled or disabled by changing the macroscopic gas parameters. For example the transverse and longitudinal can be disabled by setting the corresponding parameters D_l and D_t calculated by Magboltz to zero. This allows to visualise the electric field as shown in Figure 5.5a, where the field lines of a GEM with $U_{\text{GEM}} = 320\,\text{V}$ and fields of $E_{\text{top}} = 200\,\text{V/cm}$ and $E_{\text{bottom}} = 2500\,\text{V/cm}$ are shown. This figure illustrates clearly the high field inside the GEM hole. Furthermore, areas where field lines entering the GEM from below and end on the GEM surface are visible. If for example ions coming from below the GEM follow these field lines they will most probably be collected on the GEM surface. This hits at the intrinsic capability of GEMs to reduce the number of ions reaching the sensitive volume of the TPC. Such a field line based ansatz to characterise and model a GEM will be discussed in detail in the following chapter.

The second approach up to now is only implemented for electrons. Here electrons are tracked trough single collisions with atoms or molecules. Between collisions the electron follows a vacuum trajectory. The path length of this trajectory is drawn from an exponential function around the mean free path length, which depends on the electron energy. The subsequent collision is chosen with respect to the electron energy and the corresponding collision cross sections. Collisions are classified as one of the following types:

Elastic scattering: The electron energy after the collision is same as before.

Inelastic scattering: The electron excites the gas atom/molecule and loses energy.

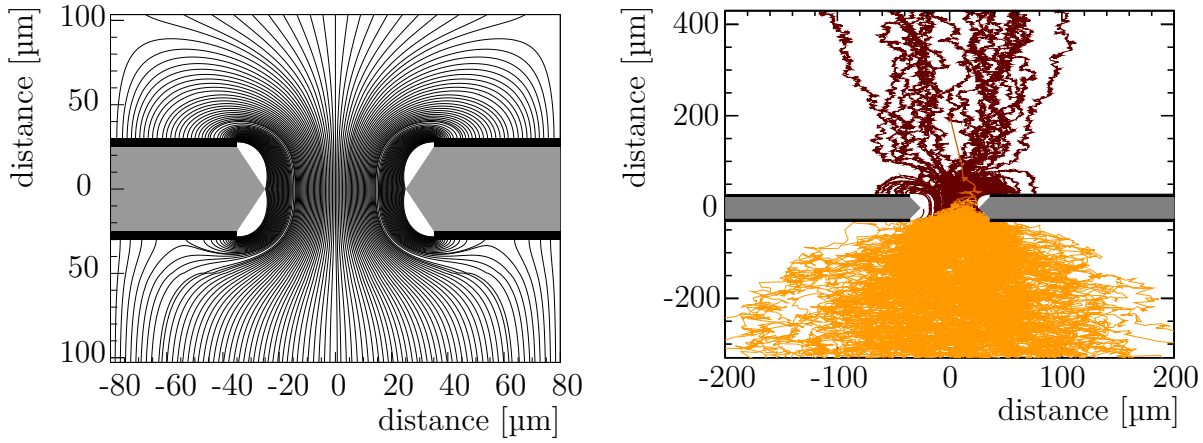

(a) Field lines of the electric field (black lines) in the vicinity of a GEM hole. The GEM Kapton® is shown as grey block and the copper layers as black blocks. The field settings and GEM voltage are given in the text.

(b) Example of the gas amplification simulated with Garfield++. One electron enters the GEM from above (orange line) and is amplified. Ions produced in this process are shown as brown lines.

Figure 5.5: Garfield++ simulation of a single GEM showing the field lines (a) and the amplification process (b). The field and voltage settings are equal for (a) and (b): $U_{\mathrm{GEM}} = 320\,\mathrm{V}$, $E_{\mathrm{top}} = 200\,\mathrm{V/cm}$, $E_{\mathrm{bottom}} = 2500\,\mathrm{V/cm}$.

Super-elastic scattering: The electron gains energy in the interaction with the gas atom/molecule.

Attachment: The electron is lost through attachment.

Ionisation: The electron produces an electron-ion pair.

Their individual cross sections are directly retrieved from the Magboltz database. In comparison to the Monte Carlo Integration, the microscopic approach leads to an accurate description of the electron drift even if the characteristic dimensions in the simulation are comparable to the electron free path.

One example, where both approaches introduced above are considered is shown in Figure 5.5b, where the same field as shown in Figure 5.5a is used. In this figure electron paths are shown as orange lines, ion paths are shown by brown lines and the GEM is depicted in in black (copper) and grey (Kapton®). This figure shows the amplification of one electron entering the GEM from top. In case of electrons the microscopic approach is used, whereas for ions produced in the avalanche process the Monte Carlo Integration is used. It can clearly be seen, that indeed a lot of ions produced in the amplification process are stopped on the GEM surface. Furthermore, individual elastic collisions with gas atoms/molecules

can be identified by kinks in the electrons paths. The analysis strategy of such a simulation is discussed in the following section.

Effects that are currently not included by one of the approaches introduced above are second order processes. Such an effect is for example the production of electrons by photons, produced in the avalanche process, that hit the GEM copper surface (photoelectric effect). Furthermore, the effect of charging up the Kapton® of the GEM will be not covered by the simulations presented in this work. The charging up is caused by electron and ions collected on the Kapton® in the GEM operation. Depending on the operation conditions at some point an equilibrium will be achieved, which means the charge collected on the Kapton® surface changes the electric field such that no further charge is collected. A study of this charge up effect is presented in Ref. [73], where it was found that this is effect does not play an important role for common operation conditions of GEMs as considered in this thesis.

5.4 Summary and analysis strategy

In this chapter a complete simulation frame work was introduced, which allows to study all processes connected to the particle detection with a TPC. By exploiting the simple mesh geometry of CST™ an efficient and fast interface was added to Garfield++. This was shown in Ref. [66], where a comparison between the interface developed here and an alternative interface to a different finite element based software is presented. The CST™ calculation was ten times faster at the same level of accuracy in the calculation.

In addition, it was shown in this chapter how to control the fields at the boundaries of CST™ simulations. This allows to add different blocks of constant fields and CST™ simulations inside Garfield++ and thus realise the efficient simulation of a GEM stack. By the combination of CST™ simulation blocks and blocks of constant fields, one avoids to simulate large volumes in CST™, with limits the number of mesh cells. In consequence the computing time in CST™ as well as in Garfield++ is reduced.

In this thesis the introduced simulation frame work is used to study the behaviour of a GEM stack as done in the following chapter, as well as to investigate the performance of different TPC readout modules as done in Chapter 7. Furthermore, the algorithm used to interpolate the potentials in brick like elements introduced here will also be used in Section 7.3 to interpolate measured field distortions.

The analysis strategy for a GARFIELD++ simulation is similar for all studies presented in the following. It is based on analysing the start- and endpoints of electrons and ions. In case of Figure 5.5b this means to count how much electrons and ions were produced by the single initial electron started above the GEM, stopped on the GEM copper surface or the GEM Kapton® and how much electrons/ions were stopped at the simulation boundary. In the case of electrons the latter case means that they reached the anode pad plane and are registered there. In the case of ions this means, that they are not collected on a certain GEM and penetrate into the sensitive volume of the TPC.

6

Characterisation of the GEM based gas amplification

As shown in the beginning (Section 2.4.4) the operation of the ILD TPC requires a blocking of ions, that are produced in the anode amplification stage and penetrate back into the sensitive volume of the TPC. As it was discussed, the option of using wire gates is not favoured, since additional material needs to be introduced to support and stretch the wires. This in the end increases the material budget of the readout modules and introduces additional dead space, which in consequence deteriorates the TPC performance.

Therefore, the idea is to modify the readout modules using other techniques. In case of GEM based modules different parameters in the GEM stack can be adapted to achieve a reduction in the ion feedback ratio (number of ions penetrating into the sensitive volume of the TPC per electron entering the amplification stage). Studies on this topic, which are presented in Ref. [74], show that the ion feedback ratio can be reduced from about 150 to about 24 by choosing proper settings of the GEM voltages and fields in the GEM stack.

Furthermore, a GEM itself can act as ion gate. This is the case if the amplification of the GEM is one (no ions are produced), the GEM is opaque for ions and transparent for electrons. If this is possible will be studied in the following. The considered strategy of this study is the following. First of all a stack of three standard GEMs is used to measure single GEM characteristics as well as characteristics of the whole stack. The measurements are done using standard settings as well as settings optimised to reduce the ion feedback ratio.

This will allow to test the reduction of the ions feedback ratio by choosing proper settings. An electrostatic model, introduced in Section 6.1, will be used to parametrise the measured single GEM characteristics. The results of the measurements and the parameterisation are presented in Section 6.3. The obtained parameterisation will serve as input to the simulation presented in Chapter 7. The second option to implement a GEM base ion gate, is to change the GEM geometry in order to influence the transparency of the GEM. An increased hole size should increase the electron transparency, which is needed to realise a GEM gate. This will be studied in Section 6.4, where the setup is modified by replacing the topmost GEM in the GEM stack with a GEM with an increased hole size.

In addition, a detailed simulation of the setup using the frame work introduced in the previous chapter will be used to characterise single GEMs and the GEM stack. A comparison of the prediction from the simulation with the measurements (Section 6.5) will show, that the simulation can reproduce the measurements only partially.

6.1 Measurement principle

The idea of the measurements presented here, is to fully characterise a GEM with three parameters – collection efficiency, gain and extraction efficiency. The collection efficiency and the extraction efficiency are referred to as transfer coefficients of a GEM, which can be calculated for ions and electrons. These transfer coefficients and the gain – the GEM parameters – are sketched in Figure 6.1. In this figure one GEM hole is shown and arrows

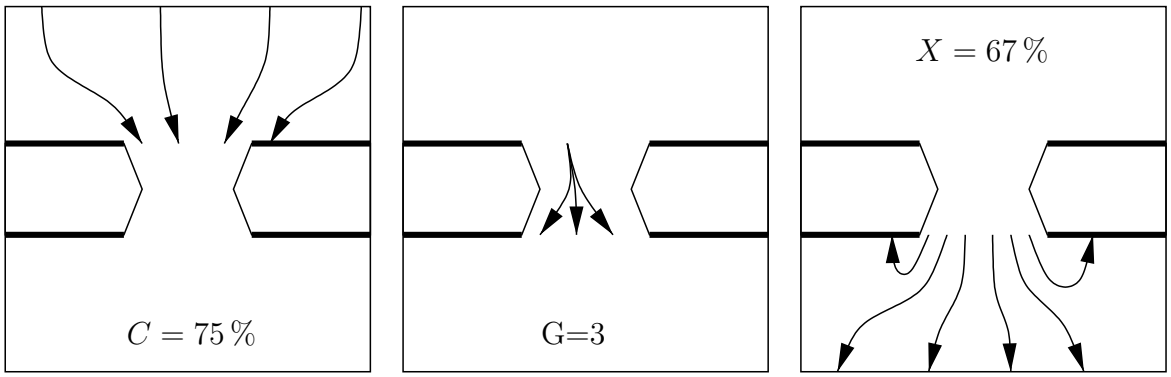

(a) Collection efficiency. **(b)** Signal gain. **(c)** Extraction efficiency.

Figure 6.1: Sketch of parameters characterising a GEM [20]. Shown is one GEM and particles (depicted by the arrows) entering and leaving it. The definition of C and X can be applied to electrons and ions, whereas an amplification G is only possible with electrons.

depict particles. In Figure 6.1a the collection efficiency is sketched, where three out of four particles enter the GEM hole leading to a collection efficiency of $C = 75\,\%$. One particle is not collected into the GEM hole, but ends on the copper surface of the GEM. Figure 6.1b illustrates the gain, where out of one particle three particles are produced. Finally, the extraction efficiency is shown in Figure 6.1c, where four out of six particles are extracted from the GEM hole.

As implied by these figures the particles ending on certain electrodes need to be counted in order to characterise a single GEM. This is the idea of the measurements presented in this chapter. The counting will be done in practice by measuring the current on the GEM electrodes. Since the current to be measured on the GEM electrode in case of a single GEM setup is very low ($< 1\,\mathrm{nA}$), a stack of GEMs in combination with a strong particle source is used in the measurements presented in the following. This increases the number of charged particles in the system and allows to evaluate currents produced by those particles.

Still, the currents on all GEM electrodes as well as on the anode and cathode electrode need to be measured very precisely at the nano ampere level for currents that are in the order of $\mathcal{O}(10\,\mathrm{nA})$. In the following the transfer coefficients and the gain are defined. Following this, an electrostatic model used to describe the transfer coefficients is introduced. The relation between the GEM parameters and the currents is given in Section 6.2.

6.1.1 Definitions for the GEM characterisation

Single GEM definitions

The definitions will follow the sketches in Figure 6.1 starting with the efficiency $C^{\pm}$ to collect signal electrons or ions into a GEM:

$$C^{\pm} = \frac{N_{e^-/I^+} \text{ collected into the GEM hole}}{N_{e^-/I^+} \text{ in front of the GEM}} \tag{6.1}$$

where the superscript plus and minus indicates electrons and ions. If electrons are collected into the GEM hole their amplification is given by the gain G:

$$G = \frac{N_{e^-} \text{ in the GEM hole}}{N_{e^-} \text{ collected into the GEM hole}} \tag{6.2}$$

Finally, the efficiency to extract electrons or ions $X^{\pm}$ from the GEM hole is given by:

$$X^{\pm} = \frac{N_{e^-/I^+} \text{ extracted from the GEM}}{N_{e^-/I^+} \text{ in the GEM hole}} \tag{6.3}$$

GEM stack definitions

Using the definitions above it is possible to calculate the effective gain of a setup where multiple GEMs are used in a stack:

$$G_{\text{eff.}} = \prod_{i=1}^{N_{\text{GEMs}}} C_i^- G_i X_i^-. \tag{6.4}$$

If the field between two GEMs or between a GEM and the anode is high enough to allow gas amplification this equation needs to be modified to take this effect into account. This addition signal gain, referred to as parallel plate gain, is defined as:

$$G_{\text{par.},i} = \frac{N_{e^-} \text{ in front of GEM}_{i+1} \text{ or the anode}}{N_{e^-}\text{extracted from GEM}_i}. \tag{6.5}$$

Furthermore, the attachment A_i in the stack needs to be taken into account. The modified effective gain finally is given as:

$$G_{\text{eff.}} = \prod_{i=1}^{N_{\text{GEMs}}} C_i^- G_i X_i^- G_{\text{par.},i} A_i = \frac{N_{e^-} \text{ on the anode}}{N_{e^-} \text{ primary ionisation}}, \tag{6.6}$$

where A_i is the attachment in the field below GEM i.

For ions the ion feedback ratio (IFR) characterising the GEM stack can is defined as:

$$\text{IFR} = \frac{N_{I^+} \text{ leaving the GEM stack}}{N_{e^-} \text{ entering the GEM stack}}, \tag{6.7}$$

where electrons enter the GEM stack of the anode amplification stage from the sensitive volume of the TPC and ions produced in the GEM stack leave the stack penetrating into the sensitive volume of the TPC. This definition is sufficient to evaluate field distortions in the TPC, but it can be directly measured with the setup presented in this chapter. What can be directly measured is ratio between the ion feedback ratio and the effective gain of

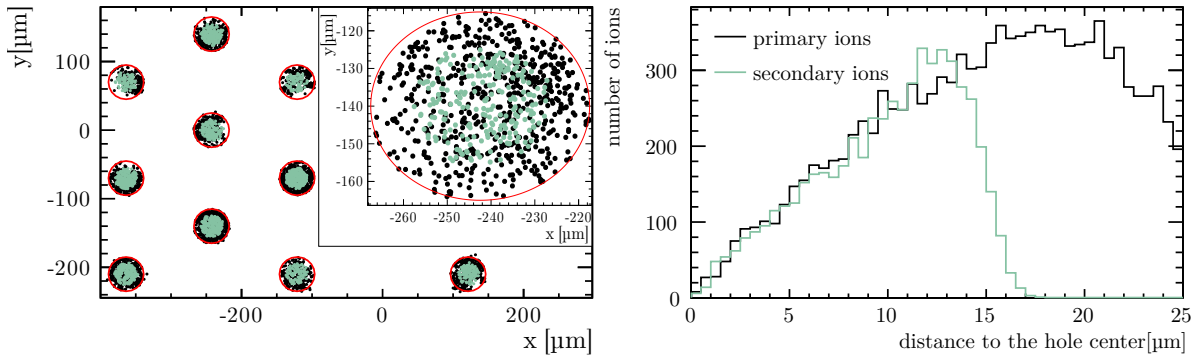

(a) Positions of primary (black) and secondary (green) ions measured in the centre of a GEM foil. The detail view shows the blow-up of one single hole.

(b) Distance of primary and secondary ions to the centre of a GEM hole measured in the centre of a GEM foil.

Figure 6.2: Positions of ions, produced in the bottom GEM, resulting from a triple GEM stack simulation with T2K gas. Black points represent the positions measured halfway through holes of the bottom GEM and the green points represent the positions measured halfway trough holes of the middle GEM of the stack.

the setup:

$$\frac{\mathrm{IFR}}{G_{\mathrm{eff.}}} = \frac{N_{I^+} \text{ leaving the GEM stack}}{N_{e^-} \text{ collected on the anode}}. \tag{6.8}$$

Definition of primary and secondary ions

According to Ref. [75] the extraction of ions depends on where the ions have been produced. This can also be observed in a detailed simulation of a GEM stack as introduced in Chapter 5, which will be shown in the following. If the ions are produced inside the holes of the GEM to be characterised, they should be distributed all over the GEM hole since the avalanche spreads over the whole hole area. This can be seen in Figure 6.2, where the position of ions produced in the bottom GEM of a triple GEM stack simulation are shown. The black points represent the position of the ions in the centre of the bottom GEM. Since the ions are produced in this GEM they are referred to as primary ions with regard to the bottom GEM. One should keep in mind that the definition of primary ions introduced here has nothing to do with ions produced in the primary ionisation. Figure 6.2b shows that the primary ions are spread over the whole hole area as expected. The extraction efficiency for primary ions is referred to as primary extraction efficiency $X^+_{\mathrm{prim.}}$. Taking into account that the field lines at the outer part of the GEM hole end on the GEM surface (see Figure 5.5), it is clear that mostly ions from this region will not be extracted from the bottom GEM.

The remaining ions that are produced in the bottom GEM reach the middle GEM. Their position in the centre of the middle GEM is shown in green in Figure 6.2. With regard to the middle GEM these ions are referred to as secondary ions, since they are not produced in the middle GEM. It can be seen from Figure 6.2b, that these secondary ions are no longer spread over the whole hole area. They are concentrated in the central area of the GEM hole, which means the probability of being extracted from the middle GEM is higher. Therefore, their extraction efficiency, called secondary extraction efficiency $X^{+}_{\text{sec.}}$, in the middle GEM will be different from the extraction efficiency of ions produced in the middle GEM.

6.1.2 Electrostatic model

In the previous section GEM parameters were defined based on the final particle positions after the drift. If diffusion is neglected and no magnetic field is present, a charged particle follows the field lines of the electric field. This allows to analyse the field lines in order to estimate final particle positions. The electrostatic model introduced in the following is based on this idea of analysing the transfer coefficients based on electrostatic field calculations. For the field calculation finite element methods similar to these presented in Chapter 5 can be used and were first presented in Ref. [76].

In practice the electric field is analysed by investigating the electric flux through an area A defined as:

$$\Phi_{\text{ext.}} = E_{\text{ext.}} A. \tag{6.9}$$

Figure 6.3 shows the field lines of a GEM simulation in light grey. They can be used to define different fluxes based on the field line characteristic. All field lines starting on top of this figure are either related to the flux Φ_5 or Φ_3. In the shown field configuration, where the field below the GEM (E_{bottom}) is higher than above the GEM (E_{top}), all field lines that end on the GEM surface are connected to Φ_5 and all field lines that reach the bottom of this figure are connected to Φ_3. In other words electrons that start in the region of Φ_5 on top of this figure would not reach the other side of the GEM, but end on the top copper surface of the GEM. Furthermore, there are field lines that start from the bottom and end on the top GEM surface attributing to Φ_2. This is again related to the fact, that in the chosen configuration $E_{\text{top}} < E_{\text{bottom}}$. Finally, there is a region close to the border of the GEM hole, which can not reached from electrons/field lines starting above or below the GEM. The corresponding flux is Φ_4.

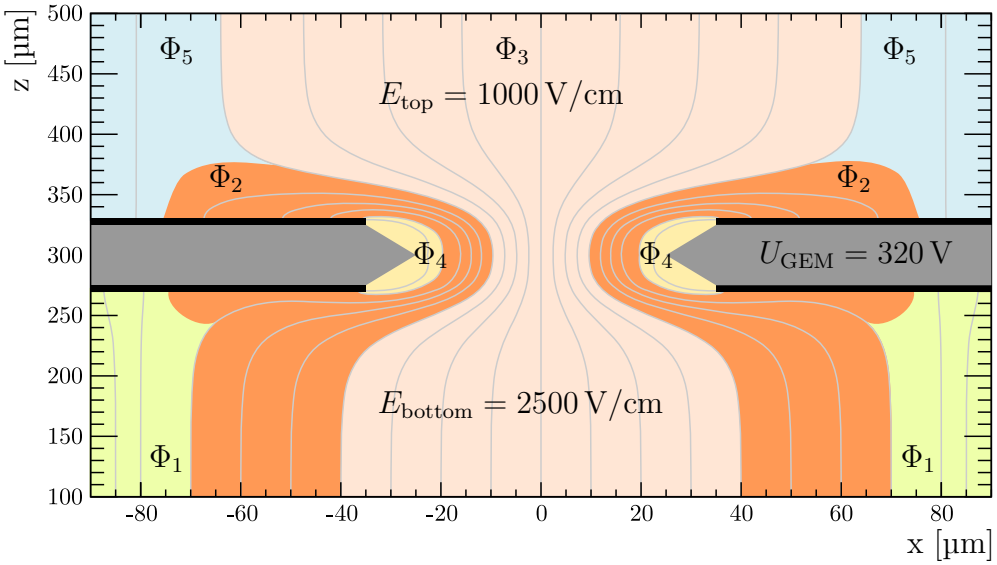

Figure 6.3: Illustration of electric fluxes in the vicinity of a GEM (grey/black). Light grey lines are field lines resulting from a CST™ simulation, where the diffusion is turned off.

By analysing the fluxes shown in Figure 6.3, which resulting from an electrostatic field simulation, the transfer coefficients can be calculated as follows:

$$C_{\text{top}} = \frac{\Phi_3}{\Phi_3 + \Phi_5} \tag{6.10}$$

$$C_{\text{bottom}} = \frac{\Phi_2 + \Phi_3}{\Phi_1 + \Phi_2 + \Phi_3} \tag{6.11}$$

$$X_{\text{top}} = \frac{\Phi_3}{\Phi_{\text{hole}}} \tag{6.12}$$

$$X_{\text{bottom}} = \frac{\Phi_2 + \Phi_3}{\Phi_{\text{hole}}}, \tag{6.13}$$

where $\Phi_{\text{hole}} = \Phi_2 + \Phi_3 + \Phi_4$ is the electric flux through the GEM hole.

Using the definition of the electric flux, the ratio of the extraction and collection efficiency can be written as follows:

$$\frac{X}{C} = \frac{E_{\text{ext.}} A}{E_{\text{hole}} A_{\text{hole}}} = \frac{1}{\tau_{\text{opt.}}} \frac{E_{\text{ext.}}}{E_{\text{hole}}}, \tag{6.14}$$

where $E_{ext.}$ is the external field E_{top} or E_{bottom}, depending on the GEM side where the ratio is calculated. Furthermore, A_{hole} is the area of a GEM hole and A is the area above the GEM. In case of GEMs with double conical holes the ratio A_{hole}/A can be identified with the optical transparency $\tau_{\text{opt.}}$, as done in Equation 6.14. The optical transparency of

a GEM can be calculated as follows:

$$\tau_{\text{opt.}} = \frac{A_{\text{GEM hole}}}{A_{\text{hexagon}}} = \frac{2\pi r^2}{\sqrt{3}p^2} = 11\,\%, \tag{6.15}$$

where the area of the hexagon corresponds to the hexagonal unit cell shown in Figure 5.2a. The calculated transparency of $\tau_{\text{opt.}} = 11\,\%$ correspond to a standard CERN GEM geometry ($p = 140\,\mu\text{m}$, $r = 25\,\mu\text{m}$). By investigating the electric fluxes for different field configurations and GEM voltages the transfer coefficients can be studied and parametrised. This was done in Ref. [76] and the following relations were found:

$$E_{\text{hole}} = aU_{\text{GEM}} + b\,(E_{\text{top}} + E_{\text{bottom}}) \tag{6.16}$$

$$C = \begin{cases} 1 & \text{for } (E_{\text{ext.}}/E_{\text{hole}}) \leq r^{1/s} \\ r\left(\frac{E_{\text{ext.}}}{E_{\text{hole}}}\right)^{-s} & \text{for } (E_{\text{ext.}}/E_{\text{hole}}) > r^{1/s}. \end{cases} \tag{6.17}$$

Here the parameters a, b and s, r are empirical parameters, which depend on the concrete GEM geometry. Parameter sets for various GEM geometries are given in Ref. [76]. Using Equation 6.14 and Equation 6.17 the parameters $C^{\pm}$, X^{-} and $X^{+}_{\text{prim.}}$ are defined and parametrised. In case of $X^{+}_{\text{sec.}}$ the following parameterisation can be retrieved in a similar way (see Ref. [74]):

$$X^{+}_{\text{sec.}} = \begin{cases} \frac{X_{\text{top}}}{X_{\text{bottom}}} & \text{for } X_{\text{top}} < X_{\text{bottom}} \\ 1 & \text{for } X_{\text{top}} > X_{\text{bottom}}, \end{cases} \tag{6.18}$$

where the $X^{+}_{\text{sec.}}$ is given with respect to the top side of the GEM.

6.1.3 Calculation of model parameters

As shown in the previous section the introduced electrostatic model can be used to parametrise GEM parameters. This is done in dependence on the field E_{hole}, which requires the determination of the parameters a and b. These parameters are given for different GEM geometries in Ref. [76]. In the measurements presented in this chapter, GEMs with an increased hole diameter of $\varnothing = 100\,\mu\text{m}$ are used, besides standard CERN GEMs with a diameter of $\varnothing = 70\,\mu\text{m}$. The model parameter for the former GEMs have not yet been calculated in Ref. [76] and therefore it is done here.

In order to do so GEM simulations done with CST™ as introduced in Chapter 5 are

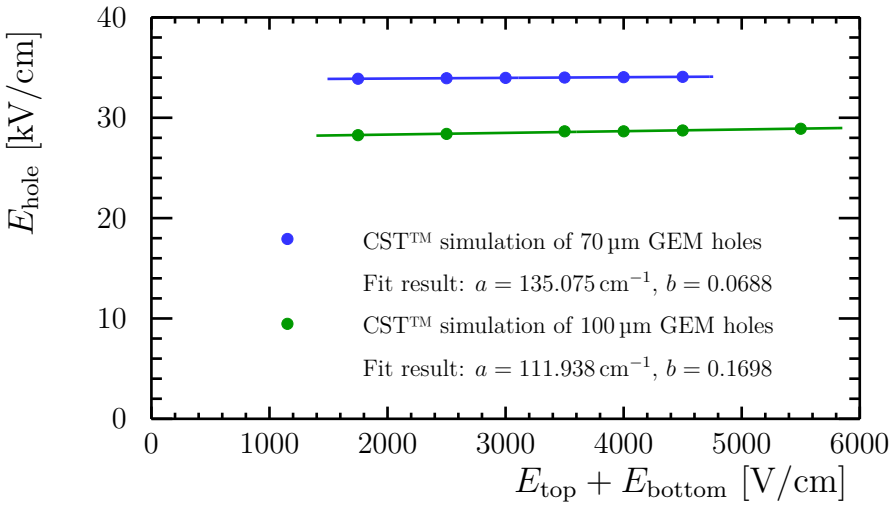

Figure 6.4: GEM hole field as a function of the outer fields for two different GEM geometries. The GEM voltage is fixed for both geometries: $U_{\text{GEM}} = 250\,\text{V}$.

analysed. In detail the average hole field defined as:

$$E_{\text{hole}} = \frac{\int_{A_{\text{hole}}} E \; \mathrm{d}A'}{\int_{A_{\text{hole}}} \mathrm{d}A'} \tag{6.19}$$

is calculated in the GEM centre. Here A_{hole} is again the hole area in the middle of the GEM. The resulting hole field for the two discussed GEM geometries in dependence on the sum of the electric field on top and on bottom of the GEM is shown in Figure 6.4. Using the parameterisation given in Equation 6.16 the simulation data are fitted, which results in the following parameter values:

- Hole size of $\varnothing = 70\,\mu\text{m}$: $a = 135.075\,\text{cm}^{-1}$, $b = 0.0688$
- Hole size of $\varnothing = 100\,\mu\text{m}$: $a = 111.938\,\text{cm}^{-1}$, $b = 0.1698$

Here the result for the standard CERN GEM geometry is in reasonable agreement with the parameter values presented in Ref. [76]: $a = 138.21\,\text{cm}^{-1}$, $b = 0.0623$.

The knowledge of the parameters a and b allows to calculate the hole field E_{hole} (see Equation 6.16). This allows to determine the parameters r and s directly from the measurements, when plotting single GEM parameters as a function of the ratio $E_{\text{ext.}}/E_{\text{hole}}$ and fitting the distribution using Equation 6.17. This is done for a stack of three standard CERN GEMs in Section 6.3.2 and for a stack where the top most GEM is replaced by a modified one in Section 6.3.2.

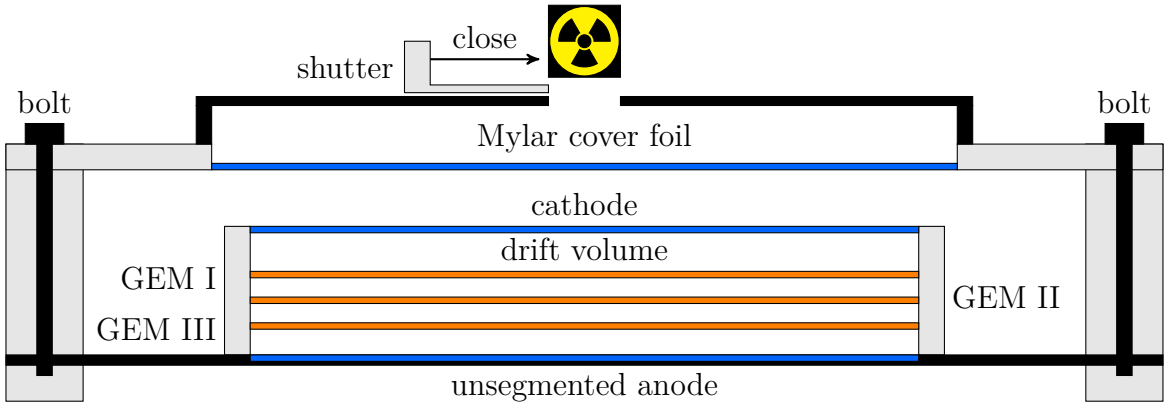

Figure 6.5: Sketch of the TPC prototype setup.

6.2 Introduction to the measurement with a small TPC prototype

In the following the measurement setup and the measurements itself are introduced.

6.2.1 Measurement setup

The setup that is used here consist of a TPC prototype with a stack of three 10 cm × 10 cm GEMs. It is sketched in Figure 6.5. Main parts of the TPC prototype were constructed and designed at *Forschungszentrum Karlsruhe* and modified at the University of Aachen and Bonn. The TPC walls are made of glass fibre resin compound Stesalit. Furthermore, the anode is a single copper surface and the cathode is made of an aluminium coated Mylar foil. On top of the chamber is an additional aluminium coated Mylar foil closing the gas volume. Relevant distances are given in Figure 6.6, where also two sets of operating parameters are given. In addition, all electrode currents, fields and GEM voltages that will be used in the following are defined

Gas system

The gas system is an open system, where the inlet of the chamber is connected via a pressure regulator to a gas bottle with the drift gas and the gas outlet is left open. Thus, the pressure in the chamber follows the air pressure. The gas temperature is monitored via a DS1820 temperature chip produced by Maxim Integrated [1] and put into the prototype chamber.

[1] Maxim Integrated, 160 Rio Robles, San Jose, CA 95134 USA

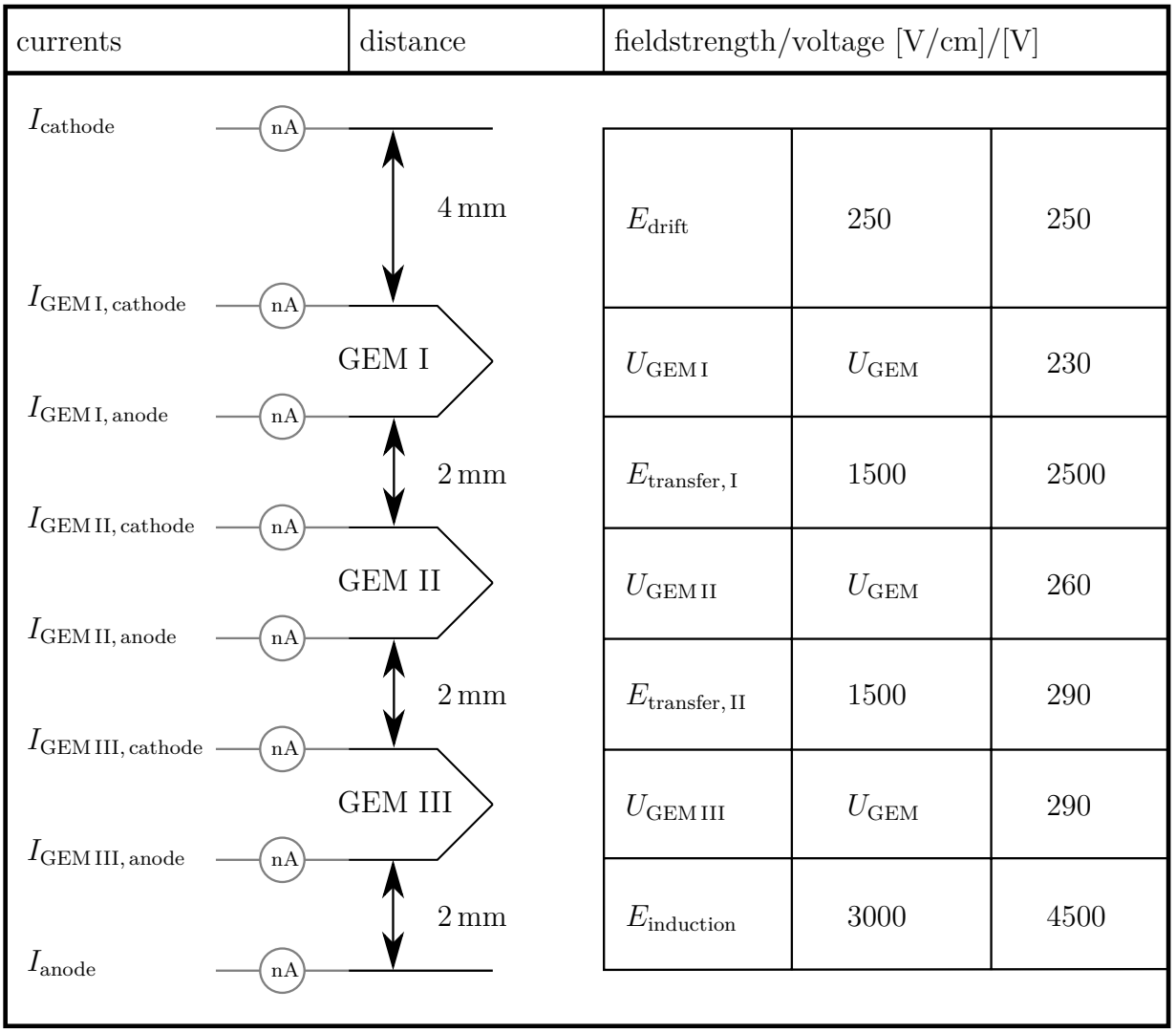

E_{drift}	250	250
$U_{\text{GEM I}}$	U_{GEM}	230
$E_{\text{transfer, I}}$	1500	2500
$U_{\text{GEM II}}$	U_{GEM}	260
$E_{\text{transfer, II}}$	1500	290
$U_{\text{GEM III}}$	U_{GEM}	290
$E_{\text{induction}}$	3000	4500

Figure 6.6: Parameters of the measurement setup including current definitions. The voltages given for individual GEMs reflect the voltage difference between the anode and cathode of the GEM. Left-hand fields/voltages show default settings. Right-hand fields/voltages show the ion back flow settings (IBF).

In the measurements presented in the following, T2K gas as introduced in Chapter 4 was used.

Power supply

All GEM electrodes as well as the cathode and anode electrode are powered by individual channels of a CAEN SY2527[2] power supply. Furthermore, all electrodes are protected with

[2]CAEN S.p.A., Via Vetraia 11, 55049 Viareggio (LU), Italy

an 10 MΩ resistor. Thereby, in case of a discharge in a GEM the current $I_{\text{trip}} = U_{\text{GEM}}/20\,\text{M}\Omega$ is limited by the two resistors in series. If such a case, called trip, is recognised by the power supply, which happens if a current larger than 4 µA is present for more than 0.2 s, all channels are ramped down in order to protect the setup. During the measurements presented here, the power supply was completely controlled by remote. After a trip all voltages are ramped up again automatically in order to recover the operating conditions prior to the trip. If during the ramp up again a trip occurs only one additional ramp up is attempted. Finally, if the last ramp up also fails the measurement is stopped.

Current measurements

All GEM electrodes as well as the cathode and anode electrode are connected to an ampere meter, called ***CU****rrent* ***MO****nitor* (CUMO). These CUMOs are NIM modules constructed in the workshop of the University of Aachen [77]. In general the measurement range is −20 µA to 20 µA. The direction of the current is defined such, that the current measured on an electrode collecting electrons is positive. In consequence, on an electrode collecting ions a negative current is measured. Furthermore, this range is subdivided in four sub-ranges with different resolutions. The smallest range is −20 nA to 20 nA with a resolution of 0.1 nA. With larger currents the resolution gets worse and in the highest range of −20 µA to 20 µA it is 100 nA. The CUMOs were used in auto range mode, where the range is chosen automatically to result in the best resolution.

On the front panel of the CUMOs there are two LEMO connector providing a voltage signal. One of these signal encodes the measured current and the other one encodes the current range. Both voltage signals are digitised using a Meilhaus ME-4610[3] data acquisition card.

Setup control via the XTC software

All measurements are controlled with a C++ based program developed at the University of Aachen called XTC. It provides a graphical user interface, which allows to monitor all channels of the power supply and all currents measured by the CUMOs. In addition, the parameters of the setup like e.g. GEM voltages can be changed. Furthermore measurement runs, varying a certain parameter of the setup, can be performed by the XTC software. Via scripts it is possible to chain several series and record a complete data set. The data is

[3] Meilhaus Electronic GmbH, Am Sonnenlicht 2, 82239 Alling, Germany

stored in ASCII files which contain measurements and condition parameters monitored by the XTC software.

An interface to the Meilhaus ME-4610 data acquisition card was already available, but in order to use this software with the CAEN SY2527 power supply the software was extended. Furthermore, the software was extended in order to read the output of the DS1820 temperature chip. This allows to monitor the temperature during measurement runs.

6.2.2 Signal creation

The gas ionisation in the TPC prototype is done using a ^{55}Fe source with an activity of 30 MBq, which is located on top of the Mylar foil closing the gas volume of the TPC prototype. It decays via electron capture leaving a vacancy in the K shell of the atom. Subsequently this vacancy is filled with an electron from a higher shell. The concerned energy difference can be released in two ways. Either it is released via a photon or the energy is transferred to an electron of a higher shell, which is released. The release of such an electron, called Auger electron, is most probable. But due to the Mylar foil between the source and the gas volume Auger electrons will not reach the sensitive volume of the TPC. Therefore, the process with the second highest probability of 24.4 % [15] is of interest here. It is characterised by a photon with an energy of $E_\gamma = 5.9\,\mathrm{keV}$ and it can be written as:

$$^{55}\mathrm{Fe} + e^- \longrightarrow {}^{55}\mathrm{Mn}^* \longrightarrow {}^{55}\mathrm{Mn} + \gamma.$$

Such photons reaching the sensitive volume of the TPC prototype have enough energy to ionise the drift gas, since the mean ionisation energy W of argon based gas mixtures is below 30 eV [30]. Therefore, the number of electrons $N_{e^-} = E_\gamma / W$ per ionisation is in the order of $\mathcal{O}(200)$.

In order to do also measurements without the photon signals, a shutter consisting of a motor and an aluminium sheet with a thickness of 1 mm is used. When the shutter is closed, the Aluminium sheet is pushed in between the source and the Mylar foil of the chamber. Thereby the photons are blocked and cannot reach the TPC gas volume anymore. The shutter is also controlled by the XTC software via the parallel port of the DAQ computer.

6.2.3 Definition of the GEM parameters

As introduced before the current on all electrodes in the setup is measured. In the following the analysis of the currents is introduced.

The most obvious measurement is the effective gain of the setup as defined in Equation 6.6. With the setup used here, only relative measurements of $G_{\text{eff.}}$ can be done by analysing the current on the anode I_{anode}:

$$I_{\text{anode}} \sim G_{\text{eff.}} \tag{6.20}$$

This allows to compare different field and voltage settings with respect to their effective gain. An absolute gain measurement would require to analyse individual signal pulses as done for example in Ref. [43]. The second measurement characterising the GEM stack that can be done, is the measurement of the ratio between the current on the anode and the current on the cathode I_{cathode}. This ratio can be identified as the ratio between the ion back flow and the effective gain of the GEM stack as defined in Equation 6.8:

$$\frac{\text{IFR}}{G_{\text{eff.}}} = \frac{I_{\text{cathode}}}{I_{\text{anode}}}. \tag{6.21}$$

In the following measurements of single GEM parameters are defined. For these definitions one should keep in mind, that most of the electrodes collect a current, which is composed of electrons and ions. This requires to define the transfer coefficients for ions and electrons with respect to different GEMs of the GEM stack. That is why for example the electron extraction efficiency will be defined with respect to GEM III, since here no ions from underlying GEMs distort the measurements. In the following subscripts will indicate the GEM, where a certain transfer coefficient is measured. Nevertheless the resulting transfer coefficients characterise a single GEM in general and not a specific GEM of the stack.

Single GEM gain

The single GEM gain can be calculated with respect to GEM III. First of all a measurement is done when GEM III is switched off by setting the voltage of its anode to its cathode voltage. The current that is measured now on its cathode $I^0_{\text{GEM III, cathode}}$ corresponds to the number of electrons reaching GEM III for the chosen settings of the setup. Afterwards the same measurement is repeated when GEM III is amplifying. All amplified electrons

end either on the anode of GEM III or the anode. Therefore, the gain of GEM III can be calculated as:

$$G_{\mathrm{GEM\,III}}(U_{\mathrm{GEM}}) = \frac{I_{\mathrm{anode}} + I_{\mathrm{GEM\,III,\,anode}}}{I^{0}_{\mathrm{GEM\,III,\,cathode}}}. \tag{6.22}$$

For this definition it is assumed that the electron collection efficiency of GEM III is 100 %. If this is not the case, some electrons are lost on the cathode electrode of GEM III, which can not be amplified.

Electron collection efficiency

The electron collection efficiency can be calculated with respect to GEM I. By changing the drift field, the collection efficiency of GEM I can be changed. This can be directly measured by investigating the current on the anode. It can be assumed that the maximum measured anode current $I_{\mathrm{anode,\,max}}$ corresponds to a collection efficiency of 100 %. This allows to calculate the collection efficiency for different drift fields by comparing the measured anode current to $I_{\mathrm{anode,\,max}}$. What needs to be also taken into account is, that the drift field has a small influence on the amplification of GEM I. This can be accounted for by weighting the anode current with the gain and finally the electron collection is given by:

$$C^{-}_{\mathrm{GEM\,I}}(E_{\mathrm{drift}}) = \frac{I_{\mathrm{anode}}/G}{I_{\mathrm{anode,\,max}}/G_{E_{\mathrm{drift,\,max}}}}, \tag{6.23}$$

where $E_{\mathrm{drift,\,max}}$ is the drift field corresponding to the measurement of $I_{\mathrm{anode,\,max}}$. In order to calculate the gain for different drift fields, it is parametrised using an exponential function according to Equation 3.17:

$$G(E_{\mathrm{hole}}) = \alpha \exp\left(\beta E_{\mathrm{hole}}\right), \tag{6.24}$$

where E_{hole} can be substituted using Equation 6.16 and the parameters α and β free parameters of the parameterisation. They are obtained from the measured single GEM gain, defined in Equation 6.22.

Finally, the collection efficiency can be written as:

$$C^{-}_{\mathrm{GEM\,I}}(E_{\mathrm{drift}}) = \frac{I_{\mathrm{anode}}}{I_{\mathrm{anode,max}}} \exp\left[\beta b \left(E_{\mathrm{drift,max}} - E_{\mathrm{drift}}\right)\right]. \tag{6.25}$$

Electron extraction efficiency

The electron extraction efficiency can be calculated with respect to GEM III, since here no ions from underlying GEMs contribute the current on the anode of GEM III. Thus, directly the current on the anode of GEM III can be compared to the total number of electrons produced in GEM III:

$$X^{-}_{\mathrm{GEM\,III}}(E_{\mathrm{induction}}) = \frac{I_{\mathrm{anode}}}{I_{\mathrm{anode}} + I_{\mathrm{GEM\,III,\,anode}}}. \tag{6.26}$$

For high induction fields gas amplification in the induction region will influence the measurement. On the one hand I_{anode} will be increased since the number of electrons reaching the anode increases. On the other hand $I_{\mathrm{GEM\,III,\,anode}}$ will be reduced, since without gas amplification in the induction region it is only composed of electrons, whereas with this additional amplification also ions are collected on the anode of GEM III.

Ion collection efficiency

The ion collection efficiency is defined with respect to GEM II, were only ions produced in GEM III contribute. The measurement is done on the anode of GEM II, were in principle also electrons not extracted from GEM II are collected. In order to measure the current component arising from these electrons, the current on the anode of GEM II is measured when GEM III is switched off ($I^{0}_{\mathrm{GEM\,II,\,anode}}$) and therefore no ions produced in GEM III contribute. The total number of ions produced in GEM III can be calculated as the sum of the currents on the anode of GEM III and the anode itself, since for each electron one ion is produced in the ionisation process. Finally, the ion collection efficiency is defined as:

$$C^{+}_{\mathrm{GEM2}}(E_{\mathrm{transfer,\,II}}) = 1 - \frac{I_{\mathrm{GEM\,II,\,anode}} - I^{0}_{\mathrm{GEM\,II,\,anode}}}{-(I_{\mathrm{GEM\,III,\,anode}} + I_{\mathrm{anode}}) + I_{\mathrm{GEM\,III,\,cathode}}}, \tag{6.27}$$

where $I_{\mathrm{GEM\,III,\,cathode}}$ is composed of ions not extracted from GEM III, assuming that the electron collection efficiency of GEM III is 100 %.

Primary ion extraction efficiency

Since pure primary ion extraction only occurs at GEM III it is defined with respect to this GEM. Again the number of produced ions is deduced from the currents cased by the electrons on the anode of GEM III and the anode. The number of not extracted ions

is $I_{\text{GEM III, cathode}}$, where again the electron collection efficiency of GEM III is assumed to be 100 %. Considering this assumption the primary ion extraction efficiency is defined as:

$$X^{+}_{\text{prim.,GEM3}}(E_{\text{transfer, II}}) = \frac{I_{\text{GEM III, anode}} + I_{\text{anode}} + I_{\text{GEM III, cathode}}}{I_{\text{GEM III, anode}} + I_{\text{anode}}}. \tag{6.28}$$

Secondary ion extraction efficiency

In principle the current on a GEM cathode is composed of primary and secondary ions, which makes it difficult to measure the extraction efficiency for secondary ions. Here the measurement of $X^{+}_{\text{sec.}}$ is done with respect to GEM I, where the number of primary ions is much less than the number secondary ions produced in GEM I and GEM II. This can be illustrated using a simulation as introduced in Chapter 5 and applying the low gain settings, which are introduced in the following section. In the simulation the number of secondary ions collected into GEM I is in the order of $\mathcal{O}(2500)$ and the number of primary ions is in the order of $\mathcal{O}(50)$. The number of secondary ions collected on the cathode of GEM II in this example is in the order of $\mathcal{O}(2000)$, which is much larger than the number primary ions. In addition, the number of secondary ions reaching the cathode ($\mathcal{O}(500)$) is large compared to the number of ions produced by the primary ionisation in the drift volume, which is one in the simulation since it is done starting one electron. Thus, the following definition of the secondary ion extraction efficiency is justified:

$$X^{+}_{\text{sec.,GEM1}}(E_{\text{drift}}) = \frac{I_{\text{cathode}}}{I_{\text{GEM I, cathode}} + I_{\text{cathode}}}. \tag{6.29}$$

The current produced by the primary ionisation process has been measured in former measurements with an even stronger ^{55}Fe source in an argon based gas. Here a current on the cathode of $I_{\text{cathode}} = (0.0102 \pm 0.0015)\,\text{nA}$ [74] was found, which is well below the measured currents of $I_{\text{cathode}} > 1\,\text{nA}$.

6.2.4 GEM stack settings

The GEM parameters introduced in the previous section are calculated for different settings of the GEM stack. In detail the considered settings are given in Table 6.1 (see also Figure 6.6). The voltages given for individual GEMs correspond to the voltage difference between the anode and cathode of this GEM. Furthermore, the low and high gain settings correspond to commonly used triple GEM stack settings, where the same voltage on all

Table 6.1: Summary of all considered setups. The induction field in the IBF settings had to be reduced when scanning $U_{\mathrm{GEM\,III}}$ to 3000 V.

Settings	E_{drift} [V/cm]	$U_{\mathrm{GEM\,I}}$ [V]	$E_{\mathrm{transfer,\,I}}$ [V/cm]	$U_{\mathrm{GEM\,II}}$ [V]	$E_{\mathrm{transfer,\,II}}$ [V/cm]	$U_{\mathrm{GEM\,III}}$ [V]	$E_{\mathrm{induction}}$ [V/cm]
low gain	250	250	1500	250	1500	250	3000
high gain	250	280	1500	280	1500	280	3000
IBF	250	230	2500	260	290	290	4500

three GEMs is used. The advantage of a higher gain is the increased overall current in the stack, which makes it easier to measure small currents as expected for example on GEM I electrodes. On the other hand a higher GEM voltage increases the probability of discharges and thus reduces the stability of the setup.

The ion back flow (IBF) setting is based on settings presented in Ref. [74], which are optimised in reducing the number of ions reaching the sensitive volume of the TPC. Here the voltage on GEM I is reduced in order to limit the number of ions produced in this GEM. This is because ions produced in this GEM will directly enter the sensitive TPC volume. The choice of the fields in the GEM stack is motivated by the behaviour of the ion transfer coefficients found in Ref. [74]. With decreasing field strength the ion collection efficiency increases and the extraction efficiency decreases, which will also be shown in this work in Section 6.3.2. This is the reason for increasing $E_{\mathrm{transfer,\,I}}$ with respect to the low and high gain settings. In other words, by increasing $E_{\mathrm{transfer,\,I}}$ many ions produced in GEM II an GEM III are collected on the anode of GEM I. Furthermore, $E_{\mathrm{transfer,\,II}}$ is reduced, which decreases the extraction efficiency of ions in case of GEM III. In order to reach a sufficient effective gain in the setup the voltage of GEM III is increased, which balances the gain reduction in GEM I. Finally, the induction field is increased in order to increase the extraction efficiency of electrons in case of GEM III.

6.2.5 Field and voltage scans

As shown in Section 6.2.3, the GEM parameters are measured as a function of different GEM stack parameters. In general, a parameter scan is based on one of the settings introduced in the previous section.

The parameters that need to be scanned in order to calculate all GEM parameters as introduced in Section 6.2.3 are the following: E_{drift}, $E_{\mathrm{transfer,\,II}}$, $E_{\mathrm{induction}}$ and $U_{\mathrm{GEM\,III}}$. A scan is done by changing constantly the field and voltage respectively. Table 6.2

Table 6.2: Summary of all considered scans.

Scanned variable	start value	end value	step size
U_{GEM}	0 V	280 V	5 V
E_{drift}	100 V/cm	4000 V/cm	10 V/cm
$E_{\mathrm{transfer}}, E_{\mathrm{induction}}$	100 V/cm	5000 V/cm	10 V/cm

shows the characteristics of different scans. In principle each point of the scan consists of several measurements. After ramping all voltages to realise a certain working point, 100 measurements of all currents with a closed shutter are performed. Between each measurement there is a break of 0.1 s. The mean value of these measurements is used to calibrate the CUMOs by requiring a vanishing current on all electrodes when the shutter is closed. This allows to correct the measurements for residual currents in the system. Afterwards the shutter is opened again 100 measurements are taken. For each CUMO, the resulting distribution of measured currents is approximated with a Gaussian distribution. The mean value and the standard deviation is recorded. In addition, also the CUMO range used to make the measurement is recorded, which allows to estimate the systematic uncertainty of the measurement. Finally, the shutter is closed and the voltages are ramped to the next working point.

6.2.6 Discussion of the uncertainties

There are two kind of uncertainties directly connected to the setup. On the one hand, there is the systematic uncertainty of the measured current. As introduced before and given in Ref. [77], this uncertainty depends on the range used by the CUMO and corresponds to one digit of the current range. This means in the smallest range it is 0.1 nA and in the highest range it is 100 nA. On the other hand, there is the statistical uncertainty of the measured current, which is given by the standard deviation of corresponding Gaussian distribution resulting from the 100 individual measurements. All individual measurements of the CUMOs are treated as uncorrelated and therefore Gaussian propagation of uncertainties is used to calculate uncertainties of the GEM parameters.

Furthermore, there is a dependence of the measured currents on the gas temperature T and the gas pressure p. Both influence the GEM gain, which is characterised by the Townsend coefficient. Assuming an inverse proportionality of the Townsend coefficient α to the mass

Table 6.3: Dependency of GEM parameters on the temperature and the pressure based on measurements done in Bonn[79].

	$\Delta C^-/C^-$	$\Delta X^-/X^-$	$\Delta C^+/C^+$	$\Delta X^+_{\text{prim.}}/X^+_{\text{prim.}}$	$\Delta X^+_{\text{sec.}}/X^+_{\text{sec.}}$
$\Delta T = 6\,\text{K}$	0.14	0.01	0.05	0.1	0.02
$\Delta p = 10\,\text{hPa}$	0.12	0.02	-	0.07	-

density ρ, and thus $\alpha \propto 1/\rho \propto T/p$, the measured current follows:

$$I \propto \exp^{b \cdot T/p}.$$

Here b is a parameter that needs to be measured and in principle depends on the parameters of the setup. Such a behaviour is also found in measurements presented in Ref. [78].

From former measurements with the same setup as used here the uncertainty can be estimated. The corresponding uncertainties for different transfer coefficients are deduced from results presented in Ref. [79]. A summary is given in Ref. Table 6.3. It can be seen, that the electron collection efficiency is most effected by pressure and temperature changes. The uncertainties shown in Table 6.3 represent only upper limits to the measurements presented here, since the temperature was stable within $\pm 1\,\text{K}$. Furthermore, the gas pressure follows the air pressure, since an open gas system is used. It can be assumed that the change in air pressure is less than $\Delta p = 10\,\text{hPa}$, as considered in Table 6.3, taking a typical measurement period of 5 hours into account.

6.3 Results with a standard CERN GEM

In the following the results of measurements using three standard CERN GEMs in the stack will be presented, starting with the parameters characterising the GEM stack followed by the measurements of single GEM parameters.

6.3.1 GEM stack parameter

Figure 6.7 shows the results of measurement for the different settings. In Figure 6.7a the current measured on the anode is shown, which according to Equation 6.20 is proportional to the effective gain of the GEM stack. The effective gain for the low gain settings is similar

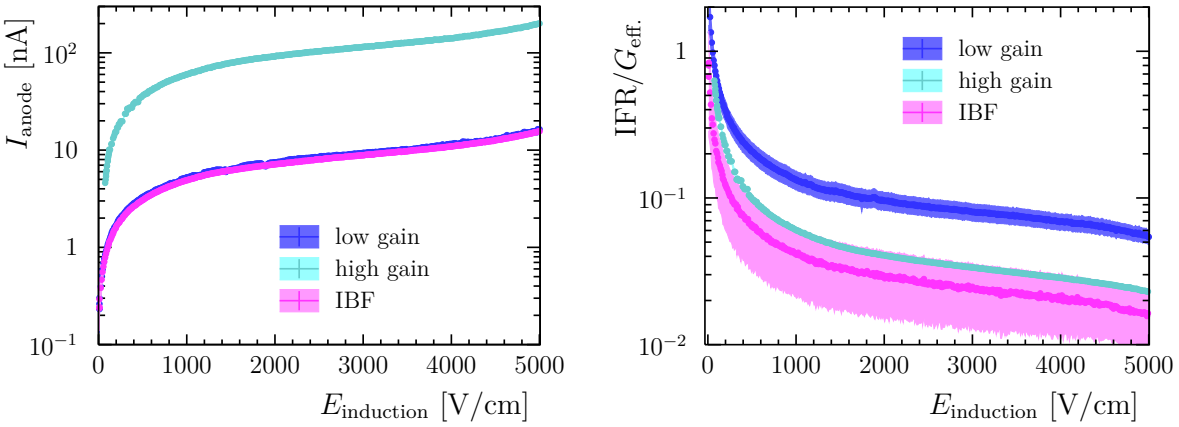

(a) Current measured on the anode as a function of the induction field. The results for the low gain and IBF settings are similar and therefore the corresponding curves overlap.

(b) Ratio between the current measured on the cathode and the anode ($I_{\text{cathode}}/I_{\text{anode}}$), which is similar to IFR/$G_{\text{eff.}}$.

Figure 6.7: Comparison between different settings of the GEM stack. The error band shows systematic uncertainties connected to the CUMOs and the error bars represent statistic uncertainties. Results are shown for T2K gas and a stack of three standard CERN GEMs.

to the effective gain observed in case of the IBF settings considering the same induction field. Therefore, they are hard to distinguish in Figure 6.7a. Furthermore, the effective gain of the high gain settings is a factor of 10 larger compared to the other settings. Both, the statistical and the systematic uncertainties are small, since the anode current is high and especially higher than the current on other electrodes in the setup.

In Figure 6.7b the ratio of the cathode and anode current is shown, which corresponds to IFR/$G_{\text{eff.}}$ (see Equation 6.21). Here the systematic uncertainty (shown as error band) is dominant for the low gain and IBF settings, since the absolute current on the cathode becomes similar to the CUMO resolution. In other words the absolute number of ions produced in the GEM stack reaching the sensitive volume of the TPC is low. The statistical uncertainty is negligible in all measurements shown in Figure 6.7, which shows that the number of 100 individual measurements per working point is sufficient.

A direct comparison of the ion feedback ratio between the settings requires the knowledge of the effective gain. It can be estimated from simulations introduced in Chapter 5, which will be done in Section 6.5 where also estimated values of the ion feedback ratio are given. At this point only a relative comparison between the settings can be done by exploiting the fact that $G_{\text{eff.}} \sim I_{\text{anode}}$. Values of the anode current and the ratio IFR/$G_{\text{eff.}}$ are shown in Table 6.4. They are taken from the results shown in Figure 6.7 at the nominal induction

Table 6.4: Summary of the measurements with a stack of three standard CERN GEMs.

setting	I_{anode} [nA]	$\delta_{\text{sys.}}$ [%]	$\delta_{\text{stat.}}$ [%]	IFR/$G_{\text{eff.}}$	$\delta_{\text{sys.}}$ [%]	$\delta_{\text{stat.}}$ [%]	IFR/IFR(high gain)
high gain	115.07	0.87	0.09	0.03	2.73	0.11	1
low gain	9.34	1.07	0.06	0.08	13.42	0.34	0.22
IBF	12.62	0.79	0.06	0.02	42.00	0.88	0.07

field corresponding to the settings (see Table 6.1). The comparison, also given in Table 6.4, shows that the ion feedback ratio of the high gain settings is reduced by 88 % using the low gain settings. Using the IBF settings a further reduction of IFR is achieved and compared to the high gain settings it is reduced by 93 %.

This shows, that by choosing proper settings of the GEM stack the ion feedback ratio indeed can be significantly reduced. The reduction itself can be understood with the help of the single GEM parameters, which are presented in the following.

6.3.2 Single GEM parameter

As shown in Equations 6.16 and 6.17 the transfer coefficients can be parametrised in terms of E_{hole} and $E_{\text{ext.}}/E_{\text{hole}}$. The latter ratio is defined and referred to as x, where one should keep in mind that the concrete hole field and external field depends on the specific transfer coefficient. For example in case of the electron extraction efficiency X^- defined in Equation 6.26 the measurement is done with respect to GEM III and thus E_{hole} corresponds to the field in GEM III. Furthermore $E_{\text{ext.}}$ in this case corresponds to $E_{\text{induction}}$.

All transfer coefficients as a function of x and the gain as a function of E_{hole} are shown in Figure 6.8 for all settings summarised in Table 6.1. Coloured vertical lines indicate the x value corresponding to the nominal field value in Table 6.1 and therefore indicate the default working point of the different settings. In the following individual GEM parameters are discussed in detail.

Figure 6.8a shows the single GEM gain measured at GEM III. Here the systematic uncertainty of the IBF setting is much larger than that of the other two settings. This is because, $I^0_{\text{GEM III, cathode}}$ for the IBF settings is very close to zero and therefore the relative systematic uncertainty is large. The gain observed for the IBF settings is slightly higher than the gain observed for the other two settings, but taking the systematic uncertainty into

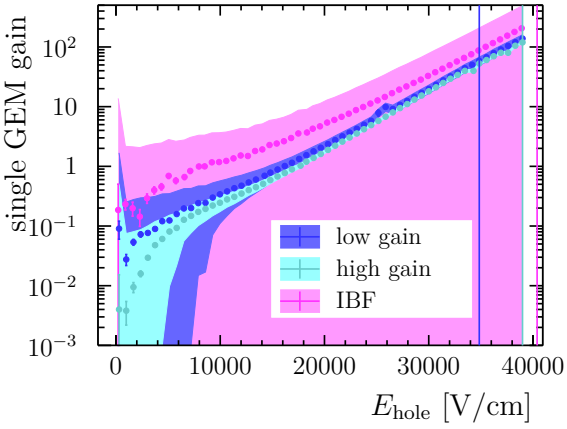

(a) Single GEM gain measured on GEM III in a scan of $E_{\text{induction}}$.

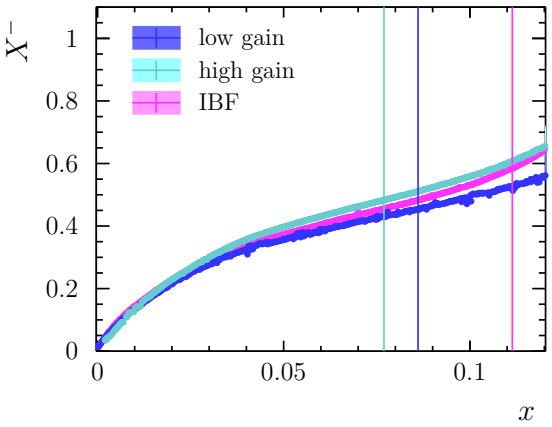

(b) Electron extraction efficiency measured on GEM III in a scan of $E_{\text{induction}}$.

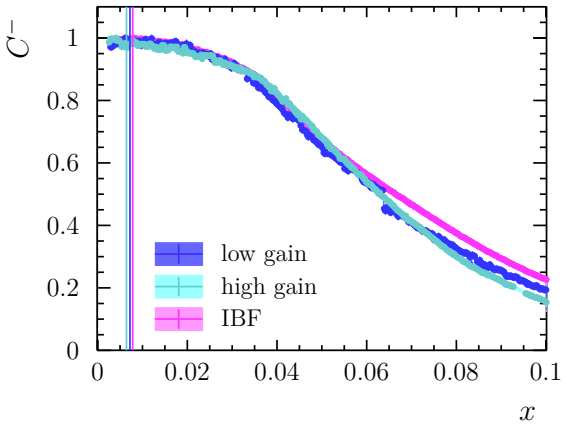

(c) Electron collection efficiency measured on GEM I in a scan of E_{drift}.

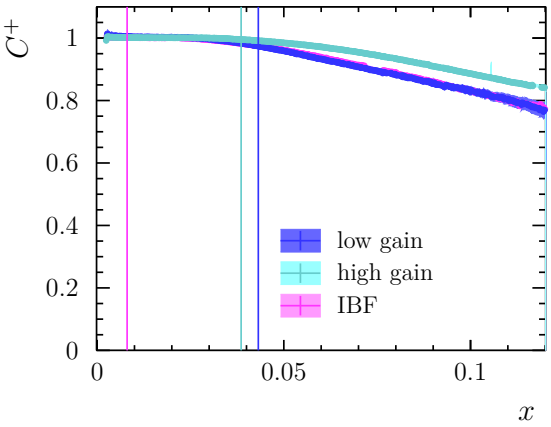

(d) Ion collection efficiency measured on GEM II in a scan of $E_{\text{transfer, II}}$.

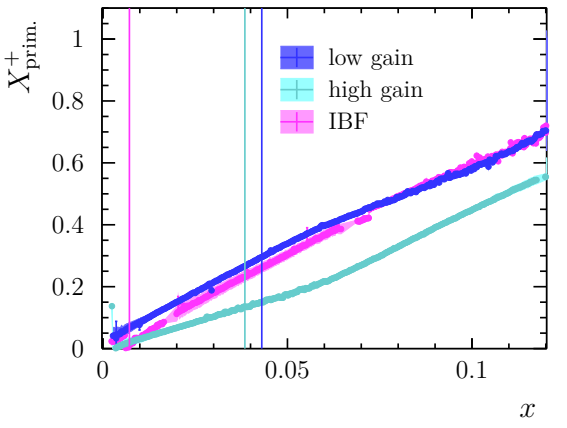

(e) Ion primary extraction efficiency measured on GEM III in a scan of $E_{\text{transfer, II}}$.

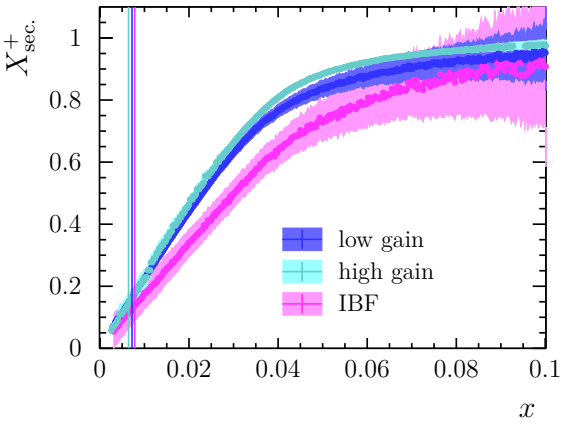

(f) Ion secondary extraction efficiency measured on GEM I in a scan of E_{drift}.

Figure 6.8: GEM parameters for different GEM stack settings with T2K gas. Coloured vertical lines indicate the value of x for each settings as given in Table 6.1. The error band shows systematic uncertainties connected to the CUMOs and the error bars represent statistic uncertainties.

account this effect is not significant. Thus, the measurements agree with the assumption that the single GEM does not depend on the chosen GEM stack settings, which is expected when plotting the gain versus the hole field. For moderate hole fields the gain shows the expected exponential behaviour (see Equation 6.24), whereas for low hole fields the gain drops more steeply. This can be understood, since for low hole fields x becomes larger and therefore the collection efficiency of GEM III is no longer 100 % (see also Figure 6.8c), which was required in the definition of the single GEM gain (Equation 6.22). As indicated by the vertical lines the default hole fields are well within the region, where the exponential behaviour is seen. The vertical line for the IBF settings is outside the measurement range in Figure 6.8a, because the GEM voltage was only increased up to $U_{\mathrm{GEM}} = 280\,\mathrm{V}$ and in the IBF settings it is set to $U_{\mathrm{GEM}} = 290\,\mathrm{V}$.

In Figures 6.8b to 6.8f a separation between the low and the high gain for large values of x can be observed, which is not expected from the electrostatic model introduced in Section 6.1.2. Measurements with a gain between the low and high gain settings confirmed a trends from the low to the high gain settings seen here.This shows that the parameterisation in terms of x does not include all effects in the GEM stack. One effect that could cause a difference and that is not covered in the electrostatic model is the attachment. It will be discussed in detail in Section 6.3.3.

Significant differences between different settings can be seen in Figure 6.8e. Here the extraction efficiency for primary ions is less for the high gain settings compared to the other settings. One possible explanation could be a difference in the form of the avalanche depending on the gain of the GEM. Interpreting the data that way, a higher gain spreads the avalanche more over the whole hole diameter. As a consequence there are more ions at the outer region of the GEM hole, which are more efficiently collected on the GEM cathode. Since the gain in GEM III for the IBF settings is even higher than for the high gain settings this should also apply for the IBF settings. But here in addition the induction field is higher, which again influences the avalanche shape and obviously leads to an increase of the extraction efficiency of ions.

Finally, the default IBF settings (pink vertical line) can evaluated considering the different GEM parameters in comparison to the other, more standard, settings (blue vertical lines). There is no big difference in the electron collection efficiency, the primary ion collection efficiency and the extraction efficiency of secondary ions. The extraction efficiency for electrons on the last GEM III is increased due to the higher induction field, which helps to achieve a reasonable effective gain. Furthermore, the extraction efficiency of primary ions

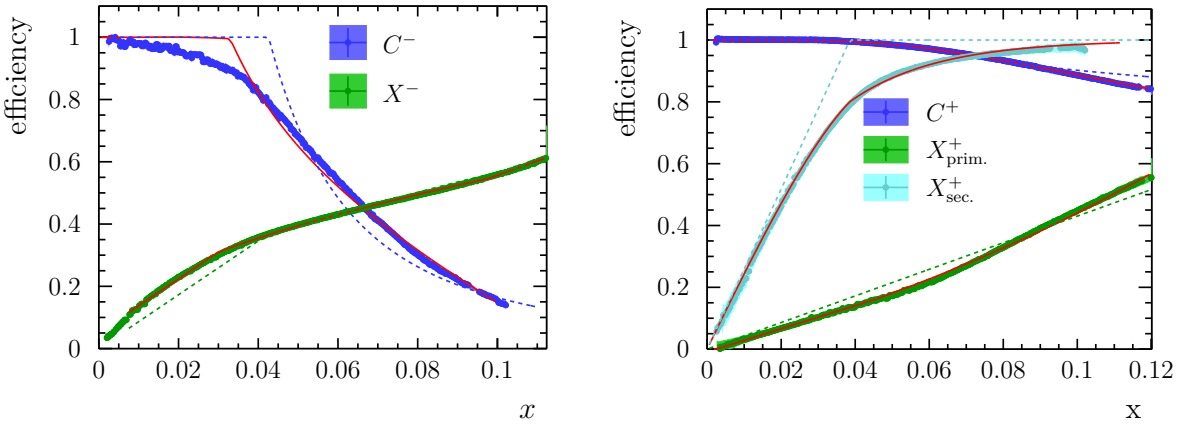

(a) Electron transfer coefficients.

(b) Ion transfer coefficients.

Figure 6.9: Parameterisation fits to the transfer coefficients of ions and electrons. The shown data corresponds to the high gain measurement settings. The dashed fits result from the parameterisation based on the electrostatic model, whereas the corresponding solid lines show the modified parameterisations.

for GEM III is reduced in case of the IBF settings. This is very good, since here most of the ions are produced and thus the total number of ions reaching the sensitive volume of the TPC is limited effectively.

This example illustrates how to use the information on single GEM parameters to understand the behaviour of a GEM stack. In a general, the information about the single GEM parameters can be used to calculate the effective gain and the ion feedback ratio using Equation 6.6 for arbitrary settings of the GEM stack. In order to so it is helpful to parametrise the measurements presented here, which allows to calculate GEM stack parameters in a convenient way. Such a parameterisation is presented in the following.

6.3.3 Parameterisation of the electron collection and extraction efficiency

The parameterisation that is presented in the following is based on the electrostatic model introduced in Section 6.1.2, which includes five parameters: $\tau_{\text{opt.}}, a, b, r, s$. The parameters $\tau_{\text{opt.}}, a$ and b are fixed by the GEM geometry and they can be found in Sections 6.1.2 and 6.1.3. Therefore, only the parameters s and r need to be calculated here.

Figure 6.9 shows the transfer coefficients for ions and electrons in case of the high gain settings. Dashed lines show the fit result using the parameterisation resulting from the electrostatic model. It can be seen that for all transfer efficiencies deviations from the measurements are present.

Therefore, modifications of the parameterisation are applied, which result in the fits shown in Figure 6.9 as solid red lines. As mentioned before the electrostatic model by definition does not account for effects like attachment or additional gas amplification between GEMs, which influence the measurements and need to be considered to describe the data. In case of the collection efficiency the deviation from the expectation of the electrostatic model can be understood by investigating the contribution of the attachment. As defined in Equation 6.25, the electron collection efficiency is the ratio between the anode current and the maximum anode current. The latter one is determined for a certain drift field $E_{\text{drift,max}}$. As Figure 6.9a shows $E_{\text{drift,max}}$ corresponds to a low drift field, where no attachment occurs. At higher drift fields the anode current is artificially reduced by attachment in the drift region. This needs to be taken into account for the calculation of the collection efficiency. Here the attachment A_i is taken from MAGBOLTZ simulations, which are parametrised with a 5th order exponential polynomial as follows:

$$A_i(|\vec{E}|) = \exp\left(-d_{\text{drift}} \sum_{i=0}^{5} a_i \left(|\vec{E}|\right)^i\right), \tag{6.30}$$

where d_{drift} is the drift distance. Results of the simulation and the resulting parameterisation for T2K gas are shown in Figure 7.36. Using this parameterisation of the attachment, the modified parameterisation of the electron collection efficiency can be written as:

$$C = \begin{cases} 1 - l_{\text{eff.}} A_i(|\vec{E}|) & \text{for } (E_{\text{ext.}}/E_{\text{hole}}) \leq r^{1/s} \\ r\left(\frac{E_{\text{ext.}}}{E_{\text{hole}}}\right)^{-s} - l_{\text{eff.}} A_i(|\vec{E}|) & \text{for } (E_{\text{ext.}}/E_{\text{hole}}) > r^{1/s}, \end{cases} \tag{6.31}$$

where $l_{\text{eff.}}$ is an additional free parameter of the fit corresponding to the effective attachment length. The result of the fit using this parameterisation describes the data well as shown in Figure 6.12a. Only in the region of $x \approx 0.02 - 0.04$ the measured electron collection efficiency is smaller than expected from the parameterisation. This region of x corresponds to the drift field region close to the threshold where attachment starts. Therefore, the observed discrepancy between the fit and the measured data could be explained with an underestimated attachment in this region in the MAGBOLTZ simulation. Furthermore impurities of the gas in the measurements could have increased the attachment.

A similar modification is applied to the ion collection efficiency fit shown in Figure 6.9b, since also here $I^0_{\text{GEM II,anode}}$ is used to normalise the current on the anode of GEM II. By changing $E_{\text{transfer, II}}$ the attachment in the transfer region between GEM II and GEM III is changed. Again the introduction of the attachment term $l_{\text{eff.}} A_i(|\vec{E}|)$ improves the fit

significantly in the high x region, where attachment is most relevant.

The extraction efficiency is modified such, that an offset y to x is allowed in the parameterisation:

$$X(x) = \begin{cases} \frac{1}{\tau_{\text{opt.}}} (x - y) & \text{for } x \leq r^{1/s} \\ \frac{r}{\tau_{\text{opt.}}} (x - y)^{1-s} & \text{for } x > r^{1/s}. \end{cases} \tag{6.32}$$

Furthermore gas amplification in the transfer regions between GEMs at high values of x, called parallel plate gain, is introduced using as:

$$G_{\text{par.}}(x) = \begin{cases} 1 & \text{for } x \leq x_0 \\ \exp\left(e_{\text{par.}} (x - x_0)\right) & \text{for } x > x_0. \end{cases} \tag{6.33}$$

Here x_0 corresponds to the threshold for additional gas amplification and $e_{\text{par.}}$ corresponds to the gas dependent strength of the additional gas amplification. This parameterisation $X(x) \cdot G_{\text{par.}}(x)$ is proposed in Ref. [74] and the resulting fits describe the the data very well, as shown in Figures 6.9a and 6.9b.

Finally, the extraction efficiency fit is modified following Ref. [74] as follows:

$$X^{+}_{\text{sec.}} = \begin{cases} \frac{X_{\text{top}}}{X_{\text{bottom}}} \left(1 - a_1 \exp\left(-a_3 \frac{|E_{\text{top}} - E_{\text{bottom}}|}{E_{\text{hole}}}\right)\right) & \text{for } X_{\text{top}} < X_{\text{bottom}} \\ \left(1 - a_1 \exp\left(-a_3 \frac{|E_{\text{top}} - E_{\text{bottom}}|}{E_{\text{hole}}}\right)\right) & \text{for } X_{\text{top}} > X_{\text{bottom}}. \end{cases} \tag{6.34}$$

As shown in Figure 6.9b this modification of $X^{+}_{\text{sec.}}$ improves the fit significantly and good agreement between the measured data and the parameterisation is achieved.

All in all, in this section a parameterisation of single GEM parameters was found, which describes the measured data very well. As mentioned before, this parameterisation can be used to calculate GEM stack parameters for arbitrary GEM stack settings, which allows to chose GEM stack settings corresponding to the needs of the experiment and predict the effective gain and the ion feedback ratio. This is illustrated in Table 6.5, where the parameters for the settings used in the measurements are given. The uncertainties in this table are calculated using the difference between two different parameter sets of the parameterisation, which are given in Table A.2. The two parameters set are calculated using the high gain setting and the low gain setting measurement results. The large uncertainties of IFR/$G_{\text{eff.}}$ and IFR in Table A.2 mainly results from the difference in the extraction efficiency of primary ions between the considered measurements, which can be seen in Figure 6.8e.

Table 6.5: Calculated GEM stack parameters and absolute uncertainties using the parameterisation of the single GEM parameters.

Settings	$G_{\text{eff.}}$	$\Delta G_{\text{eff.}}$	IFR/$G_{\text{eff.}}$	Δ(IFR/$G_{\text{eff.}}$)	IFR	ΔIFR
high gain	35289	6792	0.07	0.07	2499	2291
low gain	2088	428	0.08	0.07	172	137
IBF	435	108	0.04	0.04	18	15

The results presented in Table A.2 show that the ion feedback ratio of the IBF settings is much reduced compared to the other two considered settings. Therefore, the chosen parameters of this setting are well suited for limiting IFR. A second estimation of the effective gain and the ion feedback ration will be given based on simulation at the end of this chapter.

6.3.4 Determination of the penning rate for T2K gas

The Penning rate characterises the Penning effect introduced in Section 3.3.5 and is an input parameter to Garfield++ simulations. So far no measurements of the Penning effect in T2K have been done. With the measurements presented Section 6.3.2 it is possible to calculate the Penning rate as shown in the following. This allows to do proper simulations with T2K gas and the parameter calculated here is used for all simulations presented in this work. In particular it is used in Section 6.5, where simulations of the setup used in this chapter are presented.

First the measured single GEM gain is parametrised with an exponential function according to Equation 3.17:

$$G(U_{\text{GEM}}) = \alpha_1 \exp\left(\beta_1 U_{\text{GEM}}\right). \tag{6.35}$$

Here the parameterisation is done with respect to U_{GEM} instead of E_{hole} as done in Equation 6.24, which is possible since here the field above and below the GEMs is fixed and therefore $E_{\text{hole}} \sim U_{\text{GEM}}$ (see Equation 6.16). Figure 6.10a shows the measured single GEM gain in dependence on the GEM voltage and the result of the fit, where the default settings (see Figure 6.6) with $U_{\text{GEM}} = 260\,\text{V}$ were considered. The fit parameters are as follows: $\alpha_1 = 0.0329$, $\beta_1 = 0.0297\,\text{V}^{-1}$. Similar to the parameterisation of the gain in measurements in dependence of the GEM voltage, also the gain in simulation can be parametrised with respect to the penning rate:

$$G(r_{\text{Penning}}) = \alpha_2 \exp(\beta_2 r_{\text{Penning}}). \tag{6.36}$$

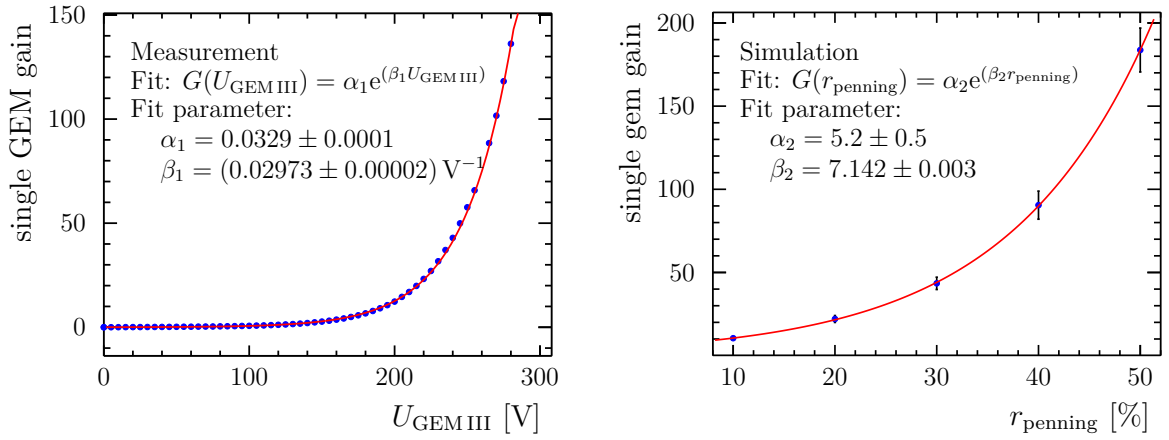

(a) Single GEM gain as a function of the GEM voltage obtained from measurements using the default settings and $U_{\mathrm{GEM}} = 260\,\mathrm{V}$.

(b) Simulated single GEM gain as a function of the penning rate. Settings in the simulation correspond to the default settings with $U_{\mathrm{GEM}} = 240\,\mathrm{V}$.

Figure 6.10: Measured and simulated single GEM gain for T2K gas.

The result of the fit ($\alpha_2 = 5.19$, $\beta_2 = 7.13$) using this parameterisation is shown in Figure 6.10b, where the gain in dependence on the Penning rate for a GARFIELD++ simulation is shown. In the simulations the gain is calculated as the mean number of electrons produced from one electron entering the GEM. The settings considered in the simulation correspond to the default settings using $U_{\mathrm{GEM}} = 240\,\mathrm{V}$. Finally, the parameterisation of the measurements ($G_{\mathrm{meas.}}(U_{\mathrm{GEM}})$) can be used to match the conditions considered in the simulation and calculate the Penning rate:

$$\begin{aligned} G_{\mathrm{meas.}}\left(U_{\mathrm{GEM}} = 240\,\mathrm{V}\right) &\stackrel{!}{=} G\left(r_{\mathrm{Penning}}^{\mathrm{T2K}}\right) \\ r_{\mathrm{Penning}}^{\mathrm{T2K}} &= \frac{1}{\beta_2}\left(\ln\left(\frac{\alpha_1}{\alpha_2}\right) + \beta_1 240\,\mathrm{V}\right) \\ r_{\mathrm{Penning}}^{\mathrm{T2K}} &= (29.1 \pm 1.4)\,\% \end{aligned} \tag{6.37}$$

6.4 Results with a modified GEM

In this section the idea of further reducing the ion feedback ratio, by replacing the top standard CERN GEM in the stack with a modified GEM, is studied. The modified GEM has a similar geometry as standard CERN GEMs, but the hole diameter is increased from $\varnothing = 70\,\mu\mathrm{m}$ to $\varnothing = 100\,\mu\mathrm{m}$. One effect of the increased hole diameter is a reduction of the hole field and therefore a reduction of the gain, which was shown in Section 6.1.2 and

can be seen in Figure 6.4. Furthermore, the optical transparency of the GEM is increased, which can be calculated using Equation 6.15:

$$\tau_{\text{opt.}}(\varnothing = 70\,\mu\text{m}) = 11\,\% \tag{6.38}$$

$$\tau_{\text{opt.}}(\varnothing = 100\,\mu\text{m}) = 24\,\%, \tag{6.39}$$

where the quoted hole diameter corresponds the outer hole radius R (see Figure 5.2a), but for the calculation of the transparency the inner hole radius r is considered. The effect of this increase of the optical transparency in combination with a reduction of the gain will be studied by investigating the GEM stack parameters as well as the single GEM parameters, as done before for the stack of three standard CERN GEMs.

One general remark about the measurements presented in this section is, that discharges were observed and in consequence the system was not as stable as in the case of using three standard CERN GEMs. In particular in case of the IBF settings, where the GEM voltage for the modified GEM is quite high ($U_{\text{GEM}} = 290\,\text{V}$) about 5 non-destructive discharges were observed in total.

6.4.1 GEM stack parameter

First of all the GEM stack parameters as discussed in Section 6.3.1 are investigated. Figure 6.11 shows the result of the effective gain and the ratio between the cathode and anode current. In two regions some data points for the high gain settings are missing, which can be explained with the CUMOs. In this regions a transition between two ranges of one CUMO appeared, which caused a change of the range within the single measurements taken for one data point. If this happens no data are recorded by the XTC software since it requires a stable range for all 100 measurements at a certain working point. In comparison to the results for a stack of three standard CERN GEMs shown in Figure 6.7 it can be seen that the effective gain is increased except for the IBF settings. Furthermore in case of all settings the ratio IFR/$G_{\text{eff.}}$ is reduced, which indicates a general reduction of the number of ions reaching the sensitive volume of the TPC. The result the GEM stack parameters for the nominal induction field is summarised in Table 6.6. The relative change of the ion feedback ratio for the different settings is similar to the results presented in Table 6.4. Again the absolute ion feedback ratio can only be estimated with results of the simulation presented in the following section. The absolute values will also allow to compare the results observed here with the results of the measurements using the stack of three standard CERN GEMs.

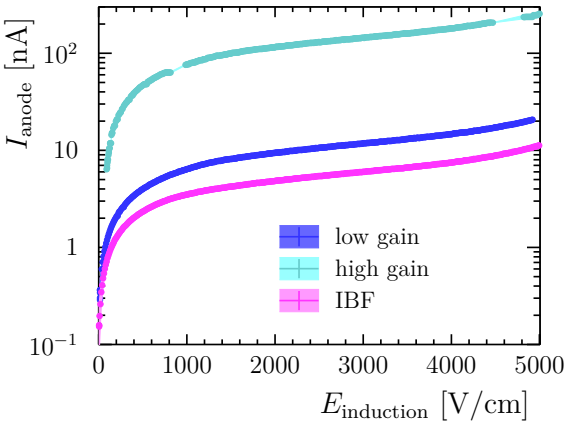

(a) Current measured on the anode as a function of the induction field.

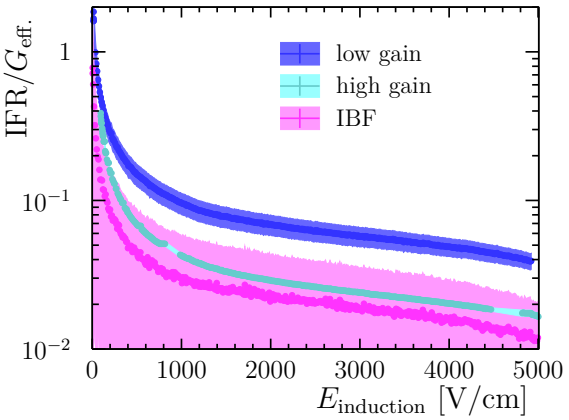

(b) Ratio between the current measured on the cathode and the anode ($I_{\text{cathode}}/I_{\text{anode}}$), which is similar to IFR/$G_{\text{eff.}}$.

Figure 6.11: Comparison between different settings of the GEM stack. The error band shows systematic uncertainties connected to the CUMOs and the error bars represent statistic uncertainties. Results are shown for T2K gas and a stack of two standard CERN GEMs with one GEM with an increased hole diameter of $\varnothing = 100\,\mu\text{m}$ on top.

Table 6.6: Summary of the measurements with a stack of two standard CERN GEMs and one GEM with an increased hole diameter of $\varnothing = 100\,\mu\text{m}$ on top.

setting	I_{anode} [nA]	$\delta_{\text{sys.}}$ [%]	$\delta_{\text{stat.}}$ [%]	IFR/$G_{\text{eff.}}$	$\delta_{\text{sys.}}$ [%]	$\delta_{\text{stat.}}$ [%]	IFR/IFR(high gain)
low gain	11.81	0.85	0.06	0.06	14.87	0.30	1
high gain	144.50	0.69	0.11	0.02	2.97	0.13	0.25
IBF	8.83	1.13	0.07	0.01	81.28	1.76	0.03

In principle one could also try to do a relative comparison of the ion feedback ratio between the different setups, as done for the different settings, but this assumes equal conditions in the measurements. Otherwise the current on the anode cannot be directly compared. For the measurements presented here one cannot assume equal conditions and thus the relative comparison between the setups is not done here. Nevertheless the a reduction of IFR using the modified GEM on top of the GEM stack can be shown with the help of the single GEM parameters, which are discussed in the following.

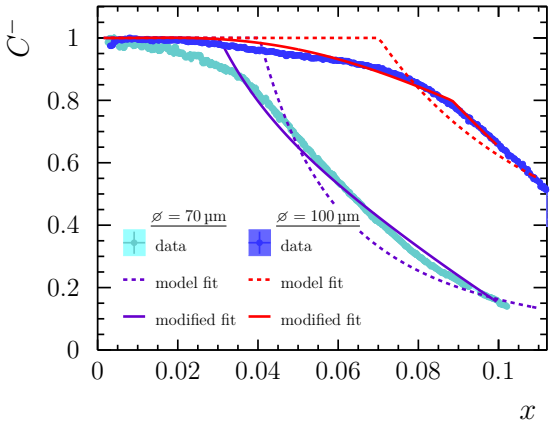

(a) Electron collection efficiency.

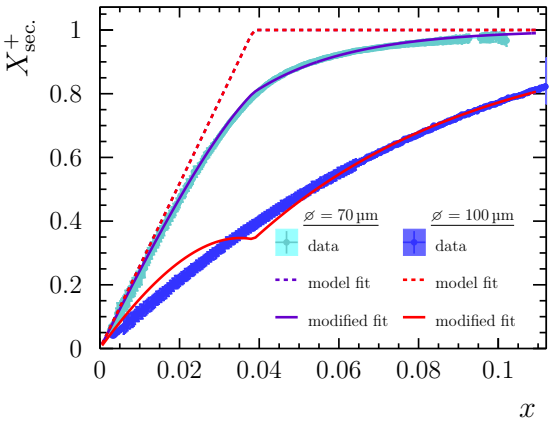

(b) Secondary ion extraction efficiency. The model fits are equal and only one is visible.

Figure 6.12: Comparison of transfer coefficients between standard CERN GEMs (70 µm) and GEMs with an increased hole size (100 µm) in T2K gas and for the high gain settings. The error band shows systematic uncertainties connected to the CUMOs and the error bars represent statistic uncertainties.

6.4.2 Single GEM parameter

All measurements of GEM parameters as presented in Section 6.3.2 were repeated and the results can be found in the appendix (Figure A.2). Since all measurements correspond to single GEM properties most of the measurements lead to similar results as shown in the previous section. Only measurements which are done with respect to GEM I are effected by the GEM exchange. Therefore, only the results of these measurements are shown here in Figure 6.12, where also the results from the previous section are included to allow a direct comparison. It can be seen that the electron collection efficiency is increased with larger GEM holes. This can be attributed to the increased hole size. In the case of the measurements with the 70 µm the limit of the optical transparency ($\tau_{\text{opt.}} = 11\,\%$) is almost reached at the maximum field ratio of $x = 0.1$ used in the measurements. For the setup which includes the modified GEM the corresponding limit is reached at higher values of x. Since the maximum drift field in the field scan is the same for both setups Figure 6.12a also illustrates that the field inside the GEM hole is smaller for larger hole sizes and therefore larger values of x ($x > 0.1$ in Figure 6.12a) are reached in this case.

In addition, Figure 6.12b shows that the extraction efficiency of secondary ions is reduced by using the GEM with larger holes as GEM I in the stack. In sum the higher values of C^- and the reduction of $X^+_{\text{sec.}}$ leads to a reduced number of ions reaching the sensitive volume

of the TPC compared to the stack of three standard CERN GEMs. This effect is most significant for high values of x. Taking usual values of the drift field and GEM voltages into account, which correspond to $x \approx 0.006$, the electron collection for both GEMs is equal and almost one. Only the $X^+_{\text{sec.}}$ is reduced by a factor of two, which results in the end in a reduced number of ions reaching the sensitive volume of the TPC.

In Figure 6.12 also the results of the parameterisation using the electrostatic model (dashed lines) and the modified parameterisations introduced in Section 6.3.3 (solid lines) are shown. In the case of C^- the modified parameterisation describes the measured data well, whereas in the case of $X^+_{\text{sec.}}$ also the modified parameterisation fails to describe the measured data over the full range of x.

In general, the GEM with the increased hole size does not need to contribute to the amplification in the GEM stack when used as an ion gating device. Therefore, one can use higher values of x for this GEM by decreasing the GEM voltage, which also reduces the probability of discharges and results in a stable operation of the GEM stack. In this case such a GEM would be placed on top of a stack of three GEMs, which are used to achieve a sufficient effective gain. For example at $U_{\text{GEM}} = 100\,\text{V}$ the field ratio is $x = 0.017$. At this point the electron collection efficiency is still close to one but the extraction efficiency for secondary ions is only 23 % compared to 41 % in case of a GEM with $\varnothing = 70\,\mu\text{m}$ holes.

6.5 Comparison of the measurements with simulation results

In the following the results of simulations of the setup will be presented. The simulations are done as introduced in Chapter 5, using three individual field simulations – one for each GEM in the stack – which are combined in the Garfield++ simulation using constant fields.

For each working point 10000 events are simulated, where one electron is released above the GEM stack in the drift region. As introduced in Chapter 5 the resulting end points of electrons and ions produced in the simulation are analysed in order to calculate GEM stack parameter as well as single GEM parameter, which are discussed in the following.

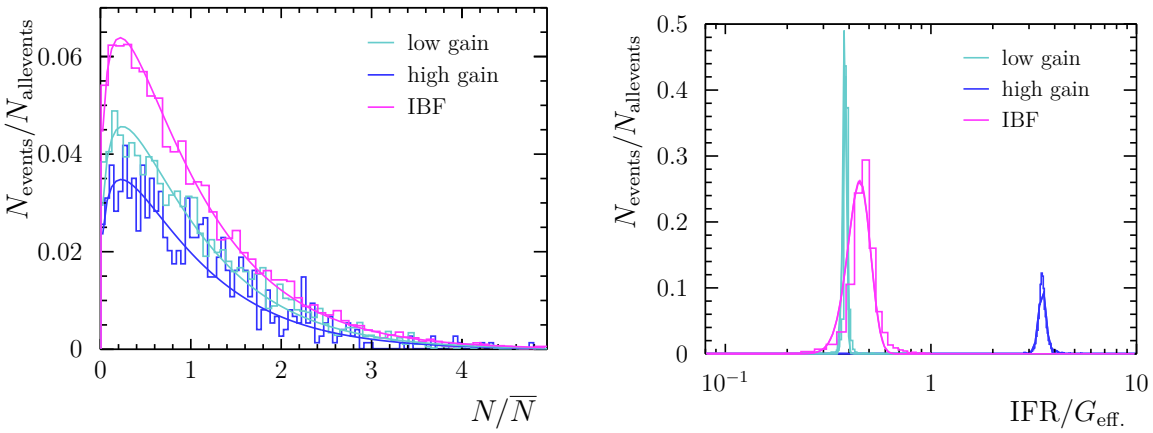

(a) Simulated gain and fits using a Polya function.

(b) Calculated ratio between electrons on the anode and ions leaving the GEM stack.

Figure 6.13: GEM stack parameter resulting from a triple GEM stack simulation for different settings.

6.5.1 GEM stack parameter

The calculation of the GEM stack parameters in the simulation is straight forward. The effective gain is given by the number of electrons reaching the bottom boundary of the simulation and the ratio $\text{IFR}/G_{\text{eff.}}$, as calculated from the measurements, is given by the number of ions reaching the top boundary of the simulation. Since, in contrast to the measurements, both quantities are known also the ion feedback can be calculated using the effective gain. Figure 6.13 shows the resulting distributions for $G_{\text{eff.}}$ and $\text{IFR}/G_{\text{eff.}}$ for the different settings used in the measurements and a stack of three standard CERN GEMs. The shown distributions are normalised to the total number of simulated events. In addition, the distributions are fitted in order to calculate a mean value. The fit function used for the effective gain distribution is a Polya distribution defined as:

$$f(N,b) = A\frac{b^b}{\Gamma(b)}\frac{1}{\overline{N}}\left(\frac{N}{\overline{N}}\right)^{b-1}\exp\left(-\frac{bN}{\overline{N}}\right), \tag{6.40}$$

where N is the number of electrons produced in the amplification process. The Polya function is characterised by the dimensionless parameter $1/b$, which is the relative variance of the distribution $\sigma^2_{\text{rel.}} = \sigma^2/\overline{N}^2$, and the parameter $\overline{N}$, which is identified as the mean number of electrons produced. This function is a common distribution used to describe gain distributions in strong non-uniform fields [30, 37]. As shown in Figure 6.13a the Polya distribution describes the simulated effective gain distribution very well. Since

Table 6.7: Simulated GEM stack parameters for the three settings considered in the measurements. The $\mathrm{IFR}_{\mathrm{data}}$ values are calculated using $\mathrm{IFR}/G_{\mathrm{eff.}}$ from the measurements and $G_{\mathrm{eff.}}$ from the simulation.

Settings	$\varnothing_{\mathrm{hole}}$	$G_{\mathrm{eff.}}$	$\sigma_{\mathrm{rel.}}$	$\mathrm{IFR}/G_{\mathrm{eff.}}$	$\sigma_{\mathrm{stat.}}$	$\mathrm{IFR}_{\mathrm{simulation}}$	$\mathrm{IFR}_{\mathrm{data}}$
high gain	70 µm	17203	0.77	0.380	0.007	6537	516
	100 µm	3193	0.79	0.92	0.03	2906	63
low gain	70 µm	919	0.76	3.49	0.146	3207	74
	100 µm	664	0.75	0.44	0.04	292	40
IBF	70 µm	524	0.78	0.451	0.057	236	10
	100 µm	361	0.82	0.44	0.06	159	4

in the simulation only one initial electron is used the number of electrons produced in the amplification N is equal to the effective gain measured in simulation for one event. Therefore, $\overline{N}$ can be identified as $G_{\mathrm{eff.}}$. Furthermore, the distributions of $\mathrm{IFR}/G_{\mathrm{eff.}}$ are fitted using a Gaussian distribution as shown in Figure 6.13b.

The results of the fits are given in Table 6.7 for all settings used in the measurements as well as for both setups – a stack of three standard CERN GEMs ($\varnothing = 70\,\mu\mathrm{m}$) and a stack of two standard CERN GEMs with a modified GEM ($\varnothing = 100\,\mu\mathrm{m}$) on top. The statistic uncertainty $\sigma_{\mathrm{stat.}}$ given for $\mathrm{IFR}/G_{\mathrm{eff.}}$ corresponds to the standard deviation of the Gaussian distribution used to fit the simulation data.

First of all the results corresponding to the stack of three standard CERN GEMs are discussed in the following. It can be seen that the effective gain of the high gain settings is a factor of 19 higher than the effective gain of the low gain settings. Furthermore, the effective gain is reduced by a factor of two in the case of the IBF settings compared to the low gain settings, whereas in the measurements the gain of the IBF settings was slightly higher compared to the low gain settings. The highest value of $\mathrm{IFR}/G_{\mathrm{eff.}}$ is found for the low gain settings followed by the high gain settings and the IBF settings. This is in agreement with the measurements, but the absolute values observed in the simulation are much higher than in the measurements. Consequently, the calculated values of the ion feedback ratio are much higher for the simulated data compared to the measured data. Comparing both setups, the general trend that $G_{\mathrm{eff.}}$ as well as $\mathrm{IFR}/G_{\mathrm{eff.}}$ is reduced by introducing the modified GEM observed in measured data can be reproduced by the simulation.

At this point the relative differences of $G_{\mathrm{eff.}}$ and $\mathrm{IFR}/G_{\mathrm{eff.}}$ resulting from the simulation comparing different settings and the two setups are in a reasonable agreement with the measurements, whereas the absolute values of $\mathrm{IFR}/G_{\mathrm{eff.}}$ are much higher in the simulation

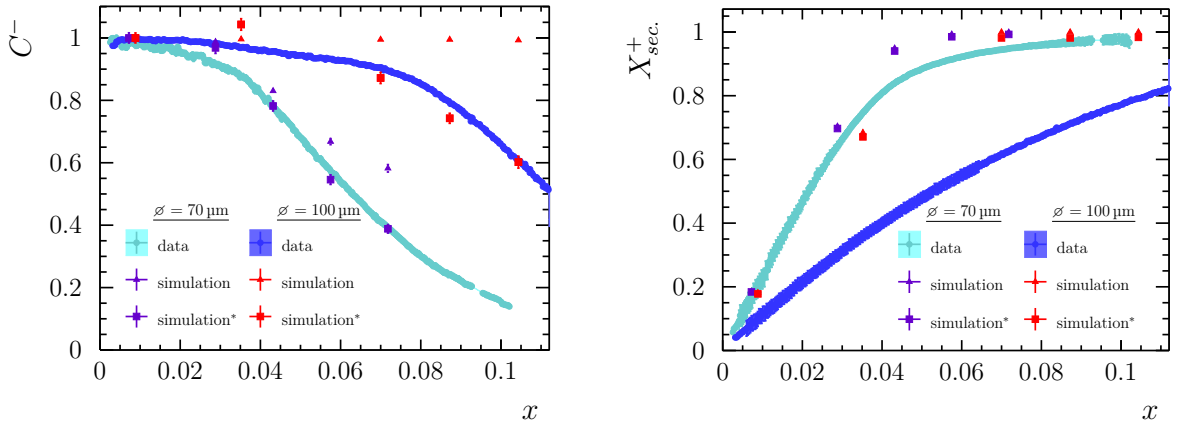

(a) Measured and simulated electron collection efficiency.

(b) Measured and simulated extraction efficiency for secondary ions.

Figure 6.14: Comparison between data and simulation for standard CERN GEMs (70 µm) and GEMs with an increased hole size (100 µm) in T2K gas for the high gain settings. The simulation results labelled with a star correspond to the transfer coefficient definitions based on currents.

compared to the measurements. This indicates that at least the description of ions in the simulations cannot reproduce the measurements. A better understanding of this effect will be gained in the investigation of the single GEM parameters.

6.5.2 Single GEM parameter

In the following simulation results for the two single GEM parameters presented in Section 6.4 are discussed, which are the electron collection efficiency and the extraction efficiency for secondary ions. These parameters are chosen for the comparison because they are different for both investigated setups and thus two different data sets can be compared to the simulation.

The measured data and the results from the simulation are shown in Figure 6.14. Here for each setup two corresponding simulation results are shown. First, the simulation results, labelled simulation in Figure 6.14, are obtained using the definitions given in Equations 6.1 and 6.3, which are based on the fundamental definitions of the transfer coefficients. In order to calculate the parameters based on these definitions the decision if an electron/ion is collected to a GEM hole or extracted from a GEM hole needs to be made. This is done based on the spacial requirements. For example if a an electron is collected into a GEM hole is decided based on the electron start and end point, namely the start point of the electron has to be above the GEM cathode surface and the electron end point has to be

below the GEM cathode surface. The simulation results based on these definitions do not agree with the measured data as can be seen in Figure 6.14a as well as in Figure 6.14b. In particular in case of the electron collection efficiency the difference between the simulation results and the measurements rise with increasing x.

This can be understood with the second definition used in the simulation, which is labelled simulation* in Figure 6.14. Here the definitions of the transfer coefficients given in Equations 6.23 and 6.29 are used, which are based on the currents measured in the experiment. In order to calculate currents in the simulation, the sum of all ions and electrons ending on a certain electrode are counted. As already discussed in Section 6.3.3 the measurement of the electron collection efficiency is sensitive to the amount of attachment. In detail it depends on the amount of attachment in the drift region since it is normalised to the measured currents at low x where no attachment in the drift region occurs. Since the attachment probability depends on the drift distance, it has to be modelled according to the experiment in order to reproduce the measured data. This means the start position of the electrons in the drift region needs to be modelled according to the conditions in the experiment.

In the measurements the Fe^{55} radiated photons, which reach the drift volume where electrons are produced if a photon conversion takes place. Therefore, the start positions of the electron depend on the conversion points in the drift region. As shown in Section 3.2 the conversion is characterised by the attenuation coefficient μ. A detailed calculation of the conversion probability is given in Appendix A.1, where the probability density function for the setup used here is calculated. This function is used to generate start positions in the drift region. Figure 6.14a shows that the data can be reproduced in the simulation very well using the calculated probability density function. Therefore, the difference between both simulations of the electron collection efficiency shown in Appendix A.1 is the different definition this quantity. This shows that the current based single GEM definitions used in the measurements are influenced by attachment and do not reflect the true electron collection efficiency. Using the simulation presented here it is possible to calculate the true electron collection efficiency from the measured one by taking the attachment into account.

In case of the extraction efficiency for secondary ions both definition used in the simulation lead to the same results, which is expected since the current based definition of $X^{+}_{\text{sec.}}$ is not affected by attachment. Moreover, the simulation fails to describe the data, which indicates that the description of ions in the simulation is not sufficient to describe the measured data.

This is in agreement with the results of the GEM stack parameters, where it was found that $\mathrm{IFR}/G_{\mathrm{eff.}}$ is much higher than in the measurements. One reason for the difference between simulation and experiment for parameters connected to ions, could be a wrong description of the macroscopic parameters characterising the ions in the simulation. The parameters used in the simulation correspond to a description of argon ions drifting in argon, which should be in principle a reasonable assumption since the drift gas T2K consists of 95 % argon. Obviously it is not sufficient to do the simulation of argon ions drifting in argon to reproduce the measured data. Therefore, in order to understand the behaviour of the ions in the setup better a detailed study of the ion drift in T2K is need, which is beyond the scope of this thesis.

6.6 Discussion of the results

In this chapter measurements with a stack of three GEMs have been presented. The measurements are used to understand the characteristics of the amplification with three GEM and to investigate the potential of using a GEM to prevent ions produced in the amplification from penetrating the sensitive volume of the TPC. The latter effect is characterised by the ion feedback ratio (IFR), which gives the number of ions reaching the sensitive volume per electron amplified in the GEM stack. A reduction of the ion feedback ratio allows to limit the field distortions in the ILD TPC induced by these ions.

The ion feedback ratio could not be directly measured with the setup used here, but the ratio between the number of ions penetrating the sensitive volume of the TPC and the number of electrons produced in the amplification could be measured ($\mathrm{IFR}/G_{\mathrm{eff.}}$). In a comparison between settings with a similar gain it was shown, that by choosing proper settings of the GEM stack voltages and fields this ratio can be reduced from $\mathrm{IFR}/G_{\mathrm{eff.}} = 0.08$ to about $\mathrm{IFR}/G_{\mathrm{eff.}} = 0.02$. Furthermore, it was observed that the calculated single GEM parameter depend on the GEM stack settings. An electrostatic model of the single GEM parameter presented in Ref. [76], did not predict this dependence on the GEM stack settings. It could be shown that this is because some effects are not covered by this model. In particular it was found that the attachment of electrons in the gas needs to be included to describe the measured data. Using this information the parameterisation given by the model was adopted and the parameters were determined using the measured data. The obtained parameterisation allows to calculate GEM stack characteristics from the given settings. This includes an estimation of the effective gain and the ion feedback ratio. Therefore,

this information serves as input to optimisations of GEM stack settings. Furthermore, the parameterisation can be used to calculate GEM stack parameters in simulations were no detailed description of the amplification process is required. The calculation of IFR based on the parameterisation showed that with the optimised GEM stack settings a value of IFR = (18 ± 15) could be reached in the measurements.

In a second step one GEM in the GEM stack was replaced by a modified GEM with larger holes. The idea was to investigate the characteristics of this GEM and to test if such a GEM can be used to further reduce the ion feedback ratio of the GEM stack. It could be shown that the electron transparency of the modified GEM is larger and the extraction efficiency of ions is lower compared to the standard GEMs. This reduced the ratio IFR/$G_{\text{eff.}}$ by a factor of two to IFR/$G_{\text{eff.}} = 0.01$. In addition, the parameterisation of the GEM parameter indicate, that if such a GEM is operated at lower voltages it reduces the number of ions reaching the sensitive volume of the TPC even further while being transparent for electrons. One drawback of the modified GEM observed in the measurements is, that more discharges compared to standard GEM happened. This fact also supports to operate such a GEM at low voltages, resulting in a low amplification. This could be recovered by adding another standard GEM to the stack, which means the modified GEM would be exclusively be used to stop ions.

Finally, a detailed simulation of the GEM stack was done. It turned out that the description of electrons agrees well with the measurements, but the results obtained for ions could not reproduce the measured data. This shows that the description of ions used in the simulation, where it is assumed that argon ions drift in pure argon, is not sufficient to describe the situation in the drift gas used in the measurements. This implies that in order to be able to simulate also the correct ion behaviour, the ion drift in the gas used here needs to be understand better, which was not part of this work. Finally, the results obtained for electrons could be used to estimate the ion feedback ratio based on the measurements of IFR/$G_{\text{eff.}}$ and the simulated values of $G_{\text{eff.}}$. It was found that a minimal value of IFR = 10 can be reached when operating a stack of three standard GEM and optimising the GEM settings, which is in good agreement with the estimated ion feedback ration obtained from the parameterisation of the single GEM parameters. The ion feedback ratio could further be reduced to IFR = 4 by using the modified GEM in the stack. The latter value is not as low as it is needed for the ILD TPC (IFR = 1), but it shows a way how to reduce IFR. In order to finally reach IFR=1 one could again change the GEM geometry or test the setup described above, where the modified GEM is operated at a low voltage above a GEM stack of three standard GEM that guarantee a sufficient gain.

7

Studies of field distortions for the ILD TPC with the LPTPC

In this chapter static field distortions in the LPTPC are discussed. In this context static means, that they don't change during a measurement run with a length in the order of $\mathcal{O}(10\,\text{min})$. Such field distortions can emerge from imperfections of the LPTPC geometry or they can be introduced by the readout modules installed in the LPTPC anode. In addition, the magnetic field inside the sensitive volume of the TPC can have inhomogeneities. Non static field distortions emerge for example from ion discs drifting through the sensitive volume of the TPC as introduced in Section 2.4.4 and investigated in the previous chapter.

The understanding of the field distortions discussed in this chapter will help to estimate their effect on the ILD TPC performance and in particular on the momentum resolution. As discussed in the beginning one would like to correct for distortions introduced by field inhomogeneities at a level of 30 µm, which would allow to keep the degradation of the momentum resolution below 5 %.

Two different kinds of static field distortions will be discussed in this chapter. Firstly, field distortions introduced by readout modules installed in the LPTPC are investigated. It will be shown that such distortions are only relevant in the vicinity of readout modules and extend a few millimetres into the sensitive volume of the TPC. In the following, they are referred to as local field distortions. The study of local field distortions, presented in Section 7.2, covers finite element based simulations of different kinds of readout modules

and estimates of their effect on the module performance. In addition, an optimisation of the GEM based readout module developed at DESY is done, which results in a reduction of the local field distortions introduced by this module.

In Section 7.3 the overall field distortions in the LPTPC are investigated. This is done by creating a signal on the TPC cathode at well known positions using a laser. By comparing the position reconstructed on the anode pad plane to the initial position of the signal creation, the integrated distortions over the full drift length of the TPC are measured. Therefore, not only local field distortions effect the measurement, but the measurement is sensitive to field inhomogeneities along the whole drift length and therefore distortions in the whole sensitive volume of the TPC are integrated and detected.

The studies of the overall field distortions in the LPTPC are based on two measurement campaigns at the DESY test beam facility in 2013 and 2014, where MicroMegas and GEM based readout modules were operated in the LPTPC anode. A large magnet available at the DESY test beam facility was used to do measurements with and without a magnetic field of 1 T, which allows to study the effect of electric and magnetic field inhomogeneities. It is know from measurements, that the field of this magnet is not perfectly homogeneous inside the TPC. In order to estimate the distortions introduced by the magnet, a simulation taking into account the known field inhomogeneities of the magnet is presented in Section 7.3.11. The comparison of the simulation results with the measured distortions allows to disentangle the contributions from the magnetic field distortions from other field distortions.

Before the two analyses introduced above are presented, a general introduction to the reconstruction of pad based readout modules is given in the following.

7.1 Reconstruction of pad based readout module data

A typical TPC reconstruction chain takes signals measured on each pad of the anode pad plane as input and results in a fitted track with corresponding track parameters, such as the curvature. The curvature in turn can be used to calculate the momentum of the particle, which corresponds to the reconstructed track. This is illustrated in Figure 7.1a, where the signals on the pads are shown in different colours and the track to be reconstructed is shown by the red line. In terms of this figure the task of the reconstruction is to calculate the track parameters of the red line by using the information of the pad colour, which is

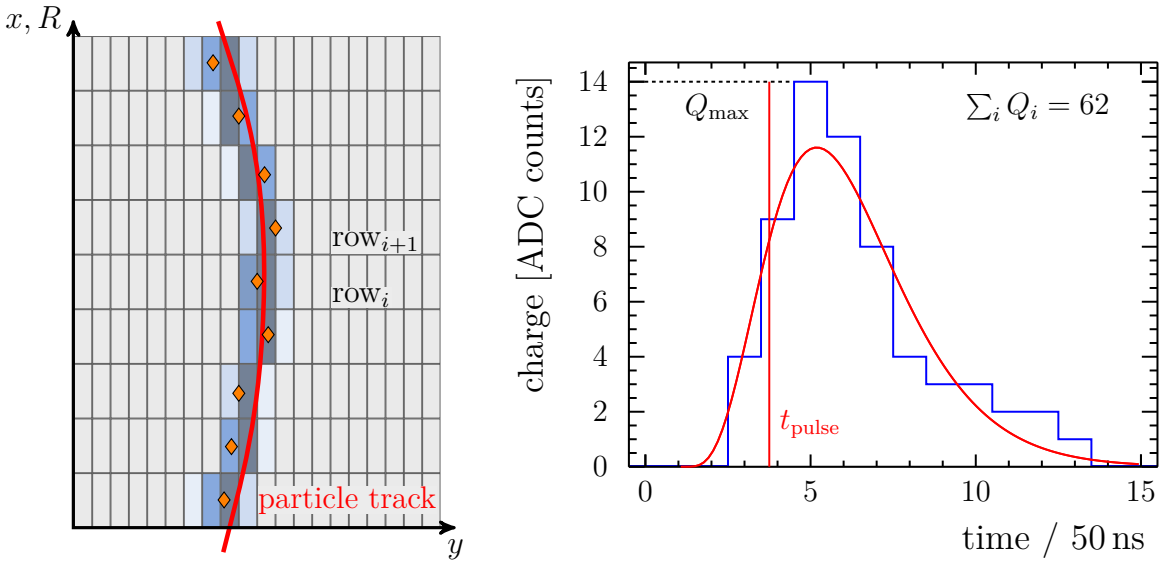

(a) Sketch of the signal on a pad plane produced by a particle track. The pad colour shows the charge collected per pad and the orange marker shows the reconstructed hit position.

(b) Charge measured on a single pad with a DESY GridGEM module in combination with the ALTRO electronics. In addition, the expected pulse shape is fitted to the pulse, which is shown in red. The vertical red line depicts the time estimate obtained via the inflection point.

Figure 7.1: Signal reconstruction using a pad based readout. (a) shows the pad plane, where individual pads collect a certain amount of charge. For one pad the charge distribution as a function of time is shown in (b).

a function of time. The reconstruction is subdivided into different tasks, which will be introduced in the following.

The starting point for the reconstruction is the integrated charge, given in units of ADC counts, measured during one readout cycle of the electronics for each pad of the pad plane. The integration time is fixed by the readout frequency of the electronics. This information of measured charge per time per pad is used in the first step to form so called pulses. A pulse is the measurement of the charge cloud produced in the sensitive volume of the TPC, for example by a charged particle that ionises the TPC gas (primary ionisation), on a certain pad. A point like cluster of electrons drifting in the TPC will form a charge cloud when it arrives at the anode, which is caused by the diffusion in the drift gas (see Section 3.3.2). This cloud is characterised by its width in $R\phi$, which is given by the transverse diffusion, and its width in time, which is given by the longitudinal diffusion. Hence the corresponding pulse is characterised by the pulse charge, which corresponds to the total charge of the charge cloud, and the pulse time, which corresponds to the arrival time of the charge cloud on the anode. How these values are calculated from the measured charge distribution is illustrated in Figure 7.1b, where the measured charge per electronics readout cycle (time

bin) is shown for one pad. First of all, it can be seen that the charge distribution is not a Gaussian distribution. This is because, the signal collected on each pad is amplified and shaped in the electronics. Therefore, the resulting charge distribution is defined by the shaper function and not by the charge cloud. In case of the electronics used for the GEM module the shaper output of the PCA16 is given in Ref. [58]:

$$f\left(B, A, t_0, \tau, k; t\right) = B + A\mathrm{e}^k \left(\frac{t - t_0}{\tau}\right)^k \exp\left(-k\frac{t - t_0}{\tau}\right) \theta\left(t - t_0\right) \tag{7.1}$$

with base line B, amplitude A, starting time t_0, peaking time τ and order k. It is normalised such that A and τ are the coordinates of the peak. For the shaper as it was used during the measurements presented in Section 7.3, the order was fixed to be $k = 4$. This shaper function is used to fit the single pulse shown in Figure 7.1b. It can be seen that the measured pulse shape – the shown pulse is taken from GEM module data presented in Section 7.3 at $E_{\mathrm{drift}} = 240\,\mathrm{V/cm}$ and $B = 0\,\mathrm{T}$ – is in good agreement with the expected pulse shape. The amplitude of each pulse represents the input charge. Therefore, the pulse charge is given by the maximum value of the charge distribution Q_{max}. An alternative method to define the pulse charge is to calculate the integral charge that is measured $Q_{\mathrm{pulse}} = \sum_i Q_i$, as given in Figure 7.1b. This charge estimator has the advantage of still giving a good charge estimate in cases, where the maximum measured charge Q_{max} exceeds the electronics range and no meaningful information on the pulse charge is given by Q_{max}.

Also the pulse time can be defined in two ways. The first possibility is to use the centre of the time bin, which includes the maximum charge Q_{max}, as pulse time estimator. A second way of defining the pulse time is to consider the inflection point of the rising slope of the charge distribution as pulse time. This point is shown in Figure 7.1b by the vertical red line. The definition of the pulse time has the advantage, that it is mostly independent of the pulse height.

Depending on the data quality and the type of data that is analysed – e.g. beam collision data at the ILC or data where only a single track is produced in the TPC – additional requirements are used to define pulses. Such requirements are for example a minimum value of Q_{max} or a maximum length of a pulse measured in time bins.

After the pulse reconstruction, the pulses are further analysed. How they are analysed depends on the data that is analysed. In the case of a physics analysis of ILD TPC data, particles will primarily traverse the TPC from the small R region to the high R region (from inside to outside the TPC), which defines a preferred direction. Along this direction (R) individual measurements of the track are made using the anode pad plane. This is done

by reconstructing the track position per pad row using the reconstructed pulses in this row, which is shown in Figure 7.1a. Here the results of the each measurement – the reconstructed track position on the row – is depicted by the orange markers. This in the end defines independent measurements of the particle track along R, called hits. The total number of measurements is given by the number of rows crossed by the track projection on the anode pad plane. Finally, individual hits are associated to tracks and the track parameters are calculated using these hit information in a track fit. In view of the momentum resolution defined in Equation 2.8, N can be identified as the number of rows and $\sigma_{\mathrm{R}\phi}$ is related to measurement resolution of the hit position.

Another way of analysing the reconstructed pulses needs to be considered if point like signals need to be reconstructed. Such point like signals result from the laser calibration system introduced in Section 7.3, which is used to study the overall field distortions in the TPC. The corresponding reconstruction will be introduced in Section 7.3.7.

7.2 Simulation of local field distortions of different ILD TPC readout modules

The studies of local field distortions introduced by readout modules, are motivated by test beam measurements from July 2011 using a GEM based DESY GridGEM module, which was introduced in Section 4.3.1. Here electrons with a momentum of up to 5 GeV traversed the sensitive volume of the LPTPC, which results in tracks perpendicular to the pad rows of the module. One result of the data analysis is shown in Figure 7.2. Here the number of reconstructed hits per module row is shown. Obviously there are two rows, which collected significant more hits compared to all other rows. This effect is understood and can be explained by pads in these rows that could not be read out. For this reason, the hit finding algorithm reconstructs two hits instead of one in these rows – one hit left to the dead pad and one hit right to the dead pad. Furthermore, comparing the number of hits collected at the borders of the module (row 1-2 and 26-28 respectively) and the central part of the module (row 4-23), it can be seen that the number of reconstructed hits is reduced at the borders. This can be explained by the modular design of the ILD TPC tested with LPTPC, which implies unavoidable gaps between individual modules. These gaps introduce local distortions of the TPC drift field, which reduce the performance of the TPC as shown for the number of reconstructed hits.

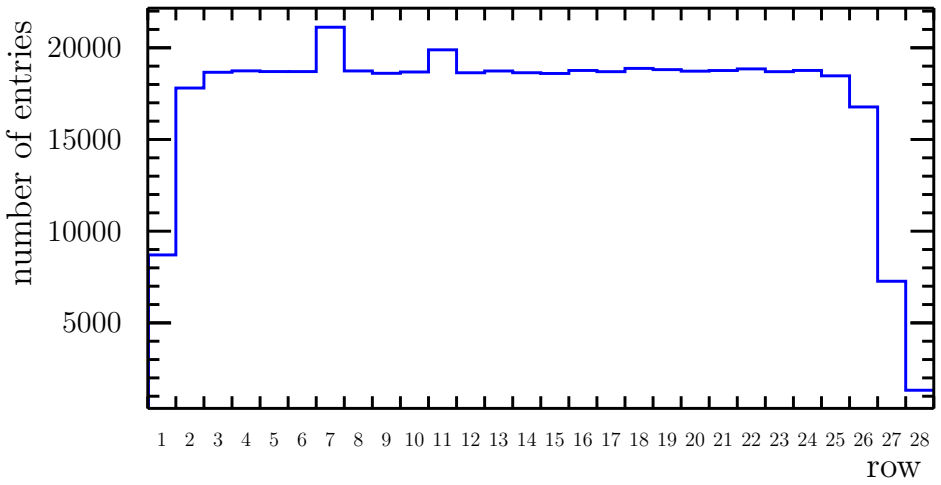

Figure 7.2: Test beam result from July 2011 showing a decreased number of reconstructed hits per row at the border of the readout module. This measurement was taken without a magnetic field with a DESY GridGEM module.

In more detail, Figure 7.2 shows that on the upper part of the module (rows 26-28) three rows are affected, whereas at the bottom only two rows (rows 1-2) are affected. One reason for this is that on the upper part of the module the high voltage is routed to the GEMs, which introduces additional field distortions. In addition, the gap between the module and the neighbouring dummy module is larger on the top (2 mm) compared the gap at the bottom (1 mm). A larger gap introduces larger field distortions. The reason for the different gap size is the design of LPTPC anode and the use of a single module size. In the ILD TPC the module size will change with radius and a constant gap of about 1 mm between modules will be realised.

Since the modular readout is fundamental to the ILD TPC design, the problem of field distortions between individual modules is a general issue and not only restricted to the DESY GridGEM module. Therefore, the understanding of the local field distortions introduced by module gaps is essential for the readout module performance optimisation. In order to study such field distortions and to confirm the proposed explanation of the observed effects the following analysis is done.

First of all, the actual field distortions introduced by readout modules are studied in Section 7.2.1. In order to do so, an electrostatic field simulation using the simulation frame work introduced in Chapter 5 is used. Effects on the module performance are evaluated using Garfield++ based simulations in Section 7.2.2. The analysis of the simulated field distortions considered in this section is derived from the analysis of measured data

and results in a direct prediction of the number of electrons per row as shown for the measurements in Figure 7.2. Furthermore, the DESY GridGEM module is optimised using the results of the simulations. The resulting module performance of the optimised module was measured in a test beam campaign in 2013 and is shown in Section 7.2.3. Finally, an alternative method to evaluate local field distortions is introduced in Section 7.2.4. It is based on data taken with the Asian GEM module in combination with a laser, that created tracks at different angles. This allows to analyse local field distortions by exploiting angle dependent effects.

7.2.1 Electrostatic simulations of readout modules

As discussed in the previous section, the reduced readout module performance at the boundaries of the module is expected to result from field distortions between modules. In order to concentrate on understanding the distortions due to the geometry of readout modules and the distance between modules the most simple gap between two modules in the LPTPC is chosen to be simulated. It is the boundary between a readout module and a Dummy module at the bottom of the readout module. Thus, effects of the HV routing on top of the module, which might influence the performance of the readout module, are omitted here. Furthermore, at the bottom of the module the gap size is similar to the gap size between ILD TPC readout modules, which allows to estimate the expected distortions between ILD TPC modules.

The simulation model deals with a small cut-out of the region where the dummy module borders the readout module (see light blue box in Figure 7.3b). Both, the dummy module and the DESY GridGEM module, are modelled corresponding to the description given in Sections 4.2 and 4.3.3. Each module is modelled up to a distance of 74.5 mm from the gap between both modules in x direction. The gap itself has a width of 1 mm. In front of the module surfaces a drift volume with a height of 25 mm is modelled in z direction, which fixes the maximum drift length. A side view of the model is shown in Figure 7.3a. Here the dummy module is shown on the left-hand side as green and grey block and the DESY GridGEM module is shown on the right-hand side. The bottom part of both modules shown as grey blocks correspond to the anode surface of the modules. The potentials considered in the simulation are summarised in Table 7.1. Here V_{boundary} is the potential applied at the simulation boundary that closes the drift volume.

The result of the field simulation with CST™ is shown in Figure 7.4. Here the electric field components in drift direction (E_z, Figure 7.4b) and transverse to the drift direction

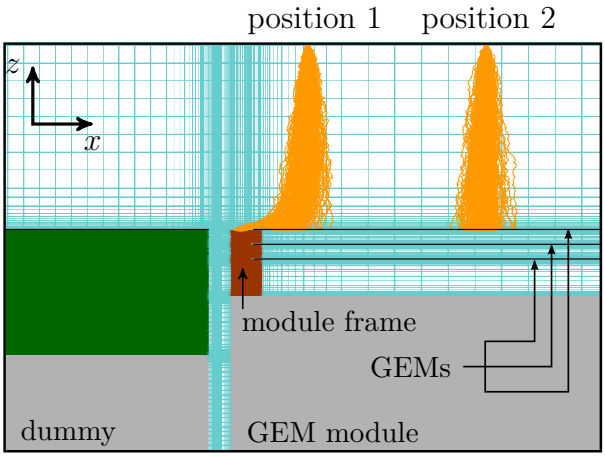

(a) Simulation model of the gap between a DESY GridGEM module and a Dummy module with electron paths shown in orange.

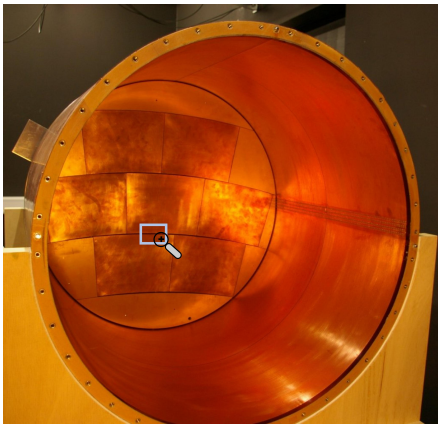

(b) LPTPC field cage, where the cathode is removed. This allows to see the 7 dummy modules installed on the anode side.

Figure 7.3: The gap between a DESY GridGEM module and a Dummy module shown in the simulation model in (a) can be seen in (b) in the case of a gap between two Dummy modules in the LPTPC end plate. The corresponding part is depicted by the light blue box.

Table 7.1: Potentials applied in the simulation.

volume	potential			
anode surface		0 V		
GEM III	cathode:	-1150 V	anode:	-900 V
GEM II	cathode:	-1700 V	anode:	-1450 V
GEM I	cathode:	-2250 V	anode:	-2000 V
dummy		-2250 V		
V_{boundary}		-2800 V		

(E_x, Figure 7.4a) are shown. In an ideal case the latter one should always be zero, but the observed field component is non zero in the region above the module. This is caused by the ground potential on anode, which is unshielded from the drift region due to the gap. In consequence a high transverse field component E_x is observed at the module boundary. Close to the boundary it even exceeds the strength of the drift field ($E_z = 220\,\text{V/cm}$). The range of this distortion of the drift field is limited to about 5 mm in z direction, which shows that the field distortions introduced by the gap effect only a small volume in the vicinity of the module gap. The reach of the distortions in x direction are discussed in following analysis.

The consequence of the transverse field component in terms of the module performance is,

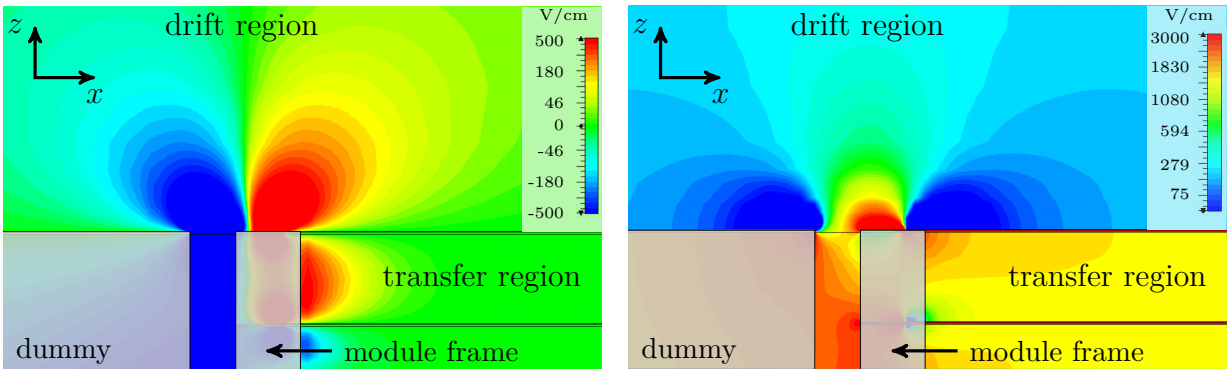

(a) Electric field component transverse to the drift direction (E_x).

(b) Electric field component in drift direction (E_z).

Figure 7.4: Simulation of the electric field for the DESY GridGEM module. Horizontal lines on the right side of both figures are two GEMs of the module. Note the different scales of the field strength used in the plots.

that electrons drifting towards the module will be bent by this field component towards the module boundary and are possibly stopped on the module frame. This means certain electrons do not reach the GEM and therefore they are not amplified and detected on the anode pad plane. Thus, the observed field distortions in the simulation can explain a worse signal sensitivity at the module boundary. Figure 7.4b shows that also the electric field component along the drift direction is influenced by the field distortions. In front of the DESY GridGEM module the nominal drift field of $E_z = 220\,\mathrm{V/cm}$ is reduced, which enhances the transverse field component and the field lines are bended towards the module frame. Contrary to this, in front the gap the field in drift direction is increased.

Furthermore, it can also be seen that there are field distortions between GEMs. This means, not only signal electrons travelling towards the module are effected by the distortions introduced by the module gap, but also electrons in the amplification process are affected. These effects will be also taken into account in the following analysis.

7.2.2 Electron drift studies and comparison with experimental data

In order to evaluate the influence of the observed field distortions on the signal electrons more qualitatively, a Garfield++ simulation is used. The drift gas in the simulation is set to T2K and the simulations are done with and without a magnetic field of $B = 1\,\mathrm{T}$, in order to match the measurement conditions.

In the simulation, initially one electron is released above the module in the drift volume from one start point. Subsequently it drifts towards the module following the drift field. If an electron reaches any modelled surface, the drift is stopped and the current position of the electron is stored. Thus, it can be decided if the electron was stopped on the Dummy surface, the module frame, or the pad plane. A first version of the simulation is introduced in Ref. [80]. In this version electrons are always stopped in front of the modules. By projecting the electron positions on the anode pad plane, it can be estimated on which row the electron would have been recorded in the experiment. This assumes no further displacements in the amplification process in the GEM stack, which is reasonable since the diffusion in the GEM stack only spreads the signal and the mean position of the detected electrons corresponds the position of the initial electron entering the GEM stack. Therefore, the number of electrons per row in the simulation can be compared with the number of hits reconstructed on a certain row in the experimental data.

The step of projecting the electron end points on anode pad plane is not necessary when drifting the electrons to the anode. The only problem is, that GEMs are modelled in the CST™ simulation as Kapton® with a copper layer on top and on bottom. The GEM holes are not modelled since there size is at a different scale ($\mathcal{O}(1\,\mu m)$ compared the rest of the model $\mathcal{O}(1\,mm)$). This is done to keep the number of mesh elements in the CST™ simulation at a reasonable level and therefore limit the required computing resources. For this reason the Kapton® and copper layer modelled in CST™ needs to become transparent in the Garfield++ simulation if one wants to drift electrons up to the anode. This is done by simply changing the material of these layers in Garfield++ to be driftable and fill them with T2K gas. Furthermore, the electric field at the former GEM position is set to the drift field, the transfer field and the induction field respectively. As a consequence, in the simulation no amplification in the GEMs is simulated. This is acceptable, since the focus of this study is to evaluate the influence of local field distortions, which is not affected by the amplification in the GEMs.

Signal modelling

In order to model a signal reaching the anode not only one electron is released in the drift volume, but $N_{e^-} = 200$ electrons are used per start point. These electrons are transported in the drift field, taking diffusion in the drift gas into account. This results in a spreading of the electrons finally forming a 2D Gaussian distribution on the anode. The centre of this

distribution is the start point position (in the case of no field distortions) and the variance corresponds to the transverse diffusion.

In order to study field distortions one start position is not sufficient, but a uniform charge cloud covering the region of interest is needed. A uniform charge cloud is created by using 50 equidistant start positions along the x direction (N_{start}) 25 mm in front of the modules. This distance corresponds to the drift length (d_{drift}). The chosen drift length ($d_{\text{drift}} = 25\,\text{mm}$) ensures that the charge cloud is created in a region, where the local field distortions are already vanished since in Figure 7.4a it was shown that they only range about 5 mm. The first start position is in front of the Dummy module (z direction) and 4.5 mm in front of the gap (x direction). Furthermore, the distance between individual start positions is 1 mm. Hence the last start position is 44.5 mm away from the gap. Considering the pad plane layout introduced in Section 4.3.1 and the distance of the pad plane to the gap (1 mm), it can be seen that the last position is above row number 8. Since the start positions are distributed along the x direction the start position in y_{start} direction is constant. Therefore, the signal modelled as described above can also be understood as a charged particle travelling in y direction at a distance of d_{drift} to the modules. Every 1 mm path length it ionises the gas and produces 200 electrons. The number of electrons per path length does not correspond to the real situation in a TPC, but it is chosen in order to achieve a reasonable small statistical uncertainty of the observables defined in the analysis.

Using this method of creating a signal, the requirement of a uniform charge distribution is fulfilled. This means, in case of no field distortions the same number of electrons will end on each of the first seven pad rows. Row number 8 might collect less electrons, since the last start position is above that row.

To illustrate the signal creation, the electron paths resulting from two different start positions are shown in Figure 7.3a (orange lines). Here the effect of local field distortions is already visible for position 1, where electrons are bent towards the module frame. Contrary to this, electrons starting at position 2 are almost not effected by field distortions and an unbiased measurement of the signal position is possible on the pad plane.

Row based signal analysis

The observables used in the row based signal analysis can be defined using the sketch shown in Figure 7.5. On the left-hand side the unbiased situation in case of no field distortions is

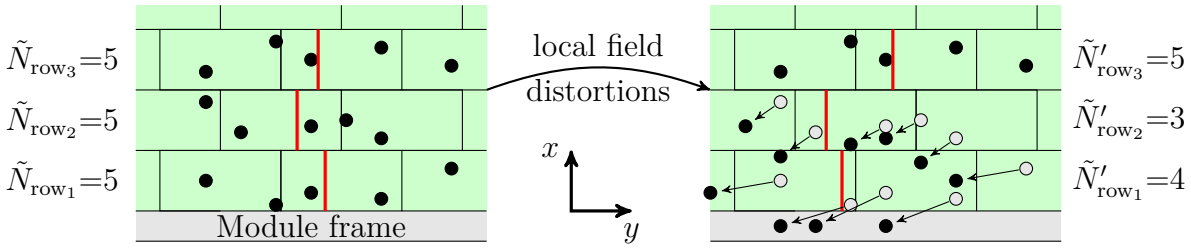

Figure 7.5: Sketch of a small section of the pad plane next to the readout module frame. Pads are shown in green and the black dots denote electron trajectory endpoints. The left- and right-hand side sketch illustrate the situation in the absence and presence of local field distortions in the vicinity of the module frame shown in grey. The red lines depict the mean electron position per row in y direction.

shown. The observables used in the row based analysis are the mean position of the electron (depicted by the black points) in y direction per row (y_{row}) and the number of electrons per row depicted by the red lines ($\tilde{N}_{\text{row}_\text{i}}$). Both observables can also be defined in measured data, which allows a comparison between simulation and measured data. Furthermore, y_{row} is sensitive to distortions in y direction whereas $\tilde{N}_{\text{row}_\text{i}}$ is sensitive to distortions in x and R direction respectively. The influence of field distortions is sketched in on the right-hand side of Figure 7.5, where electrons are bent towards the module frame. In consequence, the number of electrons per row and the mean electron position per row is different compared to the unbiased situation.

The mean position of electrons y_{row} on pad row j can be defined using the electron trajectory endpoints (y_i^j) along the pad row:

$$y_{\text{row}_j} = \sum_{i=1}^{N} \frac{y_i^j}{N} \tag{7.2}$$

$$d_{\text{row}_j} = y_{\text{row}_j} - y_{\text{start}} \tag{7.3}$$

$$\Delta d_{\text{row}_j} = \sqrt{\sum_{i=1}^{N} \frac{\left(y_i^j - y_{\text{row}_j}\right)^2}{N}}. \tag{7.4}$$

Here N is the total number of electrons that end on row j and d_{row_j} is the distortion measured for row j with the corresponding statistic uncertainty Δd_{row_j}.

The collection efficiency is defined as $\tilde{N}'_{\text{row}_\text{i}}/\tilde{N}_{\text{row}_\text{i}}$. Since it is sensitive to distortions in x direction it is used to compare the field distortions observed in simulation to the measured one presented in the beginning (Figure 7.2), where no magnetic field was present and

particle tracks were perpendicular to pad rows. Therefore, distortions caused by the gap between modules emerge only in x direction.

The expected number electrons on a certain row $\tilde{N}_{\mathrm{row_i}}$ in the case of no field distortions can be calculated with respect to the signal creation introduced in the previous section. The expected electron position is defined by the start position and the transverse diffusion $\sigma_{\mathrm{diff.}}$. Therefore, the expected number of electrons per row can be calculated by summing up the contributions of each start point. This is done by integrating the Gaussian distribution originating from the transverse diffusion of each start point for the corresponding row:

$$\tilde{N}_{\mathrm{row_i}} = \sum_{\mathrm{j=1}}^{N_{\mathrm{start}}} \left[N_{\mathrm{e^-}} \int_{x^i_{\mathrm{min}}}^{x^i_{\mathrm{max}}} \frac{1}{\sqrt{2\pi}\sigma_{\mathrm{diff.}}} \exp\left(-\frac{1}{2} \left(\frac{x - x^j_{\mathrm{start}}}{\sigma_{\mathrm{diff.}}} \right)^2 \right) \mathrm{d}x \right], \tag{7.5}$$

where x^j_{min} and x^j_{max} correspond to the borders of the i-th row, and x^j_{start} corresponds the start position j.

Results of the module simulation

Results of the GARFIELD++ simulation are shown in Figure 7.6. Here Figures 7.6a and 7.6b show the electron trajectory endpoints in presence and absence of a magnetic field. It can be observed, that the width of the electron cloud is reduced due to the lower transverse diffusion in presence of the magnetic field. In addition, it can be seen that the electron endpoint distribution on the left side in Figures 7.6a and 7.6b is much narrower than on the pad rows depicted by the black vertical lines. This is because on the left side electrons end on the module frame on top of the module, whereas the electrons above the pad rows are drifted until they reach the anode. In consequence the drift length and thus the transverse diffusion for the electrons reaching the anode is larger and the distribution of the electron endpoints is broadened. In the following the two observables introduced above shown in Figures 7.6c to 7.6f are discussed.

First, the collection efficiency $\tilde{N}'_{\mathrm{row_i}}/\tilde{N}_{\mathrm{row_i}}$ is shown in Figures 7.6c and 7.6d. It can be seen, that with and without magnetic field mainly the first pad row is affected. This means that the local field distortions range in x direction only about 5 mm, which corresponds to the row height. Hence the range in x and z direction is similar and the distortions affect only the vicinity of the module boundary. A reduction of the collection efficiency on the first pad row of 45 % ($B = 0\,\mathrm{T}$) and 30 % ($B = 1\,\mathrm{T}$) is observed. The higher collection efficiency

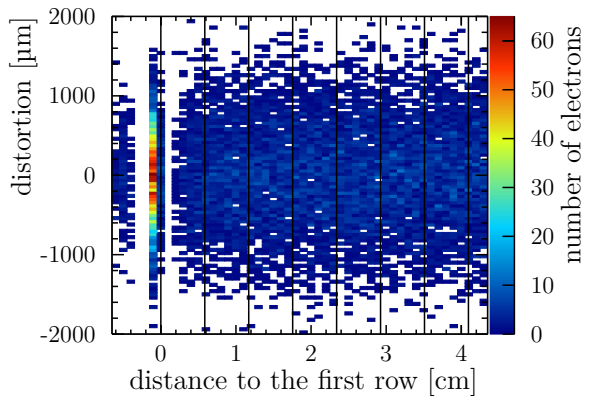

(a) $x-y$ view of the electron endpoints for $B = 0\,\mathrm{T}$.

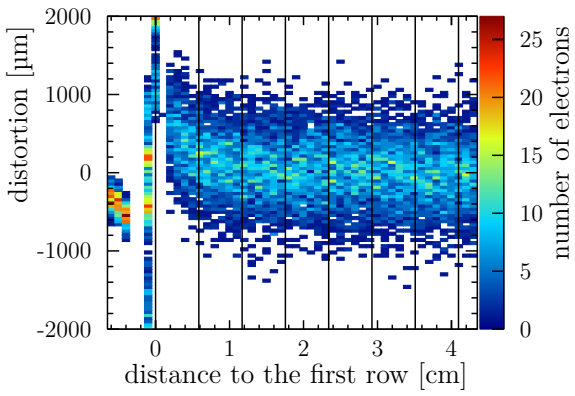

(b) $x-y$ view of the electron endpoints for $B = 1\,\mathrm{T}$.

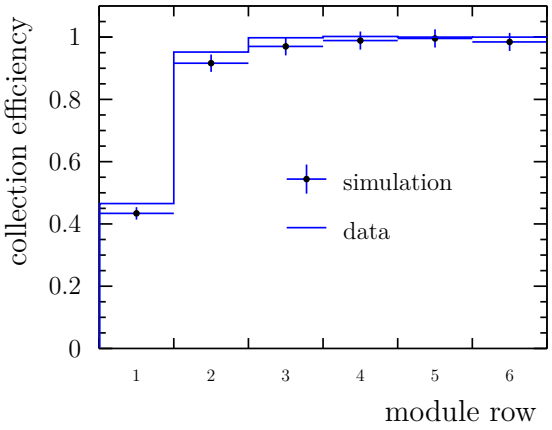

(c) Projection of electron endpoints for $B = 0\,\mathrm{T}$

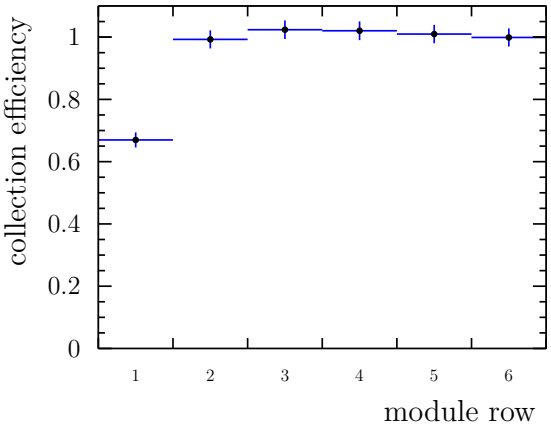

(d) Projection of electron endpoints for $B = 1\,\mathrm{T}$

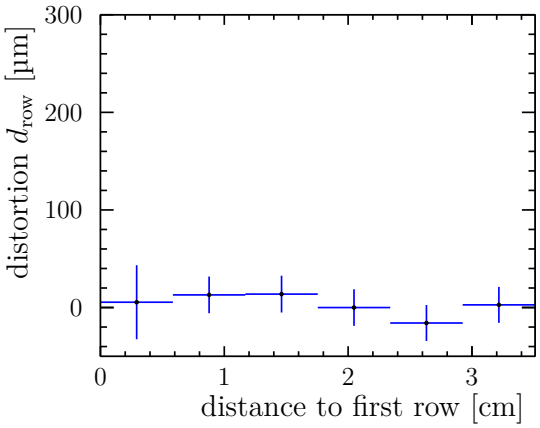

(e) Distortions in y direction per row for $B = 0\,\mathrm{T}$.

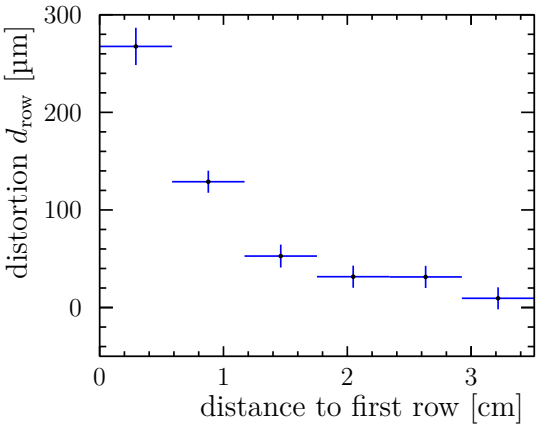

(f) Distortions in y direction per row for $B = 1\,\mathrm{T}$.

Figure 7.6: Electron trajectory endpoints resulting from the GARFIELD++ simulation of the DESY GridGEM module – Dummy module boundary. Here electrons are drifted until they reach the anode or are stopped on the module frame. Black vertical lines in the upper plots depict the first 7 pad rows of the DESY GridGEM module. (c-f) result from the figures (a-b). (c) also includes the result data measured in 2011.

in the presence of a magnetic field can be explained with $\vec{E} \times \vec{B}$ effects. In addition, in Figure 7.6c the measured data presented in the beginning is shown in order to compare it to the simulation. In general a good agreement between both data can be seen, which shows that the simulation can reproduce the effects observed in the measured data. It also shows that the observed reduction of the signal efficiency at the module boundary can be completely understood by the gap between the modules and no further effects are involved.

Second, the distortion d_{row} is shown in Figures 7.6e and 7.6f. As expected no distortions in y direction can be observed, if no magnetic field is present. If a magnetic field is present, the $\vec{E} \times \vec{B}$ effects results in a displacement in y direction of electrons in the vicinity of the gap between the modules. The binning in Figures 7.6e and 7.6f is chosen such that each bin has a width corresponding to the pad row height of the DESY module. Therefore, for the first pad row the displacement is about 260 µm, which is a significant effect.

7.2.3 Module optimisation

As discussed in the previous section field distortions connected to the boundary between modules have severe effects on the module performance. Some effects could in principle be corrected in the reconstruction, but the observed loss of signal electrons can not be corrected. Therefore, it is desirable to reduce local field distortions and keep the corrections in the reconstruction at minimum.

Basically there are two possible ways of reducing the gap between modules. The most obvious one is to reduce the size of the gap by redesigning the anode end plate. But mechanically there are constrains that do not allow to reduce the size of the gap further than it is at the moment. A second possibility is to shield the ground potential, which introduces the field distortions via the gap. This means to form a constant electrostatic potential on the whole anode surface.

Different ways of modifying the DESY GridGEM module in order to do so have been investigated. A common feature of all investigated modifications is to introduced an additional metallic surface in the gap attached to the module frame. Depending on the chosen potential on the metallic surface the field distortions can be influenced. The three options studied are sketched in Figure 7.7a.

The idea behind the strips is to metallise the ceramic grids used to separate the GEMs, whereas the wire is simply attached to the ceramic grid of the module. In the case of

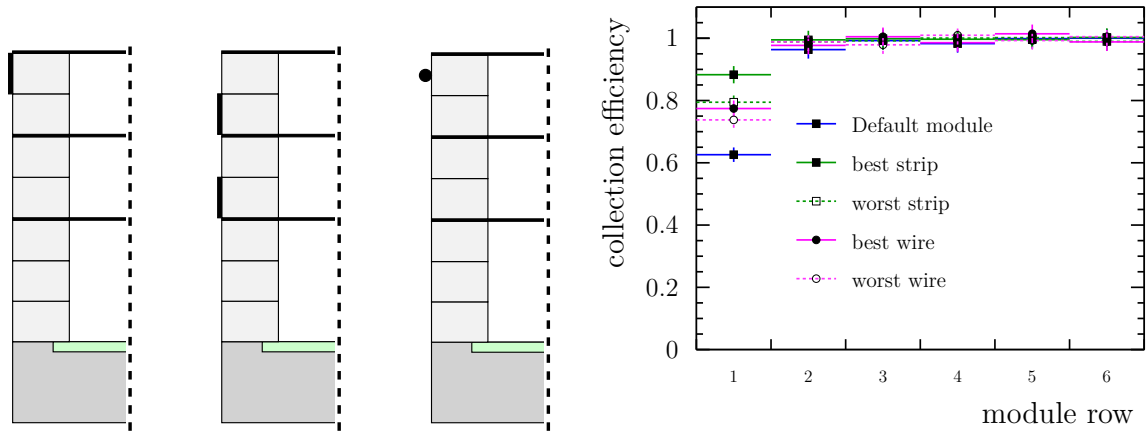

(a) Different modification option of the DESY GridGEM module. Modifications left to right: one strip, two strips, one wire.

(b) Comparison between different investigated options. Details about the options are given in the text.

Figure 7.7: Modification options of the DESY GridGEM module and the resulting improvements in terms of the collection efficiency per module row.

the wire modification different wire diameters were considered: $\varnothing = 50\,\mu\text{m}$, $\varnothing = 100\,\mu\text{m}$, $\varnothing = 150\,\mu\text{m}$. In addition, different potentials were tested on the wire and the strips. They are summarised in Table 7.2, where in the case of the wire and the one strip option the following two ideas were realised:

option a) Here the potential of the GEM cathode facing the drift volume is used.

option b) The potential is chosen such that the drift field is continued in the gap between the Dummy and the readout module.

In the case of the two strip option the potentials chosen in option a continued the drift field in the gap between the modules and in option the b the drift field is inverted in the gap between the modules.

Simulations of all configurations were done and the field distortions were evaluated by investigating the collection efficiency. The details can be found in Ref. [80]. In the end the results can be summarised as follows:

best strip: one strip

worst strip: two strip (option a)

best wire: $\varnothing = 150\,\mu\text{m}$, $U_{\text{wire}} = -2200\,\text{V}$ (option a)

worst wire: $\varnothing = 50\,\mu\text{m}$, $U_{\text{wire}} = -2200\,\text{V}$ (option a)

Table 7.2: Different wire and strip options and the corresponding potentials applied in the simulation.

	potential	
	option a	option b
wire ($\varnothing = 50\,\mu m$)	-2200 V	-2189 V
wire ($\varnothing = 100\,\mu m$)	-2200 V	-2189 V
wire ($\varnothing = 150\,\mu m$)	-2200 V	-2189 V
one strip	-2200 V	
two strips:		
top strip	-2167 V	-2233 V
bottom strip	-2123 V	-2277 V

The corresponding results of the collection efficiency are shown in Figure 7.7b. In the optimisation study electrons were stopped on top the module surfaces and thus only field distortion effects in the drift volume were considered. Comparing the resulting collection efficiency in Figure 7.7b with the result shown in Figure 7.6c, where electrons are drifted to the anode, one can see that inside the module the collection efficiency is reduced by 20 %. Concerning the modifications it can be seen in Figure 7.7b, that a wire can recover about 15 % and the best strip option allows to recover about 25 %.

One modification was realised in a new version of the readout module, which allows to verify the results of the optimisation. The option that was realised, is the best wire option, where a wire with a diameter of $\varnothing = 150\,\mu m$ is attached to the centre of the topmost ceramic frame of the module. Results of the CST™ field simulation are shown in 7.8b, where the field component transverse to the drift field is shown. In comparison to the default version of the module (Figure 7.8a) the reduction of the field distortions by the wire are visible. This is true in the drift region as well as in the transfer regions of the module. The results of the analysis of the electron trajectory endpoints is shown in Figure 7.9, which results from the Garfield++ simulation where electrons are drifted until the anode surface and thus effects inside the module are included. In addition, Figure 7.9 includes also the available data of measurements with the modified module taken at $B = 1\,T$. First of all a good agreement between measured data and the simulation can be observed, which shows that the simulation results agree with the measurements also for the modified module. The comparison between Figure 7.9a and Figure 7.6c shows that the modified module allows to recover 10 %, which is less compared to the prediction without taking the effects inside the module into account discussed above. Furthermore, the comparison between Figure 7.9b and Figure 7.6d shows that in presence of a magnetic field, limited by the $\vec{E} \times \vec{B}$ effects,

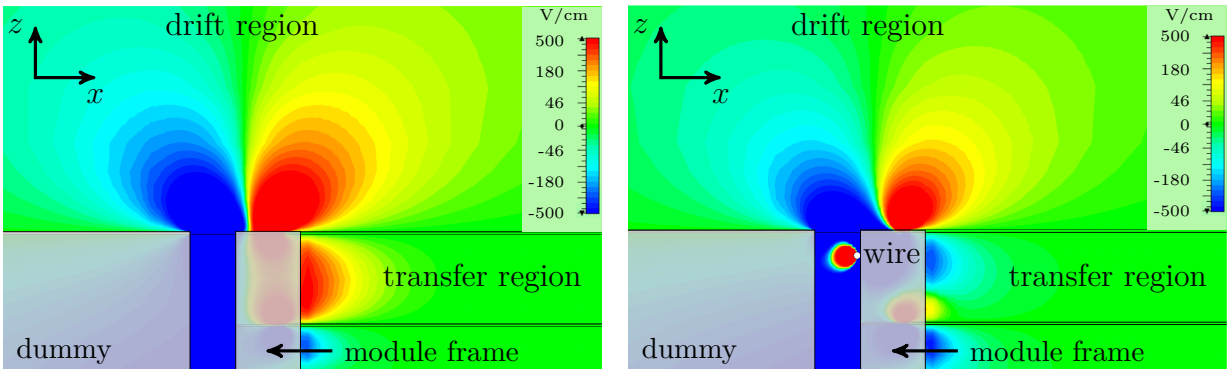

(a) Electric field component transverse to the drift direction (E_x) for the default module.

(b) Electric field component transverse to the drift direction (E_x) for the modified module.

Figure 7.8: Simulation results for the default GridGEM module and the modified version of the DESY GridGEM module, where a wire ($\varnothing = 150\,\mu\text{m}$) is attached to the module frame.

the collection efficiency is almost the same for both module versions. The distortions in y direction are reduced by about 100 µm, which can be seen by comparing Figure 7.9d with Figure 7.6f. Comparing the simulation and measured data shown in Figure 7.9d, a difference of about 80 µm is observed on the pad row at the module boundary. This illustrated the level of agreement between these data, which is sufficient for the studies presented here, in particular for the module optimisation.

7.2.4 Angle dependent effects caused by the field distortions

So far two observables – the collection efficiency per pad row and the mean electron position per pad row – are used to evaluate local field distortions. Both are suitable to evaluate the effect of local field distortions, but so far no direct measurement of the displacement in x direction caused by the field distortions was possible. In the following a method that allows to measure this displacement is presented. It is based on measuring the mean electron position per row, already used before, for different track angles.

Figure 7.10 shows a track (blue line) that crosses the pad plane with an angle α_{track}. In case of field distortions the charge produced along this track is displaced, which is indicated by the red arrow. Therefore, the charge produced at the point P will end on point P'. What is known in the measurement is the track position and the measured position of the charge. Thus, apparently a displacement of $\Delta y'$ will be measured for the bottom pad row. It can be split into individual components, which are not directly assessable in the

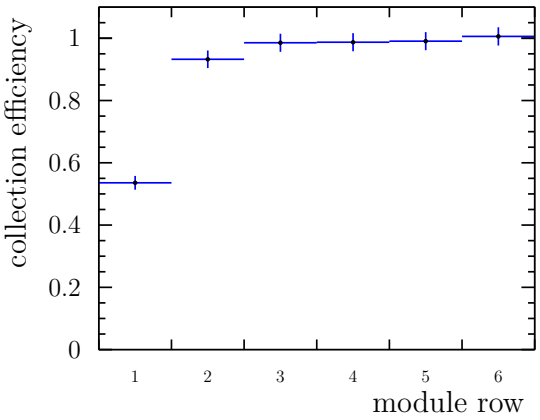

(a) Collection efficiency for $B = 0\,\mathrm{T}$.

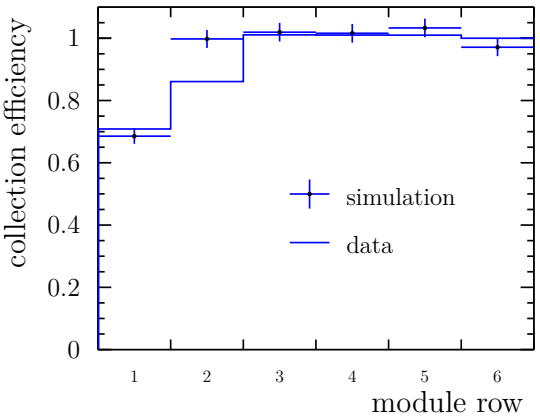

(b) Collection efficiency for $B = 1\,\mathrm{T}$.

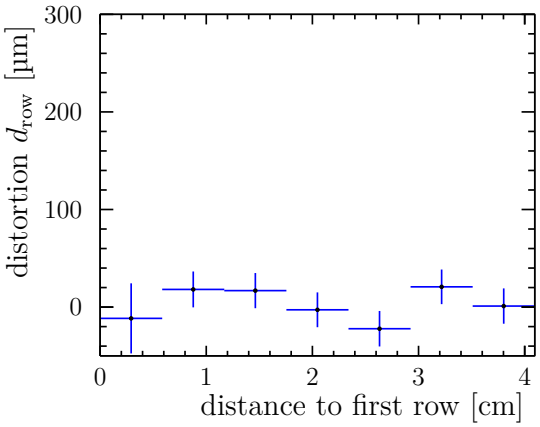

(c) Distortions in y direction per row for $B = 0\,\mathrm{T}$.

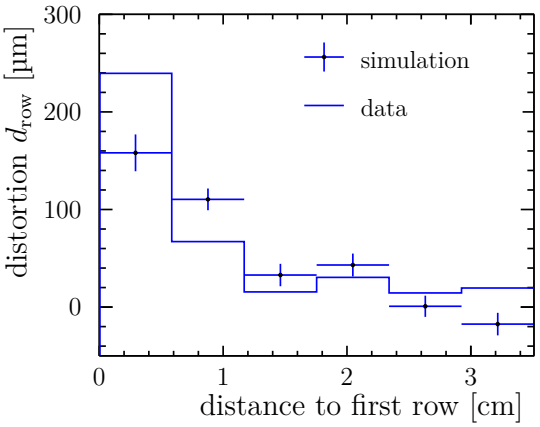

(d) Distortions in y direction per row for $B = 1\,\mathrm{T}$.

Figure 7.9: Results of the electron trajectory endpoint analysis of the modified DESY GridGEM module simulation. The data shown in (b) and (d) was taken in 2012.

measurements:

$$\Delta y' = \Delta y + \tan\alpha_{\mathrm{track}}\Delta x, \tag{7.6}$$

It can be seen that in the case of no component Δy, which true to first order for the local field distortions introduced by the readout modules, an apparent distortion $\Delta y'$ can be mimicked by Δx in case of a track angle. This can be exploited to measure the local field distortions, which are in x direction, via the distortions in y direction d_{row}. This allows to make use of the much better resolution of the readout modules in $R\phi$ (y) direction compared to the resolution in R (x) direction.

Examples of measured distortions in $R\phi$ direction are shown in Figure 7.11. In both figures a similar distortion pattern can be observed, which is caused by the field distortions

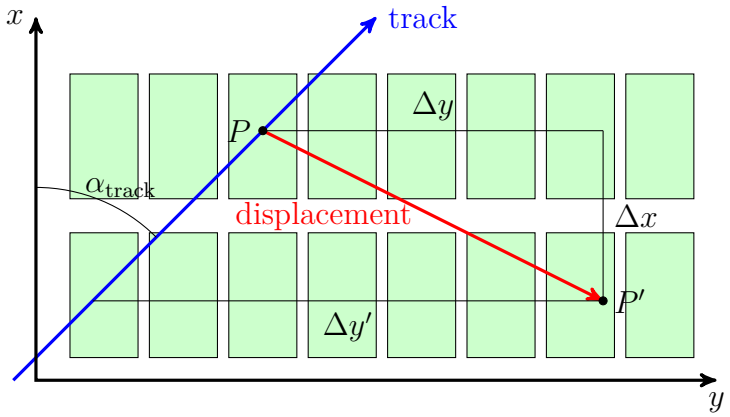

Figure 7.10: Sketch illustrating different components of the measured displacement $\Delta y'$ along a pad row. In the shown example, the assumed displacement causes charge produced in front of the upper pad row to end up on the lower pad row (Δx). In addition, a shift along pad rows of four pads is assumed (Δy).

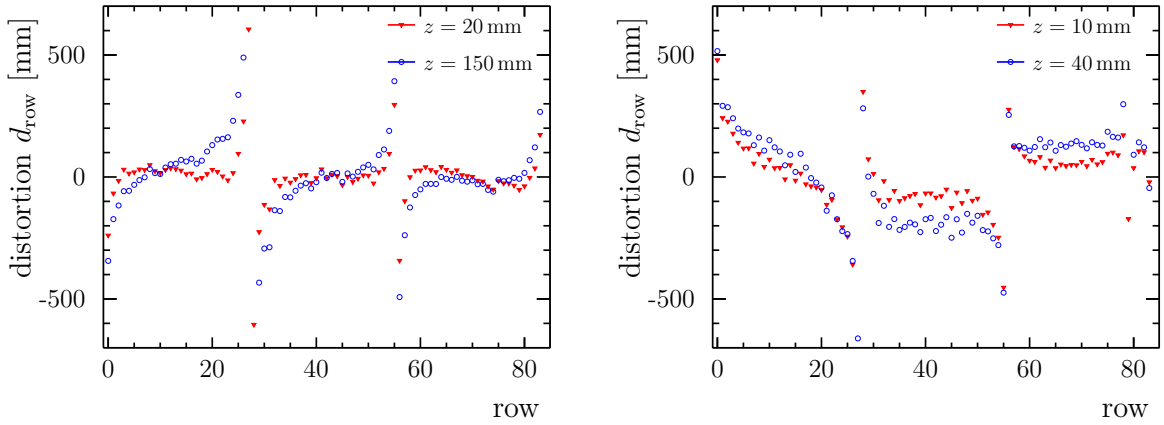

(a) Distortions caused by the magnetic field of $B = 1\,\text{T}$ without a track angle (adapted from Ref. [81]).

(b) Distortions caused by a track angle of $\alpha_{\text{track}} = 9\,^\circ$ measured at $B = 0\,\text{T}$.

Figure 7.11: Mean distance between the reconstructed track hit per row and a track fit considering all reconstructed points of the electron beam used in the measurements. Results are shown for three DESY GridGEM modules, where each module has 28 rows. The distortions are shown for two different drift distances.

introduced at module boundaries at row 0, row 84 and between rows 27,28 and 55,56. In Figure 7.11a the distortions are visible in y direction due to $\vec{E} \times \vec{B}$ (measurements are taken at $B = 1\,\text{T}$, whereas in Figure 7.11b they are visible due to the track angle of $\alpha_{\text{track}} = 9\,^\circ$ used in the measurements. In addition, both measurements are shown for two different drift distances. The corresponding observed distortions are similar for the different drift

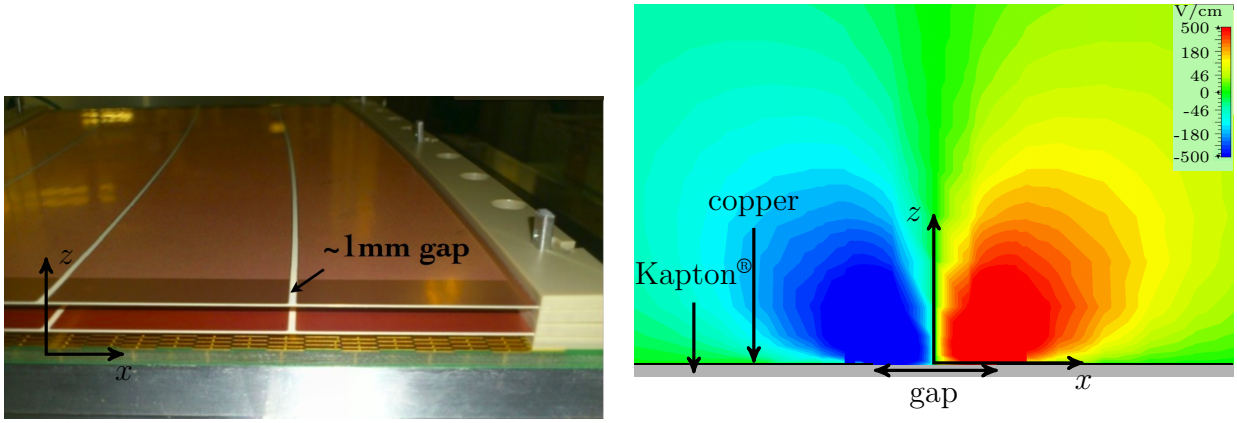

(a) Picture of the Asian module showing the gap separating individual GEM sectors.

(b) Result of the CST™ simulation showing the electric field component transverse to the drift direction (E_x).

Figure 7.12: The gap separating individual GEM sectors in reality and simulation. The origin of the coordinate system is the same in both figures.

distances, which shows that the distortions are not accumulated in the sensitive volume of the TPC, but they arise close the anode and are therefore caused by the local field distortions.

In the following a simple setup allowing angle dependent measurements is introduced and used to study the angle dependent effects.

Laser based angle dependent distortion measurements

The test setup introduced in the following is used to demonstrate the method of evaluating field distortions using angular tracks. It is realised with the Asian module, which was introduced in Section 4.3.2. The field distortions that are investigated here are produced by a GEM, where individual copper sectors on the GEM are separated by a gap with size 1 mm. This gap can be identified as white stripes on the GEM surfaces in Figure 7.12a, which shows the ASIAN module. Furthermore, Figure 7.12a include the coordinate system used in the following. Its origin in x direction in the centre between two pad rows and the gap centre is at $x = 0\,\text{cm}$.

The result of the electric field simulation with CST™ using a drift field of $E_{\text{drift}} = 230\,\text{V/cm}$ is shown in Figure 7.12b. Here the component transverse to the drift field is shown, which has a similar shape as the distortions caused by the gap between modules.

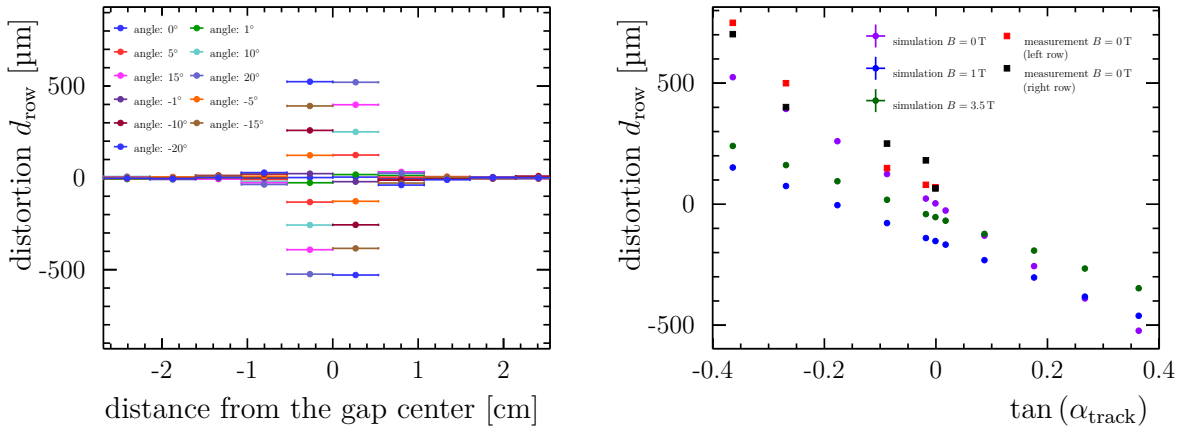

(a) Simulated distortions as a function of the distance to the gap for different angels α_{track}. The magnetic field is $B = 1\,\text{T}$ and the binning corresponds to individual pad rows.

(b) Displacements on the pad row left-hand side to the gap for the simulation at different magnetic field strengths. In addition, measured data are shown for $B = 0\,\text{T}$ [82]. The results are shown for the pad row on the left-hand and on the right-hand side of the gap.

Figure 7.13: Displacements along pad rows caused by the gap between individual GEM sectors.

In the following the analysis is done in a similar way as introduced in Section 7.2.2, meaning the uniform electron signal is produced in the same way and the electron trajectory endpoints are analysed afterwards. The only difference is that the start points are not only chosen along a line in x direction, but also an angle between this line of start positions and the x direction is considered. This angle corresponds to α_{track} in the simulation. Only electrons that end on the copper surface are considered for the calculation and electrons ending on the gap ($x \in [-0.05\,\text{cm}, 0.05\,\text{cm}]$) are excluded. Since the measurements were done with the Asian module, the row height in the analysis is set to $h_{\text{row}} = 5.35\,\text{mm}$.

Figure 7.13a shows d_{row} in dependence on the distance to the gap for different angles α_{track}. The binning corresponds to individual pad rows, since d_{row} is defined per pad row. It can be seen that mainly the two rows next to the gap are influenced by local field distortions. Since the centre of the gap is in between the two concerned rows, the effects on them is similar and in the following the distortions are evaluated for the pad row left to the gap. The results for different angles at different magnetic fields are shown in Figure 7.13b, where the linear dependency of the displacement on the angle α_{track} expected from Equation 7.6 can be seen. Furthermore, this plot shows that also in presence of a magnetic field for a certain angle the displacements apparently disappear. In this case the local distortions caused by the gap on the GEM surface are compensated by the second term of Equation 7.6.

Table 7.3: Fit results of simulated and measured data using Equation 7.6. For $B = 0\,\mathrm{T}$ the component Δy is fixed to 0.

data set	Δx [mm]	Δy [mm]
Simulation, $B = 0\,\mathrm{T}$	1.45 ± 0.01	0
Simulation, $B = 1\,\mathrm{T}$	0.852 ± 0.007	0.155 ± 0.001
Simulation, $B = 3.5\,\mathrm{T}$	0.804 ± 0.008	0.054 ± 0.001
Measurement left row, $B = 0\,\mathrm{T}$	1.82 ± 0.26	0
Measurement right row, $B = 0\,\mathrm{T}$	1.99 ± 0.12	0

Figure 7.13 includes also results of measurements done at KEK[1] with the Asian module and the GEMs shown in Figure 7.12a. The results are evaluated for the left gap in this picture, where the pad row boundary is in the centre of the gap. Thereby, the results of the simulation for $B = 0\,\mathrm{T}$ can be directly compared to the measurements. A slight offset in the order of approximately 50 µm can be observed, but in principle the measurements agree with the expected behaviour of Equation 7.6. The fit results using Equation 7.6 are shown in Table 7.3. For fits of data at $B = 0\,\mathrm{T}$ the component Δy is fixed to zero, since the local field distortions only introduce a displacement transverse to pad rows. It can be seen in Table 7.3, that the displacement introduced by the local field distortions is $(1.45 \pm 0.01)\,\mathrm{mm}$ in simulation and $(1.9 \pm 0.3)\,\mathrm{mm}$ in the measurements when combining the two measurement results. This shows a fairly good agreement between the simulation and the measurement. Comparing the observed distortions in simulation for $\tan(\alpha_{\mathrm{track}}) = 0$ for different magnetic field strengths, it can be seen that the distortions increase from $B = 0\,\mathrm{T}$ ($d_{\mathrm{row}} = 0\,\mu\mathrm{m}$) to $B = 1\,\mathrm{T}$ ($d_{\mathrm{row}} = -160\,\mu\mathrm{m}$) and decrease from $B = 1\,\mathrm{T}$ to $B = 3.5\,\mathrm{T}$ ($d_{\mathrm{row}} = -50\,\mu\mathrm{m}$). This can also be seen based on Δy shown in Table 7.3.

This can be understood with the electron drift described in Equation 3.6. At small magnetic field strengths the $\vec{E} \times \vec{B}$ term causes distortions in y and at high magnetic fields the last term of Equation 3.6 becomes dominant and electrons follow the magnetic field lines. Therefore, at high magnetic fields the influence of field distortions of the electric field becomes smaller.

7.2.5 Discussion of the local field distortions

In the first part of this chapter simulation studies of local field distortions introduced by TPC readout modules installed in the anode were presented. It was shown that the source of

[1] High energy accelerator research organisation in Tsukuba, Japan.

the field distortions is the gap (1 mm) between individual readout modules, which leads to a leakage of the anode ground potential into the sensitive volume of the TPC. The resulting effect is a reduction of the charge collection efficiency on the pad row at the module boundary to 45 % ($B = 0\,\mathrm{T}$) and 30 % ($B = 1\,\mathrm{T}$). Furthermore, a displacement of the collected charge on this row of 260 µm in case of $B = 1\,\mathrm{T}$ was observed. The direct measurement of the displacement caused by the local distortions using a simplified setup results in a displacement of the charge towards the module boundary of about $(1.45 \pm 0.1)\,\mathrm{mm}$ in simulations. A good agreement between the simulation and measurement results was found, which verifies the simulation results and allowed to test different improvements of the module design.

In the optimisation of the DESY GridGEM module a wire was attached to the module frame, which helps to reduce the local field distortions. In simulation and measurements it was shown that the charge collection efficiency on the pad row at the module boundary is increased to 55 % for $B = 0\,\mathrm{T}$. In presence of a magnetic field the increase of the collection efficiency is not significant due to $\vec{E} \times \vec{B}$ effects, but the displacement on the pad row at the module boundary is limited to 160 µm with the modified module.

Still the displacement of signal electrons close the module boundary is significant. With regard to an ILD TPC analysis this means that reconstructed hits at module boundaries will be shifted. In consequence the track finding and track reconstruction will be biased. The expected shift is in the order of $\mathcal{O}(200\,\mu\mathrm{m})$ for $B = 1\,\mathrm{T}$ (see Figure 7.9d). It is expected to be reduced at $B = 3.5\,\mathrm{T}$, which was shown in simulations (see Figure 7.13). In order to correct the distortions, reconstructed hits can be shifted according to the field distortions before the track finding and fitting. Alternatively, one has to exclude rows at the module boundaries. Both possibilities have an effect on the momentum resolution. On the one hand, the exclusion of rows reduces the number of measurement points along tracks and therefore the momentum resolution is decreased. On the other hand the field distortions need to be corrected to an accuracy of about 30 µm to limit the decrease in momentum resolution to 5 %, as discussed in the beginning. The comparison between measured and simulated data shown here implies, that this level of accuracy is not reached with correction based on the simulation results. This could be seen in particular in Figure 7.9d, where a difference between simulation and measurements of 80 µm for the row at the module boundary was observed. Therefore, either more details need to be included in the simulation or the distortions needs to be measured at all module boundaries using a know signal source like in the case of the laser calibration system introduced in the following section.

7.3 Overall field distortions in the LPTPC

In this section measurements of the overall field distortions inside the LPTPC are presented. For these measurements a laser system is used to create a defined signal at well known positions of the LPTPC cathode. The comparison of the reconstructed positions to the initial positions of the signal creation allows to measure displacements on the the anode surface, which correspond to the overall distortions accumulated over the full drift length of the LPTPC. This allows to characterise the LPTPC under controlled conditions.

In the following, different analysis will be presented, which will illustrate the benefits of the laser system and its capabilities. The measurements shown here are mainly used to study the overall field distortions, but in general the methods presented in this work can also be used in a routine TPC operations to monitor gas properties, the gain of readout modules or to align modules. With respect to the ILD TPC the big advantage is that all these measurements can be done independent of the status of the ILD meaning if it is taking data with beam collisions, if it is in parking position while the second ILC detector is taking data or even in the construction phase of ILD.

7.3.1 Measurement principle

The basic idea of characterising field distortions inside the sensitive volume of a TPC is to create a defined signal and to compare it to the corresponding measured signal. Deviations in time and position from the signal expected on the anode are used to determine field distortions in the sensitive volume. One possibility to create a signal is to ionise the TPC gas at defined positions in the sensitive volume. Possible sources of ionisation are charged particles or photons with a proper energy (see for example Ref. [83]). The advantage of this method is that in principle everywhere inside the sensitive volume a signal can be created. But the particle source needs to be characterised and the particle path needs to be known very precisely in order to gain detailed information on the field distortions.

One example of such a laser calibration system is realised in the ALICE experiment. It makes use of a laser ($\lambda = 266\,\mathrm{nm}$), which ionises the TPC gas at four different positions along z in each half of the TPC. In total there are 6 laser rods and at each z position there is a bundle of micro mirrors leading to 7 tracks (see Figure 7.14a). Thus, the overall

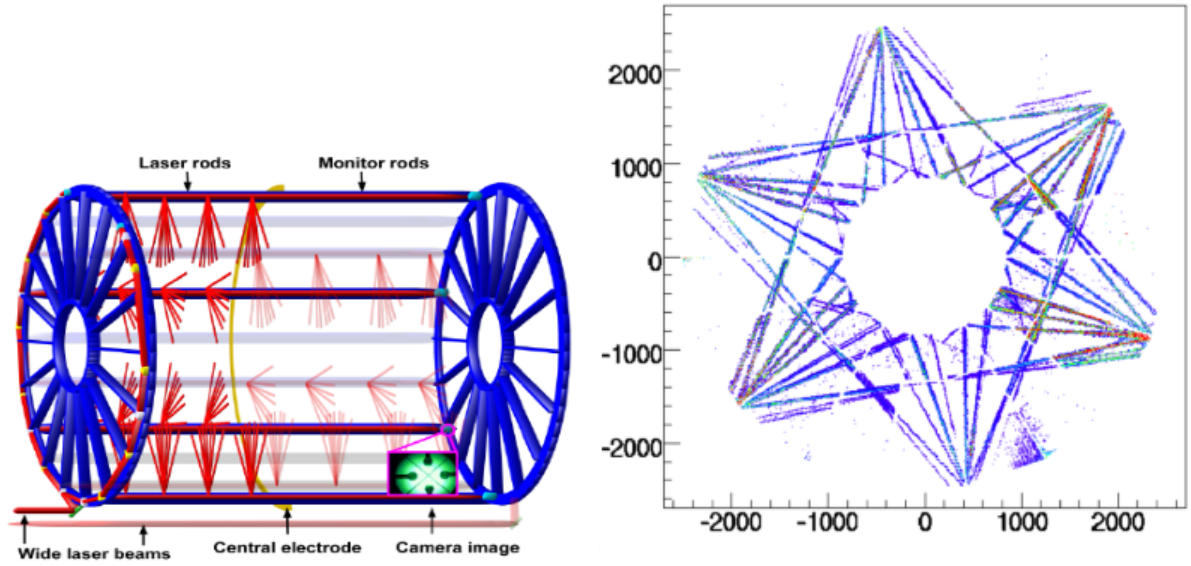

(a) Sketch of the laser calibration system build around the TPC.

(b) Measured tracks produced by laser beams.

Figure 7.14: ALICE laser calibration system [84].

number of tracks inside the TPC is 336 and the resulting pattern on the anode is shown in Figure 7.14b. Here it is also visible, that limited by the number of laser rods the outer part of the sensitive volume (region of large radius) is less monitored.

The approach considered in this work uses another method of creating a signal. Here electrons are directly created on the cathode at defined position. This is done by shining with a laser onto the cathode and electrons are produced via the photoelectric effect. The advantage of this approach is that in principle any pattern can be created on the cathode. In the following, general considerations for this approach are presented in the case of the LPTPC.

Considerations for the laser system

The positions on the cathode are defined by the alumina dots in the case of the LPTPC, as introduced in Section 4.2. In order to produce electrons only from these defined positions, the wavelength of the laser has to be chosen accordingly. The energy of electrons produced via the photoelectric effect is given as:

$$E_{e^-,\max} = E_\gamma - W, \tag{7.7}$$

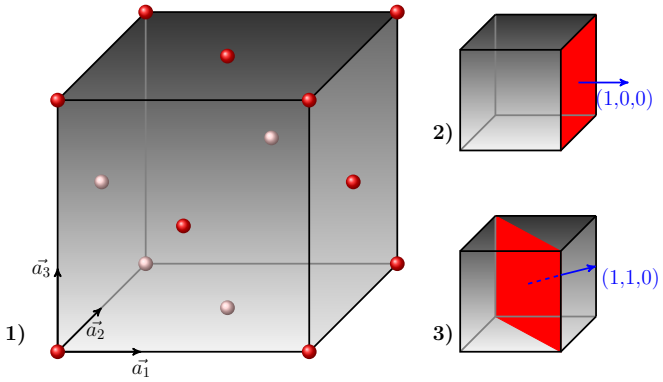

Figure 7.15: 1) Face-centred cubic unit cell with atoms shown in red. 2) shows surface (1,0,0) and 3) shows surface (1,1,0) in the unit cell.

Table 7.4: Work function of different surfaces of copper [85] and aluminium [86].

material	surface	W [eV]
aluminium	100	4.2
	110	4.06
	111	4.26
copper	100	5.1
	110	4.48
	111	4.94
	112	4.53

where W is the material dependent work function. Therefore, the minimum energy needed to release electrons is identical to the work function of the corresponding material. Table 7.4 shows the work function measured at different surfaces of copper and aluminium. The crystal structure of both materials is face-centred cubic and the surfaces are defined via the Miller indexes using the lattice vectors $\vec{a_1}$, $\vec{a_2}$ and $\vec{a_3}$. Figure 7.15 shows the atom positions (red dots) in the face-centred cubic unit cell. Furthermore, in this sketch two surfaces (1,0,0) and (1,1,0) are sketched.

The comparison of the work functions shows that the ones of aluminium are below the ones of copper. Since aluminium oxidises almost immediately if it is exposed to air, effectively there are aluminium oxide (alumina) dots at the cathode. In Ref. [87] it is shown that the oxidisation of aluminium further decreases the work function. This shows that it is in principle possible to only liberate electrons from the alumina by choosing a proper wave length of the laser light. Here the wavelength of $\lambda = 266\,\text{nm}$ is used, which corresponds to a photon energy of:

$$E_\gamma = \frac{hc}{\lambda} = 4.66\,\text{eV}, \tag{7.8}$$

where h is the Planck constant and c is the speed of light. This energy is beyond the work function of alumina and at the threshold energy for the photoelectric effect in copper. That this combination of materials and laser wavelength in the end works was shown in measurements with the STAR TPC [88], where a laser calibration system similar to the system introduced here was used.

After fixing the wavelength the laser energy has to be fixed, which will be done in following

the normal operation conditions of a TPC where electrons are produced in the sensitive volume via the primary ionisation. Usually in the order of $\mathcal{O}(100)$ electrons are produced per 1 cm path length by an ionising particle for common TPC drift gases. Scaling this number to the diameter of the aluminium dots ($\varnothing = 3\,\mathrm{mm}$) one needs to produce about 30 electrons per alumina dot to get a similar signal strength. This results in an electron density of $\rho_{e^-} = 425\,\mathrm{e}^-/\mathrm{cm}^2$. In order to estimate the required laser power one needs to know the efficiency ϵ_γ to liberate an electron with a photon from the laser. In the STAR TPC this efficiency was measured to be $\epsilon_\gamma = 10^{-8}$ [89]. This allows to estimate the photon energy density ρ_E, which is required on the cathode surface:

$$\rho_\gamma = \frac{\rho_{e^-}}{\epsilon_\gamma} \tag{7.9}$$

$$\rho_E = \rho_\gamma E_\gamma = \rho_\gamma \frac{hc}{\lambda} = 31\,\mathrm{nJ/cm}^2, \tag{7.10}$$

where ρ_γ is the required photon density on the cathode.

The light cone size required to illuminate all alumina dots on the cathode can be estimated from the module size on the anode, since the alumina dots are aligned with the readout modules (see Section 4.2). In Figure A.4 one can see that the angle from the left central module to the right central module is $\beta = 23\,^\circ$ and the radius on top of the modules is $R = 1430\,\mathrm{mm}$. This means the maximum cone size, which is the direct connection of the outermost corners of the modules, has to be $r_{\mathrm{cone}} = \sin(\beta/2)\,R = 28.5\,\mathrm{cm}$. Finally, the required energy of the light entering the LPTPC is given as:

$$E = \rho_E \pi r_{\mathrm{cone}}^2 = 0.08\,\mathrm{mJ} \tag{7.11}$$

7.3.2 Measurement setup

The measurement setup consists of two parts. The first part consists of the laser and an optical setup used to split the laser light and couple it into two laser fibres. This part of the setup is placed outside the test area, where the LPTPC is operated. The reason for this is, to protect the laser from the magnetic fields used in the experiments.

The second part of the system is LPTPC with the pattern of alumina dots on the cathode. Both parts are connected via optical fibres used to transport the light from the laser system to the LPTPC. They connected via ports in the LPTPC anode, which allows to illuminate the LPTPC cathode. This is shown in Figure 7.16, where the LPTPC itself, the pattern of

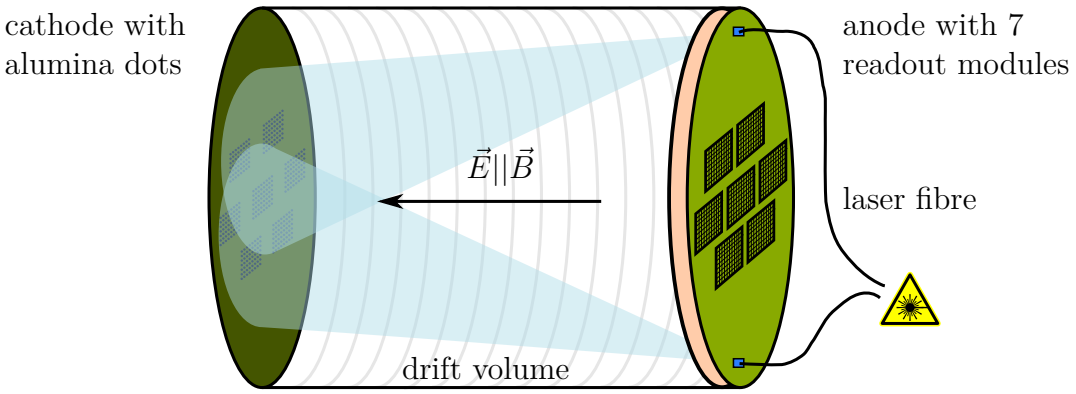

Figure 7.16: Sketch of the measurement setup used to measure field distortions in the sensitive volume of the LPTPC.

alumina dots, the ports with attached fibres and the readout modules inside the anode are sketched. The information about the cathode pattern and the LPTPC itself were already given in Section 4.2. Hence, in the following the first part of the setup, which was not yet discussed, is introduced.

The laser system

The laser used in the laser system is a neodymium doped yttrium aluminium garnet (YAG) laser rod in combination with a lamp filled with Xenon gas in close proximity. By flashing the lamp some of the broadband graybody radiation is absorbed by the rod and the neodymium ions get excited. The radiative lifetime of the excited metastable state is about $\tau = 230\,\mu s$. Through the deexitation, photons with a wavelength of $\lambda = 1064\,nm$ are produced and captured in an optical resonator, where they are amplified via stimulated emission. Behind the laser resonator there is a second harmonic generator, which uses a potassium titanyl phosphate (KTP) crystal to double the incoming photon frequency. Finally, there is a fourth harmonic generator using a beta barium borat (BBO) crystal to double the photon energy again. This results in a wavelength of $\lambda = 266\,nm$, which is primarily used in the measurements. Specification of the laser are given in Table 7.5. The flash lamp of the laser is mainly affected by magnetic fields as discussed before. In particular the discharge process is influenced by the magnetic field, which results in practice in a reduction of the power of the lamp and in consequence a reduced of the laser power. This is the reason for placing the laser system outside the test area of the LPTPC, which will be introduced in the next section.

In order to illuminate the whole cathode of the TPC, there are two ports in the anode end

Table 7.5: Specifications of the laser used in the test campaigns in 2013 and 2014.

Laser class:	IV	Divergence:	$< 1\,\text{mrad}$
Laser type:	Nd:YAG	Pulse width:	$\leq 6\,\text{ns}$
Wavelength:	$266, 532, 1064\,\text{nm}$	Diameter of the Laser pulse y_0:	$1.5\,\text{mm}$
Power:	$60\,\text{mW}$	Repetition rate:	$5 - 20\,\text{Hz}$
Energy:	$3\,\text{mJ}$		

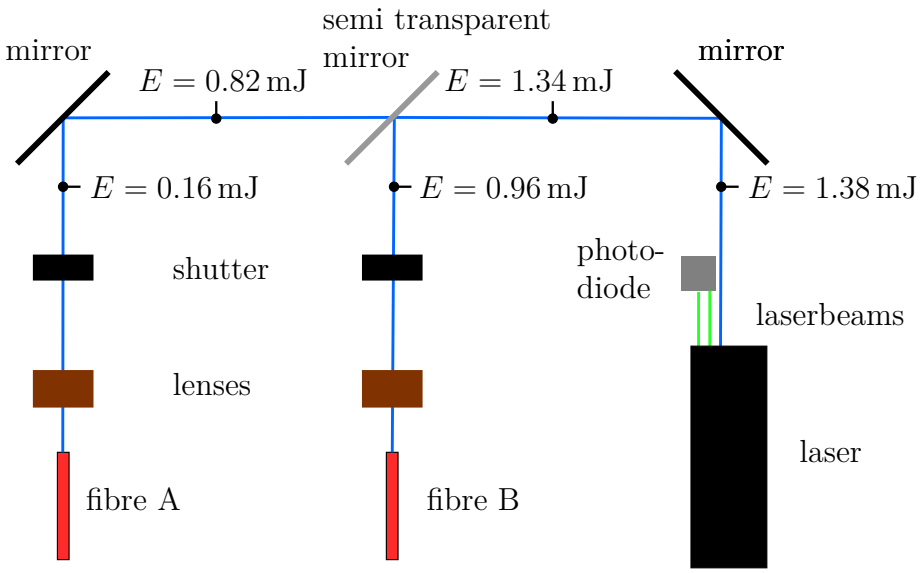

Figure 7.17: Sketch of the setup used to split the laser beam and couple it into laser fibres. In addition, the position of the trigger diode is shown and the measured energy at different positions is given. The laser power and the repetition rate was set to the maximum in the measurements.

plate to attach laser fibres (see Figure 7.16). Hence, the light of the laser is split with a dedicated setup shown in Figure 7.17. The main components of this setup are two mirrors, one semitransparent mirror, two lenses and two shutters. In addition, there is a photo diode, collecting the green light ($\lambda = 532\,\text{nm}$) from the second harmonic generator. It is used to generate a trigger signal for the readout electronics of the LPTPC. Figure 7.17 also shows the measured laser beam energy at various positions in the setup. It can be seen, that one fibre receives less energy ($E_\text{A} = 0.16\,\text{mJ}$) than the other fibre ($E_\text{B} = 0.96\,\text{mJ}$). In addition to the energy losses in this setup by splitting the beam also an energy loss inside the fibre takes place. The attenuation inside a fibre, defined as

$$D = 10 \log_{10} \left(\frac{E_\text{in}}{E_\text{out}} \right)$$

for one of the fibres was measured. The result of $D = 0.7\,\text{db/m}$ shows that only 6 % of

the light is transmitted through the fibre over the whole fibre length of $l_{\text{fibre}} = 18\,\text{m}$. In consequence, in the case of fibre B the total energy of 0.06 mJ will be available in the LPTPC. This value is close to required energy of 0.08 mJ and one can expect about 315 electrons per alumina dot on the cathode will be produced, whereas from fibre A only 52 electrons can be expected. This strong attenuation inside the fibres is because they made of fused silica, which absorb much of the ultraviolet light. Furthermore a damage to the fibre over time can be observed when using ultraviolet light as shown in Ref. [90]. There are ways of reducing this damage by using different materials for the fibre core as also discussed in Ref. [90]. One way of reducing the loss inside the fibre is to use silicon doped quartz fibres, which are much more expensive. For this reason they are not considered here.. The attenuation of the second fibre is even lower and therefor this fibre was placed at fibre position B, while the other one was placed at position A. Thus, the less transparent fibre received more light. This was motivated by achieving an as homogeneous light distribution as possible.

7.3.3 Test beam area T24 at DESY

For the measurements presented in this work the LPTPC was placed in one of the test beam areas, named T24/1, at the DESY test beam facility. In this area a superconducting magnet (PCMAG) is located, which provides a magnetic field of up to $B = 1.25\,\text{T}$. The usable volume of the magnet is a cylinder with a diameter of 85 cm and a length of about 130 cm. Since it has no return yoke, the magnetic field is not homogeneous in the usable volume. It is constant within 3 % in the region of $\pm 30\,\text{cm}$ around the centre of the magnet, which is used by the LPTPC with its drift length of 60 cm. The magnetic field of the magnet was mapped in a dedicated survey presented in Ref. [91]. Figure 7.18 shows the magnetic field component in drift direction and perpendicular to the drift direction resulting from this survey. Furthermore, the LPTPC size is illustrated by the black box in case of the LPTPC is in the magnet centre. Moreover, two additional positions of the LPTPC in the magnet are shown, which were considered in the measurements.

7.3.4 Data summary

The data presented here were taken in dedicated experiments with the DESY GridGEM and the MicroMegas modules in two periods in November 2013 and February 2014 respectively. In both periods measurements with 10000 events per run were done in order to allow a

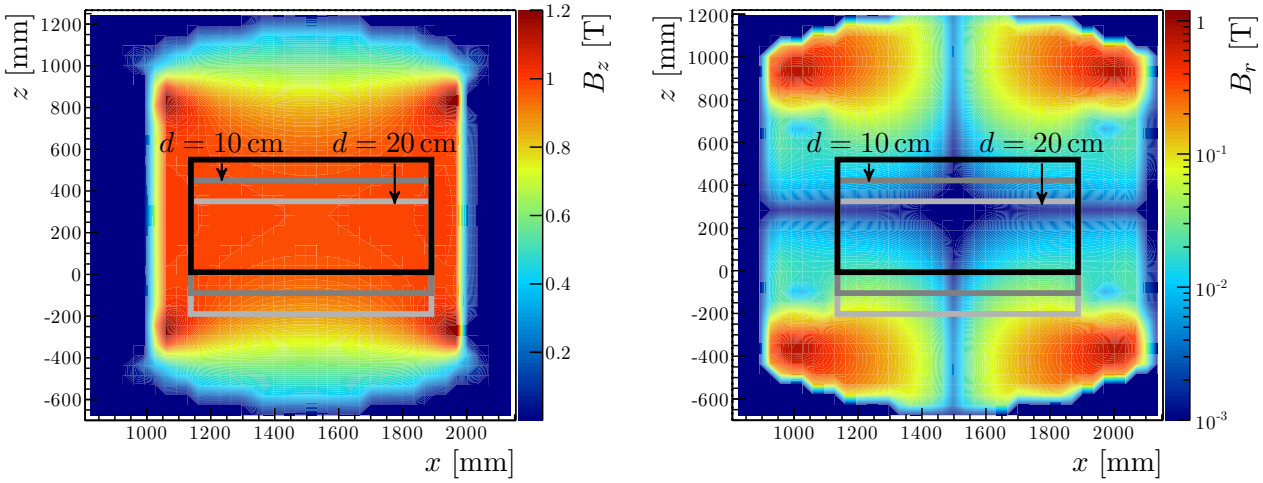

(a) Magnetic field component in drift direction.

(b) Magnetic field component perpendicular to the drift direction.

Figure 7.18: Magnetic field of the PCMAG resulting from measurements presented in Ref. [91]. The black box indicates the LPTPC, when it is placed in the centre of the magnet. Gray boxes indicate two additional positions, where the LPTPC is pulled out of the magnet centre by the distance d.

comparison. The measurements were done at seven different drift fields: $E_{\text{drift}} = 100\,\text{V/cm}$, $130\,\text{V/cm}$, $150\,\text{V/cm}$, $180\,\text{V/cm}$, $200\,\text{V/cm}$, $220\,\text{V/cm}$, $240\,\text{V/cm}$; performed with and without a magnetic field of $B = 1\,\text{T}$. Furthermore all measurements were done for three different positions of the LPTPC inside the PCMAG. Those position in the magnet can be seen in Figure 7.18. Here the distance of the LPTPC centre to the magnet centre is: 0 cm (black box), 10 cm (grey box), 20 cm (light grey). For the measurements without magnetic field the LPTPC was placed in the centre of the magnet. This adds up to three positions at $B = 1\,\text{T}$ and two positions at $B = 0\,\text{T}$ for all seven drift fields, which is in total 28 runs per campaign.

In both campaigns the laser was pulsed with a frequency of 20 Hz. The energy can be scaled in 10 steps, where 10 corresponds to the maximum power. For all measurements the power was set to 9. Fibre A (see Figure 7.17) was attached to the bottom port of the LPTPC and fibre B was attached to the top port of the LPTPC for all runs. Before any measurement the laser was fired for at least ten minutes to get stable laser conditions.

Table 7.6: Settings used in the DESY GEM test runs in November 2013. GEM I corresponds to the GEM facing the drift volume.

	voltage difference [V]		field [V/cm]
GEM I	260	$E_{\text{transfer, I}}$	1500
GEM II	250	$E_{\text{transfer, II}}$	1500
GEM III	250	$E_{\text{induction}}$	3000

DESY GridGEM module test

In the first measurement campaign the three DESY GridGEM modules introduced in Section 4.3.1 were used in the LPTPC. At this time 56 FECs of the ALTRO readout providing 7168 readout channels were available and used. The whole electronics was cooled with compressed air to provide suitable working conditions. A few FECs were also equipped with temperature sensors, in order to monitor the stability of the system. If the temperature changed by more than 1 K new pedestals were taken. This means data were taken without creating signals in the TPC and the noise of each channel is measured and stored. In the data analysis this pedestal value is subtracted from the measured charge per time bin.

Resulting from the limited number of available readout channels not all module could be fully readout. The anode pads that could be read out with the available readout channels are shown in green in Figure 7.19. Here the central module is fully read out and the other channels are used to cover as most aluminium dots on the cathode as possible. The positions of the aluminium dots on the cathode are also shown in Figure 7.19 as projections on the anode (blue dots). Projections that are not on a module are not shown in this figure. In total 16 dots are covered by the top module, 56 dots are covered by the central module and by the bottom module 20 dots are covered. The position of the three available modules in the LPTPC anode end plate was motivated by former measurements with an electron beam, where this module configuration was used to have a long lever arm for resolution studies. Thus, corrections due to field distortions calculated with data using the laser system could also be applied to these test beam data.

The voltage settings used in the GEM stack are summarised in Table 7.6. They were optimised to ensure stable operation without discharges in the GEMs and to cover the whole available ADC range of the electronics, which is illustrated in the following. Figure 7.20a shows the recorded charge per time bin for all channels of a run at $B = 0\,\text{T}$ and $E_{\text{drift}} = 240\,\text{V/cm}$. In this figure the number of entries per bin is normalised to the total number of

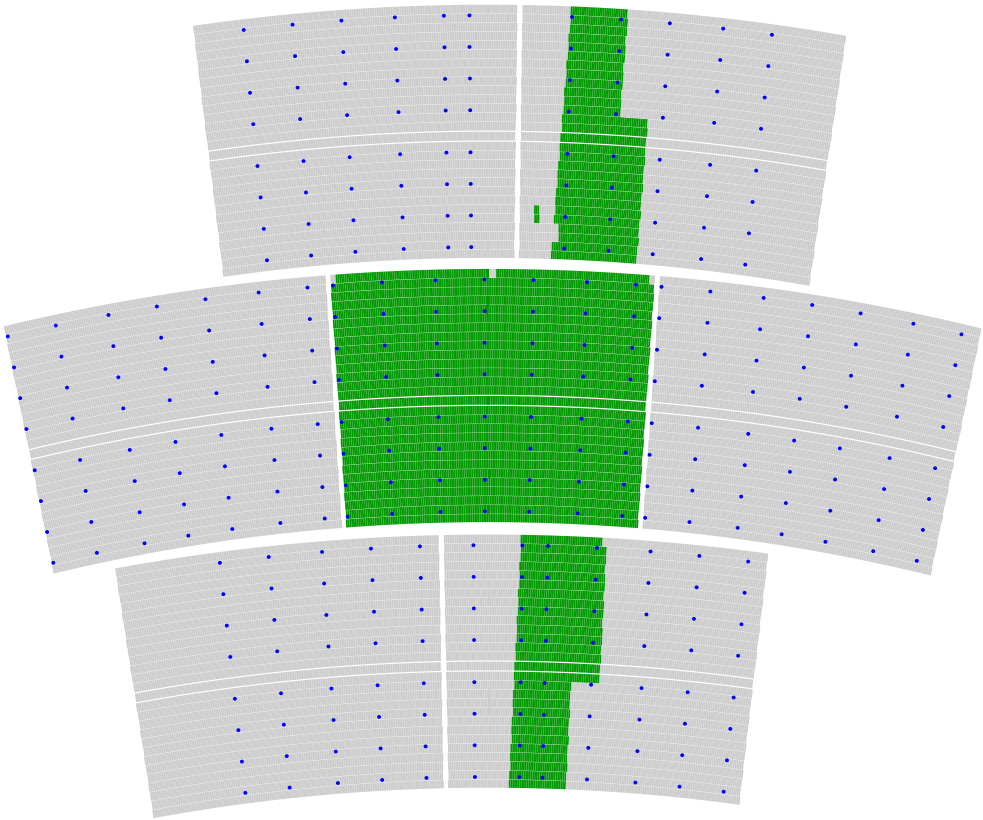

Figure 7.19: Layout of the seven LPTPC modules on the anode side. Pads that were read out in the laser test 2013 are shown in green. Blue dots illustrate the positions of the aluminium dots from the cathode projected to the anode. The projection of dots that are not on a module are not shown.

entries, which is the product of the number of readout channels $N_{\text{ch.}}$ and the number of recorded time bins N_{t}. A small peak at the end of the spectrum can be observed, which is around 925 ADC counts. The entries in this region correspond to charges, which were above the ADC range and ended up in the last ADC bin. This is at 1024 ADC counts, since the electronics uses 10 bits in the digitisation. In Figure 7.20a entries above the ADC range are not at 1024 ADC counts but in the peak around 925 ADC counts, because for each channel the channel dependent pedestal value was subtracted. This also shows that the pedestal value is approximately 100 ADC counts. Finally, the fraction of entries in the peak at the end of the spectrum is sufficiently small.

MicroMegas module test

In the second measurement campaign in 2014 seven MicroMegas modules were available and mounted in the LPTPC. With the electronics introduced in Section 4.4.2 all channels

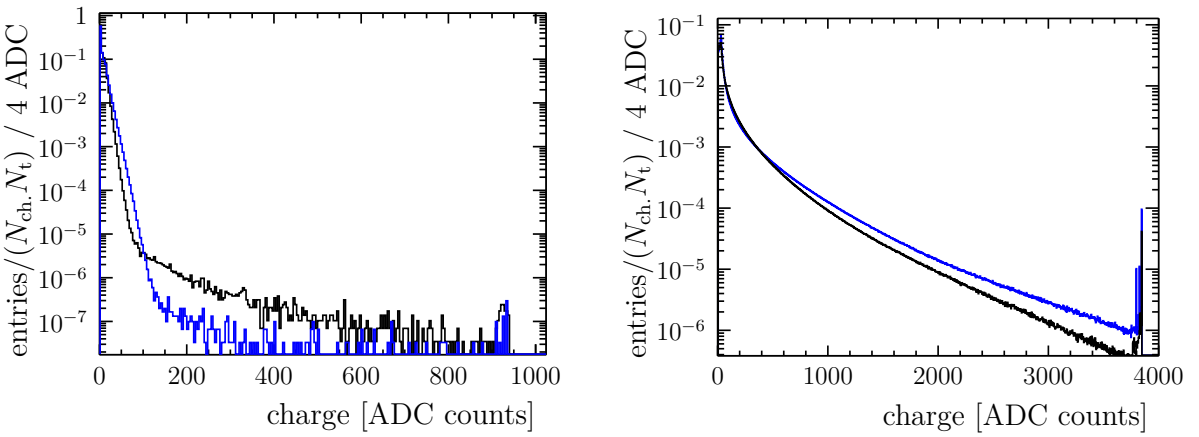

(a) DESY GridGEM module data recorded with the ALTRO electronics.

(b) MicroMegas module data recorded with AFTER chip based electronics.

Figure 7.20: Charge per time bin collected on a single pad for the DESY GridGEM module data. The plots contain the data of all time bins and all channels of a single run with 10000 laser shots taken at $E_{\text{drift}} = 240\,\text{V/cm}$. The number of entries per bin is normalised to the number of all entries.

of all modules could be read out. Unfortunately one of the modules (bottom left) broke during prior test beam measurements in the test campaign. The module was left installed in the LPTPC and the voltage on the mesh was floating. For all other modules the voltage of the mesh was set to $V_{\text{mesh}} = 420\,\text{V}$. The recorded charge per time bin for readout channels in the case of the MicroMegas module data is shown in Figure 7.20b. A similar behaviour as in the case of the DESY GridGEM spectrum can be observed. In case of the MicroMegas electronics 12 bits are used in the digitisation resulting in the maximum ADC bin of 4096 ADC counts. The peak at the end of the spectrum is around 3820 ADC counts, which shows that the subtracted pedestal value is approximately 275 ADC counts. The number of entries in this peak is small compared to the total number of entries, which indicates that the considered gain in the measurements was proper.

Pulse reconstruction in MarlinTPC

The pulse reconstruction of both data sets – DESY GridGEM module data and MicroMegas module data – is done as described in the Section 7.1. The software used for the pulse reconstruction is called MarlinTPC [92], which is part of the analysis frame work Marlin [93]. The whole frame work is designed to analyse data on an event basis. For each event algorithms, called processors, can be used to analyse input data and possibly produce output data. It is also possible to run a chain of different processors which process the input

data sequentially. The chain of processors used to reconstruct pulses of the laser test is show in Figure A.5, where it it can be seen that in addition to the pulse reconstruction first of all the raw data is converted into the data format used by MarlinTPC and the pedestals are subtracted. After the pulse reconstruction the electronics channel numbers are connected to the individual pads of the pad plane, which means that the position where the pulse was recoded on the anode pad plane is assigned to the channel numbers.

As introduced in Section 7.1 different additional requirements can be used to define signal pulses. In the DESY GridGEM module pulse reconstruction a minimum pulse height of $Q_{\max} > 8\,\text{ADC}$ counts and a minimum length of 5 time bins is required. In the MicroMegas module pulse reconstruction a requirement of $Q_{\max} > 30\,\text{ADC}$ counts is used and sufficient to select well defined pulses. In both analysis the inflection point is used to calculate the pulse time. Furthermore, in the DESY GridGEM module pulse reconstruction the integral charge is used to define the pulse charge, whereas in the MicroMegas module pulse reconstruction the maximum charge value defined the pulse charge.

7.3.5 Pulse time analysis

In the following the arrival time of pulses is analysed. Since the signal is always produced at the same position in the LPTPC, this time should be similar for all pulses. Only the longitudinal diffusion of the signal electrons causes a spread of the signal in time, since the laser pulses are very short. Therefore, the distribution of the pulse times should be described with a Gaussian distribution, where the width corresponds to the longitudinal diffusion and the mean corresponds to the time needed to drift through the whole TPC volume. In order to get the absolute drift time correct, the reconstructed pulse time needs to be corrected taking into account cables and electronics delays, as sketched in Figure 7.21. The time needed for the laser light to hit the cathode is:

$$t_{\text{light}} = \frac{l_{\text{fibre}}}{c_{\text{fibre}}} + \frac{l_{\text{drift}}}{c_{\text{gas}}} = (89.6 \pm 0.2)\ \text{ns},$$

where the speed of light in the different media (c_{fibre}, c_{gas}) is calculated using the corresponding refractive index ($n_{\text{fibre}} = c_0/c_{\text{fibre}} = 1.46$, $n_{\text{gas}} = 1$) and the speed of light in vacuum c_0. Furthermore, $l_{\text{drift}} = (567 \pm 1)$ mm is the maximum drift length of the LPTPC. The time for the trigger signal from the trigger diode to the trigger logic takes about $t_{\text{cable,1}} = 36\,\text{ns}$. Since the trigger logic and cables to the electronics were different in the different campaigns they are introduced in the following sections.

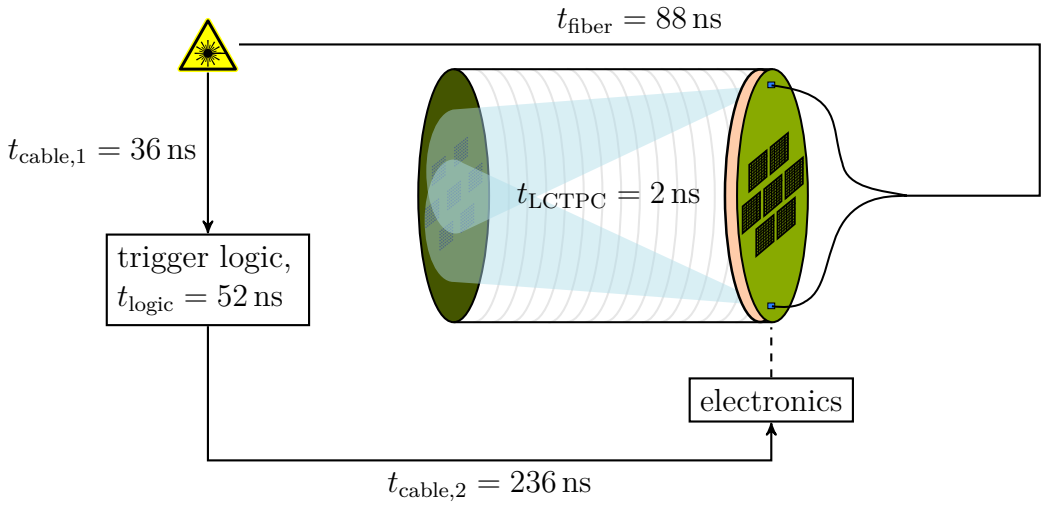

Figure 7.21: Sketch of relevant delays in the laser test. Quoted times correspond to the test with the ALTRO electronics in combination with DESY GridGEM modules.

Finally, the corrected drift time can be used to calculate the drift velocity, which can be compared to expected values from simulations with Magboltz.

DESY GridGEM module pulse data

In order to correct the time measured by the electronics, in addition to the times already introduced in the previous section, also the time of the trigger logic ($t_{\text{logic}} = 52\,\text{ns}$) and the time from the trigger logic to the electronics ($t_{\text{cable,2}} = 236\,\text{ns}$) was measured. If the laser fires, the trigger signal needs $t_{\text{trigger}} = t_{\text{cable,1}} + t_{\text{logic}} + t_{\text{cable,2}} = (324 \pm 3.5)$ ns to start the electronics assuming an uncertainty of 2 ns for the concerned times. What also needs to be taken into account, is that the ALTRO electronics stores additional 15 time samples before the trigger signal. Therefore, the electronics stores pulses that arrive up to $t_{\text{presample}} = 750\,\text{ns}$ before the trigger signal, since the sampling frequency is 20 MHz.

Furthermore, also the time needed by the electrons to pass the GEM stack needs to be corrected, since this region does not belong to the drift region and the drift velocity is different in this region. In order to estimate this time, a triple GEM simulation introduced in Chapter 5 was used. Here electrons are drifted through the GEM stack to the anode, and the corresponding time needed for the drift is found to be $t_{\text{stack}} = (248.2 \pm 5)\,\text{ns}$ for the conditions used in the measurements. This is only a simple approach of estimating t_{stack}, since an induced signal in the anode pads will also be recorded by the electronics

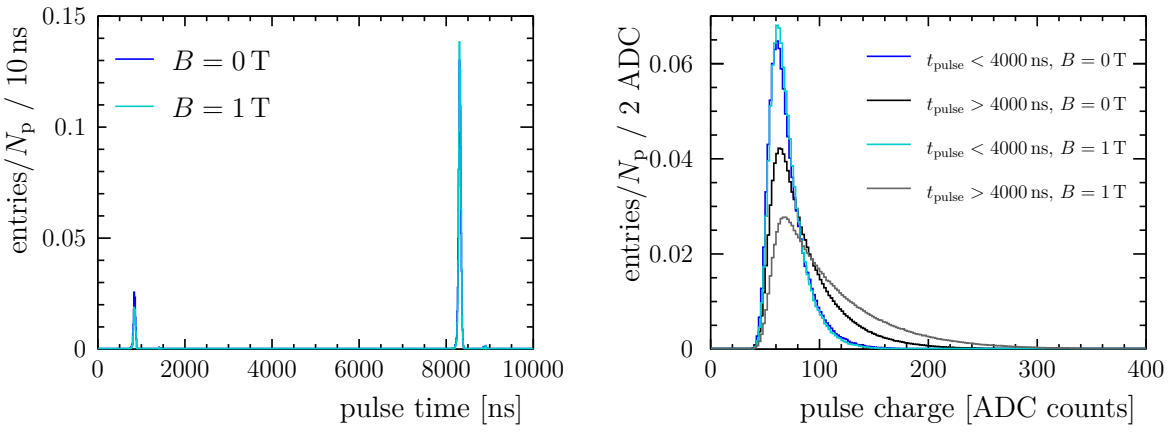

(a) Pulse time. **(b)** Pulse charge.

Figure 7.22: Reconstructed charge and pulse time for all pulses of a complete run for the DESY GridGEM module data. The drift field is $E_{\text{drift}} = 240\,\text{V/cm}$.

before the electrons arrive at the anode pads. The treatment of such effects requires a dedicated simulation including the simulation of the exact shaper response or a dedicated measurement, which is not part of this thesis.

Last but not least, the reconstructed pulse time needs to be corrected, since it does not correspond to the beginning of the pulse. This can be seen in Figure 7.1b, where the pulse time calculated with using the inflection point is $t_{\text{pulse}} = 3.6\,\text{time bins}$. The starting time t_0 calculated from the fit of the pulse shape using the shaper function is $t_0 = 1.2\,\text{time bins}$. The means the calculated pulse time needs to be corrected by 2 time bins ($t_{\text{pulse}} = 100\,\text{ns}$) in order to calculate the beginning of a pulse. Finally, the pulse time needs to be corrected by:

$$t_{\text{correction}} = t_{\text{light}} + t_{\text{presample}} + t_{\text{stack}} + t_{\text{pulse}} - t_{\text{trigger}} = (864 \pm 6.1)\ \text{ns},$$

which corresponds to (17.3 ± 0.1) time bins.

Discussion of the pulse spectrum

Figure 7.22a shows the raw pulse time spectrum, without applying the time shift introduced in the previous section. The entries in this figure are normalised to the total number of pulses N_p collected during a whole run of 10000 events. No significant difference between the $B = 0\,T$ and $B = 1\,T$ taken at $v_{\text{drift}} = 240\,\text{V/cm}$ is observed. The majority of the pulses is found in two regions, which are well separated in time. The pulse time distribution

is fitted with the sum of two Gaussian distributions

$$f(t) = A_1 \exp\left(-\frac{(t-t_1)}{2\sigma_1^2}\right) + A_2 \exp\left(-\frac{(t-t_2)}{2\sigma_2^2}\right), \tag{7.12}$$

which shows that the first region is centred around $t_1 = 841.4\,\text{ns}$ and the second region is centred around $t_2 = 8311\,\text{ns}$. Taking the time correction calculated above into account it turns out, that pulses in the first region are produced nearly at the same time as the laser pulse arrives in the TPC. The difference between the time correction and the peak position ($t_1 - t_{\text{correction}} = -23\,\text{ns}$) is less than one time bin (50 ns) and therefore it is not possible to say if such pulses are produced before, after or simultaneously to the laser pulse.

In addition, to the pulse the position of the peaks in the pulse time spectrum also the width of the peaks is of interest. For the signal pulses the width should be dominated by the longitudinal diffusion, which is $D_l = 221\,\mu\text{m}/\text{cm}^{1/2}$ at a drift field of 240 V/cm in T2K gas. For the maximum drift distance of the LPTPC and a drift velocity of 76 µm/ns, as calculated in the following section, one expects a width of $\sigma_{D_l} = 22\,\text{ns}$, which is close to the observed pulse time peak width in case of the signal pulses ($\sigma_2 = 28\,\text{ns}$ from Figure 7.22a). The slightly larger observed width can be attributed to minor effects like for example the longitudinal diffusion in the GEM stack or the pulse width of the laser.

In order to figure out the source of the pulses in the regions around t_1 and t_2, the position of the pads on the anode connected to the pulses can be investigated. Figure 7.23 shows the charge collected per pad integrated over a whole run and the central readout module. A time cut is used to investigate pulses from the two regions separately. For pulses in the second region ($t_{\text{pulse}} > 4000\,\text{ns}$) shown in Figure 7.23b clearly the pattern originating from the cathode is visible. In the following, pulses corresponding to this region are referred to as signal pulses. Contrary to this, no pattern is visible in Figure 7.23a, where a cut of $t_{\text{pulse}} < 4000\,\text{ns}$ is applied. Such pulses are in the following referred to as noise pulses.

Apart from the difference of the pulse position on the anode between noise and signal pulses, two more differences could be seen so far. There are approximately ten times less noise pulses (Figure 7.22a) and these pulses have less charge (Figure 7.23) compared to the signal pulses.

This can also be seen in Figure 7.22b, where the pulse charge is shown for both types of

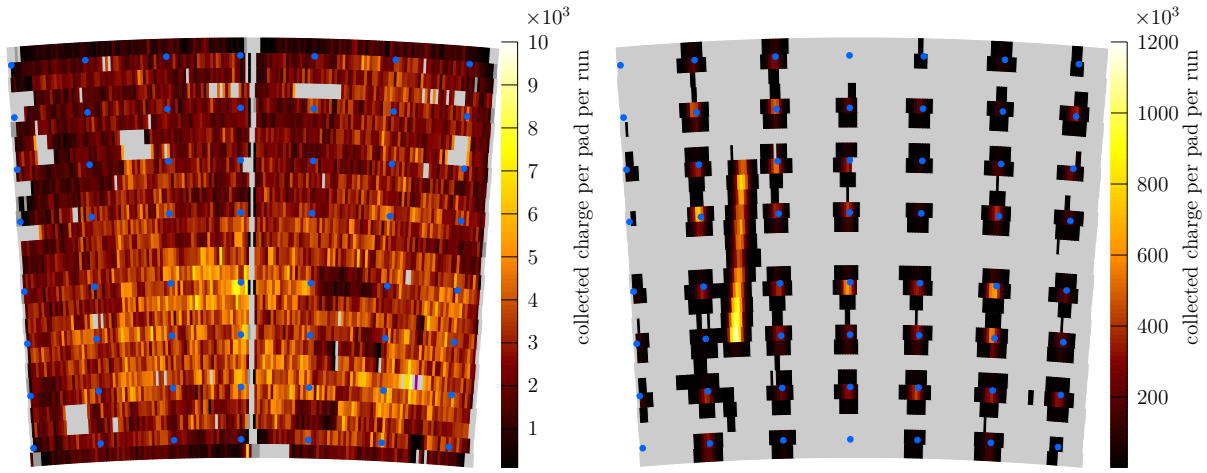

(a) Pulse charge for pulses with $t_{\text{pulse}} < 4000\,\text{ns}$. **(b)** Pulse charge for pulses with $t_{\text{pulse}} > 4000\,\text{ns}$.

Figure 7.23: Accumulated charge per pad for a single run at $B = 1\,\text{T}$ and $E_{\text{drift}} = 240\,\text{V/cm}$ for the DESY GridGEM module data. Pads that collected less than 1 % of the total charge are shown in grey.

pulses. Furthermore it can be seen, that the charge distribution of signal pulses is more asymmetric compared to noise pulses. For signal pulses this is expected, since the number of electrons, which is proportional to the charge, results from a convolution of a Poisson distribution for the electron liberation at the cathode and a Polya distributions for the amplification in the GEM stack (see Section 6.5). The charge distribution of noise pulses is more narrow, leading to a smaller mean charge.

In order to understand the origin of the noise pulses, the pulse time distribution for three runs with different light intensities on the cathode is investigated. The three runs are taken at $B = 0\,\text{T}$ and $E_{\text{drift}} = 240\,\text{V/cm}$. One run was taken with both shutters open and the other two with one shutter closed, which in consequence means that in case of shutter B is closed the fewest amount of light enters the LPTPC (see Section 7.3.2). Results of the fits to the two regions using the fit function given in Equation 7.12 are summarised in Table 7.7. Parameters with the subscript 1, correspond to parameters of the Gaussian distribution describing the noise pulses and parameters with the subscript 2 characterise the signal pulse distribution. Since the standard deviation is similar for all fits, the parameters A_1 and A_2 are proportional to the number of noise and signal pulses. The comparison shows a decrease in the number of signal pulses, corresponding to a decrease of A_1 and A_2, with the decrease of light provided by the laser. This indicates that both types of pulses are connected to the laser itself. Thus, these pulses can not be attributed to the electronics or the trigger signal. The ratio between the number of pulses in both regions given in

Table 7.7: Resulting parameters of fits to the pulse time spectrum using Equation 7.12.

	t_1 [ns]	t_2 [ns]	σ_1 [ns]	σ_2 [ns]	A_1	A_2	A_2/A_1
Shutters open	841	8311	23.3	28.2	$8.28 \cdot 10^4$	$4.18 \cdot 10^5$	5.05
Shutter A closed	841	8312	23.5	29.2	$6.33 \cdot 10^4$	$2.57 \cdot 10^5$	4.06
Shutter B closed	843	8318	25.0	31.5	$1.72 \cdot 10^4$	$6.72 \cdot 10^4$	3.91

Table 7.7 is not constant, which indicates a small dependence on the fibre and the point where the light enters the LPTPC. Furthermore in a run, where all GEMs were switched off at a certain point, it could be seen that no pulses at all could be found from this point on. This supports the statement, that the noise pulses can not be attributed to the electronics or other possible sources.

In summary, the noise pulses are produced almost instantaneously when the laser light enters the TPC. Furthermore, the number of noise pulses and their charge depends on the light intensity of the laser. No spatial structure could be observed for noise pulses and the pulse charge is less compared to signal pulses produced on the cathode. All together this indicates that the noise pulses are produced by the laser light in the LPTPC. Most likely the light is reflected inside the field cage and a subsequent signal production close to or in the amplification stage of the readout module takes place via the photoelectric effect in copper.

The noise and the signal pulses can be easily selected with a time cut and in the following only the signal pulses will be investigated. Moreover, the fact that the noise pulses are produced almost instantaneous can be exploited to calibrate the pulse time, if the calibration time is not known from a direct measurement.

DESY GridGEM module drift velocity

In order to calculate the drift velocity the mean pulse time for signal pulses needs to be calculated. Here signal pulses are selected by the pulse time cut $t_{\text{pulse}} > 4000$ introduced in the previous section. For all pulses passing this time cut the mean time is calculated. Knowing the signal is produced at the cathode and the total drift length of the LPTPC, the measured drift velocity can be calculated. Figure 7.24 shows the result for different drift fields. Runs with and without magnetic field are included, since the drift velocity does not depend on the magnetic field. The uncertainties shown in this plot result from the width of the pulse time distribution, as shown in Figure 7.22a. The root mean

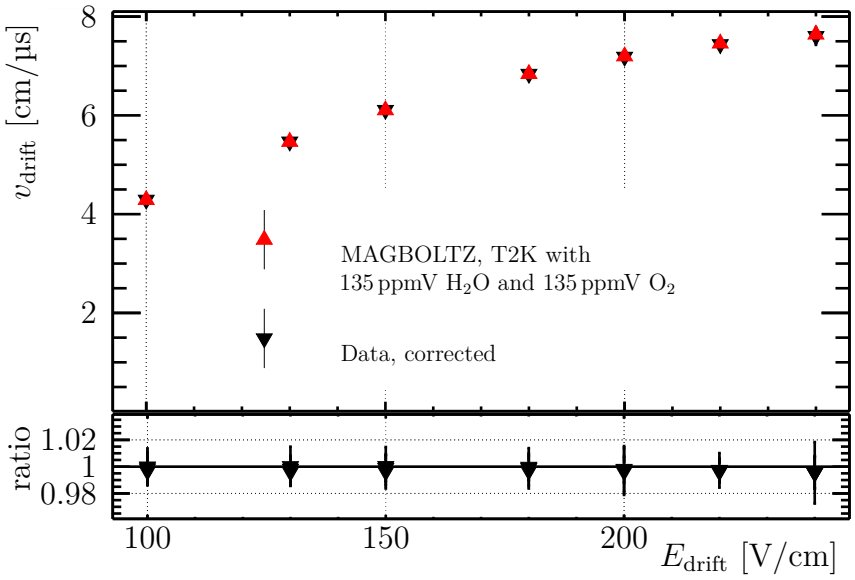

Figure 7.24: Drift velocity measured with DESY GridGEM modules. For the MAGBOLTZ simulation a water content of 135 ppmV and an oxygen content of 135 ppmV is added to the T2K gas to match the measurement conditions. The reconstructed time for data points is corrected by 17 time bins.

square value is considered as estimate for the uncertainty of the time. This uncertainty ($\mathcal{O}(0.1\,\text{cm/µs})$) is the dominant contribution to the drift velocity uncertainty compared to the uncertainty resulting from the drift length $l_{\text{drift}} = (567 \pm 1)$ mm ($\mathcal{O}(0.01\,\text{cm/µs})$). Finally, the resulting drift velocities were compared to results of a MAGBOLTZ simulation. In the simulation T2K gas with a water content corresponding to the value measured during the laser tests ($c_{H_2O} = 135\,\text{ppmV}$) was used, since it influences the drift velocity. In the MAGBOLTZ simulation the drift velocity at $E_{\text{drift}} = 240\,\text{V/cm}$ for example is reduced from $v_{\text{drift}} = (7.750 \pm 0.002)$ cm/µs to $v_{\text{drift}} = (7.639 \pm 0.002)$ cm/µs in presence of 135 ppmV H_2O and 135 ppmV O_2. The comparison between simulation and measurements is also shown in the ratio plot of Figure 7.24, which shows $v_{\text{drift,meas.}}/v_{\text{drift,sim.}}$. It indicates an agreement between the measurements and the simulation and the difference between both results is below one percent. The time shift used in this figure is 17 time bins, which corresponds to the shift calculated in the previous section. In addition, also other time shifts are tested in order to check, if the calculated one describes the data best. In order to get an estimator of the difference between the measurements and the simulation the following definition was used:

$$\chi^2 = \sum_i^{N_{\text{meas.}}} \frac{\left(v^i_{\text{drift,meas.}} - v^i_{\text{drift,sim.}}\right)^2}{\left(\Delta v^i_{\text{drift,meas.}}\right)^2 + \left(\Delta v^i_{\text{drift,sim}}\right)^2} \tag{7.13}$$

Table 7.8: χ^2 for DESY GridGEM and MicroMegas modules obtained when comparing the measured and simulated drift velocity for different time shifts applied to the measured data.

GEM module	time shift/50 ns	16	17	18	19	20
	χ^2	3.48	0.39	0.66	4.30	11.36
MicroMegas module	time shift/40 ns	25	26	27	28	29
	χ^2	1.54	1.13	0.97	1.82	3.34

The minimum of χ^2 corresponds to the best agreement between measured data and simulated data. In the analysis of different time shifts, the minimum χ^2 is found for a time shift of 17 time bins (see Table 7.8), which agrees with the calculated time shift.

MicroMegas module pulse data

Similar to the time corrections applied to pulses of data taken with the DESY GridGEM module, also the pulse time of MicroMegas data needs to be corrected. The number of time samples stored before the first sample over threshold is 10. Taking the sampling frequency of 25 MHz into account the electronics starts data taking $t_{\text{presample}} = 400\,\text{ns}$ before the trigger signal.

Figure 7.25 shows the raw distribution of pulse charge and pulse time. Again two regions of the pulse time, where most of the pulses are reconstructed, can be identified taking also the projection shown in Figure 7.25b into account. Similar to the GEM data also here the projection is fitted using Equation 7.12. Contrary to the DESY GridGEM module data here the first peak around $t_1 = 1099\,\text{ns}$ ($\sigma_1 = 36\,\text{ns}$) includes much less entries compared to the signal peak (see detail view of Figure 7.25b). The signal peak around $t_2 = 8459\,\text{ns}$ ($\sigma_2 = 51\,\text{ns}$) is only fitted partially, since on the right hand side an additional exponentially falling number of pulses are reconstructed. Such pulses, which are also visible in Figure 7.25a, can be attributed to the usage of a resistive foil in the case of the MicroMegas module. The resistive layer on top of the pads leads to a signal propagation in this layer (see Section 3.4.2). This causes a delayed signal induction in pads close to the central pad below the charge distribution produced in the amplification process. With increasing distance to the central pad the induced charge decreases and in addition the charge is induced delayed, which is visible in Figures 7.25a and 7.25b. Such a behaviour can not clearly be observed for the pulses in the noise peak of the pulse spectrum. The

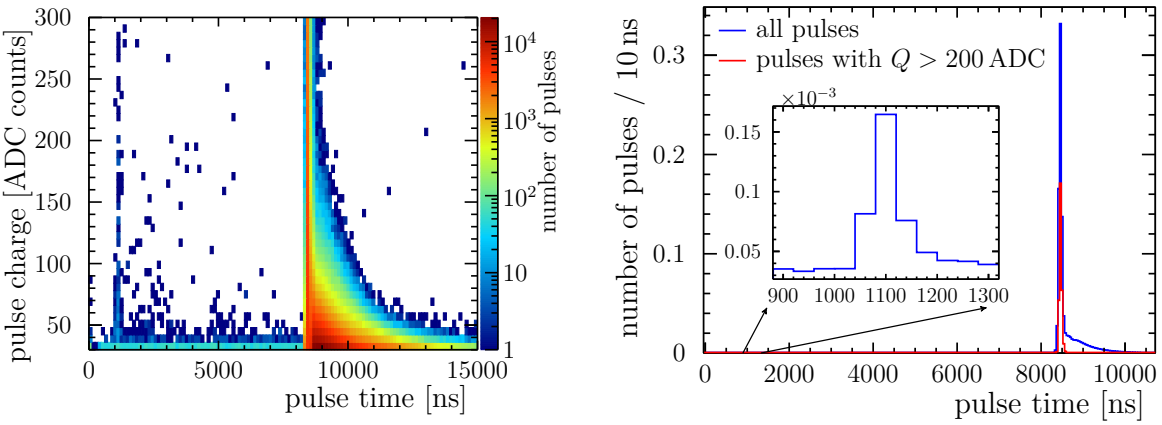

(a) Pulse time versus pulse charge for $B = 1\,\mathrm{T}$.

(b) Pulse time. The inlet shows a detail view of the region where the second peak in the spectrum is located. Note the different scale used for the detail view.

Figure 7.25: Reconstructed charge and pulse time for all pulses of a complete run for the MicroMegas module data. The drift field is $E_{\mathrm{drift}} = 240\,\mathrm{V/cm}$.

charge connected to noise pulses compared to the signal pulse region is very small. A small charge on the central pad below the avalanche results in an even smaller induced signal on the neighbouring pads. Therefore, induced signals are most probably below the electronics threshold and thus not visible in Figure 7.25.

In order to select only pulses in the centre of the charge distribution produced in the amplification process a charge cut can be applied. Here the cut $Q_{\mathrm{pulse}} > 200$ ADC bins is used to select such pulses. The resulting pulse spectrum using this cut is shown in red in Figure 7.25b. Fitting the resulting pulse time distribution with a Gaussian distribution leads to a slightly larger width of $\sigma_2 = 40\,\mathrm{ns}$ compared to the measured width in GEM module data, which is because the pulse spectrum is still biased by pulses emerging from the charge transport in the MicroMegas foil.

MicroMegas module drift velocity

Similar to the analysis of the drift velocity measured with the DESY GridGEM modules, the drift velocity is analysed for MicroMegas module data. The only difference is that due to the MicroMegas module design the drift distance is 1 mm larger compared to the DESY GridGEM modules and the charge cut introduced above is used to select signal pulses instead of a time cut.

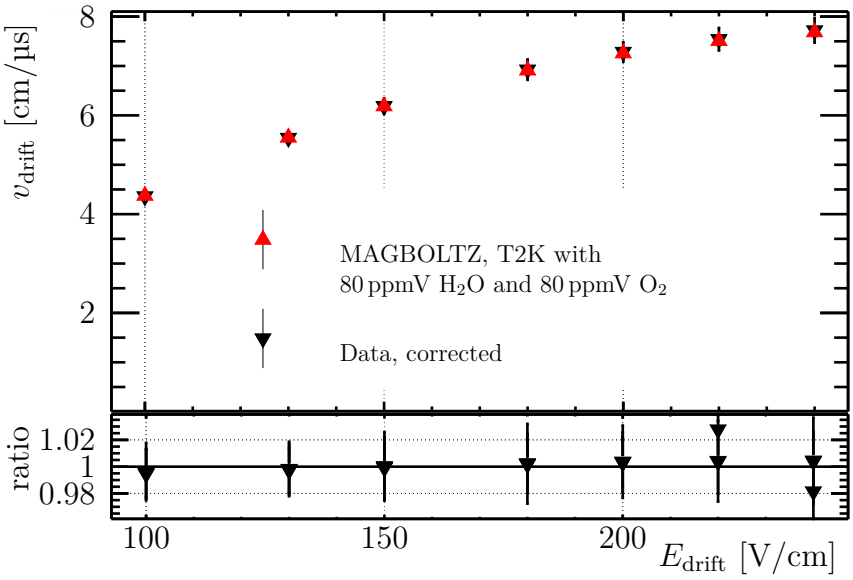

Figure 7.26: Drift velocity measured with the MicroMegas modules. A minimum pulse charge of 200 ADC bins is required for the considered pulses. For the MAGBOLTZ simulation a water content of 80 ppmV and an oxygen content of 80 ppmV is added to the T2K gas to match the measurement conditions. The reconstructed time for data points is corrected by 27 time bins.

The result of the analysis is shown in Figure 7.26, where the water contend considered in the MAGBOLTZ simulation is adapted to that, measured during the laser test with MicroMegas modules.

Again the time shift is varied and the χ^2 defined in Equation 7.13 is used to determine the time shift corresponding to the lowest χ^2. Here a time shift of 27 time bins corresponding to $t_{\text{shift}} = 1080\,\text{ns}$ leads to the best agreement between measurement and simulation (see Table 7.8). This time corresponds again to the peak position at $t_1 = 1099\,\text{ns}$ of the first peak in the pulse time spectrum.

7.3.6 Reconstruction of the signal from the cathode pattern with MarlinTPC

In order to evaluate field distortions in the LPTPC the position of the signal from the alumina dots on the cathode needs to be reconstructed. This reconstruction follows after the reconstruction of the pulses and can be seen as a post-reconstruction step. Similar to the pulse reconstruction introduced in Sections 7.1 and 7.3.4 the cluster reconstruction is done using the MARLINTPC frame work. The reconstruction of signals from the pattern alumina dot pattern on the cathode is split into two parts:

1. Search for pads on the anode pad plane that collect signals from alumina dots.
2. Collection of all pulses on the pads resulting from the search and reconstruction of the centre positions.

For the pad search done in the first step all pulses of a complete run are considered. With respect to MarlinTPC this means, that the corresponding processor (*PhotoelectricPulseExtractionProcessor* can not run sequentially after the pulse reconstruction processors on the same event, but it needs to be run on the whole data set of a measurement run, which is unusual for MarlinTPC where processors are basically event based. In the following the two steps of the reconstruction are introduced in detail.

Pad search

The idea behind the pad search is to preselect pads that collect pulses corresponding to electrons that are liberated from the alumina dots on the cathode. Input data for the pad search are reconstructed pulses and the true measured positions of the alumina dots on the LPTPC cathode. These positions are well known and have an position uncertainty of 0.01 mm. In the beginning all pulses, which are within a given time window, are searched and the corresponding pads of the anode pad plane are selected. This is sufficient to select pads that collect signal pulses out of all pads of the pad plane. The time cuts that are used for the pulse selection are the same as those used to select signal pulses in the pulse time analysis.

After processing all pulses of a whole run the selected pads are further analysed in order to find clusters of pads. An additional possibility to reduce noise in the pad search process is to require a certain fraction of events f_{event} having a pulse on the pad that is investigated. If this requirement is not fulfilled the pad is removed from the list of selected pads. In particular in the analysis of the MicroMegas data parameter can be used to tune the pad search. Since the pads of the MicroMegas pad plane are larger than the pads of the DESY GridGEM pad plane, some clusters corresponding to individual alumina dots are merged and other clusters with less charge are not found respectively depending on the chosen value of f_{event}. In order to deal with this problem, runs can be reconstructed twice. On the one hand a low value of f_{event} is used to find clusters with less charge. On the other hand a higher value of f_{event} is used to split clusters with a lot of charge, which otherwise spread too much due to the resistive foil of the MicroMegas module and merge into one cluster.

The found pads and corresponding clusters of both reconstructions are finally combined and afterwards used in the cluster forming.

The cluster forming is done based on the list of found pads. A regular grid with a spacing of 1 mm is used to created grid points for all pads of the list. This means for a pad of 1 mm × 5 mm 5 grid points are created. Now these grid points are used instead of the pads to form clusters. The cluster building starts with a certain point of the grid. As long as grid point neighbours of this point are found they are added to the cluster if the distance to the closest point found so far is below a given threshold. This is done also for the neighbours and so on until no neighbours are found anymore. Finally, a first estimator of the cluster centre is calculated as the weighted arithmetic mean pad position in the cluster, where the number of pulses per pad per run is used as weight.

After the cluster forming, the clusters are categorised. If a cluster contains more than 10 pads it is assumed to correspond to the signal of a alumina line on the cathode. Else the cluster is assumed to correspond to the signal of an alumina dot.

Clusters categorised as corresponding to a alumina dot are further analysed. The distance to the nearest true alumina dot position is calculated. If this distance is below a certain distance it is associated to this alumina dot. Else the cluster is stored as unassociated. The information of the considered time window and the associated and unassociated clusters are stored in an intermediate `xml` file.

Calculation of the reconstructed alumina dot positions

The `xml` produced by in the previous reconstruction step is used together with reconstructed pulses to calculate the reconstructed alumina dot positions. In the beginning, all pulses associated to alumina dot positions or the alumina lines are collected and stored in individual new pulse collections. In this pulse selection process again the time window cut already used in the previous reconstruction step is used to select signal pulses. The resulting pulse collection could be used for an event by event based reconstruction of the alumina dot positions, if enough pulses per alumina dot are found. If not, a second possibility is to collect all pulses of the run and analyse them all together. This is done here and presented in the following.

The final reconstruction of the alumina dot positions is performed on all pulses per run associated to alumina dots. First, an estimator of the alumina dot position analogue to the one calculated in the pad search process is calculated. The weight used here is the

pulse charge instead of the number of pulses per pad per run. This position serves as seed for a minimum likelihood estimation. The idea is, that the charge cloud originating from an alumina dot forms a two dimensional Gaussian distribution on the pad plane, which is defined in global coordinates x and y. This Gaussian distribution has a width $\sigma_x = \sigma_y = \sigma$ corresponding to the sum of the transverse diffusion in the sensitive and the amplification region of the TPC. For a certain assumed alumina dot position (in the first step the seed) the charge contributions from all considered pulses are added, via the integration of the Gaussian distribution using the error function (Erf). The corresponding likelihood estimator, which needs to be minimised, is defined as:

$$X = \mathrm{Erf}\left(\frac{\Delta x + w_{\mathrm{pad}}/2}{\sqrt{2}\sigma}\right) - \mathrm{Erf}\left(\frac{\Delta x - w_{\mathrm{pad}}/2}{\sqrt{2}\sigma}\right) \tag{7.14}$$

$$Y = \mathrm{Erf}\left(\frac{\Delta y + h_{\mathrm{pad}}/2}{\sqrt{2}\sigma}\right) - \mathrm{Erf}\left(\frac{\Delta y - h_{\mathrm{pad}}/2}{\sqrt{2}\sigma}\right) \tag{7.15}$$

$$L = \sum_{i=1}^{N_{\mathrm{pulses}}} -\log\left(\frac{X_i Y_i}{4}\right) q_i, \tag{7.16}$$

where Δx and Δy are the distances from the pad centre to the current reconstructed alumina dot position in x and y direction during the minimisation process. The expected width of the charge cloud σ is an input parameter of the processor and it is used as start parameter for the likelihood minimisation. Finally, the minimisation of L results in the estimated alumina dot position and reconstructed width of the measured charge cloud, which are stored to be used further as described in Section 7.3.8. If no minimum is found the seed position is stored instead.

For the event by event reconstruction of the alumina dot positions the same algorithm can be used, where instead of all pulses per run only the pulses of the event associated the analysed pads associated to a alumina dot are considered.

7.3.7 Pulse position analysis

The data taken in the measurement campaigns was analysed as described in the previous section. Since in the reconstruction of the signals from the alumina dots clusters of pads are analysed, in the following first of all these clusters are characterised. Characteristics of the reconstruction of the signal pattern are shown in Figure 7.27 for DESY GridGEM module and the MicroMegas module data at $B = 0\,\mathrm{T}$ and $B = 1\,\mathrm{T}$.

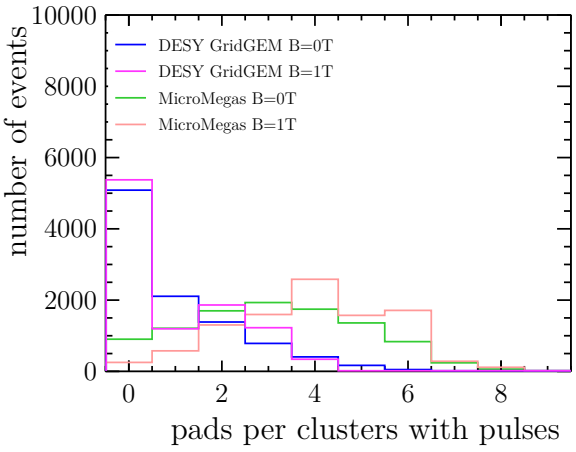

(a) Number of anode pads per cluster that collected at least one pulse in the considered event.

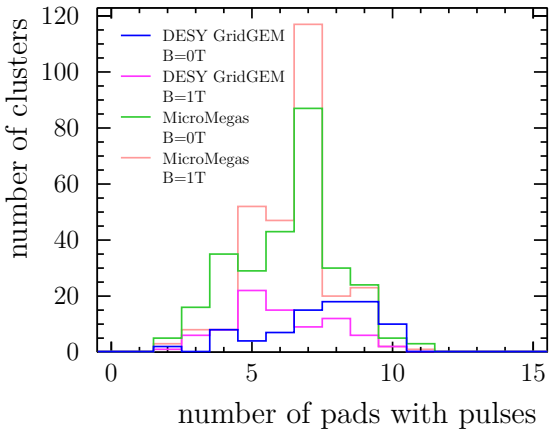

(b) Number of anode pads per cluster that collected at least one pulse in the considered run.

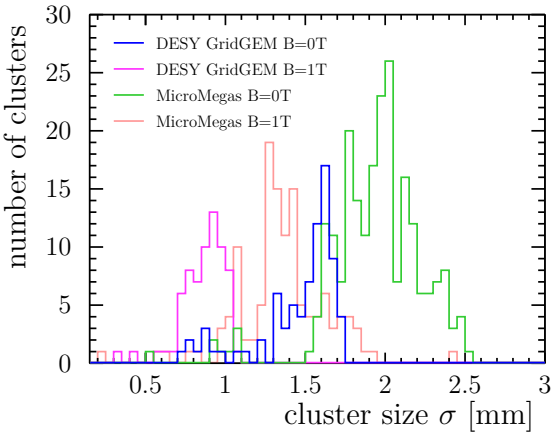

(c) Calculated cluster size resulting from the Likelihood fit of the cluster centre.

Figure 7.27: Characteristics of the cluster reconstruction with DESY GridGEM and MicroMegas modules at $B = 0\,\mathrm{T}$ and $B = 1\,\mathrm{T}$.

First of all Figure 7.27a shows the number of pads per cluster per event that collected enough charge to reconstruct a pulse. This figure includes the data of one run with 10000 events for each shown data set, which means the integral of the shown curves is 10000. It can be seen that in particular for the DESY GridGEM in half of the events no pads with pulses were found. In the case of the MicroMegas module data mostly four pads per cluster collected at least on pulse. Most likely the larger number of pads collecting pulses per event with respect to the DESY GridGEM module results from a higher gain of the MicroMegas modules in the measurements in combination with the resistive foil and the larger pad size. The number of pads with pulses in the case of the MicroMegas module data would also allow to reconstruct the alumina dot positions per event. In the case of the

Table 7.9: Resulting parameters of the fits of the cluster size using a Gaussian distribution, where the cluster size is the mean and σ_{fit} is the standard deviation of the fit.

	DESY GridGEM		MicroMegas	
	$B = 0\,\text{T}$	$B = 1\,\text{T}$	$B = 0\,\text{T}$	$B = 1\,\text{T}$
cluster size [mm]	1.6	0.9	2.0	1.4
σ_{fit} [mm]	0.2	0.1	0.2	0.3

DESY GridGEM module the number of pads per cluster is not sufficient to allow a precise position reconstruction, which requires at least 2 pads per position.

Figure 7.27b shows the number of pads per cluster when all pulses of a complete run are considered. This run based approach increases the number of pads per cluster for both module types to about 7 pads per cluster. This allows a precise position reconstruction. As introduced in the previous section, the likelihood approach also allows to calculate the size σ of the reconstructed cluster. The resulting distributions of cluster sizes are shown in Figure 7.27c. All distributions are fitted using a Gaussian distribution in order to determine the mean cluster size. The results are given in Table 7.9, which shows that the cluster size is reduced for both module types in case of the magnetic field. This is expected since the transverse diffusion is reduced by the magnetic field. Taking into account the drift length in the sensitive volume of the LPTPC and between the GEMs with the corresponding fields it is possible to calculate the expected width of the electron cloud arriving on the anode pad plane:

$$\sigma_{t,\text{MB}}(B = 0\,\text{T}) = (2.9 \pm 0.1)\,\text{mm}$$
$$\sigma_{t,\text{MB}}(B = 1\,\text{T}) = (1.3 \pm 0.1)\,\text{mm},$$

where all values of the transverse diffusion are taken from Magboltz simulations (see Figure 7.36). The comparison with the measured cluster size shows, that it is smaller in the measurements. This is most likely because the charge at the outermost region of the charge cloud arriving at the anode pad plane is not large enough to exceed the electronics thresholds or the pulse reconstruction thresholds used for the noise suppression.

After discussing the general characteristics of the cluster reconstruction, in the following the reconstructed positions are discussed qualitatively in the case of the MicroMegas module data. In the reconstruction the time cut as introduced before to select only signal pulses is used for the GEM module data as well as for the MicroMegas module data. The charge

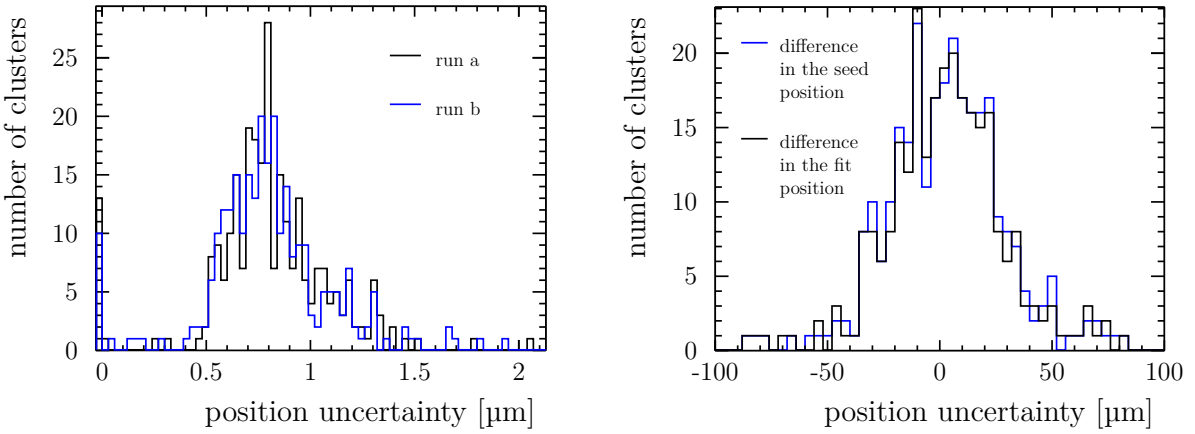

(a) Uncertainties resulting from the Likelihood fit for the two considered runs in $R\phi$ direction.

(b) Difference between the reconstructed alumina dot positions in $R\phi$ direction for run a and run b.

Figure 7.28: Results from the calculation of the uncertainty of the reconstructed alumina dot positions for two runs (a and b) that are taken with MicroMegas modules under the same conditions: $B = 0\,\mathrm{T}$ and $E_{\mathrm{drift}} = 240\,\mathrm{V/cm}$.

cut used for the MicroMegas module data in the pulse time analysis in Section 7.3.5 is not considered in the pulse position analysis. This means, that also pulses arriving delayed with respect to pulses from the centre of the cluster produced in the amplification process are considered. Applying the charge cut would remove all the side pulses of a cluster and possibly deteriorate the reconstruction of the cluster centre.

Uncertainty estimation

In order to estimate the uncertainty of the reconstructed alumina dot positions two approaches are used here. First of all in the uncertainty can be calculated from the Likelihood estimator used to calculate the alumina dot positions. This is done for the reconstructed alumina dots of one run taken at $B = 0\,\mathrm{T}$ and $E_{\mathrm{drift}} = 240\,\mathrm{V/cm}$. The Result is shown in Figure 7.28a, where the mean uncertainty of all reconstructed alumina dots is $0.8\,\mu\mathrm{m}$. A second possibility is to compare the resulting reconstructed positions between two runs taken at identical operation conditions ($B = 0\,\mathrm{T}$ and $E_{\mathrm{drift}} = 240\,\mathrm{V/cm}$). The corresponding result is shown in Figure 7.28b, where the comparison of the seed positions as well as the positions resulting from the Likelihood fit are included. In this analysis it was found, that the seed position calculated as the pulse charge weighted mean position of the pulses most often gives already a good position estimate and the Likelihood fit mostly improves the calculated alumina dot position only insignificantly. The

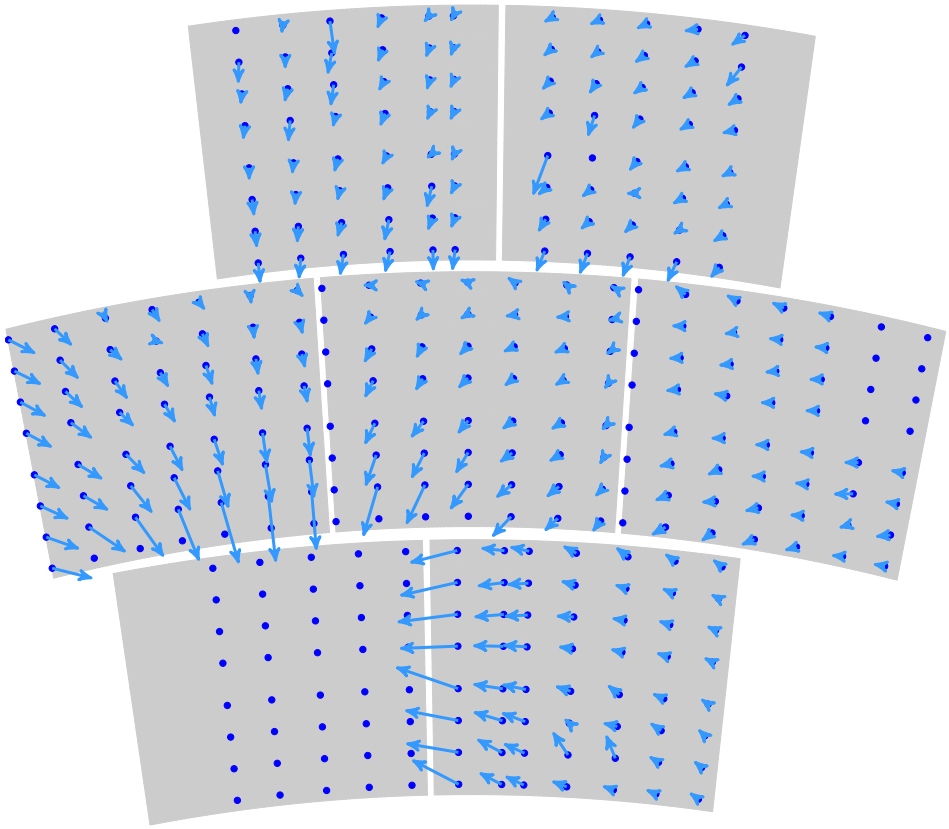

Figure 7.29: Reconstructed distortions measured with MicroMegas modules at $E_{\text{drift}} = 240\,\text{V/cm}$ and $B = 0\,\text{T}$. The distortions are scaled by a factor of four.

distributions shown in Figure 7.28b are centred around zero, which is expected for equal operation conditions. Furthermore, the standard deviation of the distribution resulting from a fit with a Gaussian distribution is $(20.7 \pm 0.1)\,\mu\text{m}$, which indicates that the resulting uncertainty from the Likelihood fit underestimates the uncertainty of the alumina dot position measurement.

In any case the uncertainty is below 30 µm, which is the accuracy required for the ILD TPC in order to keep the effect of field distortions on the momentum resolution below 5 %.

General discussion of the results

The qualitative result of the pulse reconstruction is shown in Figure 7.29, where the pad planes of all 7 modules mounted in the LPTPC anode are shown in grey. Dark blue points show the projection of the alumina dot positions on the anode pad plane and arrows point from these position in the direction of the reconstructed cluster centre. In this plot the

length of the arrow corresponds to the measured displacement scaled by a factor of four, in order to see the general trend. It can be seen that the neighbouring modules of the bottom left modules are effected by this module, which was broken and the potential on the MicroMegas foil was floating. Obviously this introduced large distortions of the drift field in the vicinity of the modules, which results in the observed displacements of the reconstructed alumina dot positions on the neighbouring modules. Furthermore, also field distortions between modules in normal operation condition, as studied in the Section 7.2 can be observed at the boundary between the top modules and the central modules. Finally, the right module in the central modules row, which is mostly unaffected by the distortions introduced by the bottom left module, indicates a constant displacement in one direction. This will be discussed later when the distortions are given quantitatively. The positions of the eight alumina dots at the top right corner of this module could not be reconstructed, because the ASIC connected to pads in this region was broken.

The situation in presence of the $B = 1\,\mathrm{T}$ magnetic field is shown in Figure 7.30 for to different positions of the LPTPC inside the magnet. When the LPTPC is in the magnet centre (Figure 7.30a) still the neighbouring modules of the bottom left module are affected by its introduced field distortions. Positions close to modules boundaries (see boundary between top modules and central modules) are no longer shifted towards the boundary, but they are shifted along the boundary. This effect was already discussed in Section 7.2. Furthermore, in the case of the top left module one can observe a displacement pointing away from the magnet centre, which is close to the bottom right corner of the central module in the $x - y$ plane. This effect is more pronounced in Figure 7.30b, which shows the displacement in the case of the LPTPC is moved 10 cm outside the magnet centre. Note that the arrows in this figure are scaled by a factor of two, which means the displacements in the shown situation are larger as in the cases discussed before. In general, Figure 7.30b shows the expected pattern of displacements, which point away from the centre of the magnet, introduced by the inhomogeneous magnetic field inside the LPTPC when it is moved outside the magnet centre.

Concluding the general discussion based on MicroMegas module data, it can be summarised that the observed displacements are in agreement with the expectations. The effects of local field distortions between module boundaries as discussed in Section 7.2 could be observed. Unfortunately three modules are affected by the broken module in the setup and bias the measurements of the overall field distortions.

Finally, the results Figure 7.31 illustrates the reconstruction of the alumina dot positions

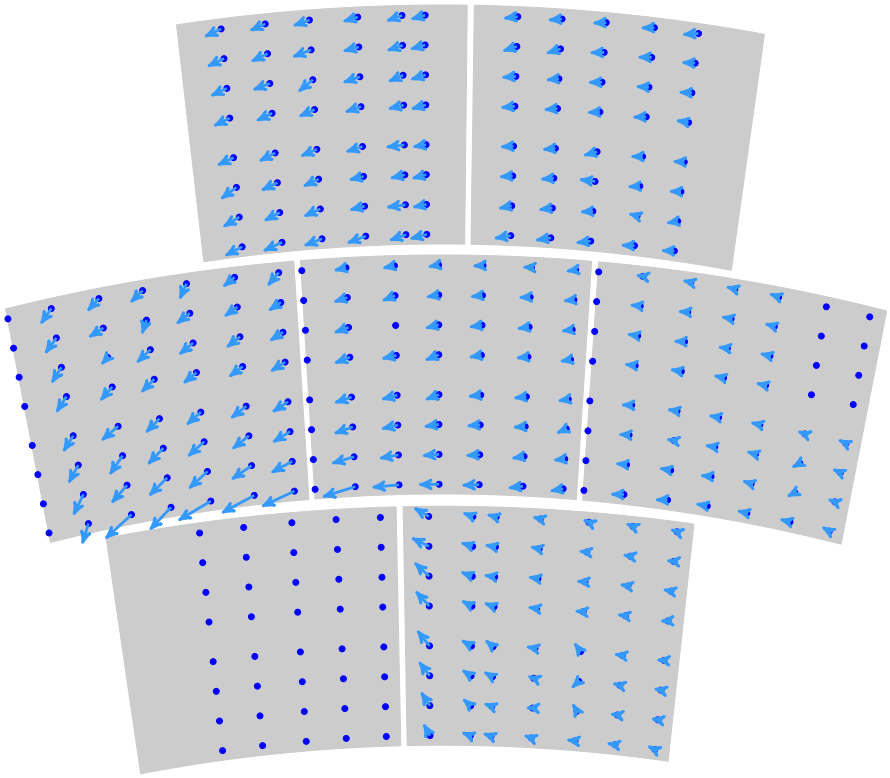

(a) The LPTPC is at the magnet centre. Displacements are scaled by a factor of four.

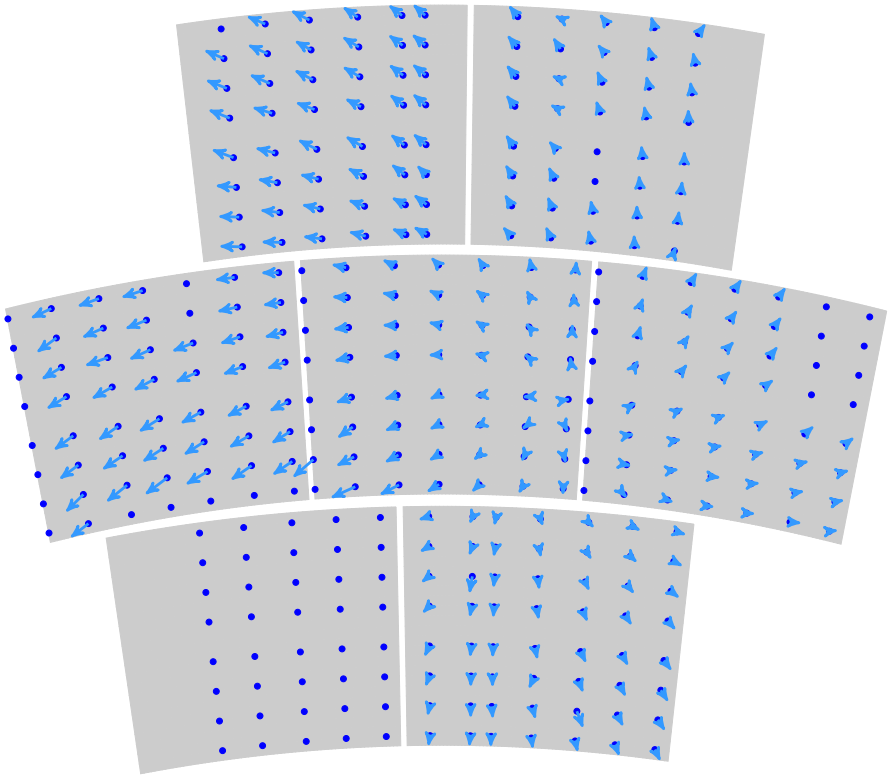

(b) The LPTPC is 10 cm outside the magnet centre. Displacements are scaled by a factor of two.

Figure 7.30: Reconstructed distortions measured with MicroMegas modules at $E_{\text{drift}} = 240\,\text{V/cm}$ and $B = 1\,\text{T}$.

based on the DESY GridGEM module data. Here the measured pulse charge per pad for the central DESY GridGEM module is shown. Again the arrows point from the expected projection of the alumina dot position towards the reconstructed alumina dot position. In order to see the general trend better, the arrows are scaled by a factor of five. Except for one cluster with a small amount of charge, all arrows point in the same direction. Thus, a constant distortion can be observed for the run shown in Figure 7.31, which was taken at $B = 1\,\mathrm{T}$ and $E_{\mathrm{drift}} = 240\,\mathrm{V/cm}$.

As shown in Figure 7.31 up to this point the field distortions can be calculated for each alumina dot. This means, the field distortions are know at these points on the anode pad plane, which allows to estimate a general trend of field distortions as shown above. If one wants to use the information about the field distortions in order to correct measured data one needs to know the distortions at every point of the pad plane. This would allow to correct the measured hit position, for example measured at the ILC, for the field distortion measured in dedicated calibration measurements with the laser system. In order to calculate the distortion at any point inside the module boundaries, the distortions are linearly interpolated as introduced in the following section.

7.3.8 Interpolation of measured distortions

As described above the idea is to measure field distortions with the laser calibration system in a dedicated measurement run and use the information about the field distortions to correct the data taken afterwards for example in runs with beam collisions at the ILC. This requires the knowledge of the field distortions at any point on the anode pad plane, since in principle hits will be found everywhere on the module in collision data. In the following it will be shown how the field distortions can be interpolated between the measured distortion of the individual alumina dots.

Similar to the calculation of the potential and the electric field at arbitrary points using the potential information at given points of a grid as introduced in Section 5.2, also here the distortion at an arbitrary point $\mathrm{P}(x, y)$ on the anode pad plane is calculated using the known distortions of the reconstructed projections of the alumina dots.

First, an element with four nodes defined by the positions of four reconstructed alumina dot positions needs to be constructed. The four element nodes (n_1, n_2, n_3, n_4) are required to form a quadrangle containing the given point $\mathrm{P}(x, y)$. One of such elements is illustrated in Figure 7.31, were D_i are the measured distortions at the element nodes. In detail, in

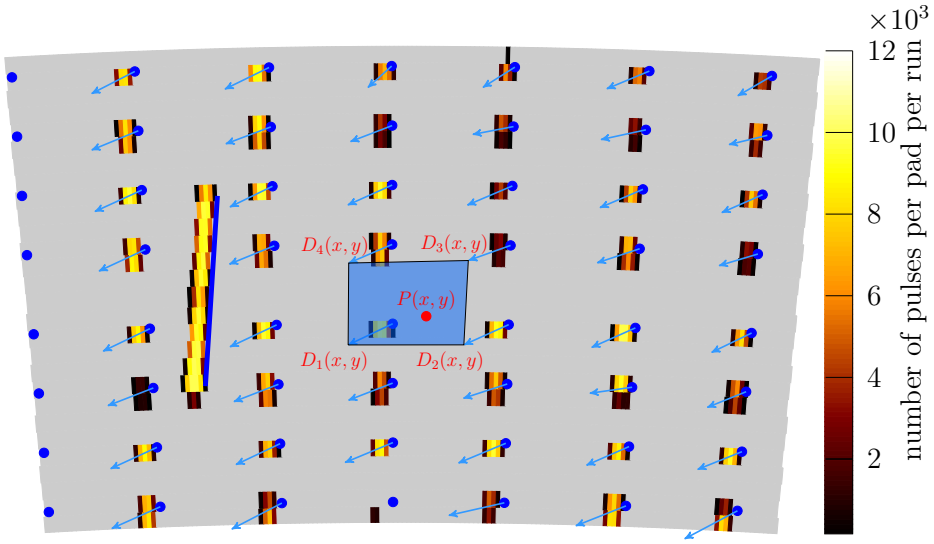

Figure 7.31: Number of pulses per pad for a run at $B = 1\,\mathrm{T}$ and $E_{\mathrm{drift}} = 240\,\mathrm{V/cm}$ measured with the central DESY GridGEM module. Blue points show the projection of the alumina dot position from the cathode. Arrows are pointing from these positions in the direction of the reconstructed cluster centre. The arrow length corresponds to the measured distortion scaled by a factor of four. The square illustrates an element used to calculate the distortions for the point P using the distortions D_1, D_2, D_3 and D_4.

the element construction each reconstructed alumina dot position with the cluster centre (x_{cluster},y_{cluster}) is tested and categorised as one possible node type. The categorisation is done using the following conditions for the four nodes:

$$n_0 : x_{\mathrm{cluster}} \leq x \quad \text{and} \quad y_{\mathrm{cluster}} \leq y \tag{7.17}$$

$$n_1 : x_{\mathrm{cluster}} > x \quad \text{and} \quad y_{\mathrm{cluster}} \leq y \tag{7.18}$$

$$n_2 : x_{\mathrm{cluster}} > x \quad \text{and} \quad y_{\mathrm{cluster}} > y \tag{7.19}$$

$$n_3 : x_{\mathrm{cluster}} \leq x \quad \text{and} \quad y_{\mathrm{cluster}} > y \tag{7.20}$$

Finally, the cluster centre which is closest to the point P is searched in each category. The resulting cluster centres for each category form the found element. Afterwards the element node coordinates are transformed into the local coordinate system of the element, where the element always is a square with an edge length of 2. This transformation is shown in Figure 7.32 and it transforms the coordinates (x, y) into (ξ, η), where $\xi, \eta \in [-1, 1]$. The

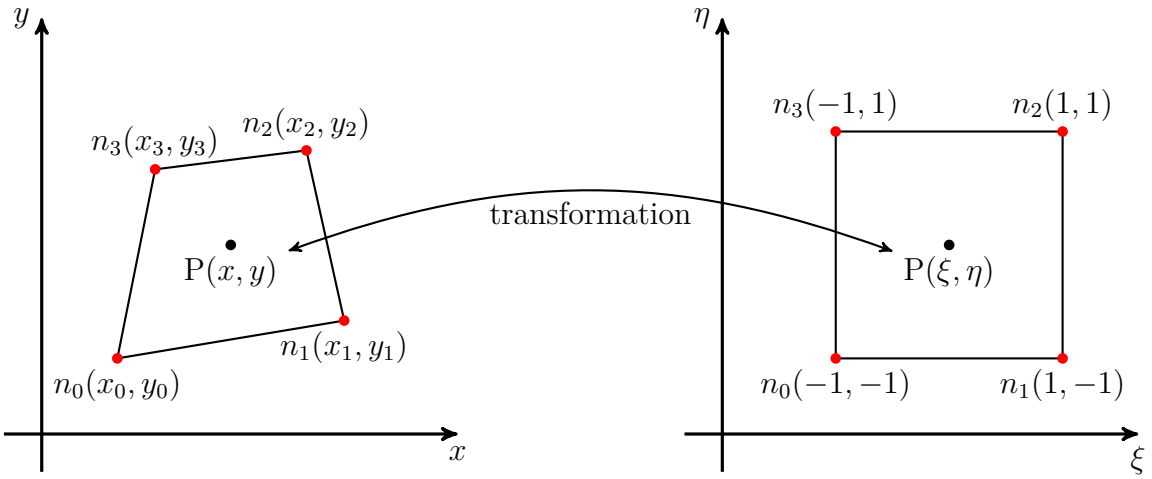

Figure 7.32: Sketch of the transformation from the global coordinate system (x, y) into the local coordinate system (η, ξ) for isoparametric elements.

Table 7.10: Node positions in the local coordinate system.

node q	0	1	2	3
ξ_q	-1	1	1	-1
η_q	-1	-1	1	1

transformation is equal to the transformation used in Section 5.2:

$$N_q = (1 + \xi_q \xi)(1 + \eta_q \eta) \tag{7.21}$$

$$x = \sum_{q=0}^{3} N_q x_q \tag{7.22}$$

$$y = \sum_{q=0}^{3} N_q y_q \tag{7.23}$$

The values of ξ_q and η_q for each node can be seen in Figure 7.32, where the four nodes of the element and their corresponding local coordinates are shown. In addition, they are listed in Table 7.10. In contrast to the cubic cells in three dimensions used in Chapter 5, here the edges are no longer parallel to the coordinate axis. Thus, the transformations $x \to \xi$ and $y \to \eta$ are no longer trivial and need to be calculated using Equations 7.22

and 7.23. The result is:

$$
\begin{aligned}
c_1 &= x\,(y_0 - y_1 + y_2 - y_3) \\
c_2 &= x_0(y_3 - y) - x_1(y_2 - y) + x_2(y_1 - y) - x_3(y_0 - y) + c_1 \\
c_3 &= x_0(y - y_1) - x_1(y - y_0) + x_2(y - y_3) - x_3(y - y_2) - c_1 \\
c_4 &= (x_0 + x_1)(y_2 + y_3 - 2y) - (x_2 + x_3)(y_0 + y_1 - 2y) + 2x(y_0 + y_1 - y_2 - y_3) \\
d_1 &= (x_1 - x_0)(y_2 - y_3) + (x_3 - x_2)(y_1 - y_0) \\
d_2 &= (x_3 - x_0)(y_1 - y_2) + (x_1 - x_2)(y_0 - y_3) \\
c_5 &= \sqrt{c_2^2 - d_1 c_4} \\
\xi_{1/2} &= \frac{c_2 \pm c_5}{d_1} \qquad (7.24) \\
\eta_{1/2} &= \frac{c_3 \pm c_5}{d_2}. \qquad (7.25)
\end{aligned}
$$

Here the unique solution for ξ and η can be found using the requirement $\xi, \eta \in [-1, 1]$. Two cases needs to be treated separately:

1. $d_1 = 0$
2. $d_2 = 0$

The first case is true if $y_0 = y_1$ and $y_2 = y_3$, since by construction $x_0 \neq x_1$ and $x_2 \neq x_3$ (see Equations 7.17 to 7.20). Similar the second case is true if $x_0 = x_3$ and $x_1 = x_2$. In these cases the solutions are given in the following:

$$
\begin{aligned}
\xi\big|_{d_1=0} &= \frac{y(x_0 + x_1 - x_2 - x_3) + y_0(x_2 + x_3 - 2x) + y_3(2x - x_0 - x_1)}{(x_2 - x_3)(y - y_0) + x_0(y - y_3) - x1(y - y_3)} \qquad (7.26) \\
\eta\big|_{d_2=0} &= \frac{x(y_0 - y_1 - y_2 + y_3) + x_0(y_1 + y_2 - 2y) + x_1(2y - y_0 - y_3)}{b + x_1(y_3 - y_0) + x_0(y_1 - y_2)}. \qquad (7.27)
\end{aligned}
$$

Finally, the distortion $D(\xi, \eta)$ for the given point P can be calculated using the distortions at each node and the coordinates of P in the local coordinate system:

$$
D(\xi, \eta) = \sum_{q=0}^{3} D_{n_q} N_q. \qquad (7.28)
$$

Figure 7.33 illustrates different situations that could happen in the interpolation of distortions. If the distortion at point P_1 need to be calculated, the four closest reconstructed clusters are forming the grey element shown in Figure 7.33 are used to calculated the

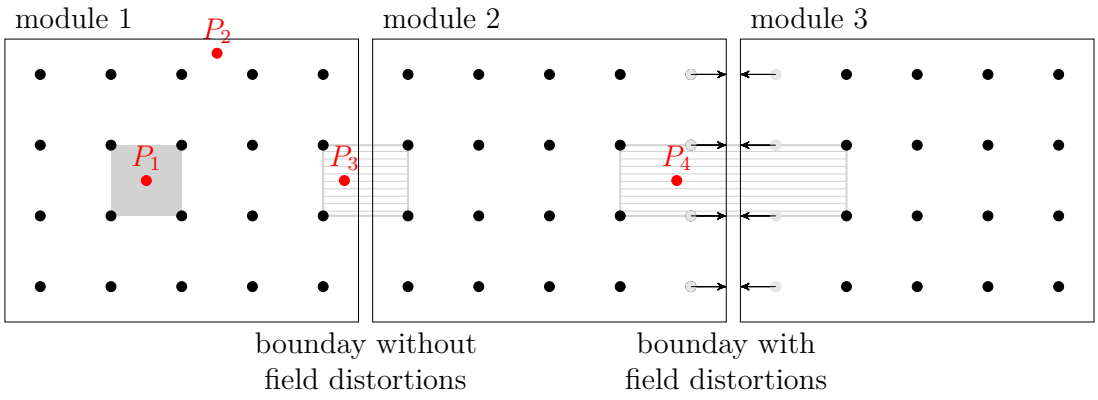

Figure 7.33: Sketch of three readout modules. Black dots show reconstructed positions of alumina dots. Grey positions of alumina dots could not be reconstructed, since the signal electrons did not reach the anode pad plane due to field distortions between module 2 and module 3. Grey boxes represent elements used to interpolate field distortions.

distortion. In the case of point P_2, there are no four surrounding reconstructed clusters, which means at point P_2 no distortions can be calculated. Obviously the calculation of distortions is limited to the module area covered by reconstructed clusters. This also means that for point P_3 no information about the distortion can be given, since it is at the module boundary similar to point P_2. In principle it also possible to construct elements out of reconstructed clusters from different modules, which is shown by the elements filled with horizontal lines in Figure 7.33. This would allow to not limit the distortion calculation on a single module. But this can only be done if the distortions would be constant at module boundaries and between modules. This case is illustrated in Figure 7.33 at the boundary between module 1 and module 2. Here it is sensible to construct an element between reconstructed clusters of module 1 and module 2 as shown in the case of point P_3.

In Section 7.2 it was shown that there are local field distortions between readout modules, which result in the situation shown at the boundary between module 2 and module 3 in Figure 7.33. Here the projections of the alumina dots close to the module boundary can not be reconstructed, since the corresponding electrons do not reach the anode pad plane due to the field distortions. If one would use the closest reconstructed clusters in the case of point P_4 in order to calculate the distortions at this point, the result would be wrong and lead to a completely wrong impression. This is because the distortions at the associated reconstructed cluster forming the element (right element filled with horizontal lines in Section 7.2) are small, since they are beyond the reach of the local field distortions at the module boundaries. The linear interpolation of these small distortions at the element nodes will in fact result in

almost vanishing distortions at the module boundary.

To avoid such misleading results, the interpolation between modules is not used for the data analysis presented in this work, but it could be used in case of no local field distortions at module boundaries or in simulations, where local distortions between modules are not considered.

7.3.9 Distortions maps

Using the method introduced in the previous section it is possible to calculate the distortions for arbitrary points on a module, if they are covered by measurement points. This allows to analyse the distortions in the following by calculating the distortions for each pad centre of a readout module, which results in a distortions map. In the following the measured displacements are split into two components. One component is defined in R direction perpendicular to rows of the pad plane and the other is in $R\phi$ along a row of the pad plane. The resolution is R direction is limited by the row height and the corresponding measurements are biased by the position of the alumina dot with respect to the module row. This is because the size of the alumina dots ($\varnothing = 3\,\mathrm{mm}$) is small compared to the row height of about 5 mm. Therefore, here only the $R\phi$ component is discussed in the following. In view of a standard data analysis of beam data, which is done row based, this is reasonable and allows to correct the measured hit position in $R\phi$ direction. The values given in the distortion maps correspond to displacements, which need to be applied to a measured point in order to correct the measurement for the field distortions calculated here. Therefore, by applying the displacements given here to other data taken with the LPTPC and corresponding readout modules, these data is corrected for global and local field distortions in the LPTPC.

Measured distortions without magnetic field

First of all, the distortions calculated by comparing reconstructed cluster positions to the expected positions defined by the pattern on the cathode, are analysed for runs without magnetic field. Assuming a perfect LPTPC with the electric field being parallel to the LPTPC field cage wall one would expect to reconstruct the cathode pattern projected onto the anode. Figure 7.34a shows the resulting distortions map for a drift field of $E_{\mathrm{drift}} = 240\,\mathrm{V/cm}$ and the central module using the DESY GridGEM module data.

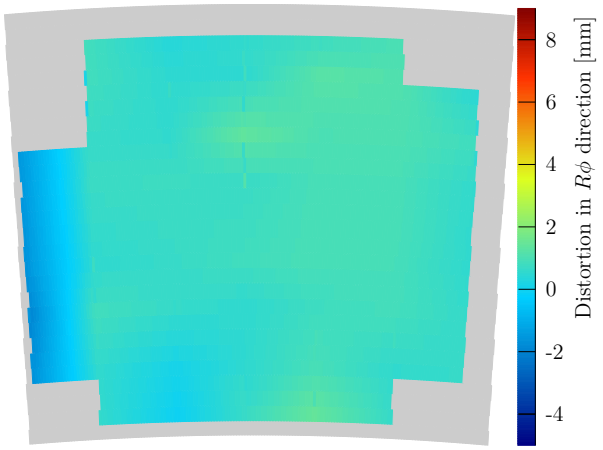

(a) Distortions along a row for DESY GridGEM data.

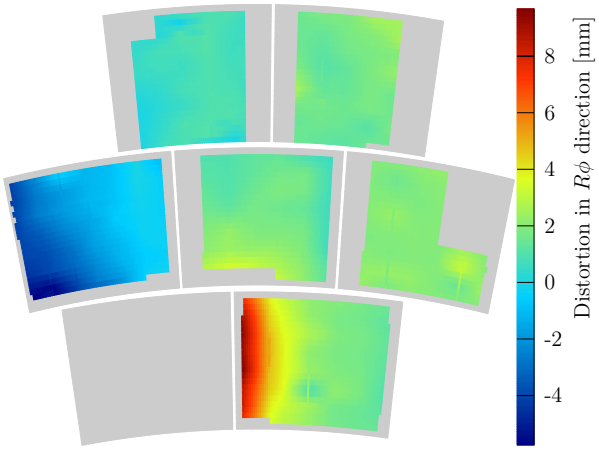

(b) Distortions along a row for MicroMegas data.

Figure 7.34: Distortion maps for MicroMegas and GEM module data at $B = 0\,\mathrm{T}$ and $E_{\mathrm{drift}} = 240\,\mathrm{V/cm}$.

It can be seen that there is an almost constant displacement in the order of 1 mm in $R\phi$ direction. Furthermore, a much larger displacement compared to the rest of the module can be observed on the left module side. This can be explained by the fact, that the expected cluster position is very close to the module boundary (see Figure 7.31). Thus, the cluster is collected only partially on the pad plane. In addition, also local field distortions might reduce the charge at the module boundary and lead to this effect. In any case, the reconstruction of a partially detected cluster leads to apparently different displacements than observed for the rest of the module.

Figure 7.34b give a more complete overview of the distortions showing MicroMegas module data with 6 modules. For the reconstruction of the positions the fraction f_{event}, introduced in Section 7.3.6, needed to be varied in order to find all pads of the clusters. The observed displacements are not the same for all modules. This results from the distortions introduced by the broken modules, which were already discussed in Section 7.3.7. The right module in the central module row and the top modules seem to be least affected and shows a constant displacement in $R\phi$ in the order of 2 mm. Comparing the distortions measured with the DESY GridGEM module and the MicroMegas modules, it can be seen that the best agreement is found for the top left MicroMegas module in comparison to the DESY GridGEM module. The central modules can not be directly compare, since the results for the central MicroMegas module are biased by the broken MicroMegas module.

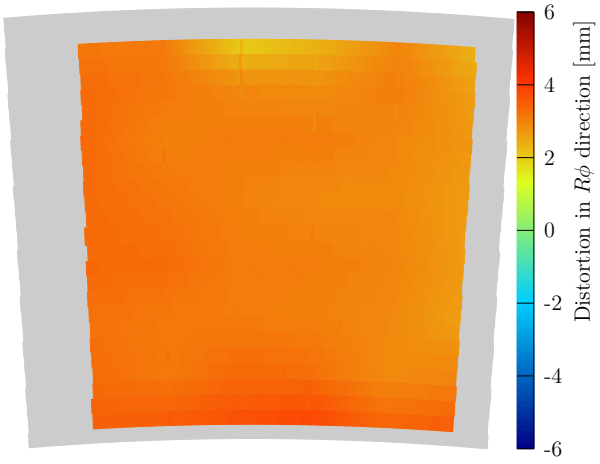

(a) Distortions along a row for DESY GridGEM module data, where the LPTPC is in the magnet centre.

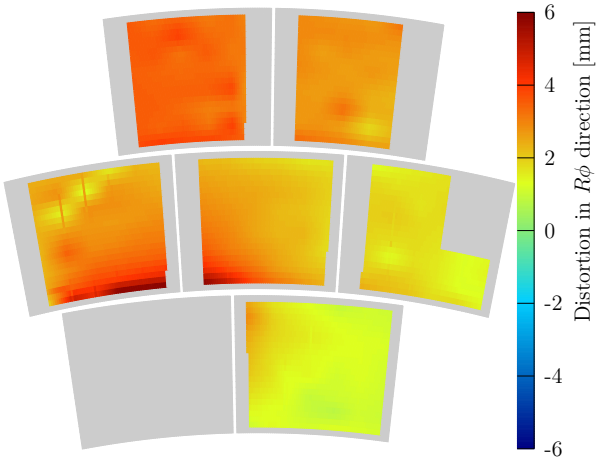

(b) Distortions along a row for MicroMegas module data, where the LPTPC is in the magnet centre.

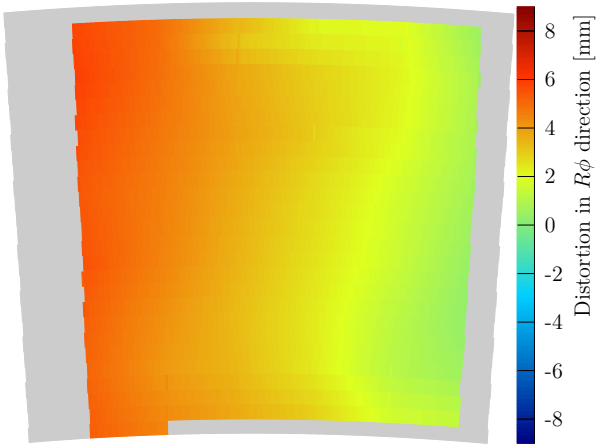

(c) Distortions along a row for DESY GridGEM module data, where the LPTPC is 10 cm outside the magnet centre.

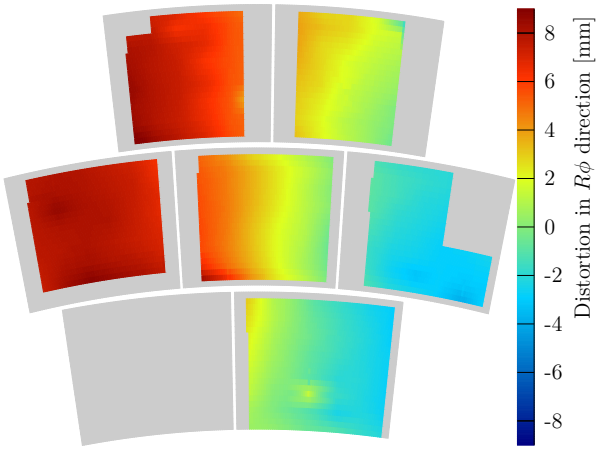

(d) Distortions along a row for MicroMegas module data, where the LPTPC is 10 cm outside the magnet centre.

Figure 7.35: Distortion maps for MicroMegas and GEM module data at $B = 1\,\mathrm{T}$ and $E_{\mathrm{drift}} = 240\,\mathrm{V/cm}$.

Measured distortions with magnetic field

After discussing the distortions cased by the electric field, the influence of the magnetic field is investigated in the following. The observed distortions in runs with a magnetic field are a combination of inhomogeneities in the electric and the magnetic field. Figure 7.35 shows the resulting distortions maps for MicroMegas and GEM module data at $B = 1\,\mathrm{T}$ and $E_{\mathrm{drift}} = 240\,\mathrm{V/cm}$. In case of the DESY GridGEM module data clearly a constant displacement in $R\phi$ direction of about 3 mm can be observed. This can also be seen in

Figure 7.31, where all arrows are pointing in the same direction. Such a constant shift is not expected from pure magnetic field inhomogeneities shown in Figure 7.18. Since in case of $\omega\tau \approx 1$ electrons tend to follow the magnetic field lines one would rather expect to see displacements pointing radial away from the magnet centre. The results of the simulation presented at the end of this chapter, will show the expected distortions from the magnetic field in detail.

In case of MicroMegas modules data with a magnetic field the problem of merging clusters was not observed due to a lower transverse diffusion and therefore a smaller cluster size. Hence, here a single cut on f_{event} is sufficient. The same tendency in terms of direction and size of displacements compared to the DESY GridGEM module can be observed in Figure 7.35b with MicroMegas module data for the top modules. This is not true for modules adjacent to the bottom left module. These modules are influenced by the distortions introduced by the bottom left module. Therefore, the distortions measured with these modules don't reflect field distortions inside the LPTPC, but only local effects.

If the LPTPC is pulled out of the PCMAG centre, the magnetic field distortions become larger (see Figure 7.18). Figures 7.35c and 7.35d show that if the LPTPC is pulled outside the centre of the PCMAG by 10 cm, the magnetic distortions become dominant and the effects from the bottom left module are reduced. This results in a similar pattern of the distortions map for the central module in DESY GridGEM module data and MicroMegas module data. Furthermore, the expected displacements pointing away from the magnet centre are visible, which result in negative displacements in $R\phi$ direction on the right-hand side of the magnet centre (bottom right and right module in the central module row) and positive displacements on the left-hand side of the magnet centre.

7.3.10 Discussion of the measured distortions

In the previous sections measured distortions for two different data sets using GEM and MicroMegas modules were presented. Both data sets have some drawbacks. On the one hand, for the DESY GridGEM module data the distortions could only be studied in the case of the central module in a reasonable manner. On the other hand, in the case of the MicroMegas module data a large area was influenced by the broken module introducing local field distortions and masking global field distortions inside the sensitive volume of the LPTPC.

Finally, both data sets show a constant displacement in the central region of the LPTPC for $B = 0\,\mathrm{T}$. This indicates a non optimal electric field shape inside the LPTPC, which can be most likely attributed to mechanical inaccuracies in the LPTPC production. With a magnetic field of $B = 1\,\mathrm{T}$ these distortions are more pronounced by the $\vec{E} \times \vec{B}$ effects. When pulling the LPTPC out of the homogeneous region of the PCMAG, its inhomogeneities become dominant and the expected radial displacements with respect to the magnet centre can be seen.

Possible corrections of measured LPTPC data

The distortion maps calculated in the previous sections are only valid for electrons drifting through the whole sensitive volume of the TPC. This is because in the measurements electrons are only produced on the cathode by the photoelectric effect and they drift through the whole sensitive volume of the TPC. But since the magnetic field map of the PCMAG is known from measurements, in principle the expected distortion at every position can be calculated. In order to do so, a simulation, where electrons start at the cathode and drift through the known magnetic field of the LPTPC, needs to be performed. The resulting reconstructed positions in simulation can then be compared to the reconstructed positions in the measurement data. Now the magnetic field can be scaled in the simulation in order to get the same position as in the measured data.

This scaling can then be fixed and simulations, where electrons start inside the sensitive volume of the LPTPC instead of starting at the cathode, can be performed. By doing so, finally a distortions map for each drift length can be calculated. This allows to correct data taken with the LPTPC in beam tests, where the particle beam is shot parallel to the anode plane at different positions in the sensitive volume of the LPTPC.

In the following the simulation is introduced in detail and results of the simulation are presented afterwards.

7.3.11 Simulations of the field distortions in the LPTPC

The signal simulation is done similar to the reconstruction introduced in Sections 7.1 and 7.3.6 with MarlinTPC and dedicated processors. In principle the simulation could also be done in a similar way as introduced in Chapter 5. But this is not done here, since the simulation would cover the treatment of $\mathcal{O}(100)$ electrons per alumina dot on the

cathode for at least 1000 events. The drift and subsequent amplification in a triple GEM stack of all the electrons would take way too much computing time and therefore here parameterisations based on the results shown in Chapter 6 are used in the amplification process. Furthermore the drift in the TPC is based on macroscopic gas parameters (v_{drift}, D_{t}, D_{l}) instead of the microscopic handling used in Garfield++.

In the MarlinTPC simulation, which is introduced in the following, five sub-processes need to be covered:

1. Creation of electrons from the alumina dots.
2. Drift of the produced electrons trough the LPTPC taking into account the inhomogeneous magnetic field of the PCMAG.
3. Amplification of the electrons in the GEM stack.
4. Simulation of the electronics response.

Signal creation

The creation of the signal electron from the known alumina dot positions on the cathode is done with the MarlinTPC processor called *PhotoelectricPulseProcessor*. The input of this processor is a `xml` file with the measured alumina dot and line positions on the cathode. For each alumina dot a random number of electrons n_e is drawn from a Poisson distribution with a mean number of electrons of $\overline{n_e} = 100$:

$$P(n_e) = \frac{\overline{n_e}^{n_e}}{n_e!} \mathrm{e}^{-\overline{n_e}}. \tag{7.29}$$

For an alumina line every 3 mm an alumina dot is simulated.

In the following the electrons produced for a certain alumina dot are treated as an electron cloud characterised by the centre position, by n_e and by the transverse and longitudinal deviation from the centre position. The transverse deviation is set to $\sigma_{t,\text{cloud}} = d_{\text{dot}}/4$, where $d_{\text{dot}} = 2\,\text{mm}$ is the diameter of the alumina dot. Here it is assumed, that the distribution of electrons produced from an alumina dot follows a Gaussian distribution with a width of $\sigma_{t,\text{cloud}}$. The longitudinal deviation is set to $\sigma_{l,\text{dot}} = 0.01\,\mu\text{s}$, which is approximately the length of a laser pulse.

Signal drift

The signal drift is handled by the *ElectronCloudDrifterProcessor*, which drifts the electron clouds produced before trough the sensitive volume of the TPC. Drifting electron clouds instead of single electrons is convenient in terms of computing time, since the result in the end is the same. The main task in the electron cloud drift simulation is to solve Equation 3.6 numerically, where the magnetic and electric field is updated in each step. This allows to consider the magnetic field map of the PCMAG introduced in Section 7.3.3 for the electron cloud drift. So far, the electric field is assumed to be constant and parallel to the wall of the TPC. The stepping method used in the simulation is a 4th order Runge-Kutta-Fehlberg method with 5th order error estimate, where the absolute error of each step is set to be below 10^{-3}. According to Equation 3.6, the input parameters needed for the drift are the macroscopic gas properties drift velocity (see Figure 7.36a) and $\omega\tau$, which are calculated with Magboltz corresponding to the simulation conditions.

If the electron cloud reaches the end of the sensitive volume the cloud position and deviations are updated. The deviations are updated by adding the transverse and longitudinal diffusion, which is given by D_l and D_t in combination with the drift length l_{drift}:

$$\sigma_{t,\text{cloud}} = \sqrt{\left(d_{\text{dot}}/4\right)^2 + \left(D_{\text{t}}\sqrt{l_{\text{drift}}}\right)^2} \tag{7.30}$$

$$\sigma_{l,\text{cloud}} = \sqrt{\sigma_{l,\text{dot}}^2 + \left(D_{\text{l}}\sqrt{l_{\text{drift}}}\right)^2} \tag{7.31}$$

Furthermore, after the electron cloud drift, the clouds are converted back to single electrons to be amplified in the amplification stage at the anode. This is done by drawing n_e random numbers from Gaussian distributions $\mathcal{G}(\mu, \sigma)$ with mean values μ corresponding to the cloud centre and deviations σ taken from the cloud:

$$P(x_{e^-}) = \mathcal{G}\left(x_{\text{cloud}}, \sigma_{t,\text{cloud}}\right) \tag{7.32}$$

$$P(y_{e^-}) = \mathcal{G}\left(y_{\text{cloud}}, \sigma_{t,\text{cloud}}\right) \tag{7.33}$$

$$P(t_{e^-}) = \mathcal{G}\left(z_{\text{cloud}}/v_{\text{drift}}, \sigma_{l,\text{cloud}}\right) \tag{7.34}$$

The corresponding processor in MarlinTPC is called *CloudToSimTrackerHitProcessor*.

Signal amplification

In the simulations presented here the amplification is done using a stack of three GEMs, as it was studied in Chapter 6. The corresponding *GEMProcessor* makes use of the parameterisation of Equations 6.14, 6.17 and 6.24 for $X^-_{\text{param.}}$, $C^-_{\text{param.}}$ and $G_{\text{param.}}$. Parameters of the parameterisation for the T2K gas are taken from the measurements presented in Chapter 6 and can be found in Table A.2. The gain calculation is based on Equation 6.6, where for each GEM random numbers X^-_i, C^-_i and G_i are used, which are introduced in the following.

Depending on the number of electrons to be amplified n_e in each GEM, the gain is drawn from the following distribution:

$$P(G_i) = \begin{cases} \mathrm{e}^{-G/G_{\text{param.}}} & \text{for } n_e < 200 \\ G_{\text{param.}}\mathcal{G}\left(n_e, \sqrt{n_e}\right) & \text{else.} \end{cases} \tag{7.35}$$

Here $\mathcal{G}$ is a Gaussian distribution with mean n_e and standard deviation $\sqrt{n_e}$.

In case of C^- and X^- a binomial distribution is used:

$$P(C^-_i) = \binom{n_e}{k} \left(C^-_{\text{param.}}\right)^k \left(1 - C_{\text{param.}}\right)^{n_e - k} \tag{7.36}$$

$$P(X^-_i) = \binom{n_e}{k} \left(X^-_{\text{param.}}\right)^k \left(1 - X_{\text{param.}}\right)^{n_e - k}, \tag{7.37}$$

if $C^-_{\text{param.}}$ and $X^-_{\text{param.}}$ are not equal to one, else they are directly set to one.

The attachment A_i needed for the final gain calculation (see Equation 6.6) is taken from the parameterisation already introduced in Section 6.3.3 and given in Equation 6.30. Results of the Magboltz simulation including the parameterisation are shown in Figure 7.36, where also the longitudinal diffusion and the drift velocity needed in the following are shown. The simulations cover the field range $E \in [0, 10000]$, whereas the parameterisation is done and valid only in the region of interest. The parameters of the parameterisation can be found in Table A.3.

Followed by the calculation of the gain, the produced charge is distributed onto the pad plane by the *ChargeDistributionProcessor*. At this point, only the entry point of each primary electron into the GEM stack and its amplification is known. Therefore, the spreading of the electrons inside the GEM stack still needs to be calculated.

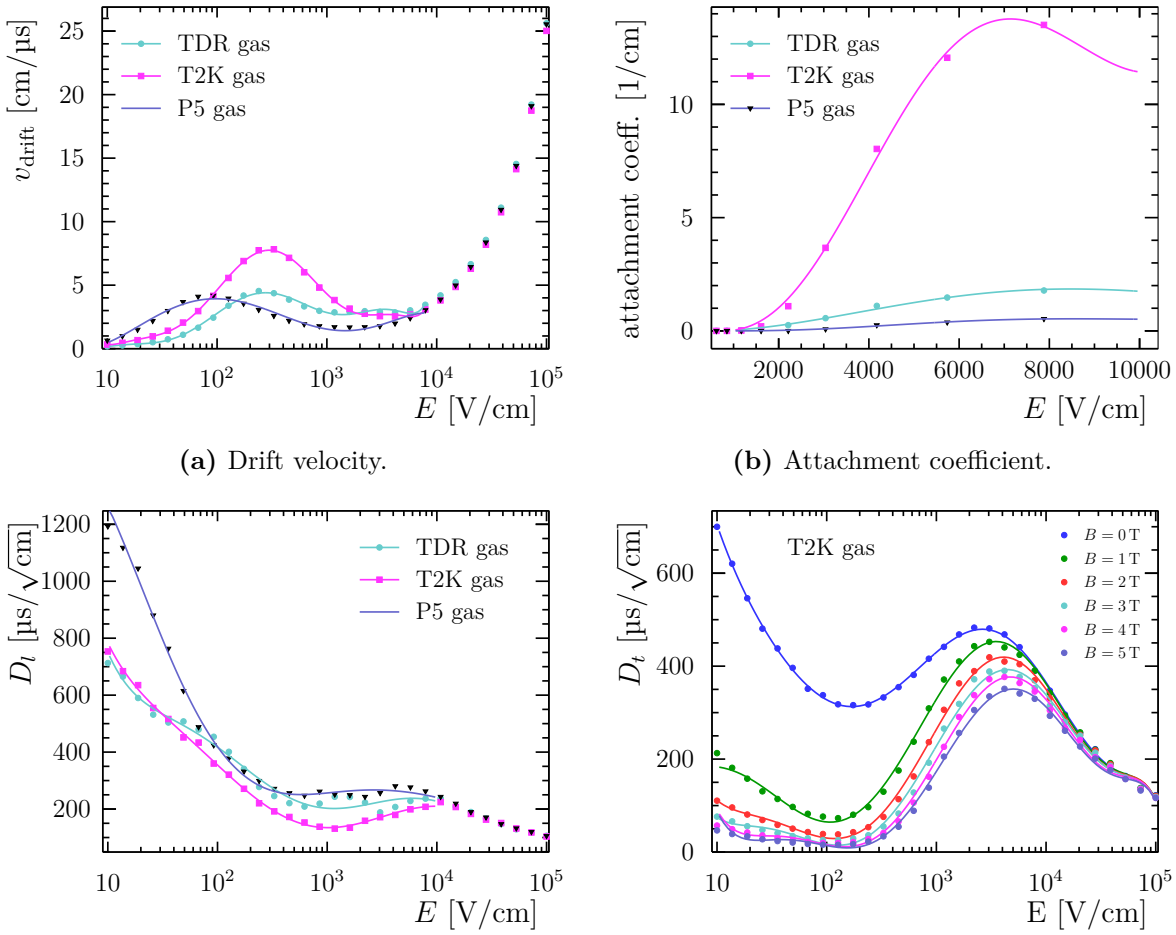

(a) Drift velocity.

(b) Attachment coefficient.

(c) Longitudinal diffusion.

(d) Transverse diffusion for different magnetic field strengths.

Figure 7.36: Gas parameters for different gases. Circle markers show the result of a Magboltz simulation using 10 collisions. Lines show the parameterisation used in MarlinTPC.

In order to do so, the total transverse and longitudinal diffusion inside the GEM stack needs to be calculated. Here again Magboltz simulations are used to parametrise these quantities as shown in Figure 7.36. The longitudinal diffusion is parametrised similar to the attachment (see Equation 6.30) using a 5th order exponential polynomial. Since the transverse diffusion also depends on the magnetic field strength a different parameterisation introduced in

Ref. [94] and already implemented in MarlinTPC is used:

$$\sigma_{\text{trans.diff.}}(E) = \sum_{i=0}^{7} a_i \log^i(E) \tag{7.38}$$

$$a_i = \sum_{j=0}^{4} b_j^i (B)^j. \tag{7.39}$$

Figure 7.36d shown the results of the Magboltz simulation in circles and the parameterisation in lines. Corresponding parameters are given in Table A.4.

Finally, the charge per pad is calculated, using the information of the transverse diffusion and the total charge produced Q_{dep} in the GEM stack. A pad is assumed to collect a signal, if its centre is within a distance of $4\sigma_t$ around the entry point of the primary electron (x_{e^-}, y_{e^-}) into the GEM stack. The deposited charge per pad is given by integrating the two dimensional Gaussian distribution over the pad surface:

$$Q_{\text{pad}} = \frac{Q_{\text{dep}}}{4} \left(\text{Erf}\left(\frac{x_{\text{pad,max}} - x_{e^-}}{\sqrt{2}\sigma_{\text{trans.,tot}}} \right) - \text{Erf}\left(\frac{x_{\text{pad,min}} - x_{e^-}}{\sqrt{2}\sigma_{\text{trans.,tot}}} \right) \right) \tag{7.40}$$

$$\cdot \left(\text{Erf}\left(\frac{y_{\text{pad,max}} - y_{e^-}}{\sqrt{2}\sigma_{\text{trans.,tot}}} \right) - \text{Erf}\left(\frac{y_{\text{pad,min}} - y_{e^-}}{\sqrt{2}\sigma_{\text{trans.,tot}}} \right) \right), \tag{7.41}$$

where $x_{\text{pad,min}}$, $y_{\text{pad,min}}$, $x_{\text{pad,max}}$ and $y_{\text{pad,max}}$ define the pad boundaries.

Electronics simulation

Finally, an electronics pulse is simulated by approximating the electronics output with a Gaussian distribution $\mathcal{G}(t_{\text{pulse}}, \sigma_{\text{pulse}})$:

$$\mathcal{G}(t_{\text{pulse}}, \sigma_{\text{pulse}}) = \frac{Q_{\text{pad}}}{\sqrt{2\pi}\sigma_{\text{pulse}}} \exp\left(\frac{(t - t_{\text{pulse}})^2}{2\sigma_{\text{pulse}}^2} \right). \tag{7.42}$$

The integral of this distribution corresponds to the total charge Q_{pad} of the processed pad. This definition is different from the ALTRO electronics introduced in Section 4.4.1, where the total charge corresponds to the maximum of the electronics output. For the simulation done here this is acceptable, since only the charge position is of relevance for the calculation of the field distortions and not the absolute charge value per time bin. The width of the distribution σ_{pulse} is chosen with respect to the electronics rise time t_{rise} such that $\sigma_{\text{pulse}} = t_{\text{rise}}/3$. In the simulation the rise time is set to $t_{\text{rise}} = 180\,\text{ns}$. For each time

bin $[t_i, t_{i+1}]$ the charge is given by:

$$Q_{i,\mathrm{pad}} = \int_{t_i}^{t_{i+1}} \mathcal{G}(t_{\mathrm{pulse}}, \sigma_{\mathrm{pulse}})\ \mathrm{d}t \tag{7.43}$$

$$= \frac{Q_{\mathrm{pad}}}{2}\left[\mathrm{Erf}\left(\frac{t_{i+1}}{\sqrt{2}\sigma_{\mathrm{pulse}}}\right) - \mathrm{Erf}\left(\frac{t_i}{\sqrt{2}\sigma_{\mathrm{pulse}}}\right)\right]. \tag{7.44}$$

This calculation is done by the *TPCElectronicsProcessor*, which is the last processor of the simulation chain. A sketch of all involved MarlinTPC processors and data types can be found in Figure A.6. The resulting charge per pad is equivalent to the measurements and therefore the data analysis, starting with the pulse reconstruction, can be done as in the case of the measured data.

7.3.12 Results of the simulation of field distortions in the LPTPC

Results of the simulation introduced in the previous sections are shown in Figure 7.37. A good agreement of the cluster characteristics (Figures 7.37a and 7.37b) between the simulation and the results of the DESY GridGEM module data (Figures 7.27b and 7.27c) can be seen. In particular the mean width of the reconstructed clusters in the simulation $\sigma = (0.904 \pm 0.02)\,\mathrm{mm}$ agrees with cluster size from the measurements $\sigma = (0.9 \pm 0.1)\,\mathrm{mm}$. In both cases the uncertainty corresponds to the standard deviation resulting from the Gaussian distribution when fitting the cluster size distribution as shown in Figure 7.37b.

As mentioned before the simulation takes the measured magnetic field of the PCMAG [91] into account. The inhomogeneities of the magnetic field are minimal in the bottom right part of the central module. With increasing distance to this region the field inhomogeneities of the magnetic field rise, which results in increasing distortions. On the left-hand side of the magnet centre the displacements are position and on the right-hand side they are negative, since they are defined such that adding the given value in $R\phi$ direction to a measured point will correct the point measurement for the observed field distortions. In consequence the point is moved towards the magnet centre, since the measured charge is displace in the direction pointing away from the magnet centre in the $x - y$ plane. It can be seen that the maximum distortion is about 5 mm if the LPTPC is in the centre of the magnet. For the central module the expected displacements are not homogeneous as observed in the measurements, but they range from $-2\,\mathrm{mm}$ to $1\,\mathrm{mm}$. The scale in Figures 7.35a and 7.35b is equal to the scale of Figure 7.37c to allow a direct comparison.

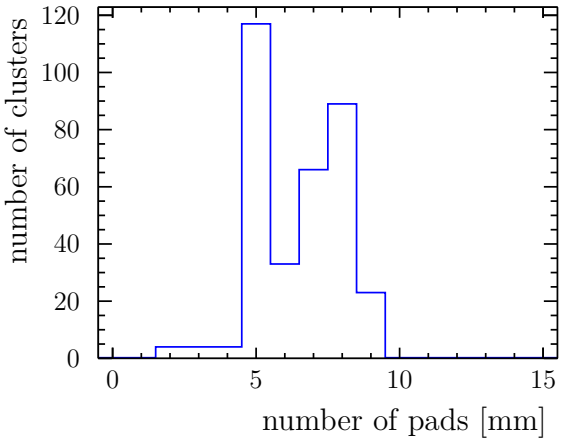

(a) Number of anode pads per cluster that collected at least one pulse in the considered run.

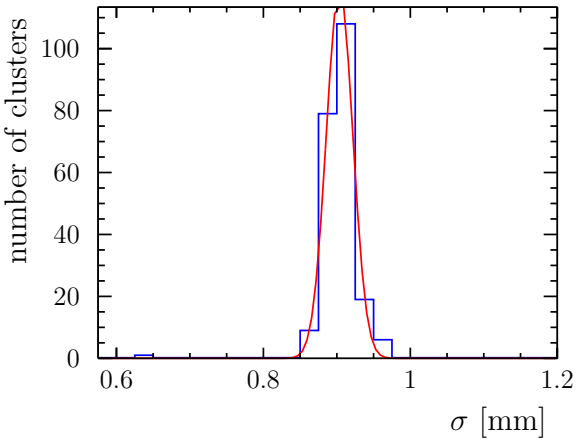

(b) Calculated cluster size resulting from the Likelihood fit of the cluster centre.

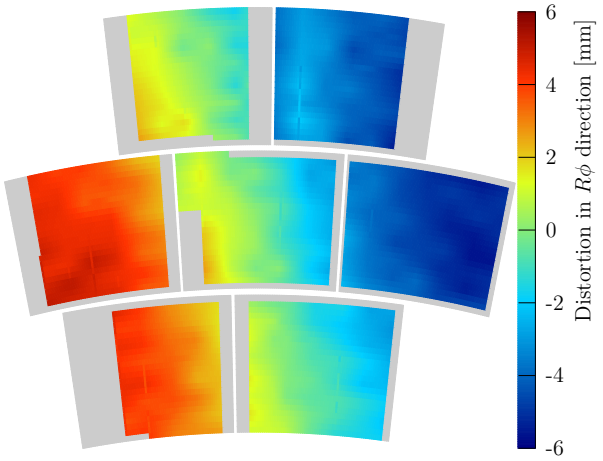

(c) Distortions along a row for simulated GEM data. The LPTPC is in the centre of the magnet.

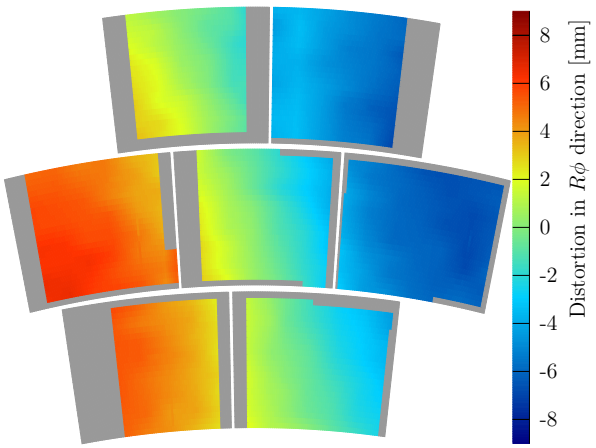

(d) Distortions along a row for simulated GEM data. The LPTPC is 10 cm outside the magnet centre.

Figure 7.37: Results of the simulation taking into account the magnetic field of the PCMAG. In the simulation a signal amplification with three GEMs and a pad plane corresponding to the DESY GridGEM module pad plane are considered.

If the LPTPC is pulled out of the magnet centre the field distortions become larger and therefore also the displacements rise as shown in Figure 7.37d. Again the scale is the same as used in Figures 7.35c and 7.35c to allow a direct comparison, which shows that in simulation displacements ranging from −3 mm to 2 mm whereas in measurements they range from 0 mm to 4 mm.

In summary the displacements calculated from the simulation are larger than the measured displacements. Furthermore, the displacements induced by the inhomogeneous field of the

magnet grow homogeneous with increasing distance to the magnet centre in the $x-y$ plane, which was not observed in the measurements. Here a rather constant displacement was observed when the LPTPC was placed in the centre of the magnet.

7.4 Discussion of the measured distortions with respect to implications on the ILD TPC

In the second part of this chapter the overall field distortions in the LPTPC were measured using a laser calibration system. The laser was used to create a signal on the LPTPC cathode at defined positions. The reconstructed signal was compared to the original position of the signal creation in order determine the displacements of the signal detected on the LPTPC anode pad plane. The measurements were done in two dedicated measurement campaigns using two different technologies for signal amplification – GEMs and MicroMegas.

In both measurement campaigns a constant displacement of about 2 mm was observed in measurements without a magnetic field. This implies, that the electric field inside the LPTPC is not aligned with LPTPC axis parallel to field cage wall. The reason for this, could be the measured misalignment of the LPTPC axis of 0.5 mm. If the field would simply be tilted with respect to the LPTPC axis one would expect to measure a displacement of the same size. Obviously this is not the case and in order to evaluate the effect of the misaligned axis an electrostatic field simulation would be required, which is beyond the scope of this thesis.

In the measurements with a magnetic field of $B = 1\,\mathrm{T}$, where the LPTPC was placed in the centre of the magnet, only positive displacements in the order of $\mathcal{O}(3\,\mathrm{mm})$ were observed, which is not expected from the simulation. Since in general for electrons the magnetic field reduces the effect of electric field distortions one would expect that the observed distortions of the electric field only have a minor effect on the measured displacements at $B = 1\,\mathrm{T}$. Following this idea, the observed difference between the measurements and the simulation can not only be attributed to distortions of the electric field observed in the measurements without magnetic field. One possible additional source of distortions introduced in the measurements with magnetic field could be, that the LPTPC was slightly misaligned with the magnet axis in the measurements. In other words the LPTPC axis is not parallel to the magnet axis in z direction and the electric field is not parallel to the LPTPC axis.

Apart from these observations, it was shown how the analysis of field distortions using a laser calibration system can be done. It was shown that the uncertainty of the reconstructed positions is below 30 µm, which is the required accuracy in order to limit the effect of field distortions on the momentum resolution to 5 %. This shows that the laser calibration system is a suitable tool for the corrections of field distortions in the ILD TPC. Moreover, a method to interpolate the measured distortions on the pad plane was introduced, which is based on the methods already used in the electric field calculations with Garfield++ presented in Chapter 5. This method allows to correct data for the measured distortions and therefore recover the momentum resolution. It was also discussed how to calculate distortions for different drift lengths in the LPTPC, since the measured displacements are only valid at the maximum drift distance due to the measurement principle of producing signal electrons on the cathode.

All in all the measurements showed the capabilities of the laser calibration system and revealed field distortions in the LPTPC. In particular the monitoring of the drift velocity was shown. The relative uncertainty in this measurement is in the order of $\mathcal{O}(0.2\,\%)$. If in the end a laser system will be considered for the ILD TPC and which system in detail will be used is not yet decided. Therefore, the results of the measurements presented here help to make a decision in a later planning phase of the ILD.

8

Conclusions

Several aspects connected to the realisation of a TPC with an excellent momentum resolution are discussed in this thesis. In order to achieve an excellent momentum resolution, as aimed for in case of the ILD TPC ($\delta(1/p_{\mathrm{t}}) \simeq 10^{-4}\,(\mathrm{GeV/c})^{-1}$), the electric and magnetic fields inside the sensitive volume of the TPC must be as homogeneous as possible. The remaining field distortions must be well know in order to correct the measurements with a high accuracy. The main sources of field distortions of the electric field are identified and studied in this thesis.

The first source of field distortions are ions, that are created in the gas amplification of the TPC and drift back from the amplification stage into the sensitive volume of the TPC. A small prototype TPC was used to study the amount of ions produced in the gas amplification process. In the measurements the ion feed back ratio (IFR), defined as the ratio between the number of electrons entering the amplification stage and the number of ions drifting back into the sensitive volume of the TPC, could not be directly measured. What could be measured is the ratio between IFR and the effective gain ($G_{\mathrm{eff.}}$) of the setup. A minimum value of $\mathrm{IFR}/G_{\mathrm{eff.}} = 2\,\%$ was achieved in measurements with one of the gases (T2K) proposed for the ILD TPC. In addition, a general characterisation of the amplification with a stack of three GEMs in T2K gas was done. This includes the measurement of all transfer coefficients of a single GEM, which are the collection and the extraction efficiency for electrons and ions and the electron gain. These transfer coefficients were parametrised using a parameterisation, which is based on an electrostatic model introduced in former studies. It turned out, that in the case of the electron collection efficiency and the ion collection efficiency the model failed to describe the measurements.

This could be attributed to the attachment in the gas, which is not included in the model. By extending the model with the gas attachment, which was parametrised using simulations, a good description of the measured data could be achieved. The final parameterisation allows to predict the behaviour of the GEM stack for different parameter sets of GEM voltages and transfer fields. It also allows to calculate the effective gain, which in turn allows to estimate the measured ion feedback ratio: IFR $= 18 \pm 15$. In addition, a second data set was produced in measurements, where the GEM, facing the sensitive volume of the TPC, was replaced by a GEM with an increased GEM hole size. These measurements could show, that by introducing the modified GEM, IFR/$G_{\text{eff.}}$ is reduced by a factor of two. Moreover, it could be shown that this is understood with a reduced ion extraction efficiency and an increased electron collection efficiency caused by the different geometry of this GEM. In a detailed simulation of the setup the measured electron transparency could be reproduced. Using the gain calculated from the simulation the measured ion feedback ratio is estimated as IFR $= 10$. Furthermore, it was found that description of ions in the simulation is not sufficient to reproduce the measurements. This implies that in order to be able to simulate the correct ion behaviour, the ion drift in the gas used here needs to be understand better. This requires dedicated studies of the ion drift in future studies.

A second source of field distortions was identified at the boundaries of individual readout modules. It was shown that the effects of these distortions, which were observed in measurements, can be described in simulations very well. These simulations were used to show that such field distortions are limited to the vicinity of the readout modules boundaries. Nevertheless they affect the module performance, which in the end degrades the momentum resolution. At maximum distortions of up to 200 µm were found in the simulations presented in this thesis, which is in good agreement with measurements. As part of the simulation analyses two different methods of analysing field distortions were developed. They follow the standard TPC reconstruction of particle tracks with anode pads, which is based on reconstructing the track position along pad rows in $R\phi$ direction. One of them is based on analysing the number electrons per pad row. It measures the collection efficiency per row, which is reduced in case of field distortions. The second method is based on analysing the mean charge position on a row for different track angles. This allows to directly measure the distortion introduced at the module boundary. In addition to the analysis of present field distortions, different optimisation options of the module developed at DESY were discussed. Here the electron collection efficiency on the row closest to the module boundary could be increased from 43 % to 53 % in case of no

magnetic field. Measurements with the optimised module could confirm the simulation results.

Finally, the third source of field distortions are imperfections of the TPC field cage and inhomogeneities of the electric and magnetic field inside the sensitive volume of the TPC. A method to measure such distortions using a laser calibration system was developed and tested with a large TPC prototype in two measurement campaigns comparing different technologies of readout modules. The calibration system creates signals at defined positions on the TPC cathode. By comparing the reconstructed position on the anode to the original cathode position distortions can be measured. In addition, the time needed for the signal electrons to drift through the whole TPC volume can be analysed. Such an analysis was used to demonstrate the capability to monitor the drift velocity. In a TPC operation at the ILC the drift velocity needs to be continuously monitored for data calibration purposes. A good agreement with the expectation from simulation was found and the obtained accuracy of the measurement of the drift velocity is about 0.2 %. Furthermore, measurements without a magnetic field could reveal distortions of the electric field inside the prototype volume, leading to spacial distortions on the anode plane in the order of 2 mm. The uncertainty of the measurement of the reconstructed positions is below 30 µm, which allows a accurate correction of measured data based on the calibration data taken with laser system. In order to allow a data correction based on the observed distortion, a dedicated method of calculating a distortions map was developed. This allows to retrieve the distortion at an arbitrary point on the anode independent of the cathode positions used in the laser calibration measurements. Moreover a simulation taking into account the known inhomogeneities of the magnetic field was presented. It allows to predict the expected distortions from the imperfect magnetic field. The mapping of the measured and simulated distortion map allows to predict the distortions for different drift length, since the measured distortions correspond only to the maximum drift length.

With respect to the ILD TPC one can conclude that the major sources of field distortions could be identified and possible improvements of the readout modules, which allow to keep the effects of field distortions at a minimum, have been discussed. In addition, the laser calibration system has been proofed to be most useful for the correction of field distortions. The obtained accuracy of the measurements with this system in the end allows to limit the deterioration of the momentum resolution caused by field inhomogeneities to 5 %. This finally fulfils the requirements of the ILD TPC.

A

Appendix

A.1 Calculation of the conversion position in the drift volume of the TPC prototype

In Chapter 6 measurements with a TPC prototype are presented. The signal source in the measurement is a Fe^{55} source, which radiates photons. These photons convert in the sensitive volume of the TPC prototype leaving electrons, which are afterwards detected in TPC. In order to implement a realistic simulation of the detected signal the probability density function, which describes the photon conversion in dependence on the drift distance, needs to be known. If it is known, electrons can be started in the simulation at positions following this probability function. This allows to skip the simulation of photons and the photon conversion. In the following the position of the photon conversion in the drift volume of the TPC prototype will be calculated.

The conversion of photons is given by Equation 3.2, which requires the knowledge of individual material thicknesses and the corresponding mass attenuation. They are given in the following. The photons are produced outside the TPC volume since the radioactive source was placed on top of the TPC (see Figure 6.5). The distance from the source to the Mylar foil is 7.7 mm and the distance from the Mylar foil to the cathode is 5.5 mm. Furthermore, the thickness of the Mylar foil and the cathode is 10 µm. The mass attenuation μ (see Section 3.2) can be calculated using the information given in Table A.1. The density of T2K gas is calculated using $\rho = \sum_i \rho_i \frac{V_i}{V}$ and the individual densities of its components given in Table A.1.

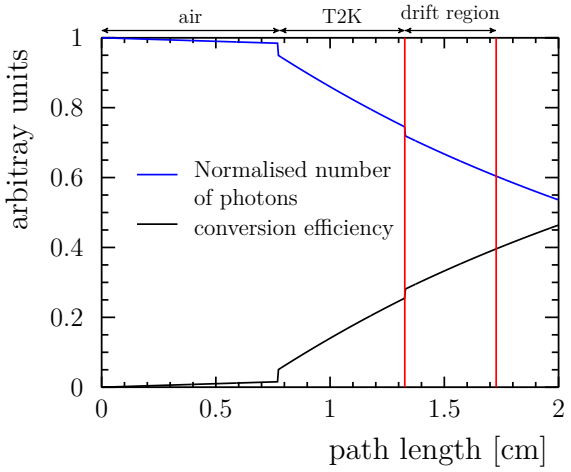

(a) Normalised number of photons (blue) and conversion efficiency (black) for a given path length in the prototype setup. Red lines depict the boundaries of the drift volume and the edges in the curves are caused by the Mylar foil of the TPC cover and the cathode.

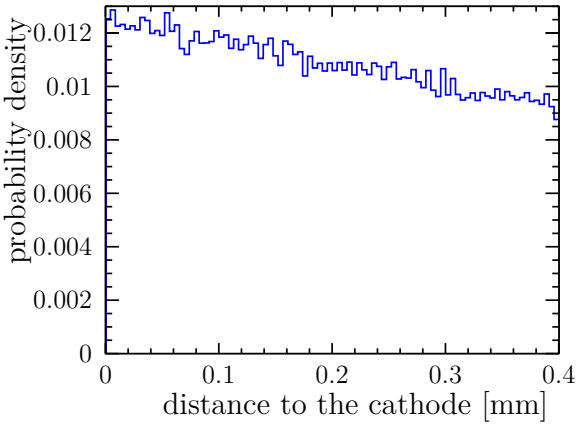

(b) Probability density in the drift volume of the TPC prototype.

Figure A.1: Photon conversion in the setup used in Chapter 5.

Finally, the normalised number of photons I/I_0 (blue curve) and the conversion efficiency $\epsilon = (I_0 - I)/I_0$ (black curve) for a certain path length in the setup is shown in Figure A.1a.

The number of conversions $N_{\text{conversion}}$ per path length l can be calculated from the number of photons $I(x)$:

$$N_{\text{conversion}}(l) = I(0) - I(l) \tag{A.1}$$

$$N_{\text{conversion}}(l) = I_0 \left(1 - \exp^{-\mu l}\right), \tag{A.2}$$

which shows that the number of conversion as a function of the path length follows the same exponential behaviour as the number of photons. A random conversion point can be generated, by drawing a random position inside the Fe^{55} source, which has a diameter of $\varnothing = 1\,\text{cm}$, and a random direction. In addition, a random path length is drawn following the distribution $N_{\text{conversion}}(l)$. In a Monte Carlo simulation, where 1 million photons were simulated, the conversion positions were used to construct a probability density function. The result is shown in Figure A.1b. It can be seen that the number of conversions decreases with the distance to the cathode. Thus, in a simulation slightly more electrons need to be started close to the TPC cathode compared to the number of electrons started close to the GEM stack.

Table A.1: Material properties used to calculate the photon conversion [29, 95].

material	density ρ [kg/m^3]	μ/ρ [cm^2/g]
Mylar	1.39×10^3	17.3
Air	1.18	25.1
T2K	1.77	247.6
Ar	1.753	
CF_4	3.72	
iC_4H_{10}	2.54	

A.2 Gas parameters

Table A.2: Parameters of the single GEM parameter parameterisation. All parameters are calculated for two different data sets corresponding to different settings of the GEM stack (low and high gain settings).

		electrons		ions	
		high gain	low gain	high gain	low gain
C	r	6.73×10^{-2}	4.24×10^{-2}	9.60×10^{-1}	7.78×10^{-1}
	s	7.62×10^{-1}	9.26×10^{-1}	1.39×10^{-2}	7.31×10^{-2}
	$l_{\text{eff.}}$	-4.20×10^{-2}	-3.13×10^{-2}	-1.56×10^{-2}	-1.78×10^{-2}
X	r	2.05×10^{-1}	1.70×10^{-1}	4.34×10^{-1}	1.39×10^{-1}
	s	4.52×10^{-1}	4.79×10^{-1}	3.73×10^{-9}	6.59×10^{-1}
	y	-1.37×10^{-12}	-2.58×10^{-14}	-4.10×10^{-3}	-6.12×10^{-3}
	g	5.09×10^{-2}	4.64×10^{-2}	-2.45×10^{-2}	-1.04×10^{-1}
	$e_{\text{par.}}$	3.23	1.49	3.42	5.24
	x_0	9.79×10^{-2}	9.32×10^{-2}	4.53×10^{-2}	4.99×10^{-2}
$X_{\text{sec.}}$	r	—	—	1.02×10^{-3}	7.84×10^{-3}
	s	—	—	5.41	5.41
	a_1	—	—	1.99×10^{-1}	2.40×10^{-1}
	a_3	—	—	4.24×10^{1}	2.70×10^{1}
G	α	-3.87	-3.54	—	—
	β	2.23×10^{-4}	2.18×10^{-4}	—	—

Table A.3: Parameters of the parameterisation of gas parameters. The attachment parameter correspond to the definition given in Equation 6.30. The drift velocity and the longitudinal diffusion are parametrised similar to the transverse diffusion as given in Equation 7.38, but here the parametes a_i are constant and do not depend on the magnetic field.

	a_0	a_1	a_2	a_3
σ_L	4.06×10^{3}	-3.38×10^{3}	1.33×10^{3}	-2.47×10^{2}
v_{drift}	2.74×10^{2}	-4.66×10^{2}	3.16×10^{2}	-1.07×10^{2}
A	-9.36×10^{-3}	2.08×10^{-4}	-6.99×10^{-7}	6.47×10^{-10}

	a_4	a_5	a_6	a_7
σ_L	1.55×10^{1}	1.10	-1.40×10^{-1}	-6.05×10^{-3}
v_{drift}	1.72×10^{1}	-5.58×10^{-1}	-1.83×10^{-1}	1.27×10^{-2}
A	-1.29×10^{-13}	9.80×10^{-18}	-2.57×10^{-22}	—

	a_8	a_9	a_{10}
σ_L	1.16×10^{-3}	-3.65×10^{-5}	5.83×10^{-9}
v_{drift}	2.18×10^{-3}	-3.08×10^{-4}	1.09×10^{-5}
A	—	—	—

Table A.4: Parameters of the parameterisation of the transverse diffusion as given in Equations 7.38 and 7.39.

	a_0	a_1	a_2	a_3	a_4
b_0	-3.34×10^{3}	5.69×10^{3}	-2.89×10^{3}	6.11×10^{2}	-2.95×10^{1}
b_1	2.07×10^{4}	-2.74×10^{4}	1.29×10^{4}	-2.60×10^{3}	1.06×10^{2}
b_2	-2.60×10^{4}	3.38×10^{4}	-1.61×10^{4}	3.32×10^{3}	-1.48×10^{2}
b_3	1.15×10^{4}	-1.49×10^{4}	7.17×10^{3}	-1.49×10^{3}	6.94×10^{1}
b_4	-2.17×10^{3}	2.82×10^{3}	-1.37×10^{3}	2.87×10^{2}	-1.37×10^{1}
b_5	1.50×10^{2}	-1.95×10^{2}	9.49×10^{1}	-2.01×10^{1}	9.79×10^{-1}

	a_5	a_6	a_7	a_8	a_9
b_0	-8.01	7.42×10^{-1}	1.23×10^{-1}	-2.13×10^{-2}	8.78×10^{-4}
b_1	3.44×10^{1}	-2.68	-5.15×10^{-1}	7.89×10^{-2}	-3.03×10^{-3}
b_2	-4.40×10^{1}	3.69	6.66×10^{-1}	-1.07×10^{-1}	4.18×10^{-3}
b_3	1.98×10^{1}	-1.72	-3.02×10^{-1}	4.93×10^{-2}	-1.96×10^{-3}
b_4	-3.81	3.39×10^{-1}	5.84×10^{-2}	-9.66×10^{-3}	3.87×10^{-4}
b_5	2.66×10^{-1}	-2.41×10^{-2}	-4.10×10^{-3}	6.85×10^{-4}	-2.76×10^{-5}

A.3 Single GEM parameter for the modified GEM

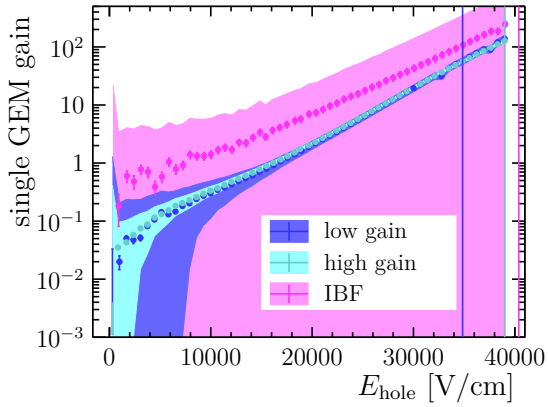

(a) Single GEM gain

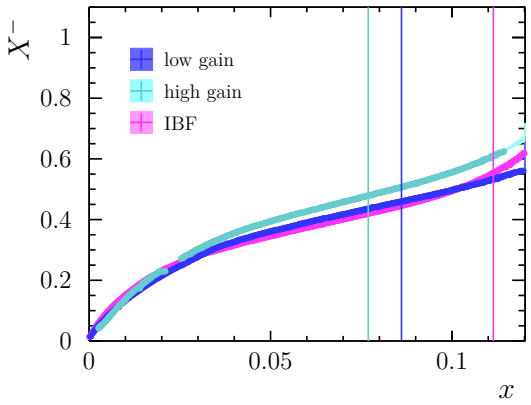

(b) Electron collection efficiency.

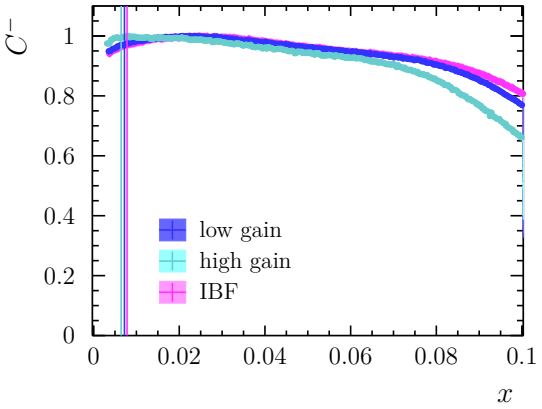

(c) Electron extraction efficiency.

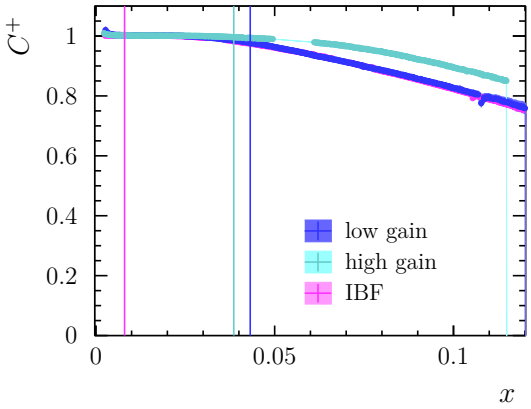

(d) Ion collection efficiency.

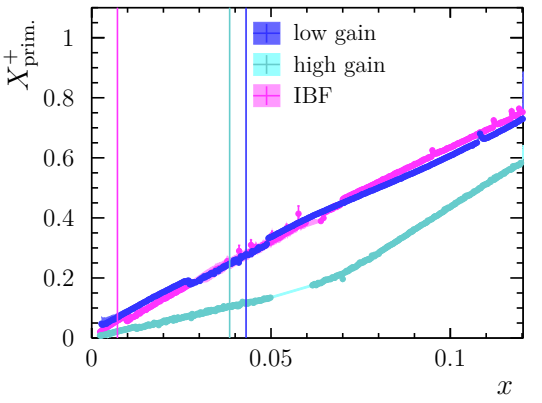

(e) Ion primary extraction efficiency.

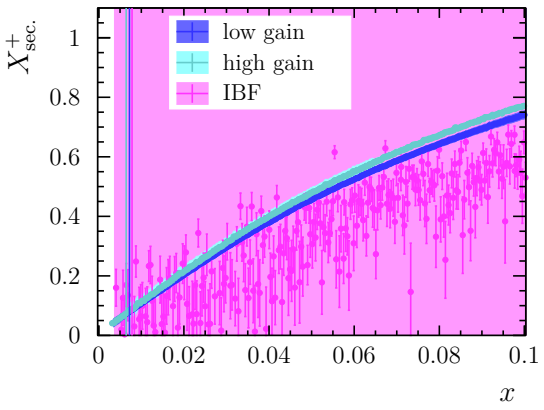

(f) Ion secondary extraction efficiency.

Figure A.2: Transfer coefficients for different GEM stack settings with T2K gas. GEM I in the setup has a hole size of 100 µm and the other GEMs are standard CERN GEM with a hole diameter of 70 µm The coloured vertical lines indicate the value of x for the settings as given in Table 6.2. The error band shows systematic uncertainties connected to the CUMOs and the error bars represent statistic uncertainties.

A.4 Additional figures of the laser test

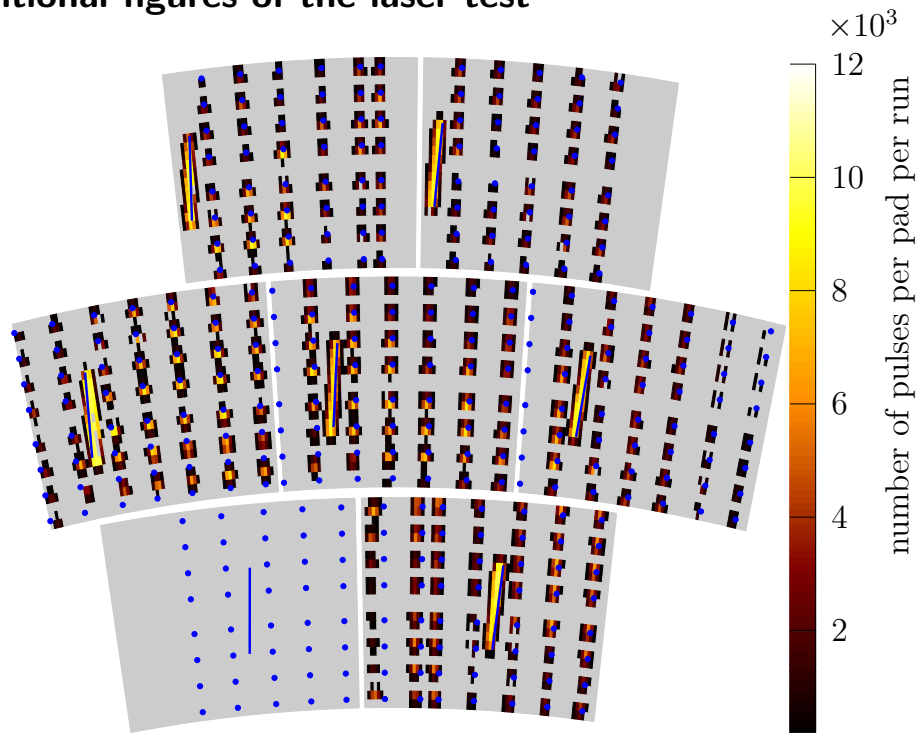

(a) Single run at $B = 0\,\mathrm{T}$.

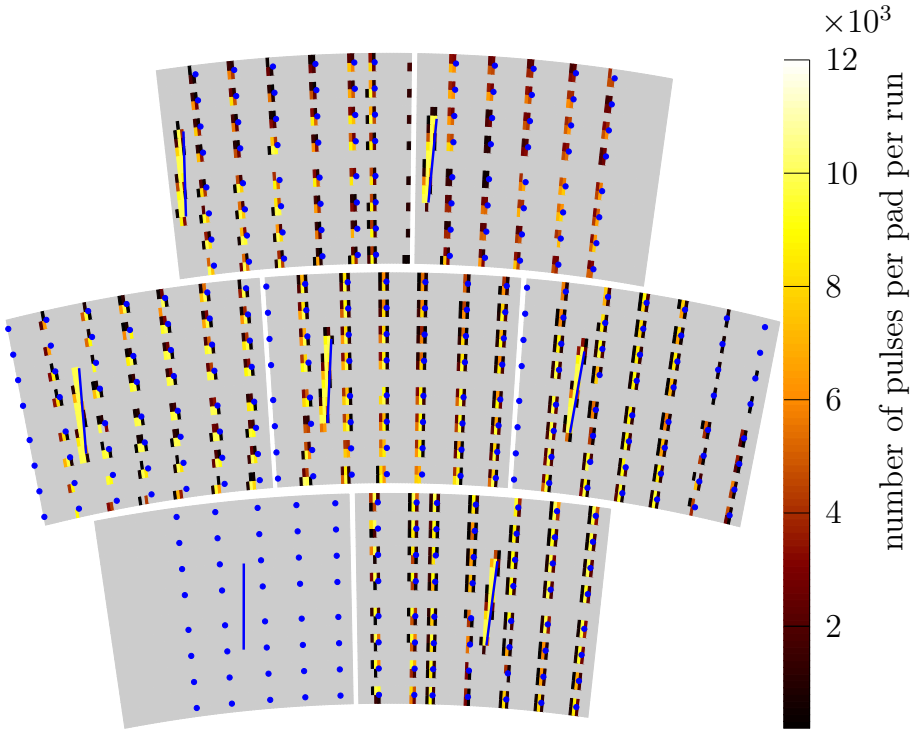

(b) Single run at $B = 1\,\mathrm{T}$.

Figure A.3: Measured signals in the MicroMegas test campaign. Blue dots and lines show the projection of the alumina dots and lines of the cathode.

A.5 Technical drawings

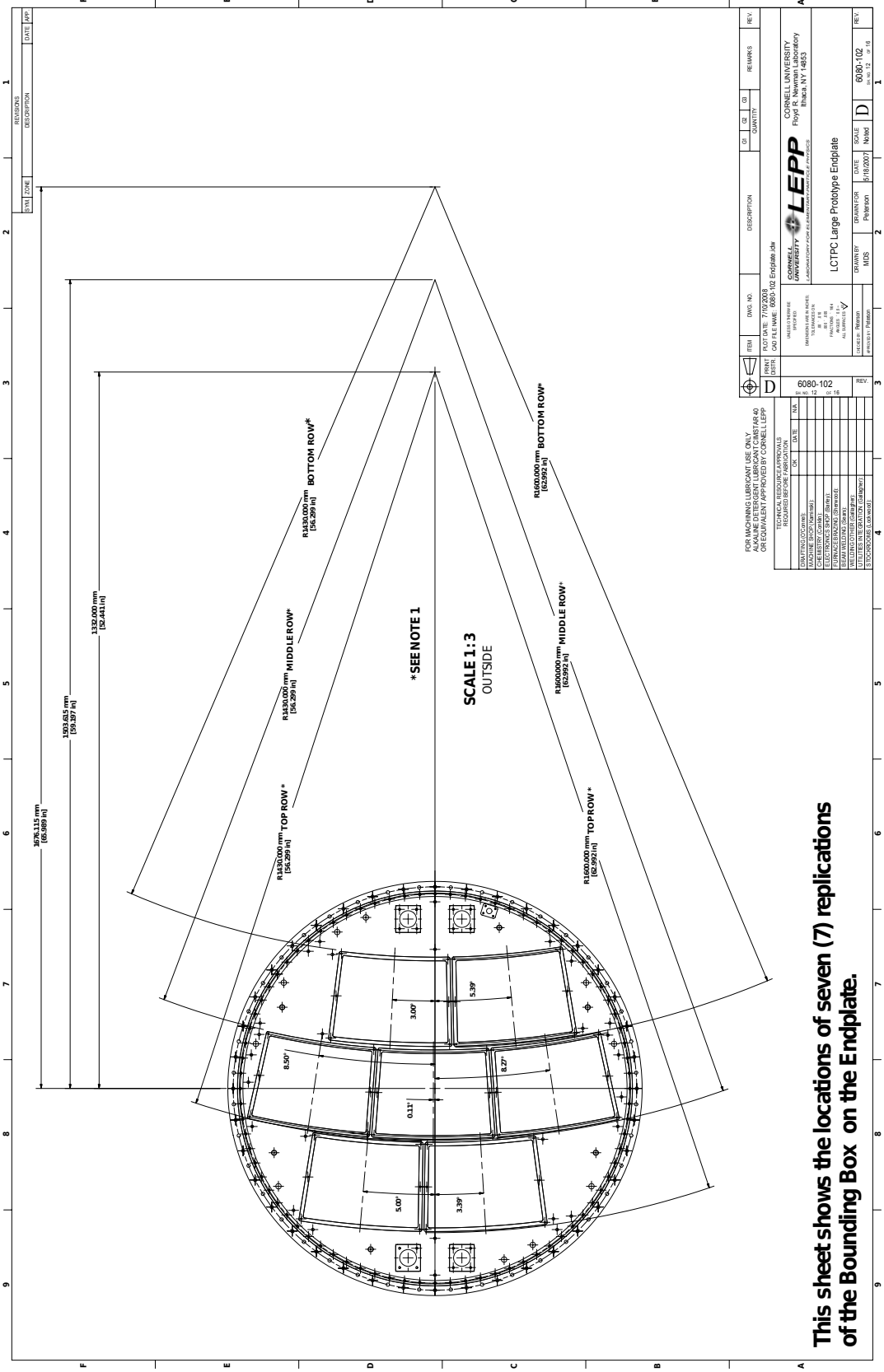

Figure A.4: Technical drawing of the LPTPC end plate showing the position of all modules.

A.6 MarlinTPC Processors

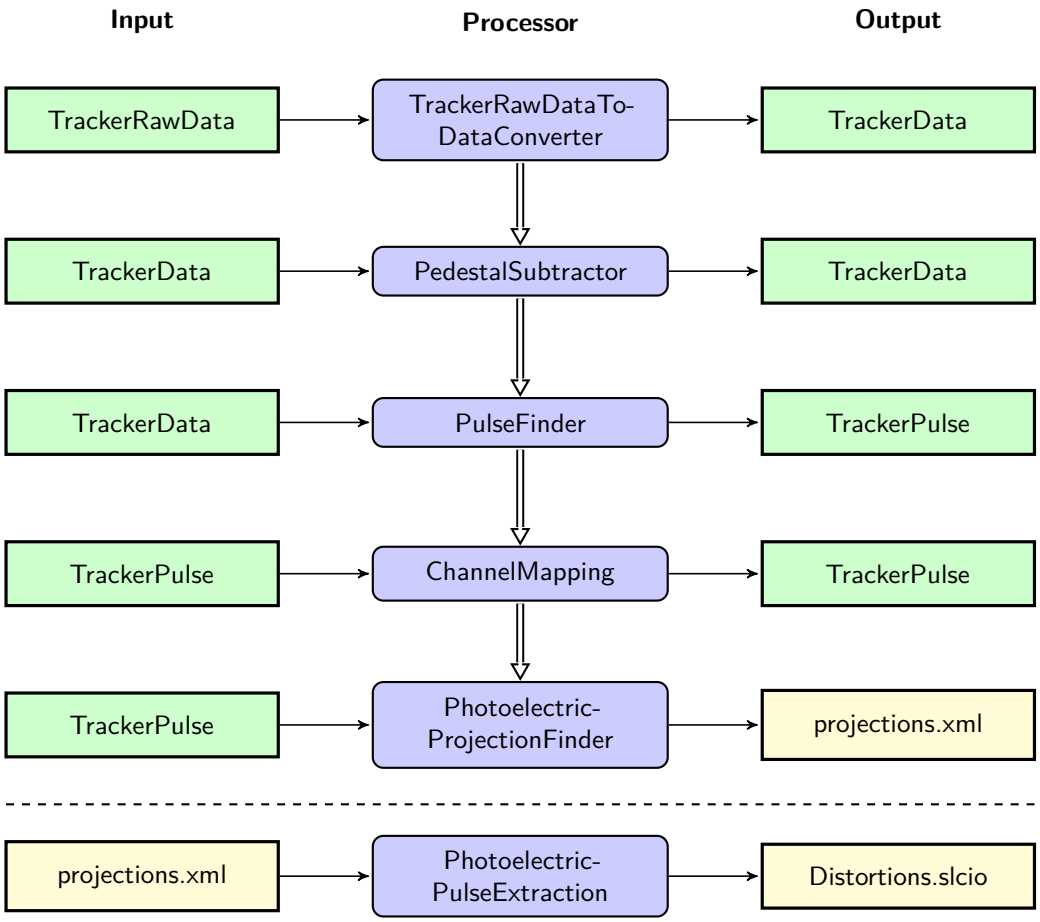

Figure A.5: MarlinTPC processor chain used in the reconstruction. Green boxes represent LCIO classes and yellow boxes represent files.

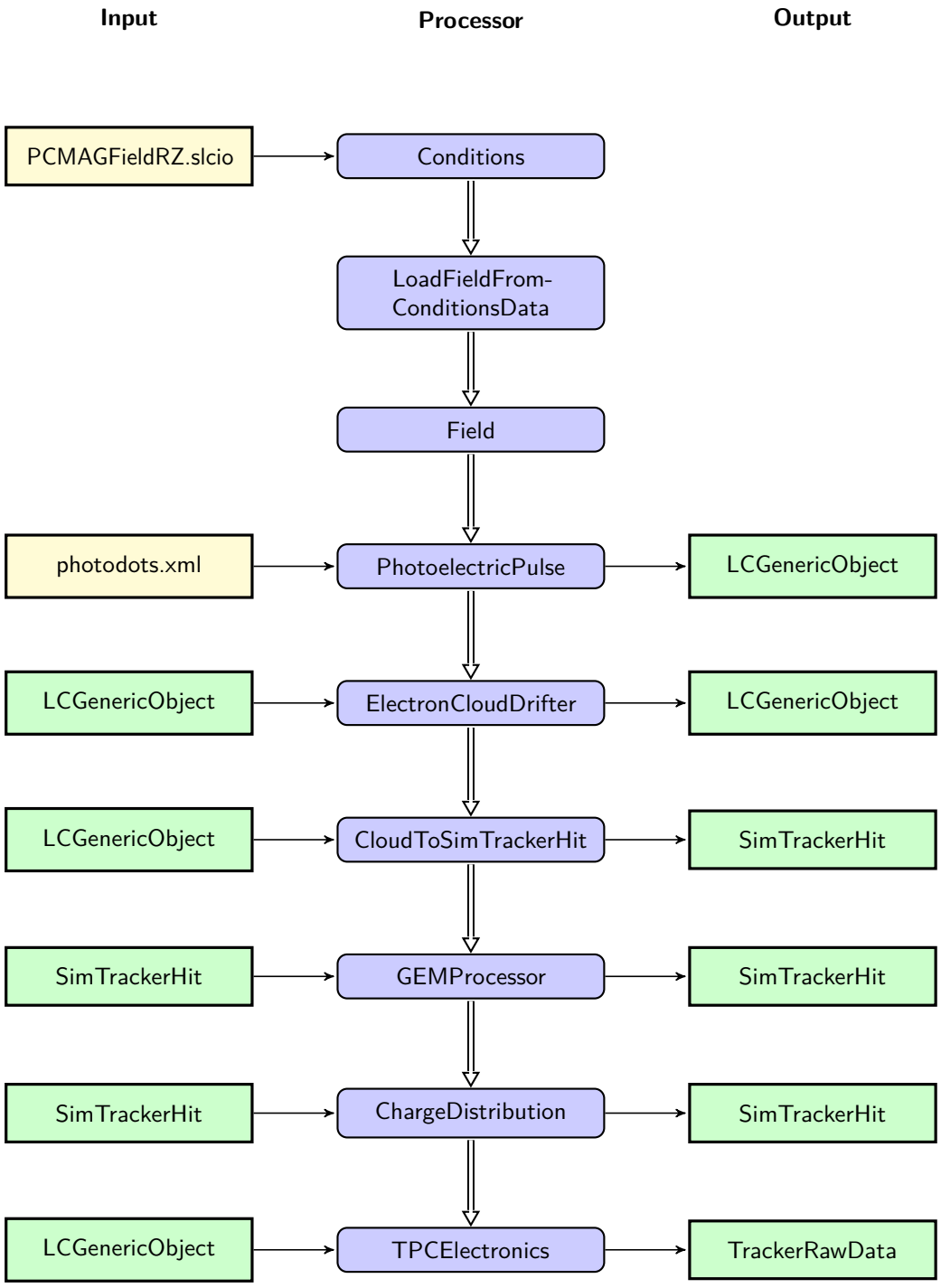

Figure A.6: MarlinTPC processor chain used in the simulation. Green boxes represent LCIO classes and yellow boxes represent files.

Bibliography

[1] G. Aad et al. *Observation of a new particle in the search for the Standard Model Higgs boson with the ATLAS detector at the LHC.* Physics Letters B, 716(1):1–29, 2012. ISSN 0370-2693.

[2] S. Chatrchyan et al. *Observation of a new boson at a mass of 125 GeV with the CMS experiment at the LHC.* Physics Letters B, 716(1):30–61, 2012. ISSN 0370-2693.

[3] F. Englert et al. *Broken Symmetry and the Mass of Gauge Vector Mesons.* Phys. Rev. Lett., 13:321–323, 1964.

[4] P. W. Higgs. *Broken Symmetries and the Masses of Gauge Bosons.* Phys. Rev. Lett., 13:508–509, 1964.

[5] The ALEPH, DELPHI, L3, OPAL Collaborations, the LEP Electroweak Working Group. *Electroweak Measurements in Electron-Positron Collisions at W-Boson-Pair Energies at LEP.* Phys. Rept., 532:119, 2013.

[6] The ALEPH, DELPHI, L3, OPAL, SLD Collaborations, the LEP Electroweak Working Group, the SLD Electroweak and Heavy Flavour Groups. *Precision Electroweak Measurements on the Z Resonance.* Phys. Rept., 427:257, 2006.

[7] F. Abe et al. *Observation of Top Quark Production in $\overline{p}p$ Collisions with the Collider Detector at Fermilab.* Phys. Rev. Lett., 74:2626–2631, 1995.

[8] T. Behnke et al. *The International Linear Collider Technical Design Report - Volume 4: Detectors.* ILC-REPORT-2013-040(Volume 4: Detectors), 2013.

[9] T. Behnke et al. *The International Linear Collider Technical Design Report - Volume 2: Physics.* ILC-REPORT-2013-040(Volume 2: Physics), 2013.

[10] G. Moortgat-Pick et al. *The Role of polarized positrons and electrons in revealing fundamental interactions at the linear collider.* Phys.Rept., 460:131–243, 2008.

[11] H. Li et al. *HZ Recoil Mass and Cross Section Analysis in ILD.* 2012.

[12] C. Dürig. *Higgs Self-Coupling Measurement at the ILC.* Americas Workshop on Linear Colliders, 2014. URL: `http://www.linearcollider.org/awlc14/`.

[13] K. Seidel et al. *Prospects for the Measurement of the Top Mass in a Threshold Scan at CLIC and ILC.* LCD-Note-2012-013, 2012.

[14] A. Hoang et al. *Top quark pair production close to threshold: Top mass, width and momentum distribution.* Phys.Rev., D60:114027, 1999.

[15] J. Beringer (Particle Data Group) et al. *The Review of Particle Physics.* Phys. Rev. D86, 010001 (2012), 2014.

[16] M. Amjad et al. *A precise determination of top quark electroweak couplings at the ILCoperating at* $\sqrt{s} = 500\,\text{GeV}$. LC-REP-2013-007, 2013.

[17] K. Agashe et al. *The minimal composite Higgs model.* Nuclear Physics B, 719(1-2):165 – 187, 2005. ISSN 0550-3213.

[18] T. Behnke et al. *The International Linear Collider Technical Design Report - Volume 1: Executive Summary.* ILC-REPORT-2013-040(Volume 1: Executive Summary), 2013.

[19] R. Abela et al. *The European X-Ray Free-Electron Laser - Technical design report.* DESY 2006-097, 2007.

[20] A. Vogel. *Beam-Induced Backgrounds in Detectors at the ILC.* Ph.D. thesis, DESY, 2008. DESY-THESIS-2008-036.

[21] J. Marshall et al. *Pandora Particle Flow Algorithm.* In *Proceedings of the International Conference on Calorimetry for the High Energy Frontier (CHEF 2013)*, pages 305–315. 2013.

[22] H. Stoeck et al. *The International Large Detector.* The ILD Concept Group, 2009.

[23] R. Gluckstern. *Uncertainties in track momentum and direction, due to multiple scattering and measurement errors.* Nuclear Instruments and Methods, 24(0):381 – 389, 1963. ISSN 0029-554X.

[24] W. Atwood et al. *Performance of the ALEPH Time Projection Chamber.* Nuclear Instruments and Methods in Physics Research Section A: Accelerators, Spectrometers, Detectors and Associated Equipment, 306(3):446 – 458, 1991. ISSN 0168-9002.

[25] P. Schade. *Correction Methods for TPC Operation in Inhomogeneous Magnetic Fields.* LC-DET-2010-001, 2010.

[26] R. Settels. *LCTPC and the Magnetic Field for ILD: Update 2010.* LC-DET-2011-002, 2011.

[27] S. Amendolia et al. *Gating in the ALEPH time projection chamber.* Nuclear Instruments and Methods in Physics Research Section A: Accelerators, Spectrometers, Detectors and Associated Equipment, 252(2-3):403 – 406, 1986. ISSN 0168-9002.

[28] O. Schäfer. *Ein Monitorsystem für Gasbasierte Detektoren am International Linear Collider (ILC).* Master's thesis, Universität Rostock, 2006.

[29] N. I. of Standards et al. *XCOM: Photon Cross Sections Data*, 2014. URL: `http://physics.nist.gov/PhysRefData/Xcom/html/xcom1.html`.

[30] W. Blum et al. *Particle detection with drift chambers.* Accelerator physics. Springer-Verlag, 1993. ISBN 9783540583226.

[31] C. Ramsauer. *Über den Wirkungsquerschnitt der Gasmoleküle gegenüber langsamen Elektronen.* Ann. Phys., 66:546, 1921.

[32] E. B. Wagner et al. *Time-of-Flight Investigations of Electron Transport in Some Atomic and Molecular Gases.* The Journal of Chemical Physics, 47(9):3138–3147, 1967.

[33] Ö. Şahin et al. *Penning transfer in argon-based gas mixtures.* Journal of Instrumentation, 5(05):P05002, 2010.

[34] G. Charpak et al. *New Particle Detectors: The Multiwire Proportional Chamber and the Drift Chamber.* Phys.Teacher, 1977.

[35] K. Ackermann et al. *Results from a TPC Prototype for the Linear Collider Tracker with the MWPC and GEM Endplate Technologies.* LC-DET-2012-066, 2012.

[36] *Gas Detectors Developement group at CERN*, 2014. URL: `www.cern.ch/GDD`.

[37] M. Chefdeville. *Development of micromegas-like gaseous detectors using a pixel readout chip as collecting anode.* Ph.D. thesis, University of Twente, Ede, 2009.

[38] The COMPASS Collaboration. *COMPASS-II Proposal.* CERN-SPSC-2010-014, 2010.

[39] G. Charpak et al. *Progress in the development of a S-RETGEM-based detector for an early forest fire warning system.* Journal of Instrumentation, 4(12):P12007, 2009.

[40] S. Duval et al. *MPGDs in Compton imaging with liquid-xenon.* Journal of Instrumentation, 4(12):P12008, 2009.

[41] F. Sauli. *GEM: A new concept for electron amplification in gas detectors.* Nuclear Instruments and Methods in Physics Research Section A: Accelerators, Spectrometers, Detectors and Associated Equipment, 386(2-3):531–534, 1997.

[42] S. D. Pinto et al. *Progress on large area GEMs.* Journal of Instrumentation, 4(12):P12009, 2009.

[43] L. Hallermann. *Analysis of GEM Properties and Development of a GEM Support Structure for the ILD Time Projection Chamber.* Ph.D. thesis, Universität Hamburg, 2010. DESY-THESIS-10-015.

[44] Y. Giomataris et al. *MICROMEGAS: a high-granularity position-sensitive gaseous detector for high particle-flux environments.* Nuclear Instruments and Methods in Physics Research Section A: Accelerators, Spectrometers, Detectors and Associated Equipment, 376(1):29 – 35, 1996. ISSN 0168-9002.

[45] D. Attié et al. *A Piggyback resistive Micromegas.* Journal of Instrumentation, 8(05):P05019, 2013.

[46] D. Petersen. *Development of a Low - Material TPC Endplate for ILD.* LC-DET-2012-72, 2012.

[47] R. Veenhof. *Choosing a gas mixture for the ALICE TPC.* ALICE-INT-2003-29, 2003.

[48] T. Behnke et al. *A lightweight field cage for a large TPC prototype for the ILC.* Journal of Instrumentation, 5(10):P10011, 2010.

[49] T. Behnke et al. *Status and Plans of the Large TPC Prototype for the ILC.* EUDET-Memo-2007-37, 2008.

[50] M. Lupberger. *The Pixel-TPC: first results from an 8-InGrid module.* Journal of Instrumentation, 9(01):C01033, 2014.

[51] C. Brezina et al. *Operation of a GEM-TPC With Pixel Readout.* Nuclear Science, IEEE Transactions on, 59(6):3221–3228, 2012. ISSN 0018-9499.

[52] J. Kaminski. *Developing studies for a Time Projection Chamber at the International Linear Collider (ILC).* Ph.D. thesis, Universität Karlsruhe, 2005.

[53] *CeramTech*. URL: `http://www.ceramtec.de/substrate/`.

[54] T. Behnke et al. *A novel self-supporting GEM-based amplification structure for a Time Projection Chamber at the ILC*. Journal of Instrumentation, 8(12):P12009, 2013.

[55] R. Yonamine. *R&D of MPGD-readout TPC for the International Linear Collider experiment*. Journal of Instrumentation, 7(06):C06011, 2012.

[56] M. Dixit et al. *Micromegas TPC studies at high magnetic fields using the charge dispersion signal*. Nuclear Instruments and Methods in Physics Research Section A: Accelerators, Spectrometers, Detectors and Associated Equipment, 581(1-2):254–257, 2007. ISSN 0168-9002. VCI 2007 Proceedings of the 11th International Vienna Conference on Instrumentation.

[57] D. Bertrand et al. *A prototype readout system for the LCTPC*. EUDET-Memo-2008-06, 2008.

[58] L. Shi. *Characterization of a compact, high resolution readout system for micro - pattern gaseous detectors*. Master's thesis, University of Lund, 2013.

[59] N. Abgrall et al. *Time projection chambers for the T2K near detectors*. Nuclear Instruments and Methods in Physics Research Section A: Accelerators, Spectrometers, Detectors and Associated Equipment, 637(1):25 – 46, 2011. ISSN 0168-9002.

[60] D. Attié. *Two-Phase CO_2 cooling*. 2013. URL: `http://irfu.cea.fr/Spp/ILC-TPC/home/talks/2013/`.

[61] B. Verlaat et al. *TRACI, A multipurpose CO_2 cooling system for R&D*. 10th IIR Gustav Lorentzen Conference on Natural Refrigerants, GL-208, 2012.

[62] D. A. Deb Sankar Bhattacharya, Paul Colas. *Test of a two-phase CO_2 Cooling System with a Micromegas Module*. LC-DET-2014-005, 2014.

[63] M. Clemens et al. *Discrete electromagnetism with the finite integration technique*. Progress In Electromagnetics Research, 32:65–87, 2001.

[64] T. Weiland. *A discretization model for the solution of Maxwell's equations for six-component fields*. Archiv Elektronik und Übertragungstechnik, 31:116–120, 1977.

[65] B. Krietenstein et al. *The perfect boundary approximation technique facing the big challenge of high precision field computation*. In *Proceedings of the XIX International Linear Accelerator Conference (LINAC 98), Chicago, USA*, pages 860–862. 1998.

[66] K. Zenker. *A Garfield++ interface for CST*. LC-TOOL-2013-022, 2013.

[67] C. A. Felippa et al. *The Finite Element Method in Solid Mechanics*. Numerical Solution of Field Problems in Continuum Physics, American Mathematical Society(SIAM-AMS Proceedings II):210–252, 1969.

[68] K. Li et al. *An 8-node brick element with mixed formulation for large deformation analyses*. Computer Methods in Applied Mechanics and Engineering, 141(1-2):157–204, 1997. ISSN 0045-7825.

[69] R. Veenhof. *GARFIELD, recent developments*. Nucl.Instrum.Meth., A419:726–730, 1998.

[70] K. Zenker et al. *Garfield++*. URL: `http://garfieldpp.web.cern.ch/garfieldpp/`.

[71] S. Biagi. *Monte Carlo simulation of electron drift and diffusion in counting gases under the influence of electric and magnetic fields*. Nuclear Instruments and Methods in Physics Research Section A: Accelerators, Spectrometers, Detectors and Associated Equipment, 421(1):234–240, 1999.

[72] J. A. Hornbeck. *The drift velocities of molecular and atomic ions in Helium, Neon and Argon*. Phys. Rev., 84:615–620, 1951.

[73] P. Correia et al. *A dynamic method for charging-up calculations: the case of GEM*. JINST, 9:P07025, 2014.

[74] S. Lotze. *Ion Backdrift Minimisation in a GEM-Based TPC Readout*. Ph.D. thesis, RWTH Aachen, 2006.

[75] M. Killenberg et al. *Modelling and measurement of charge transfer in multiple GEM structures*. Nuclear Instruments and Methods in Physics Research Section A: Accelerators, Spectrometers, Detectors and Associated Equipment, 498(1):369–383, 2003.

[76] B. Sobloher. *Simulationsstudien zu GEM-Folien für die Auslese einer TPC*. Ph.D. thesis, RWTH Aachen, 2002.

[77] F. Beißel. *HV Current Monitor*. RWTH Aachen, 1999. Revision V3.0.

[78] M. C. Altunbas et al. *Construction, test and commissioning of the triple-GEM tracking detector for COMPASS*. Nuclear Instruments and Methods, A490:177–203, 2002.

[79] R. Menzen. *Charakterisierung von GEMs*. Master's thesis, Rheinische Friedrich-Wilhelms-Universität Bonn, 2010.

[80] K. Zenker. *Study of electrostatic distortions and possible corrections for a GEM based TPC readout module.* LC-DET-2013-17, 2013.

[81] T. Behnke et al. *GEM module design for the ILD TPC.* Journal of Instrumentation, 8(10):C10010, 2013.

[82] R. Yatsukawa. *Private communication.*

[83] M. Ball. *Methods and Results for Calibration and Track Separation of a GEM Based TPC Using an UV-Laser.* Ph.D. thesis, Universität Hamburg, 2008. DESY-THESIS-2008-051.

[84] *ALICE web page*, 2014. URL: `http://aliceinfo.cern.ch/TPC/node/13`.

[85] D. Lide. *CRC Handbook of Chemistry and Physics: 1998 - 1999 ; a Ready-reference Book of Chemical and Physical Data.* CRC Press, 1998. ISBN 9780849304798.

[86] R. M. Eastment et al. *Work function measurements on (100), (110) and (111) surfaces of aluminium.* Journal of Physics F: Metal Physics, 3(9):1738, 1973.

[87] V. K. Agarwala et al. *Work function changes during low pressure oxidation of aluminum at room temperature.* Surface Science, 45(2):470 – 482, 1974. ISSN 0039-6028.

[88] J. Abele et al. *The laser system for the STAR time projection chamber.* Nucl.Instrum.Meth., A499:692–702, 2003.

[89] T. T. N. T. Group. *T2K ND280 TPC Technical Design Report.* Technical report, 2006.

[90] P. Karlitschek et al. *Suppression of solarization effects in optical fibers for 266-nm laser radiation.* Proc. SPIE, 2966:620–625, 1997.

[91] C. Grefe. *Magnetic Field Map for a Large TPC Prototype.* Master's thesis, Universität Hamburg, 2008. DESY-THESIS-2008-052.

[92] J. Abernathy et al. *MarlinTPC: A Marlin based common TPC software framework for the LC-TPC collaboration.* LCTPC Collaboration, EUDET-Report-2007-04, 2007.

[93] F. Gaede. *Marlin and LCCD: Software tools for the ILC.* Nuclear Instruments and Methods, A(559):177, 2006.

[94] A. Münnich. *Simulation Studies for a High Resolution Time Projection Chamber at the International Linear Collider.* Ph.D. thesis, RWTH Aachen, 2007.

[95] A. Liquide. *Gas Encyclopedia*. URL: http://encyclopedia.airliquide.com.

Acknowledgements

First of all I would like to thank Ties for his support of my work and all the things he organises without one even knowing that they need to be organised. This allowed me to concentrate on the scientific work. I also would like to thank Erika Garutti for taking over the duties of the second referee on short notice and Georg Steinbrück for taking part in the disputation committee on very short notice.

In order to realise my laser measurements at the DESY Test Beam I was supported by many different people: Kolja Beil and the laser research group of the University of Hamburg for providing support in the laser calibration, Reza Hodajerdi and the ALPS group for the support of the laser calibration, Leif and Ulf for the support of the electronics, David Attié for his support of the MicroMegas setup and of course all people that where involved in the data taking.
For my simulation studies I was supported by the main developers of Garfield++ – Rob Veenhof and Heinrich Schindler from CERN, who advised and supported me.
The small prototype TPC measurements were done with the setup from Bonn thanks to Jochen Kaminski.
Finally, I had the great opportunity to work for Takeshi and Keisuke in the TPC group at KEK, which allowed me to visit Japan and to get to know the interesting Japanese culture. All these people I would like to thank for their support.

I also would like to thank all members of the FLC group for the nice and friendly atmosphere. In particular, I want to thank Volker and Dörte for their technical support, Frank and Christoph for their software suggestions and Karsten and Jenny for proofreading my thesis. Last but not least I like to thank Annika, Astrid, Felix, Madalina, Oliver, Ralf and all other FLC PhD students for the daily discussion, which were luckily not always connected to physics. I also enjoyed very much the leisure activities with Benedikt and Felix, who also kindly provided help with their cars several times.

Finally, I would like to thank my family for supporting me all the time and of course most of all I thank my wife Anne for her love and support all the time.

Erklärung

Hiermit versichere ich an Eides statt, dass ich die vorliegende Dissertationsschrift selbst verfasst und keine anderen als die angegebenen Quellen und Hilfsmittel benutzt habe.

Klaus Zenker
Hamburg, November 2014